

# Numerically exact studies of ultracold atoms on optical lattices

Von der Fakultät Mathematik und Physik

der Universität Stuttgart

zur Erlangung der Würde eines

Doktors der Naturwissenschaften (Dr. rer. nat.)

genehmigte Abhandlung

Vorgelegt von

**Marcos Rigol Madrazo**

aus Holguín (Cuba)

Hauptberichter: Prof. Dr. Alejandro Muramatsu

Mitberichter: Prof. Dr. Ulrich Weiß

Tag der mündlichen Prüfung: 15.07.2004

Institut für Theoretische Physik der Universität Stuttgart

2004



*... Y comprendía, ahora, que el hombre nunca sabe para quién padece y espera. Padece y espera y trabaja para gentes que nunca conocerá, y que a su vez padecerán y esperarán y trabajarán para otros que tampoco serán felices, pues el hombre ansía siempre una felicidad situada más allá de la porción que le es otorgada. Pero la grandeza del hombre está precisamente en querer mejorar lo que es. En imponerse Tareas. En el Reino de los Cielos no hay grandeza que conquistar, puesto que allá todo es jerarquía establecida, incógnita despojada, existir sin término, imposibilidad de sacrificio, reposo, deleite. Por ello, agobiado de penas y de Tareas, hermoso dentro de su miseria, capaz de amar en medio de las plagas, el hombre sólo puede hallar su grandeza, su máxima medida en el Reino de Este Mundo.*

*Alejo Carpentier  
(El Reino de Este Mundo)*

to my parents  
to Tin, Aida, and Lula



# Contents

<b>List of figures</b>	<b>V</b>
<b>Zusammenfassung</b>	<b>IX</b>
Übersicht . . . . .	XVII
<b>1 Introduction</b>	<b>1</b>
1.1 Overview . . . . .	9
<b>2 Single species fermions confined on 1-D optical lattices</b>	<b>13</b>
2.1 Confined states and the combination lattice - trapping potential . . . . .	14
2.1.1 Single particle spectrum and its eigenfunctions . . . . .	14
2.1.2 Origin of the confined states . . . . .	17
2.1.3 The characteristic density . . . . .	19
2.2 Center-of-mass oscillations . . . . .	21
2.3 Doubling the periodicity . . . . .	23
2.3.1 Single particle spectrum and the additional ‘slicing’ . . . . .	23
2.3.2 Local density of states and the momentum distribution function . . . . .	26
2.3.3 The phase diagram . . . . .	29
<b>3 The quantum Monte Carlo method</b>	<b>31</b>
3.1 The classical Monte Carlo method . . . . .	31
3.2 The projector QMC algorithm . . . . .	34
3.2.1 Path integral formulation . . . . .	35
3.2.2 Matrix representation . . . . .	36
3.2.3 Equal-time Green’s function and observables . . . . .	39
3.2.4 Quantum Monte Carlo update . . . . .	40

3.2.5	“Wrapping” Green’s functions and the numerical stabilization . . .	43
3.3	The world-line algorithm . . . . .	45
3.3.1	Formalism . . . . .	45
3.3.2	Quantum Monte Carlo update . . . . .	47
3.3.3	The observables . . . . .	48
<b>4</b>	<b>Soft-core bosons confined on 1-D optical lattices</b>	<b>51</b>
4.1	The bosonic Hubbard model . . . . .	52
4.2	The bosonic Hubbard model in a trap . . . . .	53
4.2.1	Local phases in a harmonic trap . . . . .	53
4.2.2	The global compressibility . . . . .	54
4.2.3	The phase diagram . . . . .	57
<b>5</b>	<b>Two component fermions confined on 1-D optical lattices</b>	<b>59</b>
5.1	The Hubbard model . . . . .	60
5.2	The Hubbard model in a harmonic trap . . . . .	61
5.2.1	Local phases . . . . .	61
5.2.2	A local order parameter . . . . .	65
5.2.3	Local spin-spin correlations . . . . .	67
5.3	Local quantum criticality and universality . . . . .	68
5.4	Momentum distribution function . . . . .	72
5.5	Mean-field approximation . . . . .	77
5.5.1	The periodic system . . . . .	78
5.5.2	The harmonic trap . . . . .	81
5.6	Phase Diagram . . . . .	85
5.7	The quartic confining potential . . . . .	87
<b>6</b>	<b>Hard-core bosons on 1D lattices</b>	<b>91</b>
6.1	Exact approach to the ground state properties of hard-core bosons . . . .	91
6.2	Hard-core bosons on periodic systems . . . . .	94
6.3	Hard-core bosons confined in harmonic traps . . . . .	99
6.4	Hard-core bosons trapped in other confining potentials . . . . .	106
6.5	Universal behavior of the natural orbital occupations . . . . .	112

---

<b>7</b>	<b>Quasi-condensation of hard-core bosons at finite momentum</b>	<b>115</b>
7.1	Exact approach to the dynamics of hard-core bosons . . . . .	115
7.2	Momentum distribution function and the natural orbitals . . . . .	117
7.3	Equal-time one-particle density matrix and the quasi-condensates . . . . .	120
7.4	An atom laser . . . . .	123
<b>8</b>	<b>Summary and Conclusions</b>	<b>125</b>
<b>A</b>	<b>Single species fermions confined on 2D optical lattices</b>	<b>129</b>
<b>B</b>	<b>The central limit theorem</b>	<b>135</b>
<b>C</b>	<b>The Hubbard-Stratonovich transformation</b>	<b>139</b>
<b>D</b>	<b>Determinants of different-sized matrices</b>	<b>141</b>
	<b>Bibliography</b>	<b>142</b>
	<b>Publications</b>	<b>153</b>
	<b>Curriculum Vitae</b>	<b>157</b>
	<b>Acknowledgments</b>	<b>159</b>





# List of Figures

2.1	Single particle spectrum and level spacing in a harmonic trap . . . . .	15
2.2	Harmonic oscillator orbitals . . . . .	16
2.3	Density and momentum profiles in a harmonic trap . . . . .	18
2.4	Filling required for the formation of the local insulator . . . . .	20
2.5	Single particle spectrum and level spacing in a trap with power $\alpha = 6$ . .	20
2.6	Center-of-mass oscillations . . . . .	21
2.7	Momentum distribution function after the displacement of the trap . . .	22
2.8	Evolution of the density in a harmonic trap with an alternating potential	24
2.9	Single particle spectrum and level spacing in a harmonic trap with an alternating potential . . . . .	24
2.10	Orbitals in a harmonic trap with an alternating potential . . . . .	25
2.11	Local density of states in a harmonic trap with an alternating potential .	27
2.12	Density and momentum profiles in a harmonic trap with an alternating potential . . . . .	28
2.13	Phase diagram in a harmonic trap with an alternating potential . . . . .	29
3.1	Checkerboard decomposition with world-lines and plaquette weights . . .	47
3.2	World-lines moves . . . . .	48
4.1	Zero-temperature phase diagram for the boson-Hubbard model . . . . .	52
4.2	Evolution of the local density in a harmonic trap . . . . .	54
4.3	Density and compressibility profiles. . . . .	55
4.4	Number of bosons as a function of the chemical potential . . . . .	56
4.5	Local compressibility as a function of the local density . . . . .	56
4.6	Phase diagram of bosons confined in a harmonic potential . . . . .	57

5.1	Zero temperature phase diagrams for the fermion-Hubbard model . . . . .	60
5.2	Evolution of the local density in a harmonic trap . . . . .	62
5.3	Density and variance profiles for different fillings . . . . .	63
5.4	Density, variance, and local compressibility profiles for different values of $U/t$ . . . . .	64
5.5	Local compressibility as a function of $\ell$ . . . . .	66
5.6	Local spin-spin correlations in a harmonic trap . . . . .	68
5.7	Local compressibility as a function of the local density . . . . .	69
5.8	Exponent of the local compressibility for periodic systems vs the density . . . . .	70
5.9	Variance as a function of the local density . . . . .	71
5.10	Variance as a function of the local density close to the Mott-insulator . . . . .	72
5.11	Momentum distribution functions for different fillings . . . . .	73
5.12	Momentum distribution function for different values of $U/t$ . . . . .	74
5.13	Density and momentum profiles of noninteracting fermions in a trap with power $\alpha = 10$ . . . . .	75
5.14	Scaling of the density and momentum profiles of noninteracting fermions in a trap with power $\alpha = 10$ . . . . .	76
5.15	Density-density correlations for a periodic system at half filling . . . . .	79
5.16	Spin-spin correlations for a periodic system at half filling . . . . .	80
5.17	Mean-field momentum distribution functions for a periodic system away from half-filling . . . . .	80
5.18	$\langle S^z S^z \rangle_k$ for periodic systems away from half-filling . . . . .	81
5.19	Mean-field density and variance profiles in a harmonic trap . . . . .	81
5.20	Mean-field local compressibility as a function of $\ell$ . . . . .	82
5.21	Mean-field momentum distribution functions in a harmonic trap . . . . .	83
5.22	Local spin-spin correlations in a harmonic trap . . . . .	84
5.23	Mean-field solution in a harmonic trap with spin domain walls . . . . .	85
5.24	Phase diagram of two-component fermions confined in a harmonic trap . . . . .	86
5.25	Density and variance profiles in a harmonic trap on increasing $U/t$ . . . . .	87
5.26	Evolution of the local density in a quartic confining potential . . . . .	88
5.27	Phase diagram of two-component fermions in a quartic confining potential . . . . .	89

6.1	Momentum profiles of hard-core bosons for periodic systems . . . . .	95
6.2	Hard-core boson one-particle density matrix for periodic systems . . . . .	96
6.3	Occupation of the zero-momentum state as a function of the density . . .	97
6.4	Occupation of the first three momenta states in the continuous limit . . .	98
6.5	Density and momentum profiles in a harmonic trap . . . . .	100
6.6	Occupation of the natural orbitals in a harmonic trap . . . . .	101
6.7	Profiles of the two lowest natural orbitals in a harmonic trap . . . . .	102
6.8	One-particle density matrix in a harmonic trap . . . . .	104
6.9	Occupation of the two lowest NO as a function of $\tilde{\rho}$ in a harmonic trap .	105
6.10	Occupation of the three lowest natural orbitals in the continuous limit . .	106
6.11	Profiles of the two lowest natural orbitals in a trap with power $\alpha = 8$ . .	107
6.12	One-particle density in a trap with power $\alpha = 8$ . . . . .	108
6.13	Occupation of the two lowest NO as a function of $\tilde{\rho}$ in a trap with $\alpha = 8$	109
6.14	Level spacing in a trap with power $\alpha = 8$ . . . . .	110
6.15	Occupation of the three lowest natural orbitals in a trap with $\alpha = 8$ in the continuous limit . . . . .	111
6.16	Comparison between the occupations of the lowest NO and our fits . . .	112
6.17	Occupation of the natural orbitals vs $\eta$ . . . . .	113
6.18	Log-log plots of the momentum distribution function in harmonic traps with different fillings . . . . .	113
7.1	Density and momentum profiles for the time evolution of a Fock state of hard-core bosons . . . . .	117
7.2	Evolution of the natural orbitals and their occupations . . . . .	118
7.3	Evolution of the natural orbitals and their Fourier transform . . . . .	119
7.4	Evolution of the one-particle density matrix . . . . .	120
7.5	Scaled lowest natural orbital and its maximum occupation during the time evolution of a Fock state . . . . .	121
7.6	Evolution of the lowest natural orbital occupation for different number of particles . . . . .	123
7.7	Density and momentum profiles for the time evolution of a Fock state of hard-core bosons restricted to evolve only to the right . . . . .	124

---

A.1	Single particle spectrum and level spacing in a 2D harmonic trap . . . . .	130
A.2	Density and momentum profiles in a 2D harmonic trap . . . . .	131
A.3	Density and momentum profiles in a 2D harmonic trap with an alternating potential . . . . .	132
A.4	Local compressibility in a 2D harmonic trap with an alternating potential	133

# Zusammenfassung

Ultrakalte Quantengase sind in den letzten Jahren zu einem theoretisch wie experimentell äußerst aktiven Forschungsgebiet geworden [1–5]. Einer der Hauptgründe dafür war die Realisierung von Bose-Einstein-Kondensaten (BEC) in verdünnten Gasen der Alkalimetalle nahe dem absoluten Temperaturnullpunkt bei Bruchteilen eines Mikrokelvins [6–8]. Die Bedeutung dieser Experimente wurde 2001 mit der Verleihung des Nobelpreises an die führenden Gruppen gewürdigt [9, 10].

Die für BEC-Experimente benötigten extremen Temperaturen lassen sich durch die Kombination von Laser- und evaporativem Kühlen erreichen. Dabei werden die Alkaliatome zuerst in einer magnetooptischen Falle (MOT) mit Hilfe von drei zueinander senkrechten Laserstrahlpaaren vorgekühlt, welche leicht von einer atomaren Absorptionsslinie rotverschoben sind. Ein Atom im Kreuzungspunkt der Lichtstrahlen sieht bei Bewegung ein entgegenkommendes, zur Resonanz hin blauverschobenes Lichtfeld und wird durch Absorption eines Photons gebremst. Der Rückstoßimpuls bei der späteren Emission verschwindet im Mittel über viele Absorptionsprozesse. Die entsprechende Rückstoßenergie begrenzt diese Technik jedoch auf Temperaturen im  $\mu\text{K}$ -Bereich. Im zweiten Schritt wird das Gas in einer magnetischen Falle durch selektives Entfernen der schnellsten Atome evaporativ gekühlt. Nach Rückkehr der verbleibenden Atome ins thermische Gleichgewicht mittels Zwei-Teilchen-Stößen beobachtet man Temperaturen von einigen Nanokelvin. Allgemein ist zu beachten, dass bei den benötigten Temperaturen und Dichten BEC nur metastabil ist. Der Übergang in den kondensierten Gleichgewichtszustand wird jedoch durch die bei geringen Dichten sehr kleine Wahrscheinlichkeit von Drei-Körper-Stößen verhindert, da kaum Cluster gebildet werden.

Ein weitgehendes theoretisches Verständnis der Experimente erreicht man mit der im folgenden dargestellten *mean-field* Beschreibung. Der Hamiltonianoperator in zweiter

Quantisierung für wechselwirkende Bosonen in einem einschließenden Potential  $V(\mathbf{r})$  ist

$$H = \int d\mathbf{r} \hat{\Psi}^\dagger(\mathbf{r}) \left[ -\frac{\hbar^2}{2m} \nabla^2 + V(\mathbf{r}) \right] \hat{\Psi}(\mathbf{r}) + \frac{1}{2} \int d\mathbf{r} d\mathbf{r}' \hat{\Psi}^\dagger(\mathbf{r}) \hat{\Psi}^\dagger(\mathbf{r}') U(\mathbf{r}-\mathbf{r}') \hat{\Psi}(\mathbf{r}') \hat{\Psi}(\mathbf{r}), \quad (1)$$

Aufgrund der geringen Dichte sind hier alle Wechselwirkungen von mehr als zwei Atomen vernachlässigt worden.  $U(\mathbf{r}-\mathbf{r}')$  bezeichnet das Wechselwirkungspotential zweier Teilchen,  $m$  die Masse eines Atoms und  $\hat{\Psi}^\dagger(\mathbf{r})$  [ $\hat{\Psi}(\mathbf{r})$ ] den Operator, der am Ort  $\mathbf{r}$  ein Boson erzeugt [vernichtet], so dass folgende Kommutationsrelationen erfüllt sind:

$$[\hat{\Psi}(\mathbf{r}), \hat{\Psi}^\dagger(\mathbf{r}')] = \delta(\mathbf{r} - \mathbf{r}'), \quad [\hat{\Psi}(\mathbf{r}), \hat{\Psi}(\mathbf{r}')] = [\hat{\Psi}^\dagger(\mathbf{r}), \hat{\Psi}^\dagger(\mathbf{r}')] = 0. \quad (2)$$

Daraus erhält man die Bewegungsgleichung für das bosonische Feld  $\hat{\Psi}(\mathbf{r}, \tau)$

$$\begin{aligned} i\hbar \frac{\partial}{\partial \tau} \hat{\Psi}(\mathbf{r}, \tau) &= [\hat{\Psi}(\mathbf{r}, \tau), H] \\ &= \left[ -\frac{\hbar^2}{2m} \nabla^2 + V(\mathbf{r}) + \int d\mathbf{r}' \hat{\Psi}^\dagger(\mathbf{r}', \tau) U(\mathbf{r} - \mathbf{r}') \hat{\Psi}(\mathbf{r}', \tau) \right] \hat{\Psi}(\mathbf{r}, \tau) \end{aligned} \quad (3)$$

Man kann nun ansetzen, dass der BEC-Phasenübergang zu einer spontanen Symmetriebrechung führt, so dass man einen Ordnungsparameter einführen kann und sich der Feldoperator schreiben lässt als <sup>1</sup>

$$\hat{\Psi}(\mathbf{r}, \tau) = \Phi(\mathbf{r}, \tau) + \left[ \hat{\Psi}(\mathbf{r}, \tau) - \langle \hat{\Psi}(\mathbf{r}, \tau) \rangle \right], \quad (4)$$

$\Phi(\mathbf{r}, \tau) \equiv \langle \hat{\Psi}(\mathbf{r}, \tau) \rangle$  wird als Wellenfunktion des Kondensats bezeichnet<sup>2</sup>.

Für ultrakalte Gase von Alkaliatomen reichen die bei Atomstößen vorliegenden Energien im Falle eines nichtverschwindenden Drehimpulses nicht für die Überwindung der

---

<sup>1</sup>Korrekturen durch kollektive Anregungen lassen sich mit Hilfe der Bogoliubov-Näherung [3]

$$\hat{\Psi}(\mathbf{r}, \tau) = \Phi(\mathbf{r}, \tau) + \hat{\Psi}'(\mathbf{r}, \tau)$$

berechnen, wobei  $\Phi(\mathbf{r}, \tau) = \langle \hat{\Psi}(\mathbf{r}, \tau) \rangle$ , und

$$\hat{\Psi}'(\mathbf{r}, \tau) = \sum_j u_j(\mathbf{r}) \alpha_j(\tau) + v_j^*(\mathbf{r}) \alpha_j^\dagger(\tau),$$

die Anregungen beschreibt. Die Erzeuger- und Vernichtoperatoren für Bogoliubov-Quasiteilchen,  $\alpha_j^\dagger(\tau)$  und  $\alpha_j(\tau)$ , haben die Amplituden  $v_j^*(\mathbf{r})$  und  $u_j(\mathbf{r})$ , und erfüllen die Bogoliubov-de Gennes-Gleichungen [3].

<sup>2</sup>Bei endlicher Teilchenzahl, wie sie in Experimenten vorliegt, ist spontane Symmetriebrechung nicht möglich. Das Konzept einer Wellenfunktion des Kondensats lässt sich jedoch auf diesen Fall erweitern: es beschreibt die Eigenfunktion der Einteilchendichtematrix, die zum größten Eigenwert gehört und für BEC eine makroskopische Besetzungszahl hat.

Zentrifugalbarriere. Daher ist lediglich  $s$ -Wellenstreuung für die Beschreibung relevant und  $U(\mathbf{r} - \mathbf{r}')$  kann durch eine effektive Wechselwirkung

$$U(\mathbf{r} - \mathbf{r}') = \frac{4\pi\hbar^2 d}{m} \delta(\mathbf{r} - \mathbf{r}'), \quad (5)$$

ersetzt werden ( $d$  ist die  $s$ -Wellen-Streulänge). Nimmt man an, dass der Anteil nichtkondensierter Atome, und damit  $\left[ \hat{\Psi}(\mathbf{r}, \tau) - \langle \hat{\Psi}(\mathbf{r}, \tau) \rangle \right]$ , klein ist, so vereinfacht sich Gl. (3) zur Gross-Pitaevskii-Gleichung (GP)

$$i\hbar \frac{\partial}{\partial \tau} \Phi(\mathbf{r}, \tau) = \left[ -\frac{\hbar^2}{2m} \nabla^2 + V(\mathbf{r}) + \frac{4\pi\hbar^2 d}{m} |\Phi(\mathbf{r}, \tau)|^2 \right] \Phi(\mathbf{r}, \tau). \quad (6)$$

Diese Gleichung beschreibt in guter Näherung die in Experimenten zu beobachtende Physik verdünnter ultrakalter Bosegase. Ihr Gültigkeitsbereich beschränkt sich auf sehr niedrige Temperaturen, große Teilchenzahlen und  $s$ -Wellen-Streulängen, die viel kleiner als der Abstand der Gasatome sind.

Neuerdings erlauben Experimente auch die Untersuchung stark korrelierter Systeme. Besonders interessant aufgrund ihrer Bedeutung für die Festkörperphysik sind die durch Interferenz von Laserstrahlen erzeugten optischen Gitter [11]<sup>3</sup>. Diese bestehen aus einem periodischen optischen Potential, in dem ein Zwei-Niveau-Atom je nach Rot- oder Blauverschiebung der Laserfrequenz relativ zur Absorptionslinie von den Intensitätsmaxima oder -minima angezogen wird<sup>4</sup>.

In zweiter Quantisierung ist der Hamiltonianoperator für ein verdünntes ultrakaltes Bosegas in einem optischen Gitter gegeben durch

$$H = \int d\mathbf{r} \hat{\Psi}^\dagger(\mathbf{r}) \left[ -\frac{\hbar^2}{2m} \nabla^2 + V(\mathbf{r}) + V_0(\mathbf{r}) \right] \hat{\Psi}(\mathbf{r}) + \frac{1}{2} \frac{4\pi\hbar^2 d}{m} \int d\mathbf{r} \hat{\Psi}^\dagger(\mathbf{r}) \hat{\Psi}^\dagger(\mathbf{r}) \hat{\Psi}(\mathbf{r}) \hat{\Psi}(\mathbf{r}), \quad (7)$$

wobei

$$V_0(\mathbf{r}) = V_{0x} \cos^2(kx) + V_{0y} \cos^2(ky) + V_{0z} \cos^2(kz) \quad (8)$$

das durch das optische Gitter erzeugte Potential beschreibt und der Wellenvektor  $k = 2\pi/\lambda$  durch die Laserwellenlänge  $\lambda$  bestimmt wird. Die Periodizität des Gitters ist  $a = \lambda/2$ . Das periodische Potential sorgt für eine verstärkte Lokalisierung der Wellenfunktion. Für den Fall, dass die betrachteten Energien kleiner als der Abstand zwischen erstem und

<sup>3</sup>Für experimentelle Details siehe Ref. [12] und dort angegebene Referenzen

<sup>4</sup>siehe Ref. [13] für eine Herleitung der wirkenden Kräfte.

zweitem Energieband des Gitters sind, lassen sich die bosonischen Feldoperatoren nach den Wannierfunktionen  $[\phi_i(\mathbf{r})]$  des ersten Bandes entwickeln:

$$\hat{\Psi}(\mathbf{r}) = \sum_i b_i \phi_i(\mathbf{r}), \quad \hat{\Psi}^\dagger(\mathbf{r}) = \sum_i b_i^\dagger \phi_i^*(\mathbf{r}). \quad (9)$$

Dabei bilden die Wannierfunktionen eine Orthonormalbasis

$$\sum_i \phi_i(\mathbf{r}) \phi_i^*(\mathbf{r}') = \delta(\mathbf{r} - \mathbf{r}'), \quad \int d\mathbf{r} \phi_i(\mathbf{r}) \phi_j^*(\mathbf{r}) = \delta_{ij}, \quad (10)$$

und die Erzeuger- ( $b_i^\dagger$ ) und Vernichtoperatoren ( $b_i$ ) für ein Boson am Platz  $i$  erfüllen die Kommutationsrelationen

$$[b_i, b_j^\dagger] = \delta_{ij}, \quad [b_i, b_j] = [b_i^\dagger, b_j^\dagger] = 0, \quad (11)$$

Diese folgen aus den entsprechenden Gleichungen für die bosonischen Feldoperatoren [Gl. (2)] sowie den Eigenschaften der Wannierfunktionen [Gl. (10)].

Drückt man den Hamiltonianoperator (7) durch Erzeuger- und Vernichtoperatoren am Platz  $i$  aus, so ergibt sich

$$H = - \sum_{ij} (t_{ij} + V_{ij}) b_i^\dagger b_j + \sum_{ijkl} U_{ijkl} b_i^\dagger b_j^\dagger b_k b_l, \quad (12)$$

wobei

$$\begin{aligned} t_{ij} &= - \int d\mathbf{r} \phi_i^*(\mathbf{r}) \left[ -\frac{\hbar^2}{2m} \nabla^2 + V_0(\mathbf{r}) \right] \phi_j(\mathbf{r}) \\ V_{ij} &= \int d\mathbf{r} \phi_i^*(\mathbf{r}) V(\mathbf{r}) \phi_j(\mathbf{r}) \\ U_{ijkl} &= \frac{2\pi\hbar^2 d}{m} \int d\mathbf{r} \phi_i^*(\mathbf{r}) \phi_j^*(\mathbf{r}) \phi_k(\mathbf{r}) \phi_l(\mathbf{r}). \end{aligned} \quad (13)$$

Auf Jaksch *et al.* [14] geht die Beobachtung zurück, dass der Hamiltonianoperator (12) unter realistischen experimentellen Bedingungen in sehr guter Näherung durch den Bose-Hubbard-Hamiltonianoperator ersetzt werden kann. Aufgrund der Lokalisierung der Wannierfunktionen sind nämlich Hüpfamplituden zu übernächsten und weiteren Nachbarn (d.h.  $t_{ij}$  für  $|i - j| > 1$ ) sowie Wechselwirkungen mit nächsten und weiteren Nachbarn ( $U_{ijkl}$  für  $i \neq j \neq k \neq l$ ) vernachlässigbar. Desweiteren sind in der Summe, die das einschließende Potential beschreibt, im Vergleich zum Term  $V_i \equiv V_{ii}$  alle übrigen vernachlässigbar. Bei sich sehr langsam änderndem Potential kann man zusätzlich  $V_i \approx$



$V(\mathbf{r}_i)$  nähern. Insgesamt folgt damit aus Gl. (12) bis auf eine globale Nullpunktsverschiebung beim chemischen Potential

$$H = -t \sum_i (b_i^\dagger b_{i+1} + \text{H.c.}) + \sum_i V_i n_i + U \sum_i (n_i - 1) n_i, \quad (14)$$

wobei  $n_i = b_i^\dagger b_i$  und

$$t = - \int d\mathbf{r} \phi_i^*(\mathbf{r}) \left[ -\frac{\hbar^2}{2m} \nabla^2 + V_0(\mathbf{r}) \right] \phi_{i+1}(\mathbf{r}), \quad U = \frac{2\pi\hbar^2 d}{m} \int d\mathbf{r} |\phi_i(\mathbf{r})|^4. \quad (15)$$

Explizite Ausdrücke für  $t$  und  $U$  erhält man, wenn  $V_0$  viel größer als die sogenannte Rückstoßenergie  $E_r = \hbar^2 k^2 / 2m$  ist. In diesem Fall lässt sich  $t$  aus der exakt bekannten Breite des niedrigsten Energiebandes in der eindimensionalen Mathieschen Differentialgleichung bestimmen<sup>5</sup>;  $U$  erhält man, wenn man die Wannierfunktion  $\phi_i(\mathbf{r})$  durch die Gaußsche Wellenfunktion des Grundzustands des Potentials um einen Gitterpunkt approximiert [16]:

$$t = \frac{4}{\sqrt{\pi}} \left( \frac{V_0}{E_r} \right)^{3/4} E_r e^{-2\sqrt{\frac{V_0}{E_r}}}, \quad U = \sqrt{\frac{8}{\pi}} \left( \frac{V_0}{E_r} \right)^{3/4} k d E_r. \quad (16)$$

Die obige Herleitung zeigt, dass ultrakalte Basegase in optischen Gittern eine ideale experimentelle Realisierung des Bose-Hubbard-Modells erlauben. Die von Jaksch *et al.* [14] vorgeschlagene Möglichkeit, den Suprafluid-Mott-Isolator-Übergang [17–21] experimentell zu untersuchen, wurde erstmalig in dreidimensionalen Gittern von Greiner *et al.* [11] erreicht. Stöferle *et al.* gelang kürzlich der Nachweis in einer Dimension [22]. Wichtig ist jedoch der Unterschied durch das einschließende Potential im Vergleich zum periodischen Fall. Während beim letzteren Mott-isolierende Phasen nur bei kommensurabler Füllung auftreten [17–21], so ist dies im ersteren Fall für einen kontinuierlichen Bereich von Werten gegeben, und die Mott-Phase tritt immer zusammen mit einer suprafluiden Phase auf [23–27].

Die experimentelle Realisierung ultrakalter Fermigase ist erheblich schwieriger als im bosonischen Fall, da das Pauliprinzip für identische Fermionen  $s$ -Wellenstreuung verbietet. Damit scheitert evaporatives Kühlen bei einkomponentigen Gasen an der

---

<sup>5</sup>für die Mathiesche Differentialgleichung siehe z.B. Ref. [15]. Meist wird sie in ihrer kanonischen Form

$$\frac{d^2 y}{dv^2} + (a - 2q \cos 2v) y = 0,$$

mit zwei beliebigen Parametern  $a$  und  $q$  geschrieben.

fehlenden Rethermalisierung. Dieses Problem ist mittlerweile gelöst durch Kühlung zweikomponentiger Fermigase [28, 29] bzw. gemischter Gase von Bosonen und Fermionen, wobei die Fermionen durch Wechselwirkung mit den Bosonen wieder das thermische Gleichgewicht erreichen [30–33]. Schnelle erzwungene Verdampfung mittels Feshbach-Resonanzen zweier verschiedener Spinzustände desselben Fermions stellt eine weitere Möglichkeit dar [34]. Bei hinreichend niedrigen Temperaturen ist es dann möglich, nur eine Komponente in der Falle zu behalten und somit experimentell ein ideales Fermigas zu erreichen. Ideale Fermigase in harmonischen Fallen sind theoretisch in 1D [35–38] sowie 2D und 3D [39–41] untersucht worden. Die spezielle harmonische Form des Potentials ermöglicht dabei eine Reihe exakter analytischer Resultate für diese Systeme.

Erst kürzlich sind einkomponentige ultrakalte Fermigase in 1D optischen Gittern realisiert worden [42–45]. Untersucht wurden dabei die Eigenschaften nichtwechselwirkender Fermigase und wechselwirkender Bose-Fermi-Mischungen. Von der theoretischen Seite sind Grundzustands- (GS) und Transporteigenschaften (T) nichtwechselwirkender Fermionen in Gittern in Ref. [46, 47] (GS) und [46, 48–50] (T) analysiert worden. In der Zukunft wird man durch Experimente mit zweikomponentigen Fermigasen das fermionische Hubbard-Modell in optischen Gittern realisieren können. Damit ließe sich experimentell der Mott-Metall-Isolator-Übergang, Musterbeispiel für starke Korrelationen, ohne die in Festkörpern unausweichlichen Störeffekte und mit vollständiger Kontrolle über die Parameter realisieren.

Ähnlich zum bosonischen Fall lautet der Hamiltonianoperator für ein ultrakaltes zweikomponentiges Fermigas in einem optischen Gitter

$$\begin{aligned}
 H = & \sum_{\sigma} \int d\mathbf{r} \hat{\Psi}_{\sigma}^{\dagger}(\mathbf{r}) \left[ -\frac{\hbar^2}{2m} \nabla^2 + V(\mathbf{r}) + V_0(\mathbf{r}) \right] \hat{\Psi}_{\sigma}(\mathbf{r}) \\
 & + \frac{1}{2} \frac{4\pi\hbar^2 d}{m} \int d\mathbf{r} \hat{\Psi}_{\sigma_1}^{\dagger}(\mathbf{r}) \hat{\Psi}_{\sigma_2}^{\dagger}(\mathbf{r}) \hat{\Psi}_{\sigma_2}(\mathbf{r}) \hat{\Psi}_{\sigma_1}(\mathbf{r}), \quad (17)
 \end{aligned}$$

wobei  $\sigma_1$  und  $\sigma_2$  die beiden fermionischen Komponenten bezeichnen. In der Folge schreiben wir zur Vereinfachung der Notation  $\sigma_1 \equiv \uparrow$  und  $\sigma_2 \equiv \downarrow$ . Die fermionischen Feldoperatoren erfüllen die Antikommutationsrelationen

$$\left\{ \hat{\Psi}_{\sigma}(\mathbf{r}), \hat{\Psi}_{\sigma'}^{\dagger}(\mathbf{r}') \right\} = \delta_{\sigma\sigma'} \delta(\mathbf{r} - \mathbf{r}'), \quad \left\{ \hat{\Psi}_{\sigma}(\mathbf{r}), \hat{\Psi}_{\sigma'}(\mathbf{r}') \right\} = \left\{ \hat{\Psi}_{\sigma}^{\dagger}(\mathbf{r}), \hat{\Psi}_{\sigma'}^{\dagger}(\mathbf{r}') \right\} = 0. \quad (18)$$

In Gl. (17) werden einschließendes und optisches Potential als unabhängig von der Spezies angenommen. Außerdem sollte die Temperatur hinreichend niedrig sein, so dass nur  $s$ -

Wellenstreuung zwischen den verschiedenen Komponenten möglich ist. Unter den gleichen Voraussetzungen wie im bosonischen Fall lassen sich die Feldoperatoren nach den Wannierfunktionen des ersten Bands entwickeln

$$\hat{\Psi}_\sigma(\mathbf{r}) = \sum_i c_{i\sigma} \phi_i(\mathbf{r}), \quad \hat{\Psi}_\sigma^\dagger(\mathbf{r}) = \sum_i c_{i\sigma}^\dagger \phi_i^*(\mathbf{r}), \quad (19)$$

und man erhält näherungsweise den Hamiltonianoperator des Hubbard-Modells

$$H = -t \sum_{i,\sigma} \left( c_{i\sigma}^\dagger c_{i+1\sigma} + \text{H.c.} \right) + U \sum_i n_{i\uparrow} n_{i\downarrow} + \sum_i V_i n_i \quad (20)$$

$c_{i\sigma}^\dagger$  und  $c_{i\sigma}$  bezeichnen die fermionischen Erzeuger- und Vernichteroperatoren der Komponente  $\sigma$  am Punkt  $i$ . Sie erfüllen die Antikommutationsrelationen

$$\left\{ c_{i\sigma}, c_{j\sigma'}^\dagger \right\} = \delta_{\sigma\sigma'} \delta_{ij}, \quad \left\{ c_{i\sigma}, c_{j\sigma'} \right\} = \left\{ c_{i\sigma}^\dagger, c_{j\sigma'}^\dagger \right\} = 0, \quad (21)$$

welche aus den entsprechenden Antikommutationsrelationen der fermionischen Feldoperatoren [Gl. (18)] und den Eigenschaften der Wannierfunktionen [Gl. (10)] folgen. Der Teilchenzahloperator ist in diesem Fall  $n_i = n_{i\uparrow} + n_{i\downarrow}$ , wobei  $n_{i\sigma} = c_{i\sigma}^\dagger c_{i\sigma}$ . Die Definitionen für  $t$ ,  $U$  und  $V_i$  sind dieselben wie im bosonischen Fall [Gl. (15)].

Innerhalb der verschiedenen experimentell möglichen Konfigurationen sind niedrigdimensionale Systeme in den letzten Jahren auf immer mehr Interesse gestoßen. Diese lassen sich in stark anisotropischen Fällen [31, 51] sowie durch BEC in optischen Gittern [22, 52, 53] realisieren. Besonders interessant ist der quasi-eindimensionale Fall, in dem Quantenfluktuationen die physikalischen Eigenschaften bei sehr niedrigen Temperaturen dominieren. Es wurde gezeigt [54–56], dass sich Bosonen in einem bestimmten, durch große positive Streulänge, niedrige Dichte und geringe Temperatur charakterisierten Parameterbereich wie ein Gas undurchdringbarer Teilchen verhalten, sogenannte *hard core* Bosonen (HCB).

Im eindimensionalen Fall wurde das homogene HCB-Gas zuerst von Girardeau untersucht [57]. Insbesondere zeigte er die Äquivalenz von eindimensionalen HCB zu spinlosen Fermionen. Lenard sowie Vaidya und Tracy [58–60] zeigten später für den homogenen Fall, dass HCB in einer Dimension selbst am Temperaturnullpunkt keine echte Kondensation in den niedrigsten effektiven Einteilchenzustand (niedrigstes natürliches Orbital) aufweist. Es entsteht lediglich eine nicht-diagonale quasi-langreichweitige Ordnung, bei der die Einteilchen-Korrelationsfunktionen algebraisch abfallen. Für die Besetzung

des niedrigsten, am stärksten besetzten effektiven Einteilchenzustands ergibt sich damit  $\sim \sqrt{N_b}$  bei einer Gesamtzahl von  $N_b$  HCB.

In der letzten Zeit sind gezielt die Eigenschaften des Grundzustandes für eindimensionale HCB-Gase in einschließenden harmonischen Fallen erforscht worden [61–65]. Mit Hilfe des oben erwähnten Bose-Fermi-Mappings auf spinlose Fermionen konnten Größen wie Dichte- und Impulsprofile, Besetzungszahlen der einzelnen natürlichen Orbitale sowie deren Wellenfunktionen für endliche Teilchenzahlen berechnet werden. Einige Ergebnisse ließen sich auch auf den thermodynamischen Grenzfall ( $N_b \rightarrow \infty$ ) ausdehnen [65]. Ähnlich wie im homogenen Fall ist die Besetzungszahl des niedrigsten natürlichen Orbitals  $\sim \sqrt{N_b}$  [64, 65], so dass lediglich ein Quasikondensat vorliegt.

Ein weiteres interessantes Gebiet ist die Untersuchung von HCB in einem Gitter, was erst kürzlich experimentell realisiert wurde [66]. Für den eindimensionalen periodischen Fall ist der Hamiltonianoperator

$$H = -t \sum_i \left( b_i^\dagger b_{i+1} + h.c. \right), \quad (22)$$

mit den Nebenbedingungen

$$b_i^{\dagger 2} = b_i^2 = 0, \quad \{b_i, b_i^\dagger\} = 1. \quad (23)$$

$b_i^\dagger$  und  $b_i$  sind die Erzeuger- und Vernichtoperatoren für HCB.

Stellt man  $b_i^\dagger$  und  $b_i$  mit Hilfe von Pauli-Matrizen als

$$b_i^\dagger = \frac{1}{2} (\sigma_i^x + i\sigma_i^y), \quad b_i = \frac{1}{2} (\sigma_i^x - i\sigma_i^y), \quad (24)$$

dar, so wird der Hamiltonianoperator für HCB auf einem Gitter auf das 1D XY-Modell von Lieb, Schulz, und Mattis [67]

$$H_{XY} = -\frac{1}{4} \sum_i [(1 + \gamma)\sigma_i^x \sigma_{i+1}^x + (1 - \gamma)\sigma_i^y \sigma_{i+1}^y] + \frac{1}{2} h \sum_i \sigma_i^z. \quad (25)$$

abgebildet. Dabei sind  $\sigma_i^x, \sigma_i^y, \sigma_i^z$  die Pauli-Matrizen,  $\gamma$  beschreibt die Anisotropie ( $0 \leq \gamma \leq 1$ ) und  $h$  das Magnetfeld in  $z$ -Richtung (im periodischen HCB-Fall sind  $\gamma = 0$  und  $h = 0$ ). Dieses Modell ist in der Literatur in den vergangenen Jahrzehnten ausführlich diskutiert worden, und insbesondere ist das asymptotische Verhalten der Korrelationsfunktionen am Temperaturnullpunkt bekannt [68–71]. Im für HCB relevanten Fall  $\gamma = 0$  und  $h = 0$  fallen die Korrelationsfunktionen  $\rho_{i-j}^\alpha = \langle \sigma_i^\alpha \sigma_j^\alpha \rangle$ , für  $\alpha = x, y$ , algebraisch

wie  $\sim |i - j|^{-1/2}$  ab [68]<sup>6</sup>. Der vor kurzem experimentell realisierte Fall ist komplizierter, weil das einschließende Potential einem zusätzlichen ortsabhängigen transversalen Feld im XY-Hamiltonianoperator entspricht. Da dafür keine analytischen Ergebnisse existieren, ist er im Rahmen dieser Arbeit mit Hilfe einer neu entwickelten exakten numerischen Methode untersucht worden.

## Übersicht

In dieser Arbeit untersuchen wir die Eigenschaften eindimensionaler ultrakalter Quantengase in einer Falle und in optischen Gittern. Wir analysieren sowohl fermionische als auch bosonische System mit verschiedenen numerisch exakten Methoden, wie etwa Quanten Monte Carlo für soft-core Bosonen und zweikomponentige Fermionen sowie eine vor kurzem entwickelte exakte Methode für HCB. Die Gliederung der Arbeit ist wie folgt:

Im folgenden Kapitel (Kapitel 2) untersuchen wir einfache entartete Fermionen in eindimensionalen Gittern [46]. Wir zeigen, dass innerhalb gewisser Bereiche des Spektrums Eigenzustände existieren, welche nur in bestimmten Gebieten nichtverschwindende Teilchenzahlen aufweisen, also auf bestimmte Bereiche des Gitters beschränkt sind. Somit ergibt sich ein qualitativ neuartiges Verhalten im Vergleich zum Fall ohne Gitter [35–38]. Durch Superposition eines weiteren Potentials mit der doppelten Periodizität lassen sich die mit Teilchen besetzten Gebiete weiter aufspalten. Durch die Amplitude dieser Störung lassen sich Breite und Anzahl der Regionen innerhalb eines gegebenen Energiebereichs kontrollieren. Betrachtet man den Grundzustand der Fermionen im Gitter, so kann es zur Bildung von isolierenden Gebieten durch lokale Energielücken kommen. Diese lassen sich durch Betrachtung der lokalen Zustandsdichte identifizieren. Zusätzlich zu den eindimensionalen Ergebnissen präsentieren wir im Anhang A Resultate für zweidimensionale Gitter.

Die Nichtgleichgewichtsdynamik von Fermionen in einer Falle wird für den Fall untersucht, dass der Mittelpunkt der Falle ursprünglich nicht mit der Mitte des Systems zusammenfällt. Damit lassen sich die im Gleichgewichtsfall erhaltenen räumlich begrenzten Zustände realisieren. In bestimmten Parameterbereichen oszilliert der Massenmittelpunkt daher auf einer Seite der Falle. Die hier dargestellten Ergebnisse sind relevant

---

<sup>6</sup>Dasselbe Verhalten der Einteilchendichtematrix zeigt sich für HCB im homogenen Fall [60].

für vor kurzem durchgeführte Experimente mit idealen Fermigasen, bei denen genau diese Eigenschaften beobachtet wurden [42, 43].

Im Kapitel 3 geben wir einen relativ detaillierten Überblick über zwei Quanten-Monte-Carlo-Techniken (QMC), *worldline* QMC und *zero temperature projector* QMC, die in unseren Simulationen von soft-core Bosonen und zweikomponentigen Fermionen Anwendung fanden. Ebenso diskutieren wir die elementaren Grundlagen der klassischen Monte Carlo Methode und zeigen im Anhang B den Beweis des Zentralen Grenzwertsatzes, der theoretischen Basis von Monte Carlo.

Eigenschaften von soft-core Bosonen in optischen Gittern sind Thema des Kapitels 4. QMC-Rechnungen zeigen, dass das in periodischen Systemen verwendete Konzept der kommensurablen Füllung durch ein einschließendes Potential seine Bedeutung verliert. Mott-Gebiete entstehen für einen kontinuierlichen Bereich von Füllfaktoren und treten, wie oben bereits erwähnt, stets zusammen mit suprafluiden Phasen auf. Letzteres spiegelt sich in der Kompressibilität des Gesamtsystems wieder, welche nie verschwindet. Um die lokalen Mott-isolierenden Phasen zu charakterisieren, definieren wir eine zur Varianz der lokalen Dichte proportionale lokale Kompressibilität. Schließlich diskutieren wir das Phasendiagramm für soft-core Bosonen in einer Falle.

Im Kapitel 5 untersuchen wir die Eigenschaften des Grundzustands von zweikomponentigen Fermionen in optischen Gittern [72, 73]. Wie im bosonischen Fall gibt es Mott-isolierende Gebiete für kontinuierliche Bereiche von Füllfaktoren, die wiederum nur zusammen mit kompressiblen Phasen existieren. Wir führen einen lokalen Ordnungsparameter ein, die lokale Kompressibilität, welcher die Mott-isolierenden Phasen eindeutig charakterisiert. Damit untersuchen wir im Detail den Übergang zwischen metallischen und isolierenden Gebieten und finden einen neuen kritischen Exponenten für das Verhalten. Darüberhinaus zeigt sich, dass das Verhalten der lokalen Kompressibilität und der Varianz der Dichte, wie für ein kritisches Phänomen zu erwarten, universell sind, also unabhängig vom einschließenden Potential und der Stärke der Wechselwirkung.

Im folgenden untersuchen wir die Impulsverteilung, welche in der Regel in Experimenten gemessen wird. Der inhomogene Charakter des Systems führt dazu, dass diese Größe kein klares Anzeichen für die Bildung von Mott-Gebieten liefert. Die Untersuchung von Fermionen in einer Falle innerhalb der *mean-field* Näherung (MF) ist ein weiteres Thema dieses Kapitels. Obwohl MF ähnliche Dichteprofile wie die QMC-Simulationen

liefert, ist doch die Art der Phasen unterschiedlich. Wir beenden das Kapitel mit einem Phasendiagramm für Fermionen in einer Dimension. Es erlaubt den Vergleich von Systemen mit unterschiedlichen Füllfaktoren und Krümmungen des einschließenden Potentials, so dass es die Grundlage für das Verständnis zukünftiger Experimente liefert.

Das Kapitel 6 behandelt eine kürzlich entwickelte exakte Methode [74] zur Untersuchung von Grundzustandseigenschaften von HCB in eindimensionalen Gittern. Basierend auf der Jordan-Wigner-Transformation erlaubt es die Behandlung von Systemen mit bis zu  $\sim 10000$  Gitterplätzen. Wir untersuchen das nichtdiagonale Gleichgewichtsverhalten der Einteilchendichtematrix (OPDM) und damit zusammenhängender Größen. Wir finden einen algebraischen Abfall von  $\rho_{ij}$  wie  $x^{-1/2}$  ( $x = |x_i - x_j|$ ) für große  $x$ . Dies ist unabhängig vom konkreten einschließenden Potential und gilt selbst, wenn große Gebiete die Besetzungszahl  $n_i = 1$  aufweisen, und damit die Kohärenz dort verloren geht. Obiges Potenzgesetz bestimmt das asymptotische Verhalten der Teilchenzahl im niedrigsten natürlichen Orbital für den thermodynamischen Grenzfall. Zusätzlich diskutieren wir Korrekturen für endliche Teilchenzahlen bei beliebigen Exponenten des einschließenden Potentials. Darüber hinaus zeigt sich, dass es bei geringen Dichten zu einem algebraischen Abfall der NO Besetzungszahl ( $\lambda_\eta$ ) für große  $\eta$  kommt, ebenfalls mit einem universellen Exponenten. Schließlich analysieren wir den Grenzfall geringer Dichte, welcher äquivalent zum kontinuierlichen System ist.

Der obige Ansatz wird in Kapitel 7 auf HCB-Nichtgleichgewichtssysteme in eindimensionalen Gittern verallgemeinert [75]. Das Gitter führt zu verstärkten Korrelationen und ermöglicht so die Entstehung reiner inkohärenter Fockzustände (ein HCB pro Platz). Bei der freien Zeitentwicklung solcher Zustände beobachten wir die Bildung von quasi-langreichweitigen Korrelationen in der *equal-time* Einteilchendichtematrix (ETOPDM). Die Korrelationen führen zur Bildung von Quasikondensaten bei endlichem Impuls, wobei die Besetzungszahl einem universellen zeitlichen Potenzgesetz folgt. Dieses ist unabhängig von der Zahl der Teilchen im anfänglichen Fockzustand. Schließlich diskutieren wir, wie die diskutierten Ergebnisse zur Realisierung von Atomlasern mit durchstimmbarer Wellenlänge verwendet werden können.





# Chapter 1

## Introduction

The study of ultracold quantum gases has become in the last decade a field of intense experimental and theoretical research [1–5]. Bose-Einstein condensation (BEC) was the main motivation starting the intensive analysis of such systems. BEC was observed for the first time in a series of experiments on dilute vapors of alkali atoms cooled up to extremely low temperatures (fractions of microkelvins) [6–8]. Due to its impact, this achievement was awarded by the Nobel prize in 2001 to the pioneering groups [9, 10].

The very low temperatures required for BEC can be achieved due to the combination of laser and evaporative cooling techniques for alkali atoms, where the experiments are realized in two steps. First the atoms are trapped and precooled in a magneto-optic trap (MOT) using the laser cooling technique. In this technique atoms are illuminated with 6 orthogonal laser beams, which are slightly red-detuned for a particular atomic absorption line. Atoms moving in any direction at the intersection of the laser beams see the light blue-shifted into resonance, so that they absorb a photon in that direction slowing down their motion. The further emission of the absorbed photon occurs in any direction and averages a zero momentum change. With this technique, temperatures of the order of  $\mu\text{K}$  can be achieved. The recoil energy of the emitted photon limits the further reduction of the temperature. At this point, the gas is transferred to a magnetic trap and further cooled using evaporative cooling techniques. In the latter, the hottest atoms are selectively removed from the system and the remaining ones rethermalize via two-body collisions. Temperatures of the order of  $n\text{K}$  are achieved in this case. It is important to mention that at the temperatures and densities required to observe BEC, the equilibrium configuration of the systems would be a solid phase. However, in the experiments, the

ultracold gas is preserved in a metastable phase due to its very dilute character, which makes the three-body collisions (needed to form cluster) rare events.

Theoretically, a fairly complete understanding of the previously mentioned experimental systems can be obtained by the mean-field theory, as explained in the following. In the second quantization language, the many body Hamiltonian describing interacting bosons in a confining potential  $V(\mathbf{r})$  can be written as

$$H = \int d\mathbf{r} \hat{\Psi}^\dagger(\mathbf{r}) \left[ -\frac{\hbar^2}{2m} \nabla^2 + V(\mathbf{r}) \right] \hat{\Psi}(\mathbf{r}) + \frac{1}{2} \int d\mathbf{r} d\mathbf{r}' \hat{\Psi}^\dagger(\mathbf{r}) \hat{\Psi}^\dagger(\mathbf{r}') U(\mathbf{r} - \mathbf{r}') \hat{\Psi}(\mathbf{r}') \hat{\Psi}(\mathbf{r}), \quad (1.1)$$

where due to the very low density of the gas only two-body interactions are assumed to be relevant. The interparticle potential is denoted by  $U(\mathbf{r} - \mathbf{r}')$ , the mass of the atom by  $m$ , and  $\hat{\Psi}^\dagger(\mathbf{r})$  [ $\hat{\Psi}(\mathbf{r})$ ] is the creation [annihilation] operator of the boson field, which satisfy the commutation relations

$$[\hat{\Psi}(\mathbf{r}), \hat{\Psi}^\dagger(\mathbf{r}')] = \delta(\mathbf{r} - \mathbf{r}'), \quad [\hat{\Psi}(\mathbf{r}), \hat{\Psi}(\mathbf{r}')] = [\hat{\Psi}^\dagger(\mathbf{r}), \hat{\Psi}^\dagger(\mathbf{r}')] = 0. \quad (1.2)$$

The equation of motion of the bosonic field ( $\hat{\Psi}(\mathbf{r}, \tau)$ ) can be obtained as

$$\begin{aligned} i\hbar \frac{\partial}{\partial \tau} \hat{\Psi}(\mathbf{r}, \tau) &= [\hat{\Psi}(\mathbf{r}, \tau), H] \\ &= \left[ -\frac{\hbar^2}{2m} \nabla^2 + V(\mathbf{r}) + \int d\mathbf{r}' \hat{\Psi}^\dagger(\mathbf{r}', \tau) U(\mathbf{r} - \mathbf{r}') \hat{\Psi}(\mathbf{r}', \tau) \right] \hat{\Psi}(\mathbf{r}, \tau) \end{aligned} \quad (1.3)$$

At this point one may assume that due to the BEC phase transition there is spontaneously symmetry breaking, such that it is possible to introduce an order parameter and the field operator may be written as<sup>1</sup>

$$\hat{\Psi}(\mathbf{r}, \tau) = \Phi(\mathbf{r}, \tau) + \left[ \hat{\Psi}(\mathbf{r}, \tau) - \langle \hat{\Psi}(\mathbf{r}, \tau) \rangle \right], \quad (1.4)$$

---

<sup>1</sup>Corrections due to small collective excitations can be obtained using the Bogoliubov approximation [3]

$$\hat{\Psi}(\mathbf{r}, \tau) = \Phi(\mathbf{r}, \tau) + \hat{\Psi}'(\mathbf{r}, \tau)$$

with  $\Phi(\mathbf{r}, \tau) = \langle \hat{\Psi}(\mathbf{r}, \tau) \rangle$ , and

$$\hat{\Psi}'(\mathbf{r}, \tau) = \sum_j u_j(\mathbf{r}) \alpha_j(\tau) + v_j^*(\mathbf{r}) \alpha_j^\dagger(\tau),$$

being the excitations. In the equation above,  $\alpha_j^\dagger(\tau)$  and  $\alpha_j(\tau)$  are the creation and annihilation operators of the Bogoliubov quasi-particles, which have amplitudes  $v_j^*(\mathbf{r})$  and  $u_j(\mathbf{r})$ , respectively, satisfying the Bogoliubov-de Gennes equations [3].

where  $\Phi(\mathbf{r}, \tau) \equiv \langle \hat{\Psi}(\mathbf{r}, \tau) \rangle$  is known as the condensate wave-function<sup>2</sup>. In addition, for an ultracold alkali gas only  $s$ -wave collisions are relevant. This is so because the energies of the colliding atoms are too low to penetrate the centrifugal barrier imposed for an angular momentum higher than zero. Then it is possible to replace  $U(\mathbf{r} - \mathbf{r}')$  by an effective interaction

$$U(\mathbf{r} - \mathbf{r}') = \frac{4\pi\hbar^2 d}{m} \delta(\mathbf{r} - \mathbf{r}'), \quad (1.5)$$

where  $d$  is the  $s$ -wave scattering length. Assuming the depletion of the condensate  $[\hat{\Psi}(\mathbf{r}, \tau) - \langle \hat{\Psi}(\mathbf{r}, \tau) \rangle]$  to be small, Eq. (1.3) can be rewritten as

$$i\hbar \frac{\partial}{\partial \tau} \Phi(\mathbf{r}, \tau) = \left[ -\frac{\hbar^2}{2m} \nabla^2 + V(\mathbf{r}) + \frac{4\pi\hbar^2 d}{m} |\Phi(\mathbf{r}, \tau)|^2 \right] \Phi(\mathbf{r}, \tau). \quad (1.6)$$

This equation is known as the Gross-Pitaevskii (GP) equation, which to a good approximation describes the physics observed in the dilute and ultracold gases realized experimentally. Its validity is restricted to very low temperatures, large number of particles, and a  $s$ -wave scattering length much smaller than the interparticle distance.

Recently, new features that allow to go beyond the weakly interacting regime and access strongly correlated limits have been added to the experiments. Particularly interesting among the others, due to its relevance for condensed matter physics, has been the introduction of optical lattices [11]. Optical lattices are generated by means of interfering laser beams<sup>3</sup>. They produce a periodic potential in which two-level atoms are attracted or repelled from the maxima of the field intensity depending on the detuning of the laser beam with respect to the frequency of the atomic resonance. For red detuned lasers atoms are attracted toward the intensity maxima whereas for blue detuned lasers they are attracted toward the intensity minima<sup>4</sup>. In the second quantization language, the many body Hamiltonian describing a dilute and ultracold gas of bosons under the influence of an optical lattice can be written as

$$H = \int d\mathbf{r} \hat{\Psi}^\dagger(\mathbf{r}) \left[ -\frac{\hbar^2}{2m} \nabla^2 + V(\mathbf{r}) + V_0(\mathbf{r}) \right] \hat{\Psi}(\mathbf{r}) + \frac{1}{2} \frac{4\pi\hbar^2 d}{m} \int d\mathbf{r} \hat{\Psi}^\dagger(\mathbf{r}) \hat{\Psi}^\dagger(\mathbf{r}) \hat{\Psi}(\mathbf{r}) \hat{\Psi}(\mathbf{r}), \quad (1.7)$$

---

<sup>2</sup>In finite size systems, as the ones obtained experimentally, the concept of symmetry breaking cannot be applied. Nevertheless, the condensate wave-function still has a clear meaning. It is the eigenfunction of the one-particle density matrix corresponding to the larger eigenvalue, which acquires a macroscopic occupation due to BEC.

<sup>3</sup>For details about their experimental realization we refer to Ref. [12], and references therein.

<sup>4</sup>The derivation of the force and optical potential equations can be found in Ref. [13].

where

$$V_0(\mathbf{r}) = V_{0x} \cos^2(kx) + V_{0y} \cos^2(ky) + V_{0z} \cos^2(kz) \quad (1.8)$$

describes the potential generated by the optical lattice, the wavevector  $k = 2\pi/\lambda$  is determined by the wavelength  $\lambda$  of the laser beam. The periodicity of the lattice is then given by  $a = \lambda/2$ . Due to the presence of the periodic potential the wave-functions are more localized, so that assuming the energies involved in the dynamics to be smaller than the gap between the first and the second band in the lattice, we expand the bosonic field operators in single band Wannier functions  $[\phi_i(\mathbf{r})]$

$$\hat{\Psi}(\mathbf{r}) = \sum_i b_i \phi_i(\mathbf{r}), \quad \hat{\Psi}^\dagger(\mathbf{r}) = \sum_i b_i^\dagger \phi_i^*(\mathbf{r}). \quad (1.9)$$

The Wannier functions form an orthonormal basis

$$\sum_i \phi_i(\mathbf{r}) \phi_i^*(\mathbf{r}') = \delta(\mathbf{r} - \mathbf{r}'), \quad \int d\mathbf{r} \phi_i(\mathbf{r}) \phi_j^*(\mathbf{r}) = \delta_{ij}, \quad (1.10)$$

and the creation ( $b_i^\dagger$ ) and annihilation ( $b_i$ ) operators of a boson at a site  $i$  satisfy the following commutation relations

$$[b_i, b_j^\dagger] = \delta_{ij}, \quad [b_i, b_j] = [b_i^\dagger, b_j^\dagger] = 0, \quad (1.11)$$

which follow from the commutation relation between the bosonic field operators [Eq. (1.2)], and the properties of the Wannier functions [Eq. (1.10)].

The Hamiltonian (1.7) may be rewritten in terms of the on-site creation and annihilation operators as follows

$$H = - \sum_{ij} (t_{ij} + V_{ij}) b_i^\dagger b_j + \sum_{ijkl} U_{ijkl} b_i^\dagger b_j^\dagger b_k b_l, \quad (1.12)$$

where

$$\begin{aligned} t_{ij} &= - \int d\mathbf{r} \phi_i^*(\mathbf{r}) \left[ -\frac{\hbar^2}{2m} \nabla^2 + V_0(\mathbf{r}) \right] \phi_j(\mathbf{r}) \\ V_{ij} &= \int d\mathbf{r} \phi_i^*(\mathbf{r}) V(\mathbf{r}) \phi_j(\mathbf{r}) \\ U_{ijkl} &= \frac{2\pi\hbar^2 d}{m} \int d\mathbf{r} \phi_i^*(\mathbf{r}) \phi_j^*(\mathbf{r}) \phi_k(\mathbf{r}) \phi_l(\mathbf{r}). \end{aligned} \quad (1.13)$$

It was first noticed by Jaksch *et al.* [14] that the Hamiltonian (1.12) can be replaced, up to a very good approximation for realistic experimental systems, by the bosonic Hubbard

Hamiltonian. This because due to the localization of the Wannier functions, next-nearest-neighbors (or higher) hopping amplitudes ( $t_{ij}$  for  $|i - j| > 1$ ) and nearest-neighbors (or higher) interaction amplitudes ( $U_{ijkl}$  for  $i \neq j \neq k \neq l$ ) are negligible. In addition, from the sum related to the trap term only the element  $V_i \equiv V_{ii}$  is relevant (the other are much smaller), and for a very slowly varying confining potential it may be approximated as  $V_i \approx V(\mathbf{r}_i)$ . Then Eq. (1.12) can be written, up to a constant shift in the chemical potential, as

$$H = -t \sum_i (b_i^\dagger b_{i+1} + \text{H.c.}) + \sum_i V_i n_i + U \sum_i (n_i - 1) n_i, \quad (1.14)$$

where  $n_i = b_i^\dagger b_i$ , and

$$t = - \int d\mathbf{r} \phi_i^*(\mathbf{r}) \left[ -\frac{\hbar^2}{2m} \nabla^2 + V_0(\mathbf{r}) \right] \phi_{i+1}(\mathbf{r}), \quad U = \frac{2\pi\hbar^2 d}{m} \int d\mathbf{r} |\phi_i(\mathbf{r})|^4. \quad (1.15)$$

Explicit expressions for  $t$  and  $U$  can be obtained when  $V_0$  is much larger than the so-called recoil energy  $E_r = \hbar^2 k^2 / 2m$ . In this case  $t$  is obtained from the exact result for the width of the lowest band in the 1D Mathieu's equation<sup>5</sup>, and  $U$  by approximating the Wannier wave-function  $\phi_i(\mathbf{r})$  by the Gaussian ground state in the potential about one site [16]

$$t = \frac{4}{\sqrt{\pi}} \left( \frac{V_0}{E_r} \right)^{3/4} E_r e^{-2\sqrt{\frac{V_0}{E_r}}}, \quad U = \sqrt{\frac{8}{\pi}} \left( \frac{V_0}{E_r} \right)^{3/4} k d E_r. \quad (1.16)$$

The derivation followed above shows that optical lattices loaded with ultracold gases of bosons represent an ideal experimental scenario for the realization of the bosonic Hubbard model. The possibility of obtaining the superfluid-Mott-insulator transition (SMIT) [17–21] was proposed theoretically by Jaksch *et al.* [14], and observed experimentally for the first time by Greiner *et al.* in three dimensional lattices (3D) [11], and very recently by Stöferle *et al.* in one-dimensional (1D) lattices [22]. It should be notice that the presence of the slowly varying potential of the trap makes an important difference between the periodic [17–21] and the confined case [11, 14]. In the periodic case the Mott-insulating phase appears only at commensurate fillings, while in the trapped case it appears for a

---

<sup>5</sup>The Mathieu's equation is a very well known and studied differential equation (see for example Ref. [15]). It is usually written in the following canonical form

$$\frac{d^2 y}{dv^2} + (a - 2q \cos 2v) y = 0,$$

where  $a$  and  $q$  are arbitrary parameters.

continuous range of incommensurate fillings and always coexists with superfluid phases [23–27].

The experimental realization of ultracold fermionic gases is more difficult than in the bosonic case. Unlike bosons, single species fermions cannot be directly evaporatively cooled to very low temperatures because the  $s$ -wave scattering that could allow the gas to rethermalize during the evaporation is prohibited for identical fermions due to the Pauli's exclusion principle. This problem has been overcome by simultaneously trapping and evaporatively cooling two-component Fermi gases [28, 29], and introducing mixed gases of bosons and fermions in which bosons enable fermions to rethermalize through their interactions [30–33]. Rapid forced evaporation employing Feshbach resonances of two different spin states of the same fermionic atom has also been used [34]. Once very low temperatures have been achieved, it is possible to keep trapped only one fermionic species and obtain in this way an experimental realization of the ideal Fermi gas. Ideal Fermi gases confined in harmonic traps have been studied theoretically in 1D [35–38] and 2D, 3D [39–41] configurations, where the harmonic form of the potential allows obtaining a number of exact analytical results for these systems.

Single species ultracold fermionic gases have been loaded on 1D optical lattices very recently [42–45]. In these experiments, properties of noninteracting Fermi gases and of interacting mixtures of fermions and bosons have been studied. Theoretically, ground state (GS) and transport (T) properties of non-interacting fermions on lattices have been analyzed in Refs. [46, 47] (GS) and [46, 48–50] (T). The future possibility of loading two-component Fermi gases on optical lattices will allow to realize experimentally the fermionic Hubbard model. In this way the Mott-metal-insulator transition, a paradigm of strong correlations, could be studied experimentally with a full control of the parameter of the model, and without the extrinsic effects always present in solid state systems.

The many body Hamiltonian of ultracold two-component fermions, on an optical lattice, can be written as

$$\begin{aligned}
 H = & \sum_{\sigma} \int d\mathbf{r} \hat{\Psi}_{\sigma}^{\dagger}(\mathbf{r}) \left[ -\frac{\hbar^2}{2m} \nabla^2 + V(\mathbf{r}) + V_0(\mathbf{r}) \right] \hat{\Psi}_{\sigma}(\mathbf{r}) \\
 & + \frac{1}{2} \frac{4\pi\hbar^2 d}{m} \int d\mathbf{r} \hat{\Psi}_{\sigma_1}^{\dagger}(\mathbf{r}) \hat{\Psi}_{\sigma_2}^{\dagger}(\mathbf{r}) \hat{\Psi}_{\sigma_2}(\mathbf{r}) \hat{\Psi}_{\sigma_1}(\mathbf{r}), \tag{1.17}
 \end{aligned}$$

where  $\sigma_1$  and  $\sigma_2$  refer to the two different fermion components, which in the following we denote by  $\sigma_1 \equiv \uparrow$  and  $\sigma_2 \equiv \downarrow$  to simplify the expressions. The fermionic field operators

satisfy anticommutation relations

$$\left\{ \hat{\Psi}_\sigma(\mathbf{r}), \hat{\Psi}_{\sigma'}^\dagger(\mathbf{r}') \right\} = \delta_{\sigma\sigma'} \delta(\mathbf{r} - \mathbf{r}'), \quad \left\{ \hat{\Psi}_\sigma(\mathbf{r}), \hat{\Psi}_{\sigma'}(\mathbf{r}') \right\} = \left\{ \hat{\Psi}_\sigma^\dagger(\mathbf{r}), \hat{\Psi}_{\sigma'}^\dagger(\mathbf{r}') \right\} = 0. \quad (1.18)$$

In Eq. (1.17) the trapping and optical lattice potentials are assumed to be spin independent. In addition, the temperatures should be small enough so that only  $s$ -wave scattering between the different fermionic species is possible. Following the same assumptions than for the bosonic case, the fermionic field operators may be expanded in terms of single band Wannier functions

$$\hat{\Psi}_\sigma(\mathbf{r}) = \sum_i c_{i\sigma} \phi_i(\mathbf{r}), \quad \hat{\Psi}_\sigma^\dagger(\mathbf{r}) = \sum_i c_{i\sigma}^\dagger \phi_i^*(\mathbf{r}), \quad (1.19)$$

and the Hamiltonian of the Hubbard model

$$H = -t \sum_{i,\sigma} \left( c_{i\sigma}^\dagger c_{i+1\sigma} + \text{H.c.} \right) + U \sum_i n_{i\uparrow} n_{i\downarrow} + \sum_i V_i n_i \quad (1.20)$$

can be obtained. The creation and annihilation operator for fermions, with spin  $\sigma$  at site  $i$ , are denoted by  $c_{i\sigma}^\dagger$  and  $c_{i\sigma}$ , respectively. They satisfy anticommutation relations

$$\left\{ c_{i\sigma}, c_{j\sigma'}^\dagger \right\} = \delta_{\sigma\sigma'} \delta_{ij}, \quad \left\{ c_{i\sigma}, c_{j\sigma'} \right\} = \left\{ c_{i\sigma}^\dagger, c_{j\sigma'}^\dagger \right\} = 0, \quad (1.21)$$

which follow from the anticommutation relations between the fermionic field operators [Eq. (1.18)], and the properties of the Wannier functions [Eq. (1.10)]. The particle number operator is in this case  $n_i = n_{i\uparrow} + n_{i\downarrow}$ , with  $n_{i\sigma} = c_{i\sigma}^\dagger c_{i\sigma}$ . The definitions of  $t$ ,  $U$ , and  $V_i$  are the same than for bosons [Eq. (1.15)].

Within the possible experimental configurations to be studied, low dimensional systems have been a subject of increasing interest over the last years. They can be realized in very anisotropic traps [31, 51] and loading Bose-Einstein condensates (BEC) on optical lattices [22, 52, 53]. Particularly interesting is the case in which the quantum dynamics of the system becomes quasi-one-dimensional, where quantum fluctuation dominate the physical properties at very low temperatures. For bosonic atoms it was shown [54–56] that in certain regime of large positive scattering length, low densities and low temperatures, bosons behave a gas of impenetrable particles known as hard core bosons (HCB).

The one-dimensional (1D) homogeneous gas of HCB was first introduced by Girardeau [57], and a one-to-one correspondence between 1D HCB and spinless fermions was established. It was shown later by Lenard, and Vaidya and Tracy [58–60] that in the

homogeneous case the 1D HCB gas does not exhibit true condensation at zero temperature since there is only off-diagonal quasi-long range order (the one particle correlation functions decay as a power law), leading to an occupation of the lowest effective single particle state (the highest occupied one)  $\sim \sqrt{N_b}$ , where  $N_b$  is the total number of HCB.

Recently, theoretical studies has been focused on the ground state properties of 1D HCB gases in the presence of harmonic potentials [61–65], which are required in the experiments with quantum gases to keep the particles confined. Using the Fermi-Bose mapping quantities like density profiles, momentum profiles, occupation of the natural orbitals (effective single-particle states), and their wave-functions, have been calculated for finite number of particles, and some results have been extended for the thermodynamic limit ( $N_b \rightarrow \infty$ ) [65]. It has been found that similarly to the homogeneous case the occupation of the lowest natural orbital is  $\sim \sqrt{N_b}$  [64,65], so that only a quasi-condensate develops in the trap.

Another case of interest are the properties of HCB on a lattice. These systems have been realized experimentally very recently [66]. In the periodic case, the 1D HCB Hamiltonian can be written as

$$H = -t \sum_i \left( b_i^\dagger b_{i+1} + h.c. \right), \quad (1.22)$$

with the addition of the on-site constraints

$$b_i^{\dagger 2} = b_i^2 = 0, \quad \{b_i, b_i^\dagger\} = 1. \quad (1.23)$$

where  $b_i^\dagger$  and  $b_i$  are the HCB creation and annihilation operators, respectively. Considering that  $b_i^\dagger$  and  $b_i$  can be represented by Pauli matrices as

$$b_i^\dagger = \frac{1}{2} (\sigma_i^x + i\sigma_i^y), \quad b_i = \frac{1}{2} (\sigma_i^x - i\sigma_i^y), \quad (1.24)$$

the HCB Hamiltonian on a lattice can be mapped into the 1D XY model of Lieb, Schulz, and Mattis [67]

$$H_{XY} = -\frac{1}{4} \sum_i [(1 + \gamma)\sigma_i^x \sigma_{i+1}^x + (1 - \gamma)\sigma_i^y \sigma_{i+1}^y] + \frac{1}{2} h \sum_i \sigma_i^z. \quad (1.25)$$

where  $\sigma_i^x, \sigma_i^y, \sigma_i^z$  are the Pauli matrices,  $\gamma$  is an anisotropy parameter ( $0 \leq \gamma \leq 1$ ), and  $h$  is the magnetic field in the  $z$ -direction. (In the periodic HCB case  $\gamma = 0$  and  $h = 0$ .) This model has been extensively studied in the literature. At zero temperature the asymptotic behavior of the correlation functions is known [68–71]. In particular, for the case relevant



to HCB, i.e.  $\gamma = 0$  and  $h = 0$ , correlation functions  $\rho_{i-j}^\alpha = \langle \sigma_i^\alpha \sigma_j^\alpha \rangle$  with  $\alpha = x, y$ , decay as power-laws  $\sim |i - j|^{-1/2}$  [68]<sup>6</sup>. In the presence of a confining potential, the systems that have been realized experimentally very recently [66], the situation is more complicated. This is because the trapping potential is equivalent to the addition of a space-varying transverse field to the  $XY$  Hamiltonian, for which exact analytical results are not available. This case is studied by means of a newly developed exact numerical treatment in the present work.

## 1.1 Overview

In this thesis, we study properties of ultracold quantum gases trapped in 1D and under the influence of an underlying optical lattice. We analyze both fermionic and bosonic systems following different numerically exact approaches, like quantum Monte Carlo for soft-core bosons and two-species fermions, and a recently developed exact approach for HCB. The exposition is organized as follows.

In the following chapter (Chap. 2), we study single species degenerated fermions on 1D lattices [46]. We show that a splitting of the system takes place in a region of the spectrum with eigenstates that have a non-vanishing weight only in a fraction of the system. Hence, a qualitatively different behavior from the cases without the lattice [35–38] is found. We also show that if on top of the lattice an alternating potential is introduced, doubling the original periodicity, an additional ‘slicing’ of the system can be achieved. The width and number of such regions can be controlled in a given energy range by the amplitude of the new modulation. By filling these systems the ground state may exhibit insulating regions due to the presence of local gaps, which can be observed in the local density of states. As a complement to these 1D results we present in Appendix A results obtained in 2D lattices.

The non-equilibrium dynamics of trapped fermions is also analyzed when the center of the trap is initially displaced from the middle of the system. It allows to realize the existence of the confined states obtained in the equilibrium case, since for some values of the parameters the center-of-mass (CM) of the system oscillates in one side of the trap.

---

<sup>6</sup>This is the same behavior obtained for the power-law decay of the one-particle density matrix of HCB in an homogeneous system [60].

This analysis is relevant to recent experiments where the ideal Fermi gas was studied and the features mentioned here realized [42, 43].

In Chap. 3 we review in some detail the two quantum Monte Carlo (QMC) techniques that are relevant to our study of confined soft-core bosons and two-species fermions on optical lattices, the worldline QMC and the zero temperature projector QMC, respectively. The basis of the classical Monte Carlo method are also presented, included a proof of the Central Limit theorem (Appendix B) that establishes its foundations.

Properties of soft-core bosons confined on optical lattices [23] are presented in Chap. 4. QMC simulations show that due to the presence of the slowly varying confining potential the concept of commensurability, typical for periodic systems, loses its meaning. Mott domains appears for a continuous range of fillings and always coexist with superfluid phases, as it was mentioned before. The latter feature is reflected by the behavior of the global compressibility, which never vanishes. A local compressibility, proportional to the variance of the local density, is defined in order to characterize the local Mott-insulating phases. Finally, a phase diagram for trapped systems is also presented.

In Chap. 5 we study the ground state properties of two-components fermions confined on optical lattices [72, 73]. Like for the bosonic case, Mott domains also appear for a continuous range of fillings and always coexist with compressible phases. We define a local order parameter (that we denominate local compressibility), which characterizes the Mott insulating phases in an unambiguous way. By means of this local compressibility, we study in detail the interphase between the metallic and insulating region finding that critical behavior sets in revealing a new critical exponent. Furthermore, the behavior of the local compressibility and the variance of the density are found to be universal in this case, independently of the confining potential and the strength of the interaction, as usual in critical phenomena.

The momentum distribution function, a quantity usually accessed in the experiments, is studied in detail. The results obtained show that due to the inhomogeneous character of these systems, this quantity does not exhibit a clear signature of the formation of Mott domains. A mean-field (MF) analysis of trapped fermions is also presented in this chapter. We show that although density profiles obtained using the MF approach are similar to those of the QMC simulations, the nature of the phases obtained within MF are different to those obtained within QMC. We conclude the chapter presenting a phase

diagram for fermions confined in 1D. It allows to compare systems with different fillings and curvatures of the confining potential, so that it is relevant for the understanding of future experimental results.

We present in Chap. 6 a recently developed exact numerical approach [74] that allows to study ground state properties of HCB confined on 1-D lattices. It is based on the Jordan-Wigner transformation and enables to analyze large systems with up to  $\sim 10000$  lattice sites. This exact treatment is applied to study the off-diagonal behavior of the one-particle density matrix (OPDM) and related quantities in the equilibrium case. We find that the OPDM  $\rho_{ij}$  decays as a power-law  $x^{-1/2}$  ( $x = |x_i - x_j|$ ) for large- $x$ , irrespective of the confining potential chosen, even when portions of the system reach occupation  $n_i = 1$ , such that coherence is lost there. The power-law above is shown to determine the scaling of the occupation of the lowest natural orbital in the thermodynamic limit (TL). This scaling and its finite size corrections are also studied for arbitrary powers of the confining potential. In addition, we find a power-law decay of the NO occupations ( $\lambda_\eta$ ) for large- $\eta$  at low densities, and show that its exponent is also universal. The low density limit in the lattice, equivalent to continuous systems, is also analyzed in detail.

The approach above is generalized in Chap. 7 to study the non-equilibrium dynamics of HCB in 1-D configurations with an underlying lattice [75]. The presence of the lattice enhances correlations between particles and enables the creation of pure Fock states of HCB (a HCB per lattice site) where there is no coherence in the system. We show that quasi-long range correlations develop in the equal-time-one-particle density matrix (ETOPDM) when such states are allowed to evolve freely, and that they lead to the formation of quasi-condensates of HCB at finite momentum. In addition, we obtain an universal power-law describing the population of the quasi-condensate as a function of time, independent of the initial number of particles in the Fock-state. Finally, we discuss how such systems can be used to create atom lasers with a wave-length that can be controlled through the lattice parameter.



## Chapter 2

# Single species fermions confined on 1-D optical lattices

We analyze in this chapter properties of single species non-interacting fermions confined on 1D optical lattices. These systems are relevant for the understanding of recent experimental results [42,43], where due to the very low temperatures achieved, fermions can be considered as non-interacting particles. This is because, as it was mentioned in the introduction, only s-wave scattering is possible in the ultracold gas, but for identical fermions it is forbidden due to the Pauli principle. On the theoretical side, the Hamiltonian can be diagonalized numerically, which allows to consider any kind of trapping potential and any number of dimensions for the system. The interplay lattice-confining potential leads to a splitting of the eigenstates in a region of the spectrum where they have a non-vanishing weight only in a fraction of the trap (Sec. 2.1). Hence, such systems are qualitatively different from the cases without the lattice, which have been studied recently in 1D [35–38], and 2D, 3D [39–41].

We also study the non-equilibrium dynamics of the fermionic cloud on a lattice. In particular, we study the case in which the center of the trap is initially displaced a small distance (Sec. 2.2). It allows to realize the existence of the splitting obtained in the equilibrium case, since the center-of-mass (CM) of the system oscillates in one side of the trap. With these results, we reproduce recent experimental observations [42, 43] of the CM oscillations on single species fermions confined on optical lattices.

Finally, we analyze the case where an alternating potential is introduced doubling the original periodicity of the lattice. This leads to an additional ‘slicing’ of the eigenstates

of the Hamiltonian. By filling these systems with fermions, space separated insulating regions may appear, and they always coexist with metallic regions. This coexistence implies that that no gap appears in the single particle spectrum. An imprint of the local gap in the insulating phases can be observed in the local density of states (Sec. 2.3).

The results presented in this chapter are generalized for 2D systems in Appendix A.

## 2.1 Confined states and the combination lattice - trapping potential

We consider non-interacting fermions confined on 1D lattices. We first show results for a harmonic confining potential and then discuss the features that are generally valid for any other kind of confining potential. The spectral properties discussed are equally valid for bosons since we deal with the non-interacting case. The Hamiltonian of the system can be written as

$$H = -t \sum_i \left( c_i^\dagger c_{i+1} + \text{H.c.} \right) + V_\alpha \sum_i x_i^\alpha n_i, \quad (2.1)$$

where  $c_i^\dagger$  and  $c_i$  are creation and annihilation operators, respectively, for a spin polarized fermion on site  $i$ , the local density is  $n_i = c_i^\dagger c_i$ , and  $x_i$  measures the positions of the sites in the trap ( $x_i = ia$  with  $a$  the lattice constant). Fermions are considered to have only a nearest neighbor hopping ( $t$  is the hopping parameter), the strength of the confining potential is  $V_\alpha$ ,  $\alpha$  being its power. We call  $N$  the number of lattice sites and  $N_f$  the total number of spin polarized fermions in the system. We diagonalize the Hamiltonian numerically, and consider the cases in which all particles are confined.

### 2.1.1 Single particle spectrum and its eigenfunctions

The results obtained for the single particle spectrum of a system confined by a harmonic potential  $V_2 a^2 = 3 \times 10^{-7} t$  with  $N = 10000$  lattice sites are presented in Fig. 2.1(a). The spectrum is clearly different from the straight line in absence of a lattice. It is possible to see that in Fig. 2.1(a) the spectrum can be divided in two regions according to the behavior of the energy as a function of the level number. An arrow is introduced where a change in the curvature is observed. More detailed information can be obtained by

considering the level spacing as a function of the level number [Fig. 2.1(b)]. There it can be seen that in the low energy part of the spectrum (region A), the level spacing decreases slowly with increasing level number, in contrast to the case without the lattice in which the level spacing is constant. However, at the point signaled with the first arrow, a qualitative change in the single particle spectrum occurs, characterized by an oscillating behavior of the level spacing. The part with values of the level spacing increasing with the level number corresponds to odd level numbers and the one with a level spacing that decreases up to zero corresponds to even level numbers. That is, a degeneracy sets in that continues up to the point signaled with the second arrow, where a new change in the behavior of the level spacing shows up. The region beyond the second arrow corresponds to deconfined states, which are of no interest since experimentally they are associated to particles that scape from the trap.

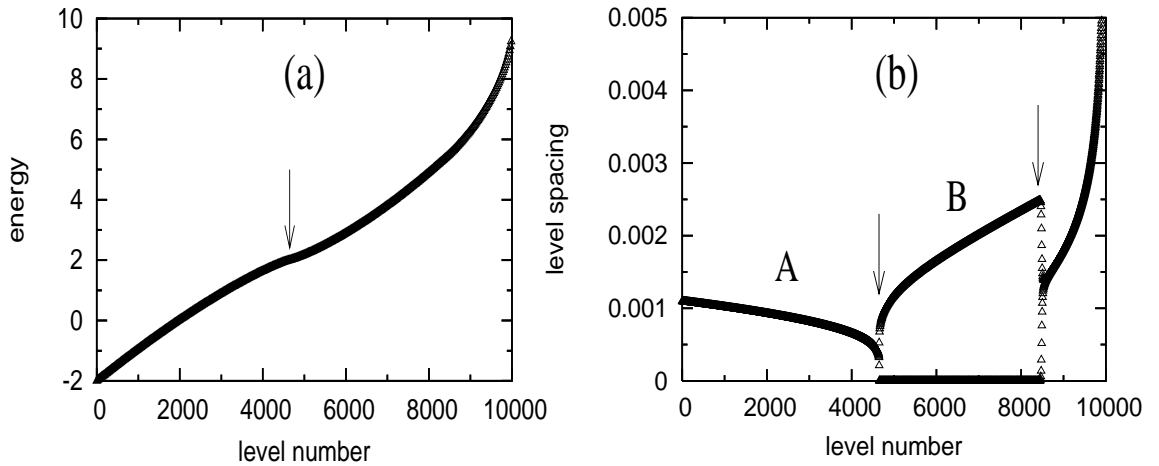


Figure 2.1: Single particle spectrum (a) and level spacing (b) for a system with  $N = 10000$  and  $V_2 a^2 = 3 \times 10^{-7} t$ . Energies are measured in units of  $t$ . For the explanation of the arrows see text.

In the lowest part of the spectrum of Hamiltonian (2.1), the eigenfunctions are essentially the harmonic oscillator (HO) orbitals in the absence of a lattice. This is shown in Fig. 2.2(a) for the first and the second eigenfunctions of Eq. (2.1), and the same parameters of Fig. 2.1. These orbitals are perfectly scalable independently of the size of the system and of the ratio between  $V_2$  and  $t$ . It is only needed to consider that the usual HO characteristic length  $R \sim (m\omega)^{-1/2}$  (without the lattice) is given in terms of the lattice parameters through  $R \sim (V_2/ta^2)^{-1/4}$ , with the effective mass  $m \sim (ta^2)^{-1}$  for

very low energies. Then the scaled orbitals are given by  $\varphi = (R/a)^{1/2} \phi$  where  $\phi$  are the HO orbitals with the lattice, i.e. the same relation as for the HO *without* the lattice holds for the lowest energy orbitals *with* the periodic potential. This implies that very dilute systems behave similarly to continuous systems, which have been already discussed in the literature so that we will not present any further analysis on them. The  $N_f$  oscillations in density profiles and the momentum distribution function (MDF), and other mentioned characteristics of the 1D trapped system without the lattice [36,37] are easily obtained in this case.

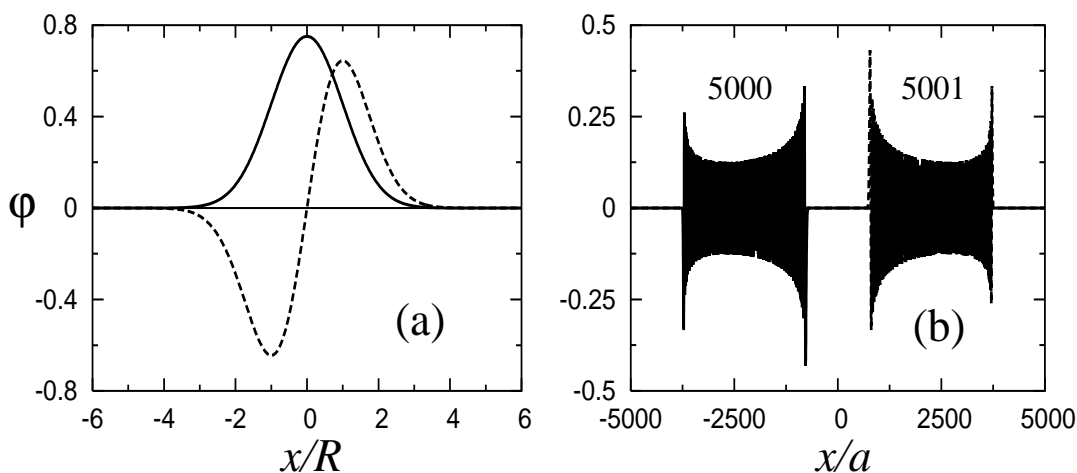


Figure 2.2: Scaled HO orbitals in the presence of a lattice for  $N = 10000$  and  $V_2 a^2 = 3 \times 10^{-7} t$ . (a) first (continuous line) and second (dashed line) HO orbitals, (b) HO orbitals 5000 (only different from zero for negative  $x$ ) and 5001 (only different from zero for positive  $x$ ). In (a) the positions are given in units of the HO length  $R = (V_2/ta^2)^{-1/4}$  (for an explanation, see text), and in (b) in units of the lattice constant  $a$ .

A qualitative difference between the cases of the trap with and without a lattice starts for levels in region B. Once the degeneracy appears in the spectrum, the corresponding eigenfunctions of the degenerate levels start having zero weight in the middle of the trap, and for higher levels the regions over which the weight is zero increases. As an example, we show in Fig. 2.2(b) two normalized eigenfunctions belonging to Region B in Fig. 2.1. The cases depicted correspond to the normalized eigenfunctions 5000 (that is only different from zero for negative values of  $x$ ) and 5001 (only different from zero for positive  $x$ ), for the same parameters of Fig. 2.1 (in principle a lineal combination of these two eigenfunctions could have been the solution since the level is degenerated).



Hence, particles in these states are confined to a fraction of the trap, showing that the combination of both a confining and a periodic potential lead to features not present either in the purely confined case without a lattice or in the case of a purely periodic potential. Furthermore, since we are dealing with a non-interacting case, such features are common to both fermions and bosons. However, in the case of fermions, it is easy to understand the reason for such effects, as discussed next.

### 2.1.2 Origin of the confined states

Figure 2.3(a) shows density profiles of fermions when the number of particles in the trap is increased. In one case ( $N_f = 4500$ ) the Fermi energy lies just below the level marked with an arrow in Fig. 2.1. A second curve ( $N_f = 4651$ ) corresponds to the case where the central site reaches a density  $n = 1$ , and in the other case ( $N_f = 5001$ ), the Fermi energy lies at the value corresponding to the levels depicted in Fig. 2.2(b). The positions in the trap are normalized in terms of the characteristic length for a harmonically trapped system when a lattice is present, which is given by

$$\zeta = (V_2/t)^{-1/2}. \quad (2.2)$$

The relation above can be easily seen from Hamiltonian Eq. (2.1).  $V_\alpha x^\alpha$  has energy units so that  $(V_\alpha/t)^{-1/\alpha}$  has length units. In a harmonic trap  $\alpha = 2$ , which leads to Eq. (2.2). When the Fermi energy approaches the level where degeneracy sets in, the density of the system approaches  $n = 1$  in the middle of the trap, and at the filling point where the degeneracy appears in the spectrum, the density in the middle of the trap is equal to one, so that an insulating region appears in the middle of the system. Increasing the filling of the system increases the region over which this insulator extends. Hence, due to Pauli principle, the eigenfunctions of such levels cannot extend over the insulating region, and for the same reason, the region over which the weight is zero increases for higher levels.

However, since the system we are considering is a non-interacting one, the confined states discussed above should be also present in the case of bosons, where the argument about the filling would not be valid anymore. It is therefore desirable to also understand such features from a single particle perspective. We first notice that the point at which degeneracy appears is at an energy  $4t$  above the lowest level ( $E_0$ ) [see Fig. 2.1(a)], corresponding to the band-width for the periodic potential. Such an energy is reached

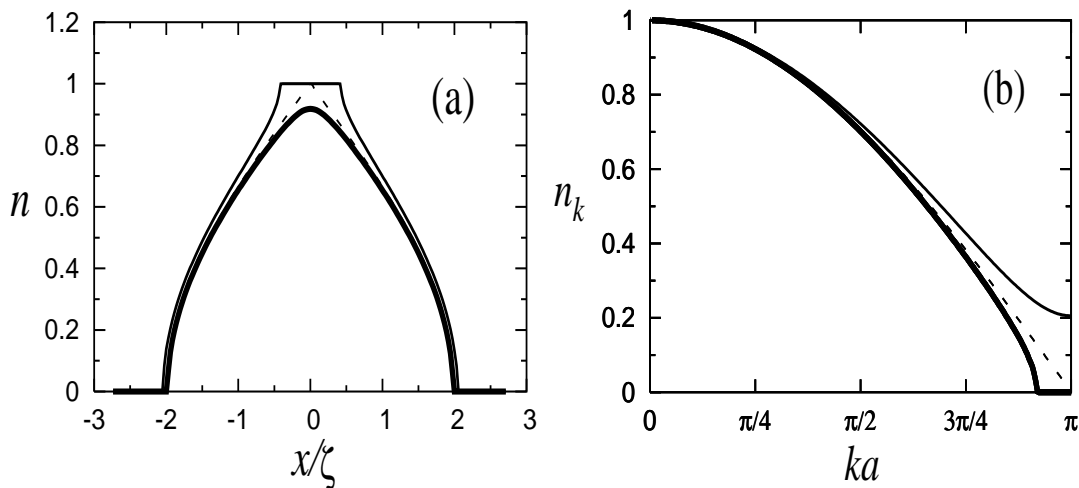


Figure 2.3: Density profiles (a) and normalized MDF (b) for  $N_f = 4500$  (thick continuous line)  $N_f = 4651$  (dashed line) and  $N_f = 5001$  (thin continuous line) for a system with  $N = 10000$  and  $V_2 a^2 = 3 \times 10^{-7} t$ . In (a) positions are given in units of the characteristic length  $\zeta$ , and in (b) the momentum is normalized by the lattice constant ( $a$ ).

when the Bragg condition is fulfilled and in the case of the tight-binding system we are considering, when all the available states are exhausted. Let us next consider the case depicted in Fig. 2.2(b). There, the energy level corresponding to the wavefunctions is  $E_{5001} - E_0 = 4.2176t$ , that is to a good approximation  $4t + V_2 x_1^2$  for  $V_2 a^2 = 3 \times 10^{-7} t$  and  $x_1 = 697a$  the inner point where the wavefunctions drops to a value  $\sim 10^{-5}$ . Therefore, the inner turning point corresponds to the Bragg condition, whereas for the outer turning point ( $x_2 = 3770a$ , again for the same drop of the wavefunction), we have that  $E_{5001} - E_0 \simeq V_2 x_2^2$ , i.e. the classical turning point corresponding to the harmonic potential, as expected for such a high level. Hence, Bragg scattering as in the well known Bloch oscillations [76], and the trapping potential combine to produce the confinement discussed here.

Further confirmation of the argument above can be obtained by considering the MDF, a quantity also accessible in time of flight experiments [11]. Due to the presence of a lattice, it is a periodic function in the reciprocal lattice and it is symmetric with respect to  $k = 0$ , so that we study it in the first Brillouin zone in the region  $[0, \pi/a]$ . In addition we normalize the MDF to unity at  $k = 0$  ( $n_{k=0} = 1$ ). For the fermionic case, it can be seen that it always has a region with  $n_k = 0$  if the insulating phase is not present in the trap, and this region disappears as soon as the insulator appears in the middle of the

system. More precisely, Fig. 2.3(b) shows that at the filling when the site in the middle reaches  $n = 1$ , also the momentum  $k = \pi/a$  is reached, such that the Bragg condition is fulfilled for the first time, confirming the discussion above. When further sites reach a density  $n = 1$ ,  $n_{k=\pi/a}$  increases accordingly. Then the formation of the local insulator in the system can be tested experimentally observing the occupation of the states with momenta  $k = \pm\pi/a$ .

### 2.1.3 The characteristic density

Since for different systems sizes and number of particles potentials with different curvatures have to be considered, it is important to determine the filling  $N_f^C$  at which the insulator appears in the middle of the trap as a function of the curvature of the harmonic confining potential. For that we define a characteristic density  $\tilde{\rho}$  in terms of the filling in the trap, and the length scale  $\zeta$  set by the combination lattice-confining potential

$$\tilde{\rho} = N_f a / \zeta. \quad (2.3)$$

We find that the insulator appears in the system always at the same value of  $\tilde{\rho}$ , independently of the other parameters, so that the filling required for its formation is  $N_f^C \sim \zeta/a$ . In Fig. 2.4(a) we show in a log-log scale how  $N_f^C$  depends on  $V_2/t$  over three decades on the total filling. In our fit the slope of the curve is  $-0.500$  (with 0.04 percent of error), as expected on the basis of Eq. (2.2). The characteristic density  $\tilde{\rho}_C = N_f^C a (V_2/t)^{1/2}$  at which the insulating region appears, is  $\tilde{\rho}_C = e^\beta$ , with  $\beta = 0.986$  (with 0.3 percent of error), which is curiously rather close to the basis of the natural logarithms.

For systems with other powers for the confining potential it is only needed to define the appropriate characteristic density  $\tilde{\rho} = N_f a (V_\alpha/t)^{1/\alpha}$ , and determine its value at the point where the insulator appears. In Fig 2.4 (b) we show in another log-log plot how  $N_f^C$  depends on the curvature of a confining potential with power six ( $V_6/t$ ). As anticipated, we obtain that the slope of the curve is  $1/6$  (with 0.01 percent of error) in this case and the characteristic density for the formation of the insulator is  $\tilde{\rho}_C = 2.09$ .

In general, for arbitrary confining potentials the same features discussed previously for the harmonic case are valid. The spectrum and level spacing will behave in a different way depending on the power of the confining potential, but always at a certain level number degeneracy will appear in the single particle spectrum and it will correspond to

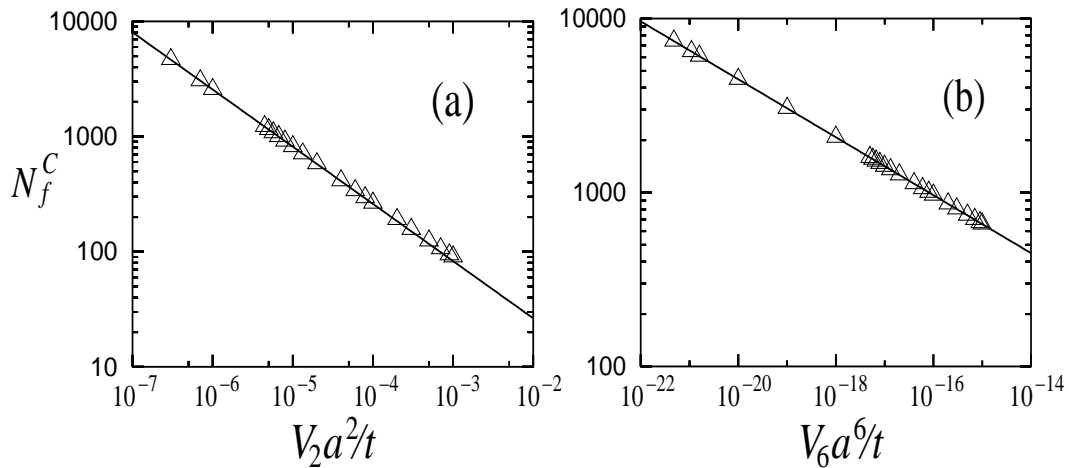


Figure 2.4: Total filling in the trap needed for the formation of the insulator as a function of the curvature of the confining potential. (a) Harmonic potential. (b) Potential with a power  $\alpha = 6$ .

the formation of an insulator in the middle of the system for the corresponding filling. In Fig. 2.5 we show the single particle spectrum [Fig. 2.5(a)] and the corresponding level spacing [Fig. 2.5(b)] for a confining potential with power  $\alpha = 6$ , where the features mentioned previously are evident. The arrow in the inset of Fig. 2.5 shows the level at which degeneracy sets in, very much in the same way as in the harmonic case.

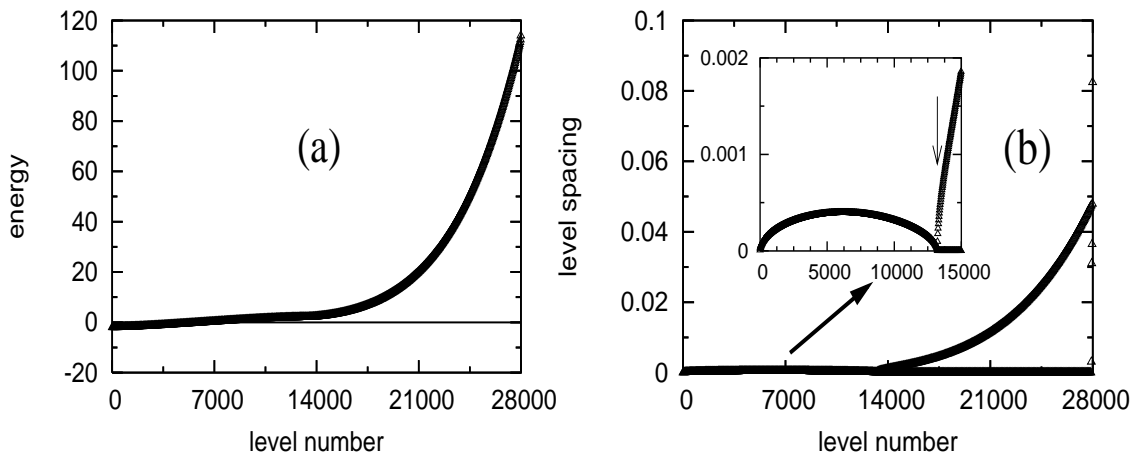


Figure 2.5: Single particle spectrum (a) and level spacing (b) for a system with a confining potential with power  $\alpha = 6$ ,  $N = 28000$  and  $V_6 a^6 = 3 \times 10^{-7} t$ . Expanded view in (b) shows the first part of the level spacing. An arrow was introduced in the inset for signaling the level at which the degeneracy appears in the spectrum.

## 2.2 Center-of-mass oscillations

As it was mentioned before, recent experiments have realized single species non-interacting fermions in 1D optical lattices [42, 43]. Transport studies in such systems revealed that under certain conditions a sudden displacement of the trap center is followed by oscillations of the CM of the fermionic cloud in one side of the trap. This is in contrast to the system without the lattice where the CM oscillates, as expected, around the potential minimum [42, 43]. Although the experimental system is three dimensional, due to a strong transversal confinement the relevant motion of the particles occurs in the longitudinal direction so that in order to qualitatively understand the observed behavior one can analyze the ideal 1D case. Given the results discussed in the previous section one expects the displaced oscillation of the CM to appear when, due to the initial displacement of the trap, particles that were located in region A of the spectrum in Fig. 2.1(b) are moved into region B so that Bragg conditions are fulfilled. Then the particles will get trapped in one side of the system [Fig. 2.2(b)].

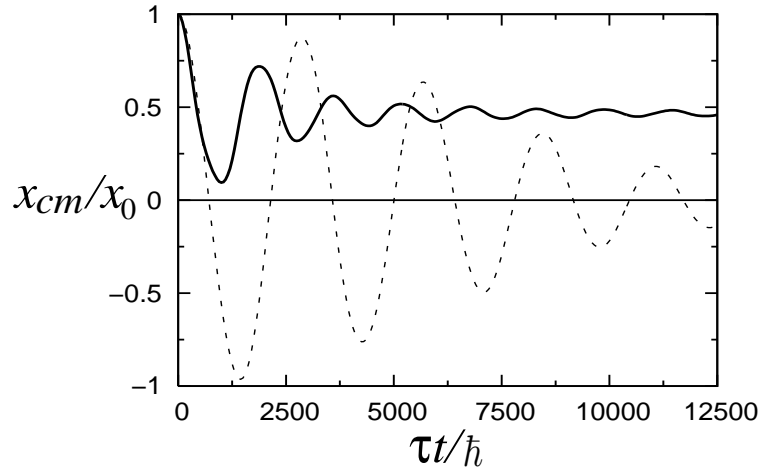


Figure 2.6: Evolution of the CM ( $x_{cm}$ ) of 1000 confined fermions when the center of the trap is suddenly displaced 200 lattice sites ( $x_0$ ), for  $V_2a^2 = 2 \times 10^{-06}t$  (dashed line), and  $V_2a^2 = 6 \times 10^{-06}t$  (continuous line).

Figure 2.6 shows exact results obtained for the CM dynamics of 1000 fermions in a trap with  $N = 3000$  when its center is suddenly displaced 200 lattice sites.  $\tau$  denotes the real time variable. The relation between the confining potential ( $V_2$ ) and the hopping parameter ( $t$ ) is increased in order to fulfill the Bragg conditions. This is equivalent in experiments to increase the curvature of the confining potential keeping constant the

depth of the lattice, which leads to an increase of the frequency of the oscillation as shown in Fig. 2.6. It is also equivalent to increase the depth of the lattice keeping the confining potential constant, but then our plots in Fig. 2.6 should be interpreted with care since there we normalize the time variable by the hopping parameter, which changes in the latter case. In Fig. 2.6 (dashed line) we show results for the case where the CM of the cloud oscillates around the minimum of energy of the trap since no Bragg conditions are fulfilled. This can be seen in the MDF [Fig. 2.7(a)] where at any time no particles have  $k = \pm\pi/a$ . Fig. 2.6 also shows that a damping of the oscillation of the CM occurs. This is due to the non-trivial dispersion relation in a lattice  $\epsilon_k = -2t \cos ka$ , which makes the frequency of oscillation of the particles dependent on their energies, leading to dephasing. In order to reduce the damping, fermions should populate after the initial displacement only levels with energies close to the bottom of the band in a lattice, so that the quadratic approximation is valid for  $\epsilon_k$ . (Notice that this is not generally fulfilled even if the initial displacement is small.)

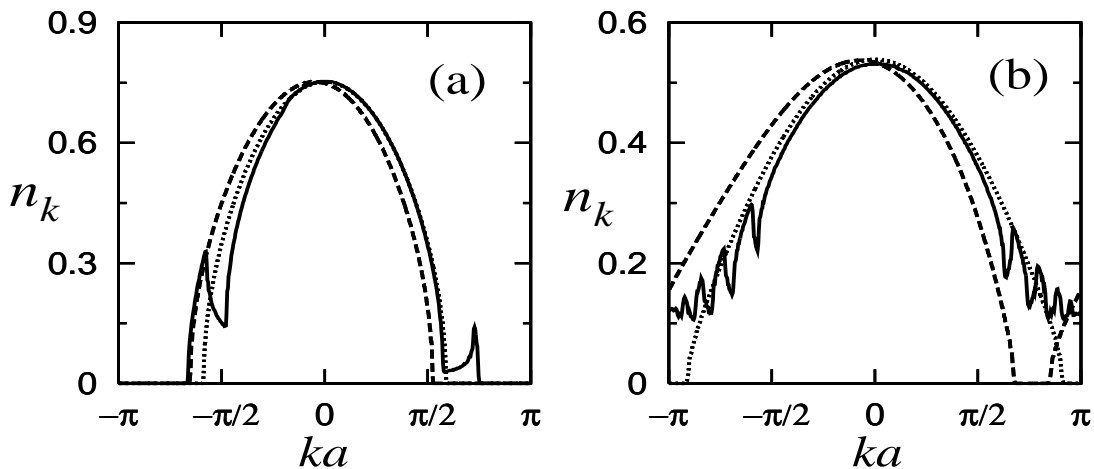


Figure 2.7: MDF of 1000 trapped fermions at three different times after displacing the trap 200 lattice sites, for  $V_2 a^2 = 2 \times 10^{-06} t$  (a), and  $V_2 a^2 = 6 \times 10^{-06} t$  (b). The times are  $\tau = 0$  (dotted line),  $\tau = 250 \hbar/t$  (dashed line), and  $\tau = 12500 \hbar/t$  (continuous line).

Increasing the relation  $V_2/t$  makes that some particles start to fulfill the Bragg conditions so that the center of oscillations of the cloud depart from the middle of the trap. In Fig. 2.6 (continuous line) we show a case where the CM never crosses the center of the trap. The MDF corresponding to this case, at three different times, is displayed in Fig. 2.7 (b). There it can be seen that initially ( $\tau = 0$ ) no Bragg conditions are satisfied

in the system, and that some time after the initial displacement the Bragg conditions are fulfilled ( $\tau = 250\hbar/t$ ). Finally, we also show the MDF long time after the initial displacement of the trap ( $\tau = 12500\hbar/t$ ), when the oscillations of the CM are completely damped and the MDF is approximately symmetric around  $k = 0$ .

## 2.3 Doubling the periodicity

In this section we study the consequences of enlarging the periodicity in the lattice. For this purpose we introduce an alternating potential. Then, the Hamiltonian of the system can be written as

$$H = -t \sum_i \left( c_i^\dagger c_{i+1} + \text{H.c.} \right) + V_\alpha \sum_i (x_i)^\alpha n_i + V_a \sum_i (-1)^i n_i, \quad (2.4)$$

where the last term represents the oscillating potential and  $V_a$  its strength. The purpose of introducing an alternating potential in the trapped system is twofold. For fermionic systems, the increase of the numbers of sites per unit cell leads to the possibility of creating insulating states (band insulators in the unconfined case) for commensurate fillings. On the other hand, by changing the periodicity, new Bragg conditions are introduced, giving the possibility of further control on the confinement discussed in the previous sections.

### 2.3.1 Single particle spectrum and the additional ‘slicing’

Figure 2.8 shows how the density profiles evolve in a harmonic trap when the total filling is increased. Since the density oscillates due to the alternating potential, we made two different plots for the odd [negative value of the alternating potential, Fig. 2.8(a)] and even [positive value of the alternating potential, Fig. 2.8(b)] sites. In the flat regions of Fig. 2.8, both even and odd sites have the same densities than the corresponding sites in the homogeneous case at half filling for the same value of the alternating potential, so that it is expected that they correspond to local insulating phases. This can be also understood since the density in these regions does not change although there is an effective local chemical potential changing, due to the existence of the trap.

In Fig. 2.9(a) and (b) we show the single particle spectrum and the level spacing respectively for the same parameters of Fig. 2.8. Although in this case the level spacing exhibits a more complicated structure, an immediate identification between the regions

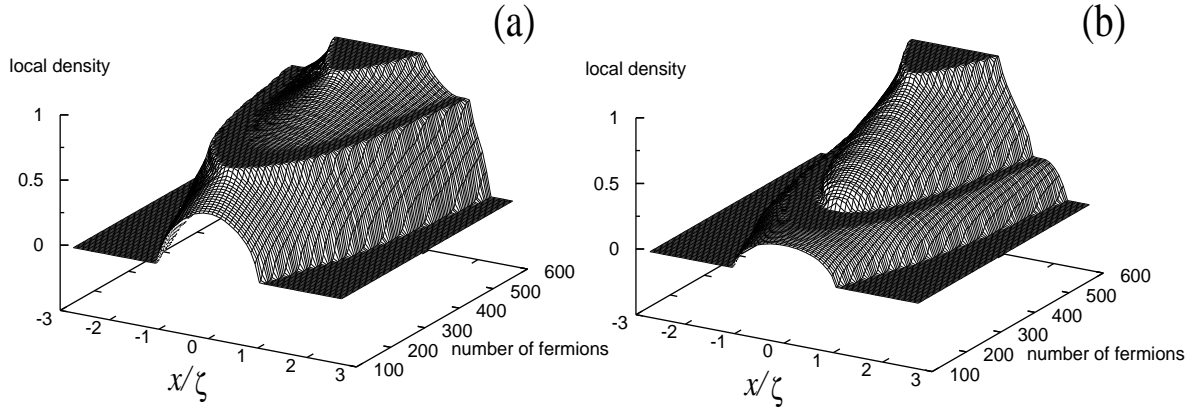


Figure 2.8: Evolution of the local density in a harmonic trap as a function of the position and increasing total number of fermions when an alternating potential  $V_a = 0.5t$  is present. (a) Odd sites. (b) Even sites. The system has 1000 lattice sites and  $V_2a^2 = 3 \times 10^{-5}t$ .

signaled in Fig. 2.9(b) between arrows and different fillings in Fig. 2.8 can be done. (A) corresponds to the fillings in Fig. 2.8 where only a metallic phase appears in the trap, (B) to the fillings where the first plateau is present in Fig. 2.8, (C) to the fillings where a metallic phase develops in the middle of the trap and it is surrounded by insulating regions, and (D) to the fillings in Fig. 2.8 where the insulator with  $n = 1$  appears in the center of the system. The region after the last arrow in Fig. 2.9(b) corresponds to deconfined states. Notice that the level spacing in regions (C) and (D) shows a behavior that was not present in Fig. 2.1.

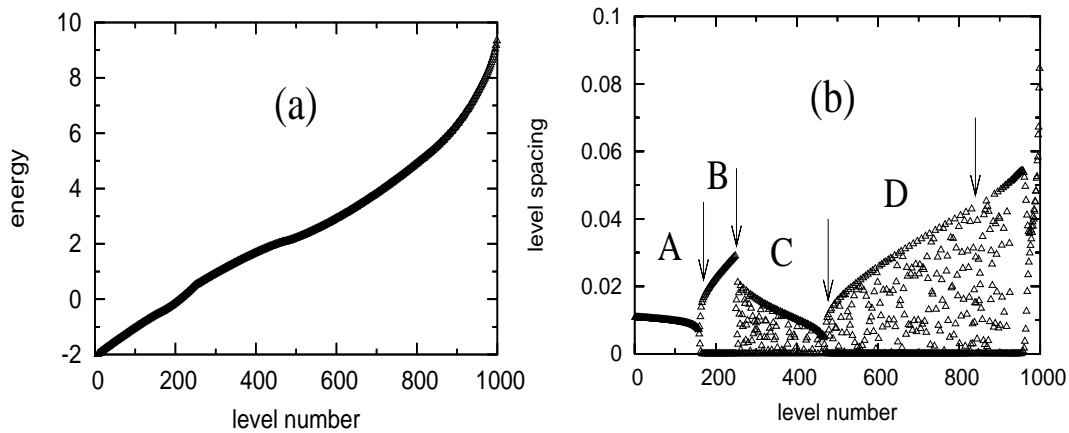


Figure 2.9: Single particle spectrum (a) and level spacing (b) for a system with an alternating potential  $V_a = 0.5t$  and with  $N = 1000$  and  $V_2a^2 = 3 \times 10^{-5}t$ . For the explanation of the regions between the arrows see text.



In order to understand the complex behavior of the level spacing we study, as in the previous section, the eigenfunctions of the system shown in Fig. 2.9. The eigenfunctions corresponding to region A in Fig. 2.1(b) behave as expected for a metallic phase, where the combination of the alternating and confining potentials generates a different modulation than the one studied in Sec. 2.1, but without qualitative differences. In the second region of the spectrum (region B) the eigenfunctions have zero weight in the middle of the trap, exactly like in the insulator discussed in Sec. 2.1. In region C there is, as pointed out above, a new feature since in this case it is possible to obtain a metallic region surrounded by an insulating one. This is reflected by the eigenfunctions shown in Fig. 2.10(a), where one of the eigenfunctions is non-zero only inside the local insulating phase (continuous line), and the other is non-zero only outside the insulating phase (dashed line), the energy levels associated with the latter ones are degenerate. For the region D the situation is similar but in this case the system is divided in four parts because of the existence of the insulator with  $n = 1$  in the middle of the trap and the insulator between the two metallic phases. This implies that all the levels are degenerate in region D, and the particles are located either between both insulating regions or outside the outermost one, as shown in Fig. 2.10(b).

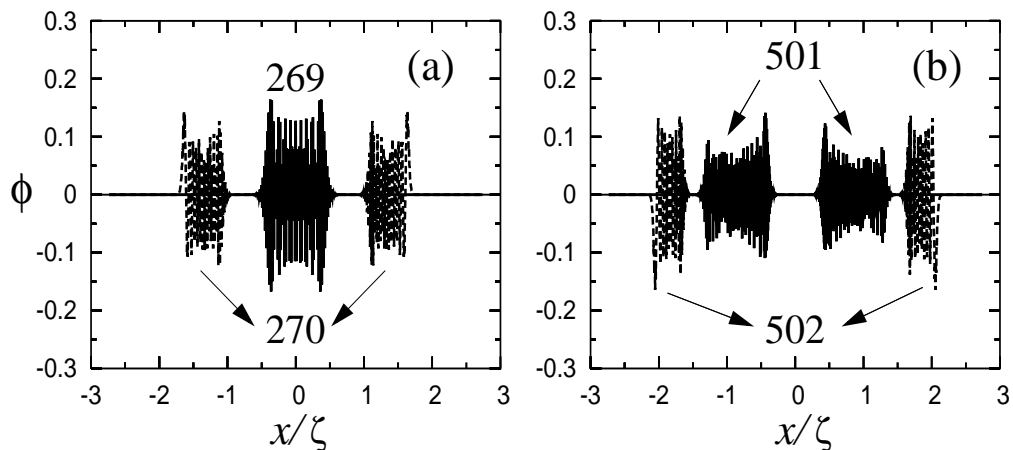


Figure 2.10: Eigenfunctions for a trapped system with an alternating potential ( $V_a = 0.5t$ ) for  $N = 1000$  and  $V_2 a^2 = 3 \times 10^{-5}t$ . The eigenfunctions correspond to the levels: 269 (a) (continuous line), 270 (a) (dashed line), 501 (b) (continuous line), and 502 (b) dashed line.

### 2.3.2 Local density of states and the momentum distribution function

As in the previous sections, the spectral features discussed here are equally valid for fermions as well as for bosons. Up to now we discussed the ‘slicing’ of the systems only in terms of fermions and based on the appearance of insulating regions along the system. As before, it would be also here desirable to understand the appearance of forbidden regions in space in terms of a single particle picture. We show now that with the introduction of new Bragg conditions, due to the altered periodicity, the ‘slicing’ of the system can be explained in an analogous way as in the previous section. In the unconfined case, the doubling of the periodicity creates new Bragg conditions at  $k = \pm\pi/2a$ , such that an energy gap  $2V_a$  appears. Fig. 2.9(a) shows that in the confined case the spectrum is continuous (in the sense that the level spacing is much smaller than  $2V_a$ ), so that the imprint of the gap can be seen only in the local density of states

$$N_i(\omega) = \frac{1}{\pi} \text{Im}G_{ii}(\omega) , \quad (2.5)$$

where  $G_{ij}(\omega)$  is the one-particle Green’s function [77], which for the non-interacting case can be easily computed.

The insets in Fig. 2.11 show the density of states per unit cell (now containing two lattice points) for two different positions along the density profile. The downward arrows in each inset corresponds to the location of the Fermi energy. The inset at the left corresponds to a situation where the Fermi energy goes through the lowest band, whereas the inset at the right belongs to sites in the middle of an insulating region. As expected, in this latter case, the Fermi energy lies inside the gap. The size of the gap is to a high degree of accuracy  $2V_a$  for the site in the middle of the trap, but slightly less on the sides. Therefore, again the same arguments as before can be used, but instead of  $4t$ , the width for each band is given by  $\sqrt{4t^2 + V_a^2} - V_a \simeq 1.56t$  in our case. Without repeating the detailed discussion in Sec. 2.1, we can understand the confinement in Fig. 2.10(a) as follows. Level 269 has an energy that for sites in the middle of the trap falls in the middle of the upper band, while for level 270 (the same value of energy), passes through the lowest band. In fact, the density of states shown in Fig. 2.11 can be viewed as approximately shifted by  $V_2 x_i^2$ , counting the sites from the middle. Finally, levels in Fig. 2.10(b) correspond to the case where in the middle of the trap they fall beyond

the highest band, then going outwards, they fall in the middle of the highest band, and further outside, they fall in the middle of the lowest band.

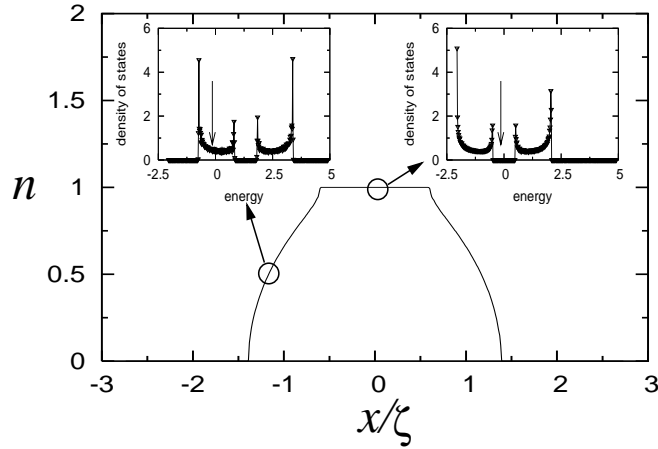


Figure 2.11: Density profile per unit cell (now containing two contiguous lattice sites) for a trap with  $N = 10000$ ,  $V_2 a^2 = 3 \times 10^{-7} t$  and  $N_f = 2000$ . The insets show the density of states per unit cell for two points in the profile. The arrows in the insets signal the Fermi energy for the selected filling.

Again, as in the previous sections, one can follow the same reasoning by considering the MDF. Due to the new periodicity it displays new features, associated with the fact that increasing the periodicity the Brillouin zone is decreased, and in the present case a second Brillouin zone will be visible. In Fig. 2.12 we show the density profiles (a)-(d) that characterize the four different situations present in Fig. 2.8. They correspond to fillings of the trap in the four regions of the single particle spectrum discussed previously in Fig. 2.9. Notice that in the figures we included all the odd and even points in the density profiles. We plotted as horizontal dashed lines the values of the densities in the band insulating phase of the homogeneous system for the odd and even sites (from top to bottom respectively), so that it can be seen where are located the local insulating phases in the trap. The corresponding normalized MDF are presented in Fig. 2.12(e)-(h).

In Figs. 2.12(a),(e) it is possible to see that when only the metallic phase is present in the trap, in the MDF an additional structure appears after  $\pi/2$ , corresponding to the contribution from the second Brillouin zone. When a first insulating phase is reached, by coming to the top of the lowest band,  $k = \pi/2a$  is reached, and increasing the fillings of the system beyond that point, the dip around  $k = \pi/2a$  disappears [Figs. 2.12(b),(f)]. On adding more particles to the system a metallic phase appears inside the insulating

plateau, [Figs. 2.12(c),(g)]. When this metallic phase widens, decreasing the size of the insulating phase,  $n_k$  starts to be similar to the  $n_k$  of the pure metallic phase in the system without the alternating potential. Increasing even further the filling of the system, when the trivial insulator ( $n = 1$ ) appears in the center of the trap, the tail with very small values of  $n_k$  disappears (like in the system without the alternating potential the region with  $n_k$  zero also disappears [Fig. 2.3(b)] and the further increase of the filling in the system makes  $n_k$  flatter [Figs. 2.12(d),(h)].

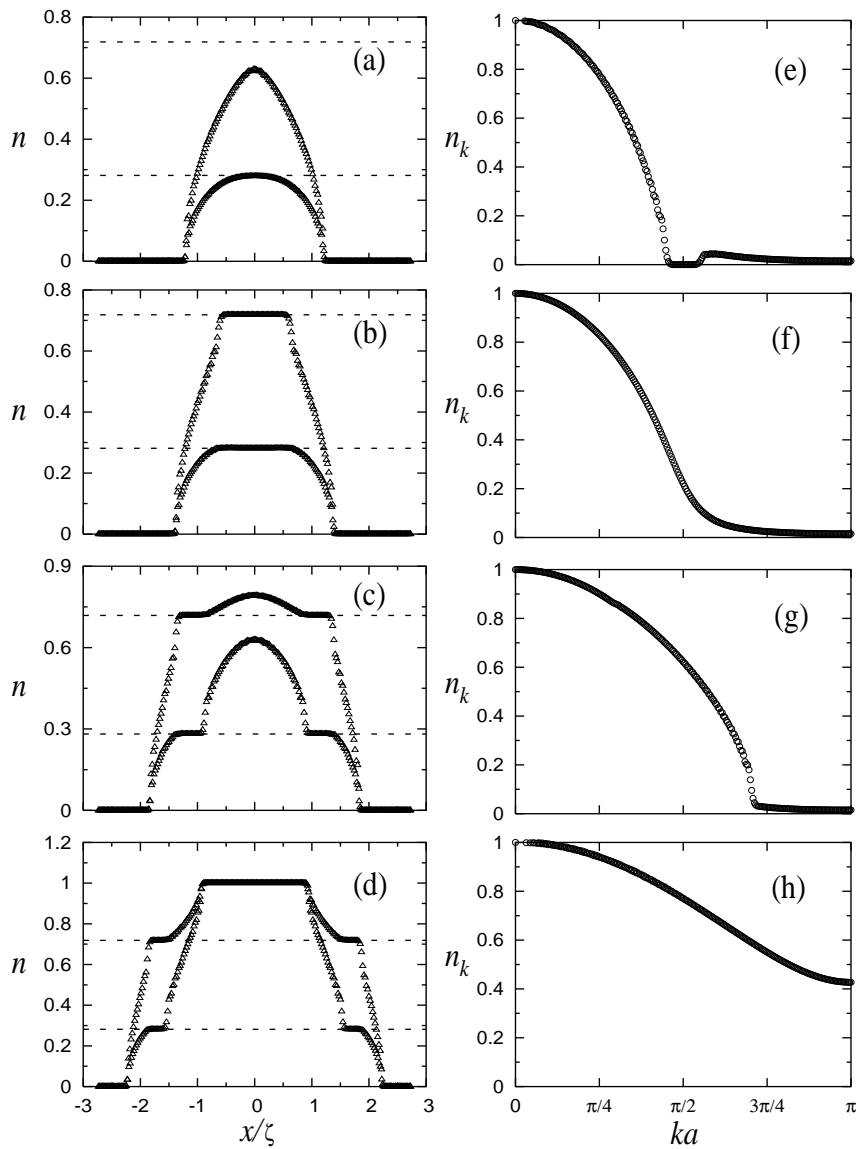


Figure 2.12: Density profiles (a)-(d) and their normalized MDF (e)-(h) for  $N_f = 150$  (a),(e), 200 (b),(f), 350 (c),(g), 600 (d),(h) and  $N = 1000$ ,  $V_a = 0.5t$ ,  $V_2a^2 = 3 \times 10^{-5}t$ .

### 2.3.3 The phase diagram

Finally we analyze the phase diagram for these systems. It can be generically described by the characteristic density  $\tilde{\rho}$  defined by Eq. 2.3. In Fig. 2.13 we show two phase diagrams for two different values of the curvature of the confining potential,  $V_2a^2 = 3 \times 10^{-5}t$  and  $V_2a^2 = 3 \times 10^{-4}t$ . There it can be seen that although there is one order of magnitude between the curvatures of the confining potentials, the phase diagrams are one on top of the other, the small differences are only due to the finite number of particles which make the changes in  $\tilde{\rho}$  discrete. Therefore, the characteristic density allows to compare systems with different curvatures of the confining potential, number of particles and sizes.

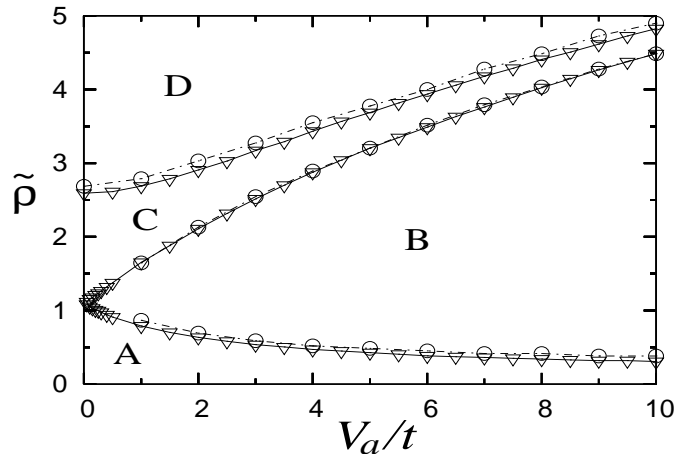


Figure 2.13: Phase diagram for systems with  $V_2a^2 = 3 \times 10^{-5}t$  ( $\nabla$ ) and  $V_2a^2 = 3 \times 10^{-4}t$  ( $\circ$ ). The different phases are explained in the text.

The different phases present in Fig. 2.13 are: (A) a pure metallic phase, (B) an insulator in the middle of the trap surrounded by a metallic phase, (C) a metallic intrusion in the middle of the insulator, (D) an insulator with  $n = 1$  in the center of the trap surrounded by a metal, an insulator and the always present external metallic phase. For very small values of the alternating potential ( $V_a$ ), the insulator surrounding the metallic phase in the center of the trap can disappear leaving a full metallic phase at the very beginning of phase C. Similarly, the insulator with  $n = 1$  can be surrounded only by a metallic phase (at the very beginning of phase D). However, these regions are small in the phase diagram and we did not include them.



## Chapter 3

# The quantum Monte Carlo method

We introduce in this chapter the quantum Monte Carlo (QMC) method usually employed to study strongly correlated electron systems, and that we apply to the analysis of strongly correlated bosonic (Chap. 4) and fermionic (Chap. 5) atoms confined on optical lattices.

We start the exposition with the basic ideas of the classical Monte Carlo (MC) method for the evaluation of multidimensional integrals (Sec. 3.1), and then we show how they are applied to quantum systems. The path integral formulation of a quantum many body problem [78] is at the heart of the QMC method. It reduces the calculation of physical observables to the evaluation of high dimensional integrals for which the MC approach is used. Our discussion will be restricted to the two QMC techniques that are relevant to our work, the zero-temperature projector QMC (Sec. 3.2) and the world-line QMC (Sec. 3.3) .

### 3.1 The classical Monte Carlo method

The Monte Carlo method<sup>1</sup> is a powerful way to calculate multidimensional integrals. It provides from accurate results that are exact within controllable stochastic sampling errors. The essence of the problem of calculating multidimensional integrals is the unfavorable way in which the accuracy of conventional quadrature formulae depends on the number of points at which the integrand is sampled in high dimensions. In general it is needed to evaluate

$$\langle f \rangle_P = \int d^d \vec{x} P(\vec{x}) f(\vec{x}), \quad (3.1)$$

---

<sup>1</sup>See Ref. [79] for a detailed description of the method.

where  $\vec{x}$  is a vector in  $d$ -dimensions and  $P(\vec{x})$  is a probability distribution satisfying the conditions<sup>2</sup>

$$\int d^d x P(\vec{x}) = 1, \quad P(\vec{x}) \geq 0. \quad (3.2)$$

Conventionally, in order to evaluate the integral in Eq. (3.1) one may break up the integration volume into hypercubes of linear dimension  $h$ , which leads to a systematic error for the integral in a single hypercube of the order  $h^{k+d}$  where  $k$  ( $k > 0$ ) is an integer that depends on the method used. The required number of points to be evaluated  $M$  is of the order  $1/h^d$ , then the total systematic error for the evaluation of the integral is of the order  $Mh^{k+d}$ , which scales as  $M^{-k/d}$ . The previous result shows that with increasing the dimension of the system the error falls off increasingly slowly with the number of points  $M$ .

The basic idea of the MC method is to sample  $\langle f \rangle_P$  statistically. This is done in such a way that, due to the central limit theorem (see Appendix B), the sampling errors decrease as an universal function ( $1/\sqrt{M}$ ) of the number of points  $M$  at which the integrand is sampled. This is independent of the dimension of the integral. For very large  $M$  is possible to calculate  $\langle f \rangle_P$  as (see Appendix B)

$$\langle f \rangle_P = \frac{1}{M} \sum_{\substack{i=1 \\ \vec{x}_i \in P(\vec{x})}}^M f(\vec{x}_i) \pm \frac{1}{\sqrt{M}} \left[ \frac{1}{M} \sum_{\substack{i=1 \\ \vec{x}_i \in P(\vec{x})}}^M f(\vec{x}_i)^2 - \left( \frac{1}{M} \sum_{\substack{i=1 \\ \vec{x}_i \in P(\vec{x})}}^M f(\vec{x}_i) \right)^2 \right]^{\frac{1}{2}} \quad (3.3)$$

where  $\vec{x}_i \in P(\vec{x})$  means that the variable  $\vec{x}$  is sampled according to the probability distribution  $P(\vec{x})$ . The latter is achieved with the use of Markov chains [79].

A Markov chain of variables  $(\vec{x}_1, \vec{x}_2, \dots, \vec{x}_t, \vec{x}_{t+1})$  is generated by a rule that specifies the probability distribution of the  $(t+1)^{\text{th}}$  element  $\vec{x}_{t+1}$  ( $P_{t+1}(\vec{x}_{t+1})$ ) solely on the basis of the  $t^{\text{th}}$  element  $\vec{x}_t$  ( $P_t(\vec{x}_t)$ ). The variable  $t$  is usually called the MC time, and should not be confused with any real or imaginary time when the method is applied to a problem in physics. Our aim is that in the limit  $t \rightarrow \infty$ , the probability distribution  $P_t(\vec{x}_t)$  converges to the desired probability distribution  $P(\vec{x}_t)$ .

---

<sup>2</sup>In practice, one usually access the unnormalized probability distribution  $p(\vec{x})$ , so that in order to obtain the normalized one it is necessary to calculate the ratio

$$P(\vec{x}) = \frac{p(\vec{x})}{Z}, \quad Z = \int d^d \vec{x} p(\vec{x}).$$

In the terminology of statistical mechanics,  $p(\vec{x})$  corresponds to the Boltzmann weight and  $Z$  to the partition function.



In order to define a Markov chain, we denote  $T(\vec{x}_t \rightarrow \vec{x}_{t+1})$  as the probability of reaching element  $\vec{x}_{t+1}$  from element  $\vec{x}_t$ . The MC time evolution of the probability distribution is obtained as

$$P_{t+1}(\vec{x}_{t+1}) = \sum_{\vec{x}_t} T(\vec{x}_t \rightarrow \vec{x}_{t+1})P_t(\vec{x}_t), \quad (3.4)$$

where  $T(\vec{x}_t \rightarrow \vec{x}_{t+1}) \geq 0$ , satisfies the normalization conditions

$$\sum_{\vec{x}_t} T(\vec{x}_t \rightarrow \vec{x}_{t+1}) = \sum_{\vec{x}_{t+1}} T(\vec{x}_t \rightarrow \vec{x}_{t+1}) = 1, \quad (3.5)$$

and has to be ergodic, i.e. once we have reached an arbitrary point  $\vec{x}_t$  there must be always a finite probability to reach any other point  $\vec{x}_{t+1}$ .

Additionally, there are two other important requirements on  $T(\vec{x}_t \rightarrow \vec{x}_{t+1})$ . The first one is that the desired distribution  $P(\vec{x}_t)$  must be an equilibrium solution of the MC evolution (stationarity), i.e. once  $P(\vec{x}_t)$  has been reached at any MC time  $t$ , a further MC evolution does not change it

$$P(\vec{x}_{t+1}) = \sum_{\vec{x}_t} T(\vec{x}_t \rightarrow \vec{x}_{t+1})P(\vec{x}_t). \quad (3.6)$$

The second requirement is that during the MC evolution, the probability distribution  $P_t(\vec{x}_t)$  approaches to the desired distribution  $P(\vec{x}_t)$ . These two requirements are satisfied when the detailed balance condition is imposed<sup>3</sup>.

$$T(\vec{x}_t \rightarrow \vec{x}_{t+1})P(\vec{x}_t) = T(\vec{x}_{t+1} \rightarrow \vec{x}_t)P(\vec{x}_{t+1}). \quad (3.7)$$

Stationarity is automatically satisfied since

$$\sum_{\vec{x}_t} T(\vec{x}_t \rightarrow \vec{x}_{t+1})P(\vec{x}_t) = P(\vec{x}_{t+1}) \sum_{\vec{x}_t} T(\vec{x}_{t+1} \rightarrow \vec{x}_t) = P(\vec{x}_{t+1}), \quad (3.8)$$

where in the last step the normalization condition was used. The fact that  $P_t(\vec{x}_t)$  approaches to the desired distribution  $P(\vec{x}_t)$  may be seen as follows

$$\begin{aligned} \sum_{\vec{x}_{t+1}} |P_{t+1}(\vec{x}_{t+1}) - P(\vec{x}_{t+1})| &= \sum_{\vec{x}_{t+1}} \left| \sum_{\vec{x}_t} T(\vec{x}_t \rightarrow \vec{x}_{t+1})P_t(\vec{x}_t) - \sum_{\vec{x}_t} T(\vec{x}_t \rightarrow \vec{x}_{t+1})P(\vec{x}_t) \right| \\ &\leq \sum_{\vec{x}_{t+1}} \sum_{\vec{x}_t} T(\vec{x}_t \rightarrow \vec{x}_{t+1}) |P_t(\vec{x}_t) - P(\vec{x}_t)| \\ &= \sum_{\vec{x}_t} |P_t(\vec{x}_t) - P(\vec{x}_t)|, \end{aligned} \quad (3.9)$$

---

<sup>3</sup>We should note here that the detailed balance condition, also known as the microreversibility condition, is sufficient but not necessary in order to satisfy the stationarity condition and the convergence to the desired distribution  $P(\vec{x}_t)$  during the MC evolution [80,81]

where, under the assumption of ergodicity, the strict equality holds only if  $P_t(\vec{x}_t) = P(\vec{x}_t)$ .

Finally, once the properties of  $T(\vec{x}_t \rightarrow \vec{x}_{t+1})$  have been defined, one can construct it explicitly using the Metropolis algorithm [82]

$$T(\vec{x}_t \rightarrow \vec{x}_{t+1}) = \begin{cases} 1 & \text{if } P(\vec{x}_{t+1}) > P(\vec{x}_t) \\ \frac{P(\vec{x}_{t+1})}{P(\vec{x}_t)} & \text{if } P(\vec{x}_{t+1}) < P(\vec{x}_t) \end{cases}, \quad (3.10)$$

or the heat bath method

$$T(\vec{x}_t \rightarrow \vec{x}_{t+1}) = \frac{\frac{P(\vec{x}_{t+1})}{P(\vec{x}_t)}}{1 + \frac{P(\vec{x}_{t+1})}{P(\vec{x}_t)}}. \quad (3.11)$$

In principle, we are now ready to perform a classical MC simulation. For that, we start with a single arbitrary configuration  $\vec{x}_0$  and perform the MC evolution. After a certain MC time  $t_e$ , at which the desired distribution  $P(\vec{x}_t)$  has been reached, one starts measuring the function of interest  $f(\vec{x}_{i=t-t_e})$ , where  $i$  is the number of the measurement. The integral of this function ( $\langle f \rangle_P$ ) may be evaluated after  $M$  measurements following Eq. (3.3).

## 3.2 The projector QMC algorithm

In the last decades, the increased interest on strongly interacting quantum systems has stimulated the development of numerical methods that are able to handle with such correlated systems. Particularly dominant among the others, because of the generality of models that can be treated and the accuracy of the results obtained, is the quantum Monte Carlo method. At the present time there are many QMC techniques that deal with different models in different ways, like: the Determinantal Algorithm [83–91], the worldline QMC [92] and its more powerful extension the Loop Algorithm [93–96], and the Green’s function QMC (GFMC) [97–99]. In addition, some constrained algorithms like the Fixed Node MC [100, 101], the Constrained Path MC [102], and the GFMC with Stochastic Reconfiguration [103], have been developed in order to circumvent the know sign problem [104], which makes very difficult dealing with fermionic degrees of freedom in some models at low temperatures and large systems sizes. Other direction of developments are hybrid algorithms, like a recent Hybrid-Loop algorithm [105–109] that combines the Determinantal Algorithm with the Loop Algorithm to deal with the well known  $t - J$  model, a paradigmatic model for high-Tc superconductors.

In the present section we review<sup>4</sup> the zero temperature projector method [86–88] adapted from the Determinantal Algorithm proposed by Blankenbecler, Scalapino and Sugar [83–85]. In order to make the exposition more clear we focus on the problem to which we apply it latter, the repulsive Hubbard model (see Chap. 5). The Hamiltonian in this case can be written as

$$\begin{aligned} H &= -t \sum_{i,\sigma} \left( c_{i\sigma}^\dagger c_{i+1\sigma} + \text{H.c.} \right) + U \sum_i n_{i\uparrow} n_{i\downarrow} + \sum_i \mu_i n_i \\ &= H_t + H_U + H_\mu \end{aligned} \quad (3.12)$$

where  $c_{i\sigma}^\dagger$ ,  $c_{i\sigma}$  are creation and annihilation operators, respectively, for fermions with spin  $\sigma$  at site  $i$  ( $i = 1, \dots, N$  with  $N$  the number of lattice sites),  $n_{i\sigma} = c_{i\sigma}^\dagger c_{i\sigma}$ , and  $n_i = \sum_\sigma n_{i\sigma}$  is the particle number operator. The hopping parameter is denoted by  $t$ , the on-site repulsive parameter by  $U$  ( $U > 0$ ), and the last term describes an arbitrary site dependent chemical potential<sup>5</sup>.

### 3.2.1 Path integral formulation

The QMC treatment of this problem is based on the path integral formulation of the partition function in imaginary time. This formulation is usual in statistical mechanics, and is in contrast to the real time formulation of quantum mechanics [78]. In the zero temperature limit, the partition function can be written as

$$Z = \langle \psi_T | e^{-\beta H} | \psi_T \rangle, \quad (3.13)$$

where the wave-function at the boundaries in the imaginary time  $|\psi_T\rangle$  (that we refer in what follows as the trial wave-function) is in principle not important since in the limit  $\beta = 1/k_B T \rightarrow \infty$  it will be always projected to the ground state<sup>6</sup>.

In order to numerically evaluate expression (3.13) the Trotter-Suzuki decomposition [110, 111] for the imaginary time  $\beta = L\Delta\tau$  (with  $\Delta\tau \rightarrow 0$ ) is introduced, so that the exponential of the sums of non-commuting pieces in the Hamiltonian (3.12) can be splitted

---

<sup>4</sup>For more extensive reviews see Refs. [89–91]

<sup>5</sup>Which could be, for example, the confining potential introduced in Chap. 5.

<sup>6</sup>The trial wave-function is assumed to have a non-zero overlap with the ground state  $|\psi_G\rangle$ , i.e.  $\langle \psi_G | \psi_T \rangle \neq 0$ .

as

$$\begin{aligned} e^{-\Delta\tau(H_t+H_U+H_\mu)} &= e^{-\Delta\tau H_t} e^{-\Delta\tau(H_U+H_\mu)} + O(\Delta\tau)^2 \\ &= e^{-\Delta\tau H_t} e^{-\Delta\tau H_U} e^{-\Delta\tau H_\mu} + O(\Delta\tau)^2 \end{aligned} \quad (3.14)$$

where in the last step no additional error was introduced since  $H_U$  and  $H_\mu$  commute.

Once the interaction term has been isolated, the discrete Hubbard-Stratonovich transformation by Hirsch [112] (see Appendix C)

$$e^{-\Delta\tau U \sum_i n_{i\uparrow} n_{i\downarrow}} = \frac{1}{2^N} e^{-\frac{1}{2}\Delta\tau U \sum_i n_i} \sum_{\vec{s}} e^{\alpha \sum_i s_i (n_{i\uparrow} - n_{i\downarrow})}, \quad (3.15)$$

can be applied. This is done in order to decouple the fermionic degrees of freedom by coupling them to an external Hubbard-Stratonovich (HS) field  $\vec{s} = \{s_i\}$  with discrete components, which can have values  $\pm 1$ , and  $i = 1, \dots, N$ . The parameter  $\alpha$  is obtained from  $\cosh \alpha = e^{\Delta\tau U/2}$ .

Then Eq. (3.13) can be substituted by its approximated value

$$Z_{TS} = \sum_{\vec{s}} \langle \psi_T | \prod_{\sigma} \prod_{m=1}^L e^{\Delta\tau t \sum_i (c_{i\sigma}^\dagger c_{i+1\sigma} + \text{H.c.})} e^{\alpha b_\sigma \sum_i s_{i,m} n_{i\sigma}} e^{-\Delta\tau \sum_i \mu_i n_{i\sigma}} | \psi_T \rangle, \quad (3.16)$$

where  $Z_{TS} \rightarrow Z$  for  $\Delta\tau \rightarrow 0$ . The parameter  $b_\sigma$  is  $+1$  for  $\sigma = \uparrow$  and  $-1$  for  $\sigma = \downarrow$ . We notice that the factor independent of the HS field  $\vec{s}$  in Eq. (3.15) is absorbed by the chemical potential in Eq. (3.16). The HS field in Eq. (3.16)  $\vec{s} = \{s_{i,m}\}$  is the generalization of the one in Eq. (3.15), including the imaginary time dependence, with  $m = 1, \dots, L$ .

Equation (3.16) makes evident the need for the ideas of the MC method. In order to perform the evaluation of this expression, the results for a total of  $2^{NL}$  configurations of the HS degrees of freedom have to be summed. This is impossible to do with the present computers for reasonable systems sizes, so that the amount of configurations to be considered needs to be reduced, and the MC method is the ideal scenario for that. Next, we introduce the matrix representation that will be employed in the calculations of Eq. (3.16) using the QMC technique.

### 3.2.2 Matrix representation

The operations in Eq. (3.16) can be all done using a matrix representation, for which there are three features that are fundamental.

- i) Once the interacting term in Eq. (3.13) has been decoupled through the Hubbard-Stratonovich transformation, all the exponentials are bilinear in the fermionic operators, and they are independent for spin up and down fermions [Eq. (3.16)].
- ii) The trial wave-function is selected to be a Slater determinant, which satisfies the antisymmetrization postulate for identical fermions, and is a product of single-particle states. It can be written as

$$|\Psi_T\rangle = |\Psi_T^\uparrow\rangle \otimes |\Psi_T^\downarrow\rangle, \quad (3.17)$$

with

$$|\Psi_T^\sigma\rangle = \prod_{l=1}^{N_f} \sum_{j=1}^N P_{jl}^\sigma c_{j\sigma}^\dagger |0\rangle, \quad (3.18)$$

and  $\mathbf{P}^\sigma$  being the matrix of components

$$\mathbf{P}^\sigma = \begin{pmatrix} P_{11}^\sigma & P_{12}^\sigma & \cdot & \cdot & \cdot & P_{1N_f}^\sigma \\ P_{21}^\sigma & P_{22}^\sigma & \cdot & \cdot & \cdot & P_{2N_f}^\sigma \\ \cdot & \cdot & \cdot & \cdot & \cdot & \cdot \\ \cdot & \cdot & \cdot & \cdot & \cdot & \cdot \\ \cdot & \cdot & \cdot & \cdot & \cdot & \cdot \\ P_{N1}^\sigma & P_{N2}^\sigma & \cdot & \cdot & \cdot & P_{NN_f}^\sigma \end{pmatrix}. \quad (3.19)$$

- iii) Finally, one can prove that the action of an exponential bilinear in fermionic operators on a Slater determinant, results in a new Slater determinant with elements [91]

$$e^{\sum_{ij} c_{i\sigma}^\dagger X_{ij} c_{j\sigma}} |\Psi_T\rangle = \prod_{l=1}^{N_f} \sum_{j=1}^N P_{jl}^\sigma c_{j\sigma}^\dagger |0\rangle, \quad (3.20)$$

where  $\mathbf{P}'^\sigma = e^{\mathbf{X}} \mathbf{P}^\sigma$ .

With the knowledge above, the imaginary time evolution of each fermionic flavor, for a given configuration of the HS field  $\vec{s}$

$$B_{\vec{s}}^\sigma(\beta, 0) = \prod_{m=1}^L e^{-\Delta\tau \sum_i (c_{i\sigma}^\dagger c_{i+1\sigma} + \text{H.c.})} e^{\alpha b_\sigma \sum_i s_{i,m} n_{i\sigma}} e^{-\Delta\tau \sum_i \mu_i n_{i\sigma}}, \quad (3.21)$$

can be written in a matrix representation as

$$\mathbf{B}_{\vec{s}}^\sigma(\beta, 0) = \mathbf{B}_{\vec{s}}^\sigma(\beta, \beta - \Delta\tau) \mathbf{B}_{\vec{s}}^\sigma(\beta - \Delta\tau, \beta - 2\Delta\tau) \cdots \mathbf{B}_{\vec{s}}^\sigma(\Delta\tau, 0), \quad (3.22)$$

where

$$\mathbf{B}_s^\sigma(\tau, \tau - \Delta\tau) = \mathbf{A}_s^\sigma(\tau) e^{\Delta\tau \mathbf{K}}, \quad (3.23)$$

with

$$\mathbf{A}_s^\sigma(\tau) = \begin{pmatrix} e^{\alpha b_\sigma s_1(\tau) - \Delta\tau \mu_1} & & & & 0 \\ & e^{\alpha b_\sigma s_2(\tau) - \Delta\tau \mu_2} & & & \\ & & \ddots & & \\ & & & \ddots & \\ 0 & & & & e^{\alpha b_\sigma s_n(\tau) - \Delta\tau \mu_n} \end{pmatrix}, \quad (3.24)$$

and  $\mathbf{K}$  being the sparse matrix of the kinetic term. Its exponentiation can be very efficiently done by using a checkerboard breakup [89]

$$e^{\Delta\tau \mathbf{K}} = e^{\Delta\tau \sum_{\langle i,j \rangle} \mathbf{K}^{(ij)}} \approx \prod_{\langle i,j \rangle} e^{\Delta\tau \mathbf{K}^{(ij)}}, \quad (3.25)$$

where  $\mathbf{K}^{(ij)}$  can be easily exponentiated since its only non-zero elements are  $K_{ij}^{(ij)} = K_{ji}^{(ij)} = t$ . Then

$$\begin{aligned} e^{\Delta\tau \mathbf{K}^{(ij)}} &= \exp \Delta\tau \begin{pmatrix} 0 & \cdots & 0 & 0 & \cdots & 0 \\ \vdots & & \vdots & \vdots & & \vdots \\ 0 & \cdots & 0 & K_{ij} & \cdots & 0 \\ 0 & \cdots & K_{ij} & 0 & \cdots & 0 \\ \vdots & & \vdots & \vdots & & \vdots \\ 0 & \cdots & 0 & 0 & \cdots & 0 \end{pmatrix} \\ &= \begin{pmatrix} 1 & \cdots & 0 & 0 & \cdots & 0 \\ \vdots & & \vdots & \vdots & & \vdots \\ 0 & \cdots & \cosh(\Delta\tau t) & \sinh(\Delta\tau t) & \cdots & 0 \\ 0 & \cdots & \sinh(\Delta\tau t) & \cosh(\Delta\tau t) & \cdots & 0 \\ \vdots & & \vdots & \vdots & & \vdots \\ 0 & \cdots & 0 & 0 & \cdots & 1 \end{pmatrix}. \end{aligned} \quad (3.26)$$

Another way to exponentiate the kinetic matrix is to make use of an unitary transformation, such that  $\mathbf{U}^\dagger \mathbf{K} \mathbf{U} = \mathbf{D}$  where  $\mathbf{D}$  is diagonal, then

$$e^{\Delta\tau \mathbf{K}} = \mathbf{U} e^{\Delta\tau \mathbf{D}} \mathbf{U}^\dagger. \quad (3.27)$$

Provided that we know at this point that the action of the strings of exponential operators in Eq. (3.16) on the trial wave-function (to the right) will generate a new Slater determinant  $|\Psi_{\vec{s}}^{\sigma}(\beta)\rangle = \prod_{l=1}^{N_f} \sum_{j=1}^N P_{jl,\vec{s}}^{\sigma}(\beta) c_{j\sigma}^{\dagger} |0\rangle$ , and that using the matrix representation above we are able to evaluate its components as  $\mathbf{P}_{\vec{s}}^{\sigma}(\beta) = \mathbf{B}_{\vec{s}}^{\sigma}(\beta, 0) \mathbf{P}^{\sigma}$ , then the weight of a given HS field configuration  $\vec{s}$  can be obtained as

$$\begin{aligned} p[\vec{s}] &= \prod_{\sigma} \langle 0 | \prod_{i=1}^{N_f} \sum_{k=1}^N P_{ki}^{\sigma} c_{k\sigma} \prod_{j=1}^{N_f} \sum_{l=1}^N P_{lj,\vec{s}}^{\sigma}(\beta) c_{l\sigma}^{\dagger} | 0 \rangle \\ &= \prod_{\sigma} \sum_{\substack{i_1, \dots, i_{N_f} \\ j_1, \dots, j_{N_f}}}^N P_{i_1 1}^{\sigma} \cdots P_{i_{N_f} N_f}^{\sigma} P_{j_1 1, \vec{s}}^{\sigma}(\beta) \cdots P_{j_{N_f} N_f, \vec{s}}^{\sigma}(\beta) \langle 0 | c_{i_1 \sigma} \cdots c_{i_{N_f} \sigma} c_{j_{N_f} \sigma}^{\dagger} \cdots c_{j_1 \sigma}^{\dagger} | 0 \rangle \\ &= \prod_{\sigma} \det [\mathbf{P}^{\sigma \dagger} \mathbf{P}_{\vec{s}}^{\sigma}(\beta)] = \prod_{\sigma} \det [\mathbf{P}^{\sigma \dagger} \mathbf{B}_{\vec{s}}^{\sigma}(\beta, 0) \mathbf{P}^{\sigma}], \end{aligned} \quad (3.28)$$

where in the last step the following identity was used [90]

$$\langle 0 | c_{i_1 \sigma} \cdots c_{i_{N_f} \sigma} c_{j_{N_f} \sigma}^{\dagger} \cdots c_{j_1 \sigma}^{\dagger} | 0 \rangle = \epsilon^{k_1 \cdots k_{N_f}} \delta_{i_1 j_{k_1}} \cdots \delta_{i_{N_f} j_{k_{N_f}}}, \quad (3.29)$$

with  $\epsilon^{k_1 \cdots k_{N_f}}$  the Levi-Civita symbol in  $N_f$  dimensions, and the indices  $k$  have values between one and  $N_f$ .

The partition function can be written in terms of the weights (3.28) as

$$Z_{TS} = \sum_{\vec{s}} p[\vec{s}] \quad (3.30)$$

### 3.2.3 Equal-time Green's function and observables

The equal-time Green's function is the central object in our numerical simulations. It is defined for each HS field configuration as

$$G_{ij,\vec{s}}^{\sigma}(\tau) = \langle c_{i\sigma}(\tau) c_{j\sigma}^{\dagger}(\tau) \rangle_{\vec{s}} = \delta_{ij} - \langle c_{j\sigma}^{\dagger}(\tau) c_{i\sigma}(\tau) \rangle_{\vec{s}} \quad (3.31)$$

with

$$\langle c_{j\sigma}^{\dagger}(\tau) c_{i\sigma}(\tau) \rangle_{\vec{s}} = \langle \Psi_T^{\sigma} | B_{\vec{s}}^{\sigma}(\beta, \tau) c_{j\sigma}^{\dagger} c_{i\sigma} B_{\vec{s}}^{\sigma}(\tau, 0) | \Psi_T^{\sigma} \rangle / p[\vec{s}]. \quad (3.32)$$

The expectation value  $\langle c_{j\sigma}^{\dagger}(\tau) c_{i\sigma}(\tau) \rangle_{\vec{s}}$  can be calculated by coupling the action, determined by the Hamiltonian (3.12), to a source term of the form  $h c_{j\sigma}^{\dagger} c_{i\sigma}$  at the imaginary time  $\tau$ . In this case the weight of a given configuration  $\vec{s}$  ( $p_h[\vec{s}]$ ) becomes dependent on the parameter  $h$

$$p_h[\vec{s}] = \det [\mathbf{P}^{\sigma \dagger} \mathbf{B}_{\vec{s}}^{\sigma}(\beta, \tau) e^{h\mathbf{O}} \mathbf{B}_{\vec{s}}^{\sigma}(\tau, 0) \mathbf{P}^{\sigma}] \det [\mathbf{P}^{-\sigma \dagger} \mathbf{B}_{\vec{s}}^{-\sigma}(\beta, 0) \mathbf{P}^{-\sigma}], \quad (3.33)$$

where the matrix  $\mathbf{O}$  has only the element  $O_{ji} = 1$  different from zero.

Introducing the definitions

$$\mathbf{L}_s^\sigma(\tau) = \mathbf{P}^{\sigma\dagger} \mathbf{B}_s^\sigma(\beta, \tau), \quad \mathbf{R}_s^\sigma(\tau) = \mathbf{B}_s^\sigma(\tau, 0) \mathbf{P}^\sigma, \quad (3.34)$$

the Eq. (3.32) can be evaluated as follows

$$\begin{aligned} \langle c_{j\sigma}^\dagger(\tau) c_{i\sigma}(\tau) \rangle_{\vec{s}} &= \frac{\partial}{\partial h} \ln p_h[\vec{s}]|_{h=0} = \text{Tr} \frac{\partial}{\partial h} \ln [\mathbf{L}_s^\sigma(\tau) e^{h\mathbf{O}} \mathbf{R}_s^\sigma(\tau)]|_{h=0} \\ &= \text{Tr} [\mathbf{L}_s^\sigma(\tau) \mathbf{R}_s^\sigma(\tau)]^{-1} \mathbf{L}_s^\sigma(\tau) \mathbf{O} \mathbf{R}_s^\sigma(\tau) \\ &= \{ \mathbf{R}_s^\sigma(\tau) [\mathbf{L}_s^\sigma(\tau) \mathbf{R}_s^\sigma(\tau)]^{-1} \mathbf{L}_s^\sigma(\tau) \}_{ij}. \end{aligned} \quad (3.35)$$

The previous result implies that the equal time Green's function can be obtained completely in just one step, and it can be written in the form

$$\mathbf{G}^\sigma(\tau) = \mathbf{1} - \mathbf{R}_s^\sigma(\tau) [\mathbf{L}_s^\sigma(\tau) \mathbf{R}_s^\sigma(\tau)]^{-1} \mathbf{L}_s^\sigma(\tau) \quad (3.36)$$

The importance of this quantity for the numerical simulations is mainly due to two reasons. The first one is that it allows to calculate all the fermionic observables<sup>7</sup> with the application of Wick's theorem [113], which is justified in this case since fermions do not interact with each other. (They only interact with the HS field.) Given a measurement operator  $A$  its expectation value can be obtained for a fixed HS field configuration using Wick's theorem ( $\langle A \rangle_{\vec{s}}$ ), and the observed value is given by the expression

$$\langle A \rangle = \frac{1}{2^{NL}} \sum_{\vec{s}} \langle A \rangle_{\vec{s}}, \quad (3.37)$$

where the sum was considered to be over all the possible  $\vec{s}$  configurations.

The second important role of the Green's function is in the quantum Monte Carlo sampling. As it was mentioned before, it is impossible to consider all the HS field configurations in order to evaluate the partition function or any observable. Then the MC method has to be employed, and as it will be shown in the next subsection the Green's function plays a central role in its application to the determinantal algorithm.

### 3.2.4 Quantum Monte Carlo update

In the previous subsections we have shown how to calculate the weight of a fixed HS field configuration in our quantum problem [Eq. (3.28)]. Since we will apply the MC ideas in

---

<sup>7</sup>We refer here to equal time observables, i.e. static properties, the equilibrium dynamics can be also studied with the use of the time-displaced Green's function [89–91].



order to avoid the sum over the huge amount of possible HS field configurations in the measurement of physical observables, we are interested in the evaluation of the ratio

$$R = \frac{p[\vec{s}']}{p[\vec{s}]}, \quad (3.38)$$

which is required for both, the Metropolis and heat bath algorithms.

The determinants in  $p[\vec{s}']$  and  $p[\vec{s}]$  [Eq. (3.28)] are very expensive to evaluate for each given field  $\vec{s}$ . However, the ratio  $R$  can be easily calculated if only one component of  $\vec{s}$  is changed to obtain  $\vec{s}'$ . In the latter case, the new matrix

$$\begin{aligned} \mathbf{A}_{\vec{s}'}^\sigma(\tau) &= \begin{pmatrix} e^{\alpha b_\sigma s_1(\tau) - \Delta\tau\mu_1} & & & & & 0 \\ & \ddots & & & & \\ & & \ddots & & & \\ & & & \ddots & & \\ & & & & e^{\alpha b_\sigma s'_i(\tau) - \Delta\tau\mu_i} & \\ & & & & & \ddots \\ & & & & & & \ddots \\ & & & & & & & \ddots \\ & & & & & & & & e^{\alpha b_\sigma s_n(\tau) - \Delta\tau\mu_n} \\ 0 & & & & & & & & & 0 \end{pmatrix} \\ &= [\mathbf{1} + \mathbf{\Delta}^\sigma(i, \tau)] \mathbf{A}_{\vec{s}}^\sigma(\tau), \end{aligned} \quad (3.39)$$

where the only nonzero matrix element of  $\mathbf{\Delta}^\sigma(i, \tau)$  is  $\Delta_{ii}^\sigma(i, \tau) = e^{\alpha b_\sigma [s'_i(\tau) - s_i(\tau)]} - 1$ . The corresponding change in the single-particle propagator is given by

$$\mathbf{B}_{\vec{s}'}^\sigma(\beta, 0) = \mathbf{B}_{\vec{s}}^\sigma(\beta, \tau) [\mathbf{1} + \mathbf{\Delta}^\sigma(i, \tau)] \mathbf{B}_{\vec{s}}^\sigma(\tau, 0). \quad (3.40)$$

The ratio for each spin  $R^\sigma$ , ( $R \equiv R^\uparrow R^\downarrow$ ) is then determined as

$$\begin{aligned} R^\sigma &= \frac{\det(\mathbf{L}_{\vec{s}'}^\sigma(\tau) [\mathbf{1} + \mathbf{\Delta}^\sigma(i, \tau)] \mathbf{R}_{\vec{s}'}^\sigma(\tau))}{\det[\mathbf{L}_{\vec{s}}^\sigma(\tau) \mathbf{R}_{\vec{s}}^\sigma(\tau)]} \\ &= \frac{\det(\mathbf{L}\mathbf{R} + \mathbf{L}\mathbf{\Delta}\mathbf{R})}{\det(\mathbf{L}\mathbf{R})} = \det(\mathbf{1} + [\mathbf{L}\mathbf{R}]^{-1} \mathbf{L}\mathbf{\Delta}\mathbf{R}) = \det(\mathbf{1} + \mathbf{\Delta}\mathbf{R} [\mathbf{L}\mathbf{R}]^{-1} \mathbf{L}) \\ &= \det(\mathbf{1} + \mathbf{\Delta}^\sigma(i, \tau) [\mathbf{1} - \mathbf{G}_{\vec{s}}^\sigma(\tau)]), \end{aligned} \quad (3.41)$$

where we have dropped the indices of the matrices in the intermediate expressions to simplify the equations. To obtain the final result in Eq. (3.41) we used the following property valid for determinants of different-sized matrices (see Appendix D)

$$\det(\mathbf{1}_N + \mathbf{A}\mathbf{B}) = \det(\mathbf{1}_M + \mathbf{B}\mathbf{A}), \quad (3.42)$$

where  $\mathbf{A}$  is an  $N \times M$  rectangular matrix and  $\mathbf{B}$  is an  $M \times N$  rectangular matrix. We also introduced indices to the unit matrices to remark that they have different sizes.

The determinant in Eq. (3.41) can be easily evaluated since  $\Delta^\sigma(i, \tau)$  has only one non-zero element. The ratio (3.38) then reduces to the scalar expression

$$R = \prod_{\sigma} (1 + \Delta_{ii}^{\sigma}(i, \tau) [1 - G_{ii, \vec{s}}^{\sigma}(\tau)]). \quad (3.43)$$

Once  $R$  has been determined it is possible to decide stochastically if the proposed change in the boson field configuration ( $\vec{s} \rightarrow \vec{s}'$ ) is accepted or rejected. In case of acceptance the Green's function has to be updated, this is done upgrading

$$\begin{aligned} [\mathbf{L}_{\vec{s}'}^{\sigma}(\tau) \mathbf{R}_{\vec{s}'}^{\sigma}(\tau)]^{-1} &= (\mathbf{L}_{\vec{s}}^{\sigma}(\tau) [\mathbf{1} + \Delta^{\sigma}(i, \tau)] \mathbf{R}_{\vec{s}}^{\sigma}(\tau))^{-1} \\ &= (\mathbf{LR} + \mathbf{L}\Delta\mathbf{R})^{-1} = (\mathbf{1} + [\mathbf{LR}]^{-1} \mathbf{L}\Delta\mathbf{R})^{-1} (\mathbf{LR})^{-1}, \end{aligned} \quad (3.44)$$

where for the moment we drop the indices of the matrices. The calculation of the inverse  $(\mathbf{1} + [\mathbf{LR}]^{-1} \mathbf{L}\Delta\mathbf{R})^{-1}$  is done using the sparse nature of  $\Delta$ <sup>8</sup>, assuming that

$$(\mathbf{1} + [\mathbf{LR}]^{-1} \mathbf{L}\Delta\mathbf{R})^{-1} = (\mathbf{1} + x [\mathbf{LR}]^{-1} \mathbf{L}\Delta\mathbf{R}) \quad (3.45)$$

with  $x$  being a scalar to be determined. Since only one component of  $\Delta$  is non-zero one has that

$$\Delta\mathbf{R} [\mathbf{LR}]^{-1} \mathbf{L}\Delta = \Delta (\mathbf{1} - \mathbf{G}) \Delta = \Delta_{ii} (1 - G_{ii}) \Delta, \quad (3.46)$$

and given the Ansatz in Eq. (3.45)  $x$  is obtained as

$$\begin{aligned} \mathbf{1} &= (\mathbf{1} + [\mathbf{LR}]^{-1} \mathbf{L}\Delta\mathbf{R}) (\mathbf{1} + x [\mathbf{LR}]^{-1} \mathbf{L}\Delta\mathbf{R}) \\ &= \mathbf{1} + [1 + x + x\Delta_{ii} (1 - G_{ii})] (\mathbf{LR})^{-1} \mathbf{L}\Delta\mathbf{R}, \end{aligned} \quad (3.47)$$

i.e.

$$x = -\frac{1}{1 + \Delta_{ii} (1 - G_{ii})} = -\frac{1}{R^{\sigma}}, \quad (3.48)$$

and

$$\begin{aligned} [\mathbf{L}_{\vec{s}'}^{\sigma}(\tau) \mathbf{R}_{\vec{s}'}^{\sigma}(\tau)]^{-1} &= [\mathbf{L}_{\vec{s}}^{\sigma}(\tau) \mathbf{R}_{\vec{s}}^{\sigma}(\tau)]^{-1} \\ &\quad - \frac{1}{R} [\mathbf{L}_{\vec{s}}^{\sigma}(\tau) \mathbf{R}_{\vec{s}}^{\sigma}(\tau)]^{-1} \mathbf{L}_{\vec{s}}^{\sigma}(\tau) \Delta^{\sigma}(i, \tau) \mathbf{R}_{\vec{s}}^{\sigma}(\tau) [\mathbf{L}_{\vec{s}}^{\sigma}(\tau) \mathbf{R}_{\vec{s}}^{\sigma}(\tau)]^{-1}. \end{aligned} \quad (3.49)$$

---

<sup>8</sup>General solutions can be obtained using the Sherman-Morrison formulas [114, 115].

The new Green's function can be finally obtained as

$$\begin{aligned}
\mathbf{G}_{s'}^\sigma(\tau) &= \mathbf{R}_{s'}^\sigma(\tau) [\mathbf{L}_{s'}^\sigma(\tau) \mathbf{R}_{s'}^\sigma(\tau)]^{-1} \mathbf{L}_{s'}^\sigma(\tau) \\
&= [1 + \Delta^\sigma(i, \tau)] \mathbf{R}_s^\sigma(\tau) [\mathbf{L}_{s'}^\sigma(\tau) \mathbf{R}_{s'}^\sigma(\tau)]^{-1} \mathbf{L}_s^\sigma(\tau) \\
&= \mathbf{G}_s^\sigma(\tau) - \frac{1}{R} \mathbf{G}_s^\sigma(\tau) \Delta^\sigma(i, \tau) [1 - \mathbf{G}_s^\sigma(\tau)],
\end{aligned} \tag{3.50}$$

where the results of Eq. (3.49) for  $[\mathbf{L}_{s'}^\sigma(\tau) \mathbf{R}_{s'}^\sigma(\tau)]^{-1}$  were substituted<sup>9</sup>.

### 3.2.5 “Wrapping” Green's functions and the numerical stabilization

In the previous subsection we have shown how to modify the HS field configurations at a given time  $\tau$  following the MC idea, and how the equal time Green's function, the only quantity needed for such a process, can be updated efficiently. In order to consider other imaginary times, we notice that for a given HS field configuration  $\vec{s}$  the inverse

$$[\mathbf{L}_s^\sigma(\tau) \mathbf{R}_s^\sigma(\tau)]^{-1} = [\mathbf{P}^{\sigma\dagger} \mathbf{B}_s^\sigma(\beta, \tau) \mathbf{B}_s^\sigma(\tau, 0) \mathbf{P}^\sigma]^{-1} = [\mathbf{P}^{\sigma\dagger} \mathbf{B}_s^\sigma(\beta, 0) \mathbf{P}^\sigma]^{-1} \tag{3.51}$$

is independent of the imaginary time  $\tau$  at which the updates are performed. Then in order to calculate the Green's function at imaginary time ( $\tau' = \tau + \Delta\tau$ ) one has

$$\begin{aligned}
\mathbf{G}_s^\sigma(\tau') &= \mathbf{1} - \mathbf{R}_s^\sigma(\tau') [\mathbf{L}_s^\sigma(\tau') \mathbf{R}_s^\sigma(\tau')]^{-1} \mathbf{L}_s^\sigma(\tau') \\
&= \mathbf{1} - \mathbf{B}_s^\sigma(\tau', \tau) \mathbf{R}_s^\sigma(\tau) [\mathbf{L}_s^\sigma(\tau) \mathbf{R}_s^\sigma(\tau)]^{-1} \mathbf{L}_s^\sigma(\tau) [\mathbf{B}_s^\sigma(\tau', \tau)]^{-1} \\
&= \mathbf{B}_s^\sigma(\tau', \tau) \mathbf{G}_s^\sigma(\tau) [\mathbf{B}_s^\sigma(\tau', \tau)]^{-1}.
\end{aligned} \tag{3.52}$$

In the zero temperature calculations, the most efficient way to proceed is to update only the inverse  $[\mathbf{L}_s^\sigma(\tau) \mathbf{R}_s^\sigma(\tau)]^{-1}$ , which is independent of  $\tau$ , and is a matrix  $N_f \times N_f$  in contrast to the Green's function that is a matrix  $N \times N$ . Then during the “wrapping” process, only the diagonal elements of the green's function (the ones needed for the updates) are calculated at every time step. Finally, at the moment of the measurement the full Green's function is calculated from the scratch.

Up to this point we have developed everything we would need to perform quantum Monte Carlo simulations in an infinite precision computer. Unfortunately, real computers have a finite precision, and numerical instabilities could appear. In the case of the

---

<sup>9</sup>The equality (3.46) has to be used once again in order to obtain the final result shown.

projector method we have described here, the source of such instabilities are the big amount of multiplications one has to do during the time evolution with the exponentials of positive and negative numbers that are present in the single particle propagator  $\mathbf{B}_s^\sigma(\tau', \tau)$ . In general, these multiplications wash out small scales and lead to ill defined inversions of the matrices ( $\mathbf{L}_s^\sigma(\tau)\mathbf{R}_s^\sigma(\tau)$ ). In order to avoid this problem for the zero temperature algorithm, matrix decomposition techniques were introduced [86–89]. We follow here the approach described in Ref. [89], which is based in a modified Gram-Schmidt (MGS) decomposition of possible ill-conditioned matrices as an  $\mathbf{UDV}$  product. The idea is to orthonormalize the ill-conditioned matrices storing the orthonormal vectors in  $\mathbf{U}$ , and their norm in the diagonal matrix  $\mathbf{D}$ . The latter will keep all the scales of the problem. Finally, the matrix  $\mathbf{V}$  contains mainly the overlap between the vectors of the original matrix, and is an upper triangular matrix. In our case the matrices to be factorized are

$$\mathbf{R}_s^\sigma(\tau) = \mathbf{U}_{s,R}^\sigma(\tau)\mathbf{D}_{s,R}^\sigma(\tau)\mathbf{V}_{s,R}^\sigma(\tau), \quad \mathbf{L}_s^\sigma(\tau) = \mathbf{V}_{s,L}^\sigma(\tau)\mathbf{D}_{s,L}^\sigma(\tau)\mathbf{U}_{s,L}^\sigma(\tau), \quad (3.53)$$

where it should be noticed that the order of  $\mathbf{U}$ ,  $\mathbf{D}$ , and  $\mathbf{V}$  has been reversed for  $\mathbf{L}_s^\sigma(\tau) = \mathbf{P}^{\sigma\dagger}\mathbf{B}_s^\sigma(\beta, \tau)$ , since the product builds up on the right side [89]. Given that the dimension of the rectangular matrices  $\mathbf{R}_s^\sigma(\tau)$  [ $\mathbf{L}_s^\sigma(\tau)$ ] are  $N \times N_f$  ( $N_f \times N$ ), the  $\mathbf{U}_{s,R}^\sigma(\tau)$  [ $\mathbf{U}_{s,L}^\sigma(\tau)$ ] are also  $N \times N_f$  ( $N_f \times N$ ) rectangular matrices, while  $\mathbf{D}_{s,R}^\sigma(\tau)$  [ $\mathbf{D}_{s,L}^\sigma(\tau)$ ], and  $\mathbf{V}_{s,R}^\sigma(\tau)$  [ $\mathbf{V}_{s,L}^\sigma(\tau)$ ] are  $N_f \times N_f$  ( $N_f \times N_f$ ) square matrices.

The Green's function can be then calculated as

$$\begin{aligned} \mathbf{G}^\sigma(\tau) &= \mathbf{1} - \mathbf{R}_s^\sigma(\tau) [\mathbf{L}_s^\sigma(\tau)\mathbf{R}_s^\sigma(\tau)]^{-1} \mathbf{L}_s^\sigma(\tau) \\ &= \mathbf{1} - (\mathbf{U}_R\mathbf{D}_R\mathbf{V}_R) [(\mathbf{V}_L\mathbf{D}_L\mathbf{U}_L) (\mathbf{U}_R\mathbf{D}_R\mathbf{V}_R)]^{-1} \mathbf{V}_L\mathbf{D}_L\mathbf{U}_L \\ &= \mathbf{1} - \mathbf{U}_{s,R}^\sigma(\tau) [\mathbf{U}_{s,L}^\sigma(\tau)\mathbf{U}_{s,R}^\sigma(\tau)]^{-1} \mathbf{U}_{s,L}^\sigma(\tau), \end{aligned} \quad (3.54)$$

where some of the matrix indices were dropped in the intermediate step to simplify the expression. Eq. (3.54) shows that the Green's function is only dependent on the well defined rectangular matrices  $\mathbf{U}_{s,R}^\sigma(\tau)$  and  $\mathbf{U}_{s,L}^\sigma(\tau)$ . Then the stabilization can be performed orthonormalizing the columns of  $\mathbf{U}_{s,R}^\sigma(\tau)$  and the rows of  $\mathbf{U}_{s,L}^\sigma(\tau)$  without the need of keeping any further information.

### 3.3 The world-line algorithm

The world-line (WL) algorithm was first introduced by Hirsch *et al.* [92]. It is, like the determinantal methods, based on the path integral formulation of the partition function in imaginary time. Very attractive features of the WL algorithm are its simplicity and the large freedom in the choice of systems that can be simulated, in contrast to the determinantal methods which are complex and require interaction terms in the Hamiltonian that can be transformed into squares of bilinear forms. In the present section we review the basic features of the WL algorithm<sup>10</sup>.

#### 3.3.1 Formalism

We consider the partition function at finite temperatures, which can be written as

$$Z = \text{Tr} e^{-\beta H}. \quad (3.55)$$

Our aim is to compute the observables  $\langle \widehat{O} \rangle$  for a given system. They can be obtained as

$$\langle \widehat{O} \rangle = \frac{\text{Tr} \left( e^{-\beta H} \widehat{O} \right)}{Z}. \quad (3.56)$$

The idea of the WL algorithm is based on the possibility of splitting the Hamiltonian  $H$  into a set of independent problems. For definiteness we consider the case of spinless fermions with nearest neighbor interactions in a one dimensional periodic lattice

$$H = -t \sum_i \left( c_i^\dagger c_{i+1} + \text{H.c.} \right) + U_n \sum_i \left( n_i - \frac{1}{2} \right) \left( n_{i+1} - \frac{1}{2} \right), \quad (3.57)$$

where  $c_i^\dagger$ ,  $c_i$  are creation and annihilation operators, respectively, for spinless fermions at site  $i$ , and  $n_i = c_i^\dagger c_i$  is the particle number operator. Fermions are considered to hop only between nearest neighbors with a hopping amplitude  $t$ , and the nearest neighbor interaction parameter is denoted by  $U_n$ . It is easy to realize that Hamiltonian (3.57) can be splitted in two terms  $H_{\text{odd}}$  and  $H_{\text{even}}$ , which consist of a sum of mutually commuting pieces

$$H = H_{\text{odd}} + H_{\text{even}}$$

$$H_{\text{odd(even)}} = -t \sum_{i \text{ odd(even)}} \left( c_i^\dagger c_{i+1} + \text{H.c.} \right) + U_n \sum_{i \text{ odd(even)}} \left( n_i - \frac{1}{2} \right) \left( n_{i+1} - \frac{1}{2} \right). \quad (3.58)$$

---

<sup>10</sup>See Refs. [92, 116] for more extensive analysis of the algorithm.

$H_{\text{odd}}$  and  $H_{\text{even}}$  are easily solvable two-sites problems. Since they do not commute, in order to decouple the exponential of their sum in Eq. (3.55), the Trotter-Suzuki decomposition [110, 111] is introduced

$$e^{-\Delta\tau(H_{\text{odd}}+H_{\text{even}})} = e^{-\Delta\tau H_{\text{odd}}}e^{-\Delta\tau H_{\text{even}}} + O(\Delta\tau)^2, \quad (3.59)$$

and  $Z$  is approximated by  $Z_{TS}$  (as in the previous section)

$$\begin{aligned} Z_{TS} &= \text{Tr} \prod_{m=1}^L e^{-\Delta\tau H_{\text{odd}}} e^{-\Delta\tau H_{\text{even}}} \\ &= \sum_{m_1 \cdots m_{2L}} \langle m_1 | e^{-\Delta\tau H_{\text{odd}}} | m_{2L} \rangle \langle m_{2L} | e^{-\Delta\tau H_{\text{even}}} | m_{2L-1} \rangle \\ &\quad \cdots \langle m_3 | e^{-\Delta\tau H_{\text{odd}}} | m_2 \rangle \langle m_2 | e^{-\Delta\tau H_{\text{even}}} | m_1 \rangle, \end{aligned} \quad (3.60)$$

where  $L\Delta\tau = \beta$ , and  $\{|m_\ell\rangle\}$  are complete sets of states introduced at each time slice. Since  $H_{\text{odd}}$  and  $H_{\text{even}}$  consist of a sum of mutually commuting peaces, the matrix elements of Eq. (3.60) are reduced to products

$$\begin{aligned} \langle m_\ell \text{ odd(even)} | e^{-\Delta\tau H_{\text{odd(even)}}} | m_{(\ell-1) \text{ even(odd)}} \rangle \\ = \prod_{i \text{ odd(even)}} \langle m_\ell \text{ odd(even)} | e^{-\Delta\tau H_{i,i+1}} | m_{(\ell-1) \text{ even(odd)}} \rangle. \end{aligned} \quad (3.61)$$

The error introduced by the Trotter-Suzuki decomposition can be proven to be of the order  $(\Delta\tau)^2$  not only for the partition function but also for hermitian observables [91, 117].

A graphical representation of the last two equations leads to a checkerboard decomposition of space-time [Fig. 3.1(a)], where the shaded plaquettes are the areas in space-time where fermions can hop and interact. In Fig. 3.1(a) the occupied sites at each  $\tau$  have been connected by lines, which are known as world-lines. Notice that the particle number is conserved at each  $\tau$ , and that periodic boundary conditions are applied to the imaginary time axis. The weight of each plaquette configuration can be easily calculated for the Hamiltonian (3.58)<sup>11</sup>.

$$\begin{aligned} \langle 0, 0 | e^{-\Delta\tau H_{i,i+1}} | 0, 0 \rangle &= \langle 1, 1 | e^{-\Delta\tau H_{i,i+1}} | 1, 1 \rangle = e^{-\Delta\tau U/4} \\ \langle 1, 0 | e^{-\Delta\tau H_{i,i+1}} | 1, 0 \rangle &= \langle 0, 1 | e^{-\Delta\tau H_{i,i+1}} | 0, 1 \rangle = e^{+\Delta\tau U/4} \cosh(\Delta\tau t) \\ \langle 1, 0 | e^{-\Delta\tau H_{i,i+1}} | 0, 1 \rangle &= \langle 0, 1 | e^{-\Delta\tau H_{i,i+1}} | 1, 0 \rangle = e^{+\Delta\tau U/4} \sinh(\Delta\tau t) \end{aligned} \quad (3.62)$$

<sup>11</sup>We should notice here that we apply later the WL algorithm to the Bosonic Hubbard model where there is no restriction to the site occupation. In this case the two-site problem involves an infinite dimensional Hilbert space. The calculation of the matrix elements can be done either diagonalizing  $H$  in a truncate Hilbert space [118], or exactly [119]

and are shown Fig. 3.1(b). The total weight of a world line configuration is then calculated as the product of all the plaquettes weights.

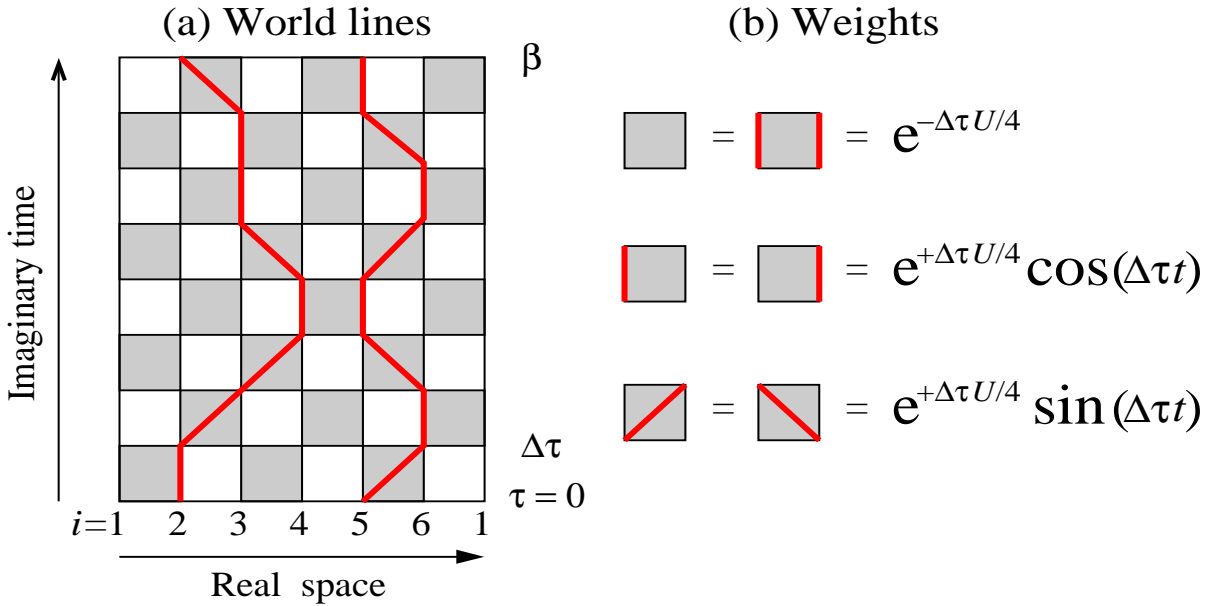


Figure 3.1: Checkerboard decomposition of space-time for a one-dimensional problem with nearest-neighbor interactions. (a) A world-line configuration. (b) Weights of the plaquettes.

### 3.3.2 Quantum Monte Carlo update

As in the previous section, the Monte Carlo technique will be used to avoid the sum over all the possible world line configurations. In order to be able to generate any allowed WL (starting from an allowed one) one realizes that it is not possible to cut it, since this leads to non-conservation of the fermion number. Then, the minimum change that can be made to a given WL configuration is to move two fermions from one side of an unshaded plaquette to the opposite side. The possible moves for the spinless fermion problem considered here are shown in Fig. 3.2.

The ratio between the weights of the WL configuration after and before the move is calculated in what follows. We denote each lattice point of the checkerboard decomposition by  $(i, j)$  with  $i$  and  $j$  representing the spatial and imaginary time coordinates respectively. The occupation of each lattice point is given by  $n(i, j)$ , which can be 0 or 1 for spinless fermions. With this notation the move across an unshaded plaquette will be

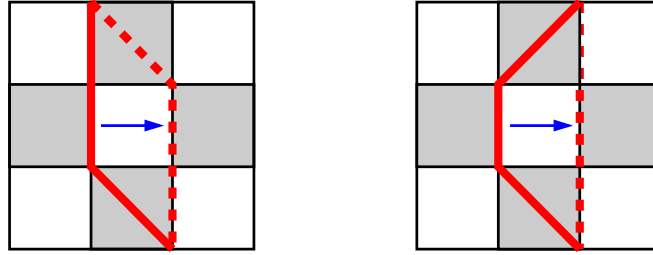


Figure 3.2: Possible changes to a WL for the model of spinless fermions with nearest-neighbor interactions. Thick solid and dashes lines show the world lines before and after the moves respectively.

possible only if  $s = \pm 2$ , with

$$s = n(i_u, j_u) + n(i_u, j_u + 1) + n(i_u + 1, j_u) + n(i_u + 1, j_u + 1), \quad (3.63)$$

where we have denoted the coordinates of the lower left-hand corner of the unshaded plaquette by  $(i_u, j_u)$ . The ratio  $R$  between the weights of the new and old configurations can be obtained as

$$R = [\tanh(\Delta\tau t)]^{su} [\cosh(\Delta\tau t)e^{\Delta\tau U/2}]^{sv} \quad (3.64)$$

where

$$u = 1 - n(i_u + 1, j_u - 1) - n(i_u + 1, j_u + 2), \quad v = n(i_u - 1, j_u) - n(i_u + 2, j_u). \quad (3.65)$$

The occupations at  $(i_u + 1, j_u - 1)$  and  $(i_u + 1, j_u + 2)$  determine whether we are moving vertical or diagonal WL in the unshaded boxes below and above the one we are analyzing, and the occupations at  $(i_u - 1, j_u)$  and  $(i_u + 2, j_u)$  determine whether there are additional WL on the shaded boxes to the left and right, respectively, of the unshaded one we are considering. Once  $R$  has been obtained, a proposed new configuration can be accepted or rejected using the Metropolis or heat-bath algorithms.

### 3.3.3 The observables

In order to perform measurements within the WL algorithm, one has to distinguish three different classes of observables. The first class contains operators that are diagonal in the occupation number, such as the density-density operator  $\chi_{ij} = n_i n_j$ . Measurements for these kind of operators are easily realized as

$$\langle \hat{O} \rangle = \frac{1}{M2LN} \sum_{k=1}^M \sum_{j=1}^{2L} \sum_{i=1}^N O[n_k(i, j)], \quad (3.66)$$



where  $N$  is the number of lattice sites,  $2L$  the number of time slices, and  $M$  the total number of configurations sampled.

The second class of observables corresponds to that operators that conserve the number of particles on two sites, like the kinetic energy operator  $H_t = -t \sum_i (c_i^\dagger c_{i+1} + \text{H.c.})$ , and the current operator  $j = i \sum_i (c_i^\dagger c_{i+1} - \text{H.c.})$ . In such cases, the operator ( $\widehat{O}$ ) allows an identical decomposition as the Hamiltonian [Eq. (3.58)]

$$\widehat{O} = \overbrace{\sum_{i \text{ odd}} \widehat{O}_{i,i+1}}^{\widehat{O}_{\text{odd}}} + \overbrace{\sum_{i \text{ even}} \widehat{O}_{i,i+1}}^{\widehat{O}_{\text{even}}}, \quad (3.67)$$

and its expectation value can be calculated as

$$\begin{aligned} \langle \widehat{O} \rangle &= \frac{1}{Z_{TZ}} \text{Tr} \prod_{m=1}^L \widehat{O} e^{-\Delta\tau H_{\text{odd}}} e^{-\Delta\tau H_{\text{even}}} \\ &= \sum_{m_1 \dots m_{2L}} P(m_1, \dots, m_{2L}) \left[ \frac{\langle m_1 | \widehat{O}_{\text{odd}} e^{-\Delta\tau H_{\text{odd}}} | m_{2L} \rangle}{\langle m_1 | e^{-\Delta\tau H_{\text{odd}}} | m_{2L} \rangle} \right. \\ &\quad \left. + \frac{\langle m_2 | e^{-\Delta\tau H_{\text{even}}} \widehat{O}_{\text{even}} | m_1 \rangle}{\langle m_2 | e^{-\Delta\tau H_{\text{even}}} | m_1 \rangle} \right], \quad (3.68) \end{aligned}$$

where the weight of a particular WL configuration is given by

$$P(m_1, \dots, m_{2L}) = \langle m_1 | e^{-\Delta\tau H_{\text{odd}}} | m_{2L} \rangle \dots \langle m_2 | e^{-\Delta\tau H_{\text{even}}} | m_1 \rangle. \quad (3.69)$$

Then it is only left to compute the two-site matrix elements given in Eq. (3.68) for the particular observables of interest.

The third class of observables contains operators that do not conserve the fermion number locally. We analyze here as an example the single particle Green's function  $G_{ij} = \langle c_i c_j^\dagger \rangle$ . Its evaluation, following a procedure like the one used in Eq. (3.68), is not well defined

$$\begin{aligned} G_{ij} &= \frac{1}{Z_{TZ}} \text{Tr} \prod_{m=1}^L c_i c_j^\dagger e^{-\Delta\tau H_{\text{odd}}} e^{-\Delta\tau H_{\text{even}}} \\ &= \sum_{m_1 \dots m_{2L}} P(m_1, \dots, m_{2L}) \frac{\langle m_1 | c_i c_j^\dagger e^{-\Delta\tau H_{\text{odd}}} | m_{2L} \rangle}{\langle m_1 | e^{-\Delta\tau H_{\text{odd}}} | m_{2L} \rangle}, \quad (3.70) \end{aligned}$$

since for  $|i - j| > 1$  there are configurations where the denominator vanishes whereas the numerator does not. For example, a configuration where the state  $|m_1\rangle$  has a WL

terminating at site  $j$ , and state  $|m_{2L}\rangle$  has a WL starting a site  $i$ . This problem can be solved inserting additional states as follows

$$\begin{aligned}
 G_{ij} &= \frac{\sum_{m_1 \dots m_{2L} m'_1} \langle m_1 | c_i c_j^\dagger | m'_1 \rangle \langle m'_1 | e^{-\Delta\tau H_{\text{odd}}} | m_{2L} \rangle \dots \langle m_2 | e^{-\Delta\tau H_{\text{even}}} | m_1 \rangle}{\sum_{m_1 \dots m_{2L} m'_1} \langle m_1 | m'_1 \rangle \langle m'_1 | e^{-\Delta\tau H_{\text{odd}}} | m_{2L} \rangle \dots \langle m_2 | e^{-\Delta\tau H_{\text{even}}} | m_1 \rangle} \\
 &\equiv \frac{\sum_{m_1 \dots m_{2L} m'_1} \tilde{P}(m_1, \dots, m_{2L}, m'_1) \langle m_1 | c_i c_j^\dagger | m'_1 \rangle}{\sum_{m_1 \dots m_{2L} m'_1} \tilde{P}(m_1, \dots, m_{2L}, m'_1) \langle m_1 | m'_1 \rangle}, \tag{3.71}
 \end{aligned}$$

where the weights of the WL configurations are given in this case by

$$\tilde{P}(m_1, \dots, m_{2L}, m'_1) = \langle m'_1 | e^{-\Delta\tau H_{\text{odd}}} | m_{2L} \rangle \dots \langle m_2 | e^{-\Delta\tau H_{\text{even}}} | m_1 \rangle. \tag{3.72}$$

Since there is no time-evolution operator connecting the states  $|m_1\rangle$  and  $|m'_1\rangle$ , the WL are allowed to be disconnected across these states. The fact that the observable is now a ratio of two averages leads to a deterioration of the statistics.

We conclude this introduction to the WL algorithm pointing out that due to the the local update strategy followed, the WL algorithm could suffer from long autocorrelation times [95] in a way similar to classical simulations with local updates. This problem can be in general reduced by global moves in cluster algorithms, as it was proposed by Swendsen and Wang [93] for the classical Ising model, and extended latter for quantum systems [94–96]. In addition, other limitations of the WL method are removed by the loop algorithm since in the latter simulations are made in the grand canonical ensemble, where neither the number of particles nor the total spin of the system are conserved. This is crucial in order to describe the transition to a ferromagnetic state.

## Chapter 4

# Soft-core bosons confined on 1-D optical lattices

In this chapter we discuss quantum Monte Carlo simulations used to study the ground state properties of soft-core bosons confined on optical lattices<sup>1</sup>. We find that the inhomogeneous character of such systems, resulting from the trapping potential, is crucial for the understanding of the Mott regions obtained at incommensurate fillings [11], in contrast to the commensurate filling required in the periodic case. In a trap, local incompressible Mott domains always coexist with compressible superfluid phases so that the global compressibility never vanishes.

A first step towards the definition of a local order parameter to characterize the incompressible Mott phases is taken. The variance of the local density is used as a measure of the compressibility of local phases in the system. It exhibits a reduction (a local minimum) in the Mott domains. In addition, a phase diagram characterized by the topology of the density and variance profiles is obtained. It shows the phases that are present in the experiments, and reflects the effects of the confining potential since insulating and superfluid regions coexist for a wide range of parameters.

---

<sup>1</sup>The results presented in this chapter were obtained in collaboration with G. G. Batrouni, V. Rousseau, R. T. Scalettar, P. J. H. Denteneer, and M. Troyer, and published in Ref. [23]. The simulations were performed by our collaborators.

## 4.1 The bosonic Hubbard model

A considerable amount of work has been done in the last decade to determine the ground state phase diagram of correlated bosons on a periodic lattice described by the boson-Hubbard Hamiltonian [17–21]. The on-site repulsion can produce a Mott insulating phase at commensurate fillings, with a quantum phase transition to a superfluid, as the density is shifted or the interaction strength weakened. Longer range interactions can cause charge density wave, stripe, or even supersolid order [120, 121]. Extensions to disordered systems have allowed the detailed study of the interplay of randomness and interactions in quantum systems [122].

The Hamiltonian of the periodic boson Hubbard model, with nearest neighbors hopping and on-site repulsion, can be written as

$$H = -t \sum_i (b_i^\dagger b_{i+1} + \text{H.c.}) + U \sum_i n_i (n_i - 1) - \mu \sum_i n_i, \quad (4.1)$$

where the bosonic creation and annihilation operators are denoted by  $b_i^\dagger$  and  $b_i$  respectively,  $t$  is the hopping parameter,  $U$  is the on-site repulsion parameter ( $U > 0$ ),  $\mu$  is the chemical potential, and  $n_i = b_i^\dagger b_i$  is the particle number operator.

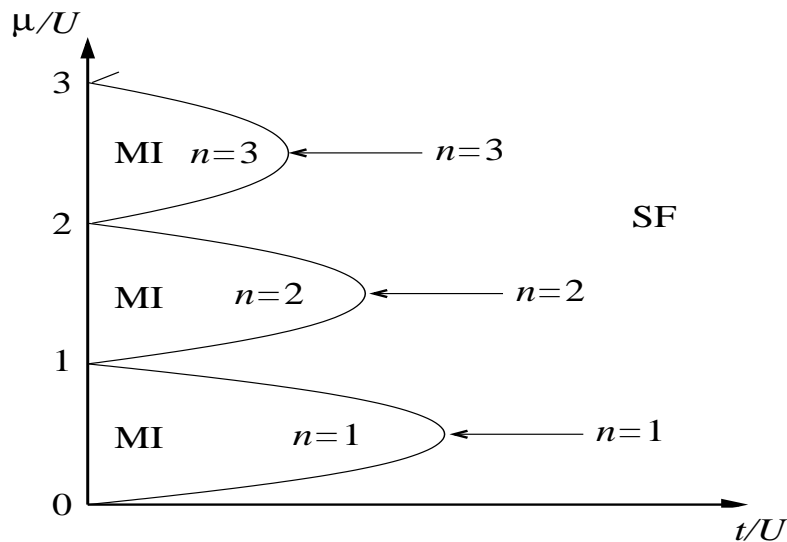


Figure 4.1: Schematic zero-temperature phase diagram for the boson-Hubbard model. The lobes correspond to Mott-insulating (MI) phases with commensurate fillings. The MI phases are incompressible since a change of the chemical potential  $\mu$  does not change the density. The arrows signal the transition from superfluid (SF) to Mott insulator at constant commensurate fillings.

The schematic zero temperature phase diagram for this model is shown in Fig. 4.1, and was discussed for the first time by Fisher *et.al.* [17]. For large values of  $t/U$  there is off-diagonal long range order and bosons are in a superfluid phase, i.e. delocalized in the lattice. The decrease of  $t/U$  makes the superfluid phase unstable under the formation of incompressible Mott insulators for commensurate fillings, and bosons become localized on the system sites [17, 18]. The critical behavior is of two types: mean field for transitions induced by tuning the density, and of the  $(d+1)$  dimensional XY universality class when the interaction strength is swept at fixed commensurate filling (arrows in Fig. 4.1). The critical values at which the transitions occur depend on the dimension of the systems, but the schematic view presented in Fig. 4.1 is valid for all dimensions.

## 4.2 The bosonic Hubbard model in a trap

We are interested in the ground state properties of ultracold bosons confined on optical lattices. In this case the Hamiltonian can be written as

$$H = -t \sum_i (b_i^\dagger b_{i+1} + h.c.) + U \sum_i n_i (n_i - 1) - \mu \sum_i n_i + V_2 \sum_i x_i^2 n_i, \quad (4.2)$$

where the last term has been added to the usual boson-Hubbard Hamiltonian (4.1) in order to characterize the trapping potential, which up to a good approximation can be considered harmonic [1]. The value of  $N$  is chosen such that all bosons are confined, i.e. they do not see the edge of the system and therefore do not leak out. The simulations were done with the world-line quantum Monte Carlo algorithm in the canonical ensemble [18, 92]. The chemical potential  $\mu = \partial E / \partial N$  is obtained by differentiating numerically the energy with respect to the particle number [118]. In the presence of the confining potential, the quantities measured were the local density of bosons  $n_i$  and a local compressibility  $\kappa_i^0 = \beta [\langle n_i^2 \rangle - \langle n_i \rangle^2]$ , which is proportional to the variance of the density.

### 4.2.1 Local phases in a harmonic trap

Figure 4.2 shows the evolution of the local boson density with increasing total occupancy of the lattice. At low fillings the density profile is smooth, with an inverted parabolic shape reflecting the confining potential. Above a critical filling of about 30 bosons (for

this choice of  $U$  and  $V_2$ ) a plateau with a local filling of one boson per site develops in the density profile which is analogous to the Mott structure of  $n$  vs  $\mu$  in the unconfined model. This plateau indicates the presence of an incompressible, insulating region where  $\kappa_i^0$ , as defined above, drops to a small but finite value as shown in Fig. 4.3) (it only vanishes for  $U \rightarrow \infty$ ). Here, this behavior of  $\kappa_i^0$  is taken as a signal for the Mott region. As

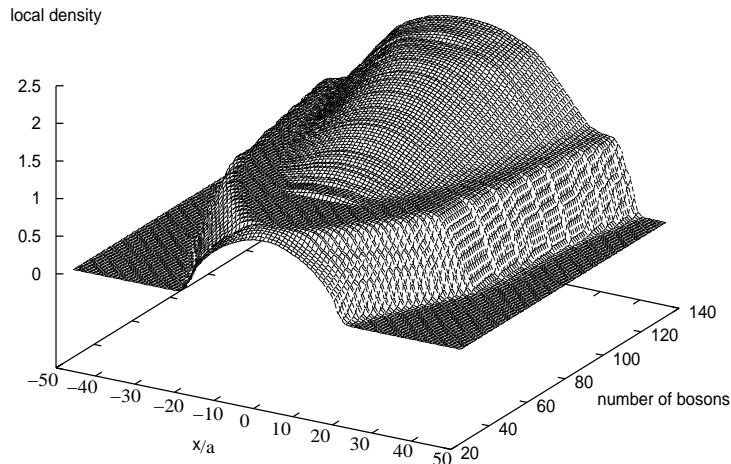


Figure 4.2: Evolution of the local density  $n_i$  as a function of the position  $x/a$ , increasing the total number of bosons. The trap curvature is  $V_2 a^2 = 0.008t$ ,  $N = 100$  and the on-site repulsion is  $U = 4t$ .

the density is increased further, the plateau widens spatially. But when the energy cost of extending the plateau to increasingly large values of the confining potential becomes very large, the occupancy begins to exceed one at the center of the lattice, indicating a breakdown of Mott behavior there, but not everywhere. Increasing the filling further, for example  $N_b = 116$ , eventually produces a second Mott region in the center of the system with a local filling of two bosons per site without destroying totally the first Mott region. At higher boson numbers, richer structures with coexistence of more superfluid and insulating regions will occur. This qualitative picture is similar to the one obtained for fermions [72,73] and discussed in the next section. In fermionic systems, the superfluid phases in the bosonic case are substituted by metallic phases.

### 4.2.2 The global compressibility

A central feature of the Mott phase transition of the unconfined boson-Hubbard model is global incompressibility: A charge gap opens up, i.e. the density gets “stuck” at  $n$

integer, for a range of chemical potentials  $\mu$ . One might, then, crudely interpret the spatial dependence of the local density in the confined case, Fig. 4.3, as rather analogous to the chemical potential dependence in the unconfined case [14]. This assumption, and the  $\rho$  versus  $\mu$  curve in the unconfined case, allow to calculate the site at which a Mott domain is entered or exited. These are shown as arrows in Fig. 4.3. However it is vital to emphasize that while the confined system has locally incompressible regions, the global compressibility is *never* zero which is seen clearly in Fig. 4.4. The main figure should be contrasted with the nonconfined case (inset).

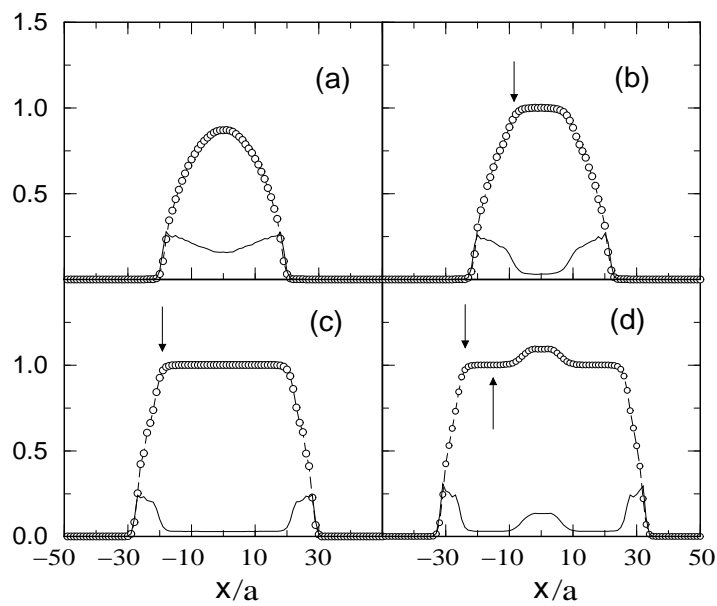


Figure 4.3: Cuts across Fig. 4.2 show the compressibility profile  $\kappa_i^0$  (solid line) associated with the local density  $n_i$  (circles). The fillings are  $N_b = 25$  (a), 33 (b), 50 (c) and 60 (d).  $\kappa_i^0$  is very small when  $n_i = 1$ . For an explanation of the arrows see text.

An important difference in the behavior of the local  $\kappa_i^0$  is especially evident in one dimension where, in the unconfined case, the global compressibility diverges [18] as the Mott lobe is approached,  $\kappa \propto |n - 1|^{-1}$  for the first lobe. Here, instead,  $\kappa_i^0 \propto (n_i - 1)$ , as shown in Fig. 4.5. The origin of these differences is of course that the global compressibility,  $\kappa = \beta(\langle \sum_{ij} n_i n_j \rangle - \langle n \rangle^2)$ , probes density correlations at all length scales. In the unconfined case, contrary to the confined system, the establishment of the Mott phase is a quantum phase transition that happens collectively throughout the system with a correlation length that diverges. There is, however, an interesting collapse of data in the trapped system as a Mott region is approached, which may be an indication of

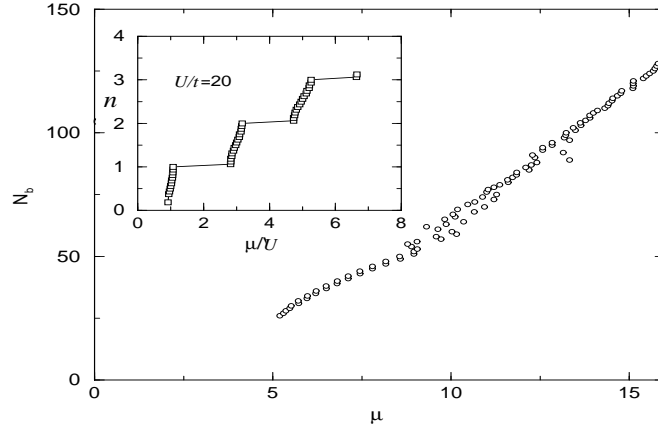


Figure 4.4:  $N_b$  (number of bosons) as a function of the chemical potential,  $\mu$  for  $V_0 = 4.5$ . No globally incompressible Mott plateau is observed. Inset shows the unconfined case.

universal behavior on the interphase superfluid-Mott-insulator<sup>2</sup>. That is, the values of  $\kappa_i^0$  behave similarly when the total filling is changed, as it shown in Fig. 4.5. Similar results are obtained when the on-site repulsion is changed, and for the  $n = 2$  locally incompressible phase.

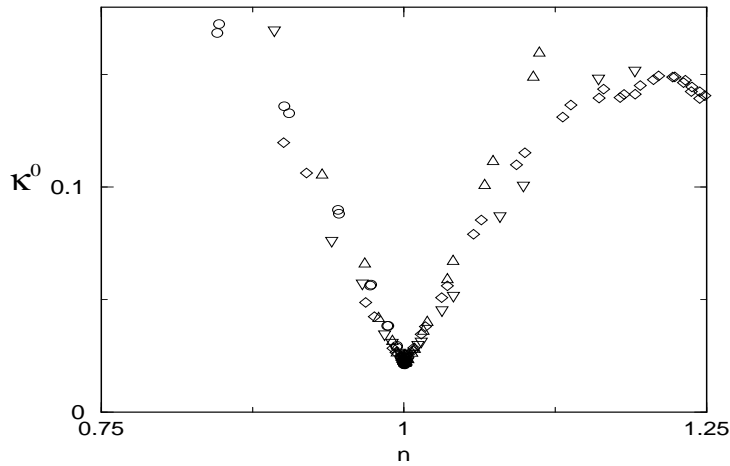


Figure 4.5: The local compressibility  $\kappa_i^0$  as a function of the local density for  $U = 4t$ ,  $N_b = 35$  ( $\circ$ ),  $N_b = 80$  ( $\diamond$ ); and for  $U = 4.5t$ ,  $N_b = 90$  ( $\triangle$ ),  $N_b = 141$  ( $\nabla$ ).  $\kappa_i^0$  decreases linearly with  $n_i$  as the Mott region ( $n = 1$ ) is approached from below or above. This behavior is different from the unconfined system where  $\kappa$  diverges.

<sup>2</sup>This feature is discussed in more detail in next section on the interphase metal-Mott-insulator for fermionic systems.



### 4.2.3 The phase diagram

Sets of runs such as those shown in Fig. 4.2 allowed to determine a phase diagram as a function of boson filling and interaction strength for a given trap curvature. This is shown in Fig. 4.6. As the filling is increased at fixed interaction strength, one crosses from a smooth density profile to one which has locally incompressible “Mott” domains, if  $U$  is large enough. Further increase in the filling ultimately leads to the formation of regions at the well center where  $n_i > 1$ . In Fig. 4.6, region A admits a locally incompressible region with  $n_i = 1$  surrounded by a superfluid, as in Figs. 4.3(b) and (c). Region B has  $n_i > 1$  surrounded by incompressible regions, Fig. 4.6(d). Region C is where the central part of the system has an  $n_i = 2$  incompressible region which, when the boundary of the system is approached, falls off to a shoulder of  $n_i = 1$  Mott region before reaching zero density. The  $n_i = 1$  and  $n_i = 2$  incompressible regions are separated by compressible regions. Region D is where the center of the system is compressible  $n_i > 2$ , bounded by  $n_i = 2$  which in turn is bounded by  $n_i = 1$  incompressible regions. Region E has no incompressible regions.

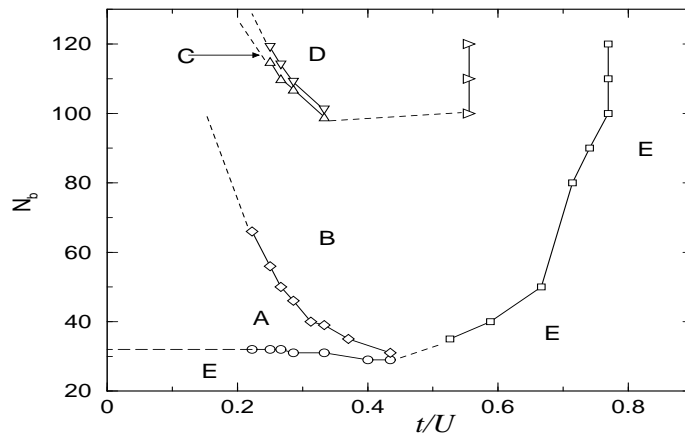


Figure 4.6: Phase diagram of correlated bosons in a quadratic confining potential. Solid lines are drawn to guide the eye, dashed lines are extrapolations. See text for details.

Note that the values of  $U$  at which the A and C regions in Fig. 4.6 are entered are of the same order as those of the first two true Mott lobes in the nonconfined case [18]. This is consistent with the experimental results on three-dimensional optical lattices [11] which appear to be in agreement with the expected value in the nonconfined case. Furthermore, the narrowness of region C could help understand why the experiments [11] have not shown signs of the  $n = 2$  Mott region, even though  $n_i = 2.5$  in the core of the system.



## Chapter 5

# Two component fermions confined on 1-D optical lattices

In this chapter we study ground state properties of the one-dimensional fermionic Hubbard model with an additional confining potential and with repulsive contact interaction, using QMC simulations. Like in the bosonic case discussed in the previous Chapter, Mott-insulating domains appear over a continuous range of fillings and always coexist with compressible phases, such that in general global quantities are not appropriate to characterize the system. We define a local compressibility that characterizes the Mott-insulating regions in an unambiguous way, and analyze other local quantities (Sec. 5.2).

The region where the transition between the metallic and Mott-insulating phase occurs, is studied in detail. We find that the local compressibility displays critical behavior on entering the Mott-insulating phase, revealing a new critical exponent. In addition, both the local compressibility and the variance of the local density exhibit universal behavior with respect to the confining potential and the strength of the interaction, as expected in critical phenomena (Sec. 5.3).

It is shown that the momentum distribution function (MDF), a quantity that is commonly considered in experiments, fails in giving a clear signal of the Mott-insulator transition (Sec. 5.4). Furthermore, we analyze a mean-field (MF) approach to these systems and compare it with the numerically exact QMC results (Sec. 5.5). The comparison shows the qualitative good information that can be obtained within MF and where it fails. Finally, we determine the phase diagram that allows to predict the phases to be observed in the experiments (Sec. 5.6), and analyze the generic features that are valid for different kinds of confining potentials (Sec. 5.7).

## 5.1 The Hubbard model

The Hubbard model in a periodic lattice [123, 124] has been intensively studied as a prototype for the theoretical understanding of the Mott-metal-insulator transition (MMIT). This model considers electrons in a single band, and its Hamiltonian can be written as

$$H = -t \sum_{i,\sigma} \left( c_{i\sigma}^\dagger c_{i+1\sigma} + \text{H.c.} \right) + U \sum_i n_{i\uparrow} n_{i\downarrow} \quad (5.1)$$

where  $c_{i\sigma}^\dagger$ ,  $c_{i\sigma}$  are creation and annihilation operators, respectively, for electrons with spin  $\sigma$  at site  $i$ , and  $n_{i\sigma} = c_{i\sigma}^\dagger c_{i\sigma}$  is the particle number operator. Electrons are considered to hop only between nearest neighbors with a hopping amplitude  $t$ , and the on-site interaction parameter is denoted by  $U$ , which will be considered repulsive ( $U > 0$ ).

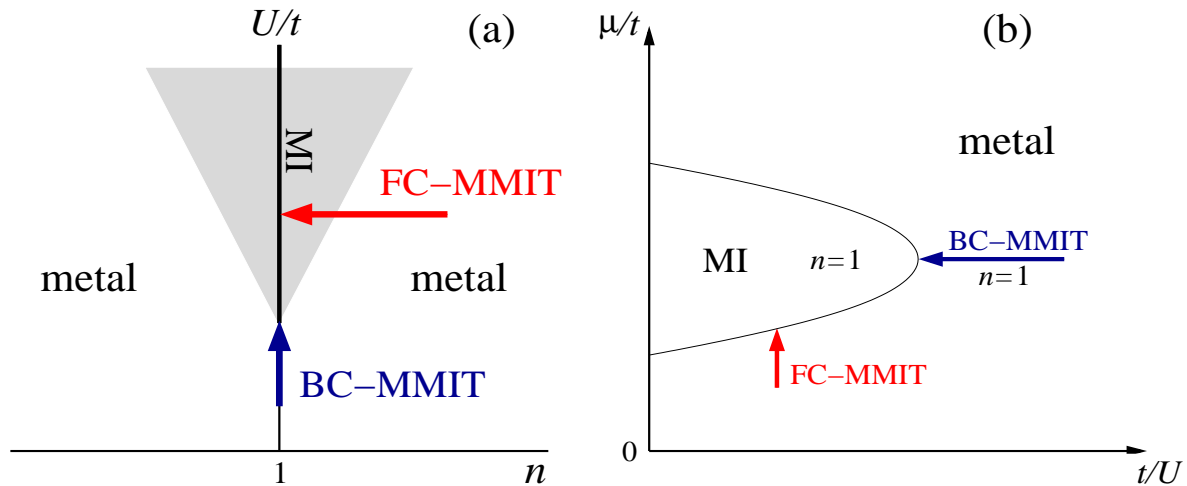


Figure 5.1: General schematic phase diagram for the Mott-metal-insulator transition obtained from the Hubbard model. (a) In the plane of  $U/t$  vs  $n$ . The shaded area represents a metallic region that is under the strong influence of the MMIT. (b) In the plane of  $\mu/t$  vs  $t/U$ . The routes for the MMIT (see text) has been signaled with arrows.

It is well known that the Hubbard model [Eq. (5.1)] displays MMIT phase transitions at half filling and at finite values of the on-site repulsive interaction  $U$ . In the case of perfect nesting<sup>1</sup> the transition occurs at  $U = 0$ . The schematic phase diagram is shown in Fig. 5.1 in the planes  $U/t$  vs  $n$  (a), and  $\mu/t$  vs  $t/U$  (b). The two routes for

<sup>1</sup>Nesting refers to the existence of parallel sections in the Fermi surface. This means that excitations of vanishing energy are possible at finite momentum. Perfect nesting appears for periodic systems in 1D at any filling since in 1D the Fermi surface consists only of two points. In addition, it appears for hypercubic lattices at half filling since in that cases the Fermi surface is an hypercube.

the MMIT are the filling-controlled MMIT (FC-MMIT), and the bandwidth-controlled MMIT (BC-MMIT) [125]. It is interesting to note that in contrast to the boson-Hubbard model where the FC-MMIT is mean field for all dimensions, in the fermionic-Hubbard model the FC-MMIT exhibits two different universality classes for 1D and 2D (for 3-D systems the universality class is not well known) [125]. The metallic regions very close to the Mott-insulating phase [shaded area in Fig. 5.1(a)] are under the strong influence of the MMIT, and exhibit diverse anomalous features like mass enhancement and carrier number reduction (the carriers can be easily localized by extrinsic forces). At  $n = 0, 2$  the system is in a band insulating state within this model.

## 5.2 The Hubbard model in a harmonic trap

Ultracold fermionic atoms on optical lattices represent nowadays the most direct experimental realization of the Hubbard model, since atoms interact only via a contact potential. In addition, in the experiments all parameters can be controlled with an unprecedented precision. Since the particles are trapped by a confined potential, it is possible to drive the MMIT by changing the total filling of the trap, the on-site repulsive interaction, or varying the curvature of the confining potential. The Hamiltonian in this case can be written as

$$H = -t \sum_{i,\sigma} \left( c_{i\sigma}^\dagger c_{i+1\sigma} + \text{H.c.} \right) + U \sum_i n_{i\uparrow} n_{i\downarrow} + V_2 \sum_{i\sigma} x_i^2 n_{i\sigma}, \quad (5.2)$$

where  $V_2$  is the curvature of the harmonic confining potential, and  $x_i$  measures the position of the site  $i$  ( $x_i = ia$  with  $a$  the lattice constant). The number of lattice sites is  $N$  and is selected so that all the fermions are confined in the trap. We denote the total number of fermions as  $N_f$  and consider equal number of fermions with spins up and down ( $N_{f\uparrow} = N_{f\downarrow} = N_f/2$ ). In our simulations, we used the zero-temperature projector QMC method described in Chap. 3.

### 5.2.1 Local phases

The results for the evolution of the local density ( $n_i = \langle n_{i\uparrow} + n_{i\downarrow} \rangle$ ), as a function of the total number of the confined particles, are shown in Fig. 5.2. For the lowest filling, so that  $n < 1$  at every site, the density shows a profile with the shape of an inverted

parabola, similar to that obtained in the non-interacting case [36], and hence, such a situation should correspond to a metallic phase. Increasing the number of fermions up to  $N_f = 60$ , a plateau with  $n = 1$  appears in the middle of the trap, surrounded by a region with  $n < 1$  (metallic). Since in the periodic case, a Mott insulator appears at  $n = 1$ , it is natural to identify the plateau with such a phase. The Mott-insulating domain in the center of the trap increases its size when more particles are added, but at a certain filling ( $N_f = 70$  here) this becomes energetically unfavorable and a new metallic phase with  $n > 1$  starts to develop in the center of the system. Upon adding more fermions, this new metallic phase widens spatially and the Mott-insulating domains surrounding it are pushed to the borders. Depending on the on-site repulsion strength, they can disappear and a complete metallic phase can appear in the system. Finally, a “band insulator” (i.e.,  $n = 2$ ) forms in the middle of the trap for the highest fillings (after  $N_f = 144$  here). Due to the full occupancy of the sites, it will widen spatially and push the other phases present in the system to the edges of the trap when more fermions are added.

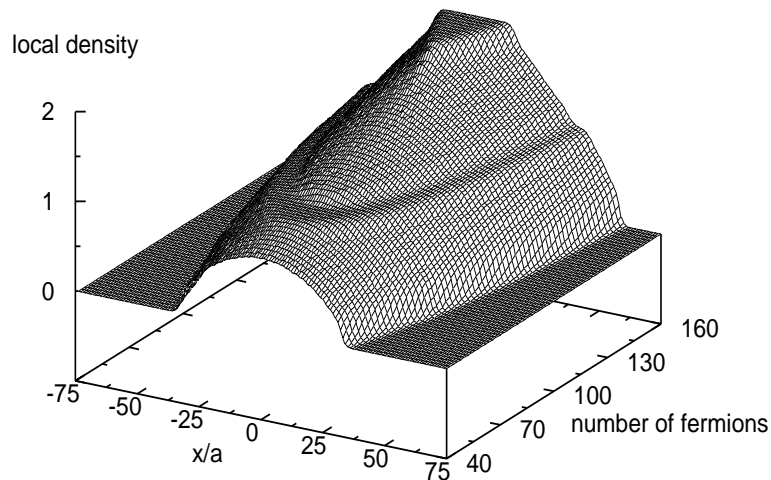


Figure 5.2: Evolution of the local density in a parabolic confining potential as a function of the position in the trap and increasing total number of fermions. The parameters involved are  $N = 150$ ,  $U = 4t$  and  $V_2a^2 = 0.002t$ . The positions are measured in units of the lattice constant  $a$ .

Although the existence of flat regions in the density profile is an indication that there is an insulator there, a more quantitative characterization is needed. As it was shown in the previous Chapter, a measure of the local compressibility was obtained by the variance of the local density ( $\Delta_i = \langle n_i^2 \rangle - \langle n_i \rangle^2$ ), which may be used on a first approach (from

here on, we refer to the variance as the variance of the local density). In Fig. 5.3 we show four characteristic profiles present in Fig. 5.2 and their respective variances. For the case in which only a metallic phase is present [Fig. 5.3(a)], it can be seen that the variance decreases when the density approaches  $n = 1$  and has a minimum for densities close to that value. For the Mott-insulating domain [ $n = 1$  in Fig. 5.3(b)], the variance has a constant value that is smaller than that of the metal surrounding it. As soon as the Mott-insulating phase is destroyed in the middle of the trap and a new metallic region with  $n > 1$  develops there [Fig. 5.3 (c)], the variance increases in this region. The variance in the metallic region with  $n > 1$  will start to decrease again when the density approaches  $n = 2$  and will have values even smaller than those in the Mott-insulating phase. Finally, when the insulator with  $n = 2$  is formed in the center of the trap the variance vanishes there [Fig. 5.3(d)].

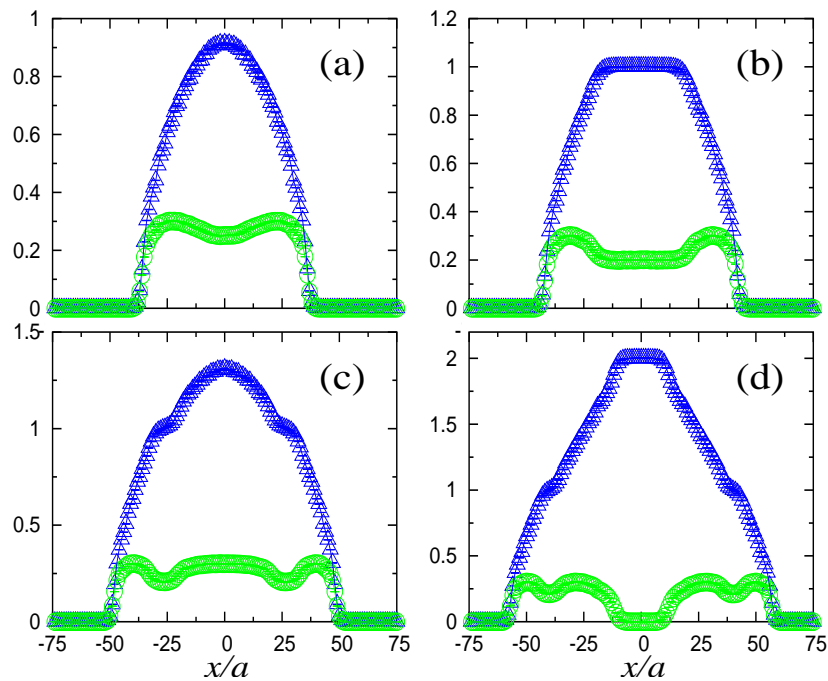


Figure 5.3: Four density profiles ( $\triangle$ ) (cuts across Fig. 5.2) and their variances ( $\circ$ ). The fillings are  $N_f = 50$  (a), 68 (b), 94 (c), and 150 (d).

Alternatively, Mott-insulating regions can be obtained by increasing the ratio between the on-site repulsive interaction and the hopping parameter as was done in experiments for bosons confined in optical lattices [11]. Fig. 5.4(a) shows the evolution of the density profiles in a trapped system with  $N = 100$ ,  $N_f = 70$ , and  $V_2 a^2 = 0.0025t$  when this ratio is increased from  $U/t = 2$  to  $U/t = 8$  [for more details of these density profiles see Fig.

5.12(e)-(h)]. It can be seen that for small values of  $U/t$  ( $U/t = 2$ ) there is only a metallic phase present in the trap. As the value of  $U/t$  ( $U/t = 4$ ) is increased, a Mott-insulating phase tries to develop at  $n = 1$  while a metallic phase with  $n > 1$  is present in the center of the system. As the on-site repulsion is increased even further ( $U/t = 6, 8$ ), a Mott-insulating domain appears in the middle of the trap suppressing the metallic phase that was present there. In Fig. 5.4(b) we show the variance of the density for the profiles

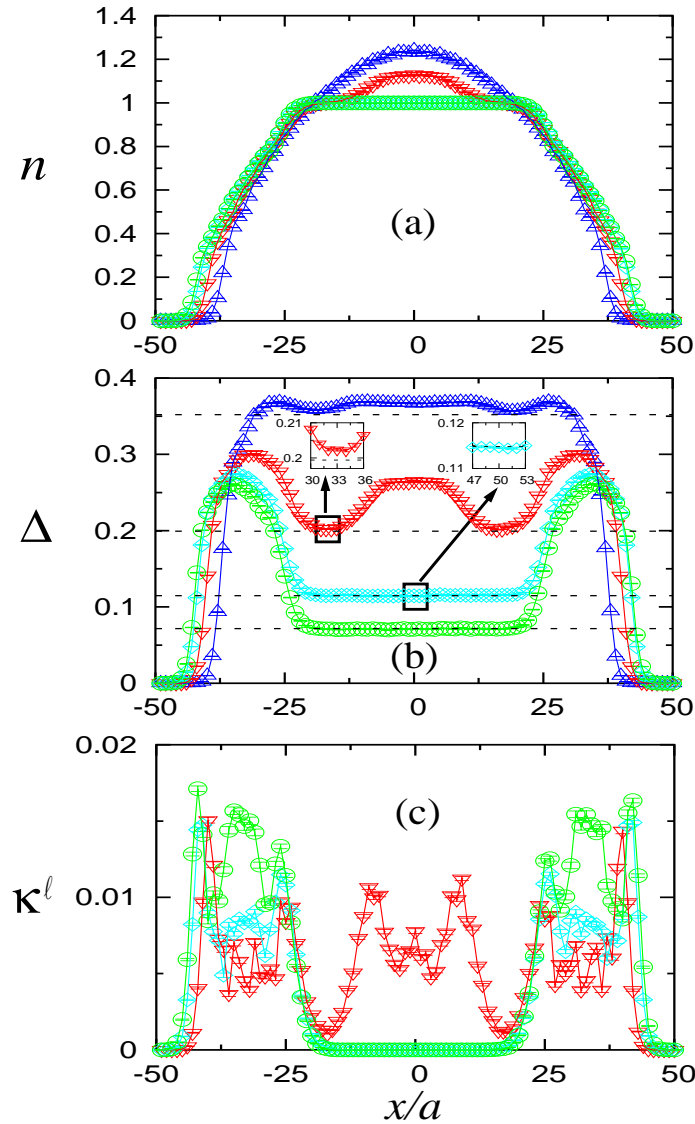


Figure 5.4: Profiles for a trap with  $V_2 a^2 = 0.0025t$  and  $N_f = 70$ , the on-site repulsions are  $U/t = 2$  ( $\triangle$ ),  $4$  ( $\nabla$ ),  $6$  ( $\diamond$ ), and  $8$  ( $\circ$ ). (a) Local density, (b) variance of the local density, (c) local compressibility  $\kappa^\ell$  as defined in Eq. (5.3). The dashed lines in (b) are the values of the variance in the  $n = 1$  periodic system for  $U/t = 2, 4, 6, 8$  (from top to bottom).



in Fig. 5.4(a) (from top to bottom, the values presented are for  $U/t = 2, 4, 6, 8$ ). As expected, the variance decreases in both the metallic and Mott-insulating phases when the on-site repulsion is increased. When the Mott-insulating plateau is formed in the density profile, a plateau with constant variance appears in the variance profile with a value that will vanish only in the limit  $U/t \rightarrow \infty$ . As shown in Fig. 5.4(b), whenever a Mott-insulating domain is formed in the trap, the value of the variance on it is exactly the same as the one for the Mott-insulating phase in the periodic system for the same value of  $U/t$  (horizontal dashed lines). This would support the validity of the commonly used local density (Thomas-Fermi) approximation [126]. However, the insets in Fig. 5.4(b), show that this is not necessarily the case, since for  $U/t = 4$ , the value of the variance in the Mott-insulating phase of the periodic system is still not reached in the trap, although the density reaches the value  $n = 1$ . Therefore, in contrast to the periodic case, a Mott-insulating region is not determined by the filling only. In the cases of  $U/t = 6$  [inset in Fig. 5.4(b) for a closer look] and  $U/t = 8$ , the value of the variance in the periodic system is reached and then one can say that Mott-insulating phases are formed there.

### 5.2.2 A local order parameter

Although the variance gives a first indication for the formation of a local Mott insulator, an ambiguity is still present, since there are metallic regions with densities very close to  $n = 0$  and  $n = 2$ , where the variance can have even smaller values than in the Mott-insulating phases. Therefore, an unambiguous quantity is still needed to characterize the Mott-insulating regions. We propose a new local compressibility as a local-order parameter to characterize the Mott-insulating regions, that is defined as

$$\kappa_i^\ell = \sum_{|j| \leq \ell(U)} \chi_{i,i+j}, \quad (5.3)$$

where

$$\chi_{i,j} = \langle n_i n_j \rangle - \langle n_i \rangle \langle n_j \rangle \quad (5.4)$$

is the density-density correlation function and  $\ell(U) \simeq b \xi(U)$ , with  $\xi(U)$  the correlation length of  $\chi_{i,j}$  in the unconfined system at half-filling for the given value of  $U$ . As a consequence of the charge gap opened in the Mott-insulating phase at half filling in the periodic system, the density-density correlations decay exponentially [ $\chi(x) \propto \exp^{-\frac{x}{\xi(U)}}$ ]

enabling  $\xi(U)$  to be determined. The factor  $b$  is chosen within a range where  $\kappa^\ell$  becomes qualitatively insensitive to its precise value. Since there is some degree of arbitrariness in the selection of  $b$ , we will examine its role in the calculation of  $\kappa^\ell$  here. Fig. 5.5 shows

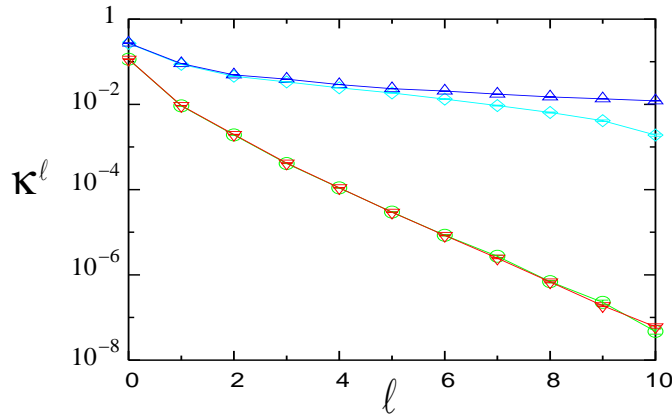


Figure 5.5: Local compressibility as a function of  $\ell$  for the periodic and trapped ( $V_2a^2 = 0.0025t$ ,  $N_f = 70$ ) systems in the Mott-insulating and metallic phases,  $U = 6t$ . ( $\nabla$ )  $n = 1$  periodic, ( $\circ$ )  $n_{i=0} = 1$  trapped, ( $\triangle$ )  $n = 0.66$  periodic, and ( $\diamond$ )  $n_{i=-32} \sim 0.66$  trapped. The position of the point  $i$ , where we measure the local compressibility in the trapped case, can be seen in Fig. 5.4.

how the local compressibility behaves as a function of  $\ell$  for a periodic and a trapped systems in the Mott-insulating and metallic phases. In the Mott-insulating phase, it is possible to see that in the periodic and confined systems the local compressibility decays exponentially (like density-density correlations) in exactly the same way due to the charge gap present there. In the metallic case there is no charge gap so that density-density correlations decay as a power law and the local compressibility, shown in Fig. 5.5, decays very slowly. In Fig. 5.5, a departure in the behavior of the local compressibility for the trapped system from the periodic case for large values of  $\ell$  can be seen. This occurs because correlations with points very close to the band insulating ( $n = 0$ ) and the Mott-insulating ( $n = 1$ ) regions surrounding the metallic phase [see Fig. 5.4(a)] are included in  $\kappa$ . However, this effect does not affect the fact that the value of the local compressibility is clearly different from zero as long as the size of the metallic phase is larger than  $2\ell$ . We see that considering  $b \sim 10$  (no matter what the exact value of  $b$  is), the local compressibility is zero with exponential accuracy (i.e.  $\sim 10^{-6}$  or less) for the Mott-insulating phase and has a finite value in the metallic phase. For the case in

Fig. 5.5 where  $U = 6t$ , the correlation length is  $\xi \sim 0.8$  so that  $\ell \sim 8$  in order to obtain  $\kappa \sim 10^{-6}$ . Physically, the local compressibility defined here gives a measure of the change in the local density due to a constant shift of the potential over a finite range but over distances larger than the correlation length in the unconfined system.

In Fig. 5.4(c), we show the profiles of the local compressibility for the same parameters as Figs. 5.4(a) and (b) (we did not include the profile of the local compressibility for  $U = 2t$  because for that value of  $U$  we obtain that  $\ell$  is bigger than the system size). In Fig. 5.4(c), it can be seen that the local compressibility only vanishes in the Mott-insulating domains. For  $U = 4t$ , it can be seen that in the region with  $n \sim 1$  the local compressibility, although small, does not vanish. This is compatible with the fact that the variance is not equal to the value in the periodic system there, so that although there is a shoulder in the density profile, this region is not a Mott insulator. Therefore, the local compressibility defined here serves as a genuine local order parameter to characterize the insulating regions that always coexist with metallic phases.

### 5.2.3 Local spin-spin correlations

We discuss in this section the spin-spin correlation function, since in periodic chains, quasi-long-range antiferromagnetic correlations appear in the Mott-insulating phase. In Fig. 5.6 we show the local  $\langle S_i^z S_j^z \rangle$  correlation function for some points of the profiles presented in Fig. 5.3. We measured the spin-spin correlations in the trap at the points in Figs. 5.6 where it can be seen that  $\langle S_i^z S_j^z \rangle$  has the maximum value. In Fig. 5.6(a) it can be seen that in the metallic phase with  $n < 1$ , the spin-spin correlations decay rapidly and do not show any clear modulation, which is due to the fact that the density is changing in this region. In the local Mott-insulating phase, the center of the trap in Fig. 5.6(b), antiferromagnetic correlations can be observed. They disappear completely only on entering in the metallic regions. For the shoulders with  $n \sim 1$  [Fig. 5.6(c)], the antiferromagnetic correlations are still present but due to the small size of these regions they decay very rapidly. Finally for the metallic regions with  $n > 1$ , the spin correlations behave like in the metallic phases with  $n < 1$  as shown in Fig. 5.6(d). Then we conclude that based on the known behavior of spin-spin correlations in periodic systems, a good qualitative understanding of spin-spin correlations in a trap can be obtained.

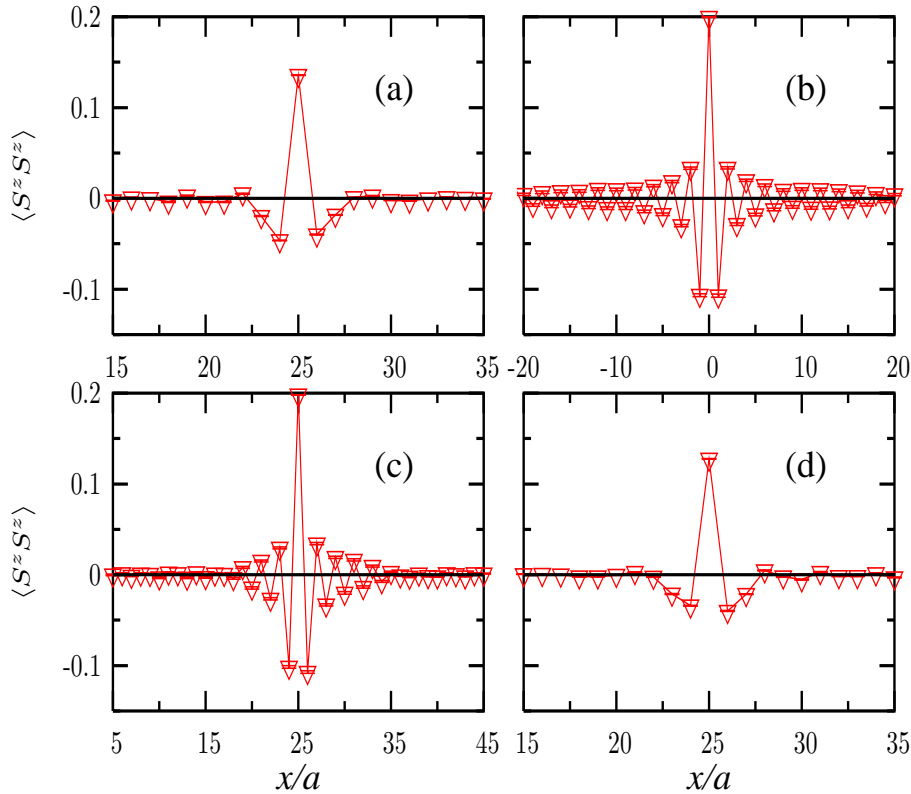


Figure 5.6: Local spin-spin correlations in a trap measured with respect to the points in which in the figure they show a maximum value. The density at each point (total filling in the trap) is  $n_{i=25} = 0.61$  ( $N_f = 50$ ) (a),  $n_{i=0} = 1.00$  ( $N_f = 68$ ) (b),  $n_{i=25} = 1.01$  ( $N_f = 94$ ) (c), and  $n_{i=25} = 1.44$  ( $N_f = 150$ ) (d), for a trap with  $N = 150$ ,  $U = 4t$ , and  $V_2 a^2 = 0.002t$  (for the corresponding density and variance profiles see Fig. 5.3).

### 5.3 Local quantum criticality and universality

In the previous section we have characterized the local Mott-insulating and metallic phases quantitatively. We study in this section the regions where the system goes from one phase to another. Criticality can arise, despite the microscopic spatial size of the transition region<sup>2</sup>, due to the extension in imaginary time that reaches the thermodynamic limit at  $T = 0$ , very much like the case of the single impurity Kondo problem [127], where long-range interactions in imaginary time appear for the local degree of freedom as a result of the interaction with the rest of the system. An intriguing future question, for both theory and experiment, will be the role of spatial dimension in the critical behavior of systems in the thermodynamic limit. In the fermionic case, as it was mention before,

<sup>2</sup>Recent experiments leading to a MMIT [11] considered a system with linear dimension  $\sim 65a$ , i.e. still in a microscopic range.

the FC-MMIT in 1D and 2D belong to different universality classes [125]. This route to the transition, in the periodic case, is the one relevant for the trapped systems where the density changes on entering in the local Mott insulator, and could lead to different local quantum critical behavior between traps with different dimensionalities. In the bosonic case the FC-MMIT is a mean-field transition in all dimensions [17, 18], which could also lead to a different local quantum critical behavior for trapped bosons as compared with trapped fermions.

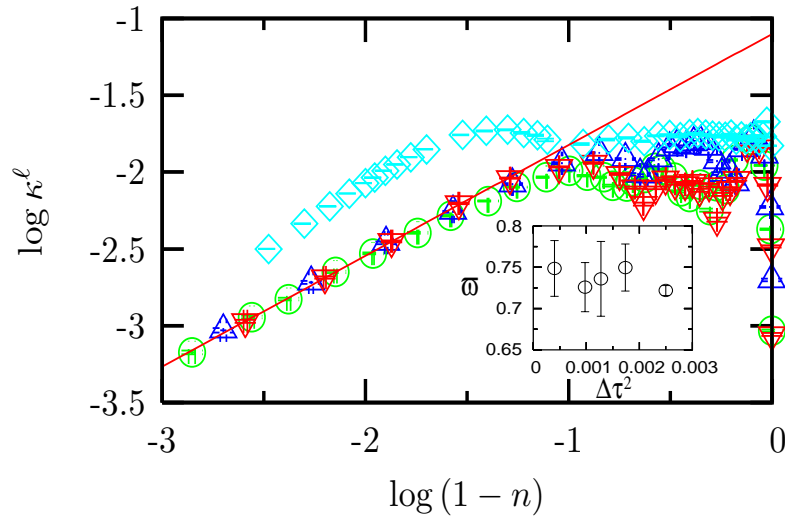


Figure 5.7: The local compressibility  $\kappa^\ell$  vs  $\delta = 1 - n$  at  $\delta \rightarrow 0$  for ( $\Delta$ )  $N_f = 70$ ,  $U = 8t$  and  $V_2a^2 = 0.0025t$ ; ( $\nabla$ )  $N_f = 70$ ,  $U = 6t$  and  $V_2a^2 = 0.0025t$ ; ( $\circ$ )  $N_f = 72$ ,  $U = 6t$  and a quartic potential with  $V_4a^4 = 1.0 \times 10^{-6}t$ ; ( $\diamond$ ) unconfined periodic system with  $U = 6t$ . The straight line displays a power-law behavior. Inset: Dependence of the critical exponent  $\varpi$  on  $\Delta\tau^2$ .

Figure 5.7 shows the local compressibility vs  $\delta = 1 - n$  for  $\delta \rightarrow 0$  in a double logarithmic plot. A power law  $\kappa^\ell \sim \delta^\varpi$  is obtained, with  $\varpi < 1$ , such that a divergence results in its derivative with respect to  $n$ , showing that critical fluctuations are present in this region. Since the QMC simulation is affected by systematic errors due to discretization in imaginary time, it is important to consider the limit  $\Delta\tau \rightarrow 0$  in determining the critical exponent. The inset in Fig. 5.7 shows such an extrapolation leading to  $\varpi \simeq 0.68 - 0.78$ . At this point we should remark that the presence of the harmonic potential allows the determination of the density dependence of various quantities with unprecedented detail on feasible system sizes as opposed to unconfined periodic systems, where systems with  $10^3 - 10^4$  sites would be necessary to allow for similar variations in density. In addition to

the power law behavior, Fig. 5.7 shows that for  $\delta \rightarrow 0$ , the local compressibility of systems with a harmonic potential but different strengths of the interaction or even with a quartic confining potential, collapse on the same curve. Hence, universal behavior as expected for critical phenomena is observed also in this case. This fact is particularly important with regard to experiments, since it implies that the observation of criticality should be possible for realistic confining potentials, and not only restricted to perfect harmonic ones, as usually used in theoretical calculations. However, Fig. 5.7 shows also that the unconfined case departs from all the others. Up to the largest systems we simulated (600 sites), we observe an increasing slope rather than the power law of the confined systems. Actually, we observe that the exponent of the power law obtained between contiguous points in Fig. 5.7 for the periodic case extrapolates to  $\varpi = 1$ , as it is shown in Fig. 5.8.

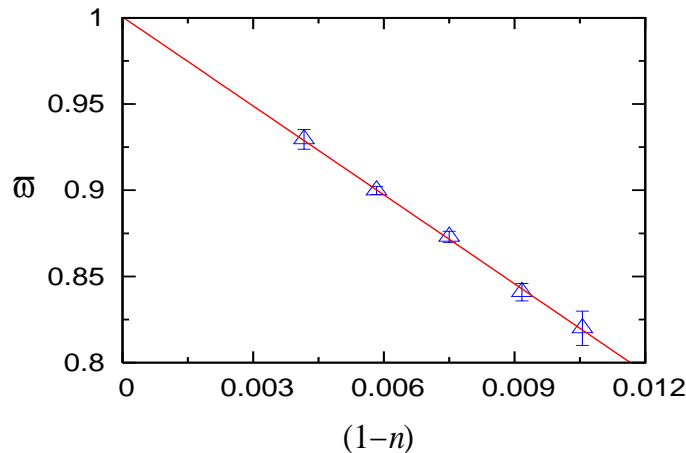


Figure 5.8: Exponent  $\varpi$  of the local compressibility for the periodic system, obtained between contiguous points in Fig. 5.7, vs  $(1-n)$ . The extrapolation leads to  $\varpi = 1$  for  $n \rightarrow 1$ .

Having shown that the local compressibility displays universality on approaching a Mott-insulating region, we consider the variance  $\Delta$  as a function of the density  $n$  for various values of  $U$  and different confining potentials. Figure 5.9 shows  $\Delta$  vs  $n$  for a variety of systems, where not only the number of particles and the size of the system are changed, but also different forms of the confining potential were used. Here we considered a harmonic potential, a quartic one, and a superposition of a harmonic, a cubic and a quartic one, such that even reflection symmetry across the center of the system is broken. It appears at first glance that the data can only be distinguished by the strength of the interaction  $U$ , showing that the variance is rather insensitive to the

form of the potential. The different insets, however, show that a close examination leads to the conclusion that only near  $n = 1$  and only in the situations where at  $n = 1$  a Mott insulator exists, universality sets in. The inset for  $n$  around 0.6 and  $U = 8t$ , shows that the unconfined system has different variance from the others albeit very close on a raw scale. This difference is well beyond the error bars. Also the inset around  $n = 1$  and for  $U = 4t$ , shows that systems that do not form a Mott-insulating phase in spite of reaching a density  $n = 1$ , have a different variance from those having a Mott insulator. Only the case where all systems have a Mott-insulating phase at  $n = 1$  ( $U = 8t$ ), shows universal behavior independent of the potential, a universality that encompasses also the unconfined systems. For the unconfined system, the behavior of the variance can be

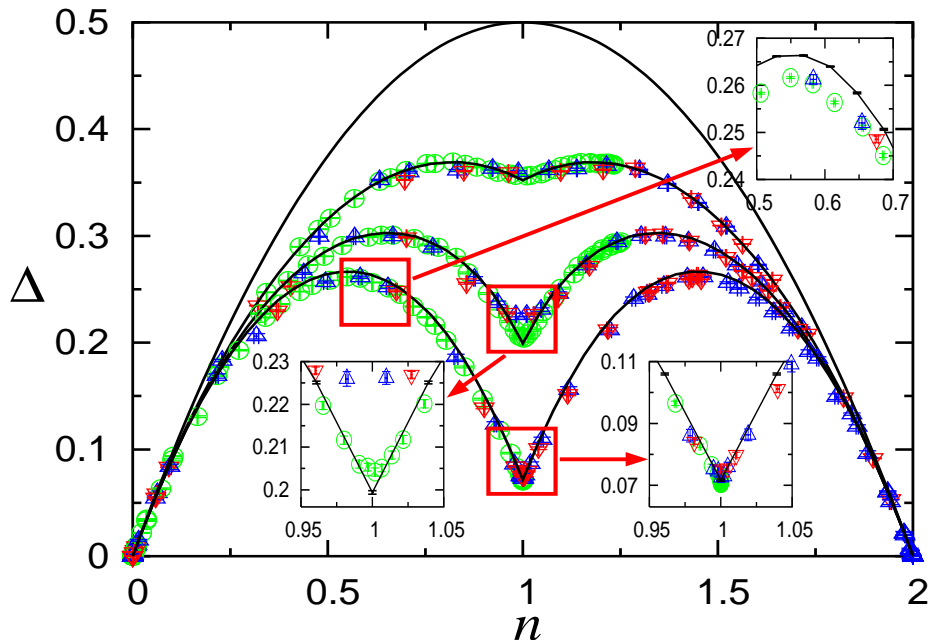


Figure 5.9: Variance  $\Delta$  vs.  $n$  for ( $\circ$ ) harmonic potential  $V_2a^2 = 0.0025t$  with  $N = 100$ ; ( $\triangle$ ) quartic potential  $V_4a^4 = 5 \times 10^{-7}t$  with  $N = 150$ ; ( $\nabla$ ) harmonic potential  $V_2a^2 = 0.016t$  + cubic  $V_3a^3 = 1.6 \times 10^{-4}t$  + quartic  $V_4a^4 = 1.92 \times 10^{-5}t$  with  $N = 50$ ; and (full line) unconfined periodic potential with  $N = 102$  sites. The curves correspond from top to bottom to  $U/t = 0, 2, 4, 8$ . For a discussion of the insets, see text.

examined with Bethe-*Ansatz* [128] in the limit  $\delta \rightarrow 0$ . In this limit and to leading order in  $\delta$ , the ground state energy is given by [129]  $E_0(\delta)/N - E_0(\delta = 0)/N \propto \delta$ , such that the double occupancy, which can be obtained as the derivative of the ground-state energy with respect to  $U$ , will also converge as  $\delta$  towards its value at half-filling. Such behavior is also obtained in our case as shown in Fig. 5.10 for the same parameters of Fig. 5.7.

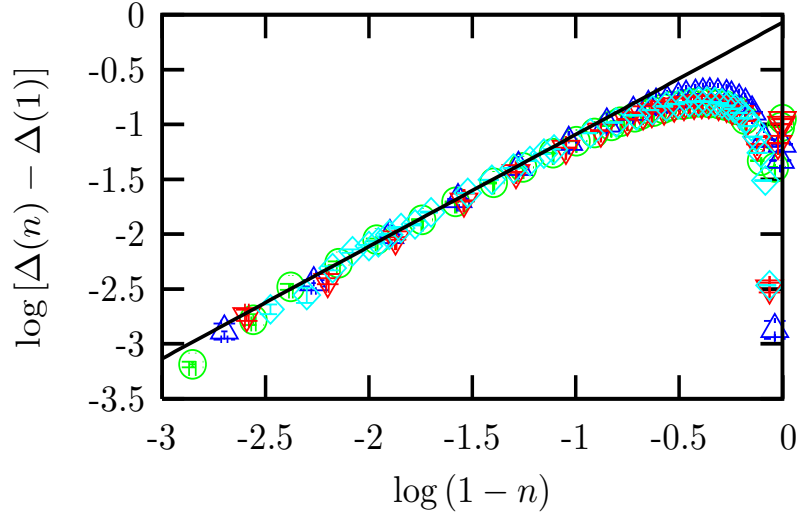


Figure 5.10: Variance of the density vs  $\delta = 1 - n$  at  $\delta \rightarrow 0$  for ( $\triangle$ )  $N_f = 70$ ,  $U = 8t$  and  $V_2 = 0.0025t$ ; ( $\nabla$ )  $N_f = 70$ ,  $U = 6t$  and  $V_2 = 0.0025t$ ; ( $\circ$ )  $N_f = 72$ ,  $U = 6t$  and a quartic potential with  $V_4 = 1.0 \times 10^{-6}t$ ; ( $\diamond$ ) unconfined periodic system with  $U = 6t$ . The straight line displays linear behavior, i.e. it has a slope equal to one.

## 5.4 Momentum distribution function

In most experiments with quantum gases carried out so far, the MDF, which is determined in time-of-flight measurements, played a central role. A prominent example is given by the study of the superfluid-Mott-insulator transition [11] in the bosonic case. Also a QMC study relating this quantity to the density profiles and proposing how to determine the point at which the superfluid-Mott-insulator transition occurs was presented in Ref. [24]. As shown below, we find that the MDF is not appropriate to characterize the phases of the system in the fermionic case, and does not show any clear signature of the MMIT.

In Fig. 5.11 we show the normalized MDF ( $n_k$ ) for the same density profiles presented in Fig. 5.3. For the trapped systems, we always normalize the MDF to be unity at  $k = 0$ . In the case presented in Fig. 5.11, transitions between phases occur due to changes in the total filling of the trap. We first notice that  $n_k$  for the pure metallic phase in the harmonic trap [Fig. 5.11(a)] does not display any sharp feature corresponding to a Fermi surface, in clear contrast to the periodic case. The lack of a sharp feature for the Fermi surface is independent of the presence of the interaction and is also independent of the size of the system. In the non-interacting case, this can be easily understood: the spatial density and the momentum distribution will have the same functional form because the Hamiltonian



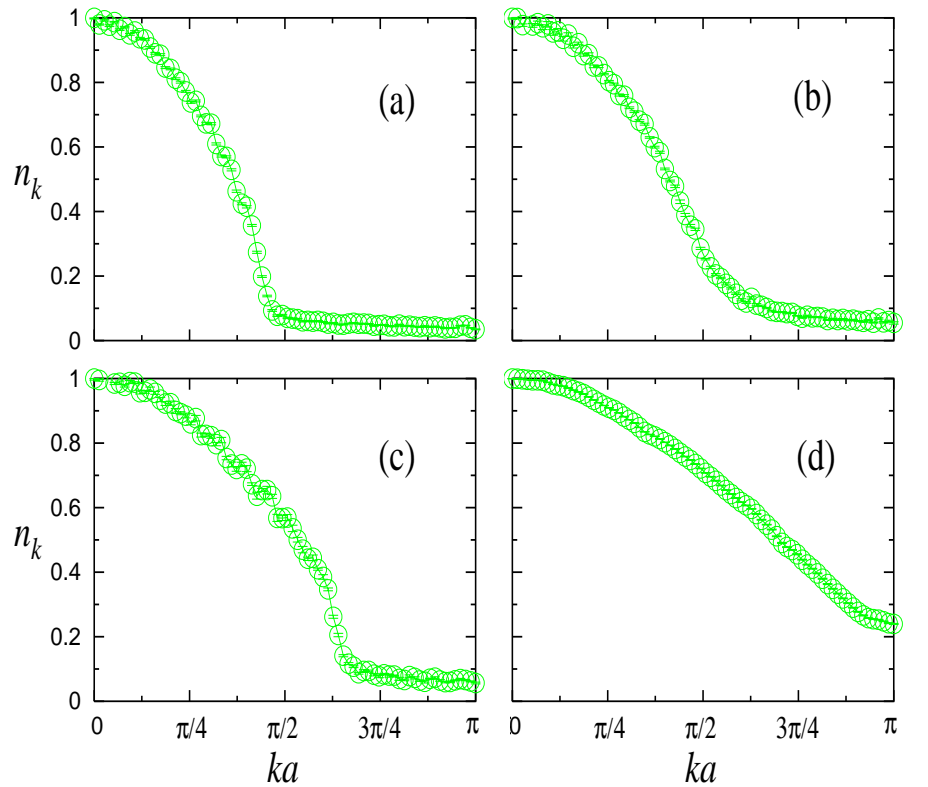


Figure 5.11: Normalized momentum distribution function for the same parameters of Fig. 5.3. The fillings are  $N_f = 50$  (a), 68 (b), 94 (c), and 150 (d).

is quadratic in both coordinate and momentum. When the interaction is present, it could be expected that the formation of local Mott-insulating domains generates a qualitatively and quantitatively different behavior of the momentum distribution, like in the periodic case where in the Mott-insulating phase the Fermi surface disappears. In Fig. 5.11(b), it can be seen that there is no qualitative change of the MDF when the Mott-insulating phase is present in the middle of the trap. Quantitatively  $n_k$  in this case is very similar to the pure metallic cases Fig. 5.11(a) (for densities smaller than one) and Fig. 5.11(c) (where in the middle of the trap the density is higher than one). Only when the insulator with  $n = 2$  appears in the middle of the system we find a quantitative change of  $n_k$  for  $U = 4t$ , as shown in Fig. 5.11(d).

We also studied the momentum distribution function when the MMIT is driven by the change of the on-site repulsion. We did not observe any clear signature of the formation of the Mott-insulating phase in  $n_k$ . In Fig. 5.12 we show the normalized momentum distribution function [Fig. 5.12(a)-5.12(d)] for density profiles [Fig. 5.12(e)-5.12(h)] in which the on-site repulsion was increased from  $U/t = 2$  to 8. It can be seen that the

same behavior present in Fig. 5.11 and the quantitative changes in  $n_k$  appear only when the on-site repulsion goes to the strong-coupling regime, but this is long after the Mott-insulating phase has appeared in the system.

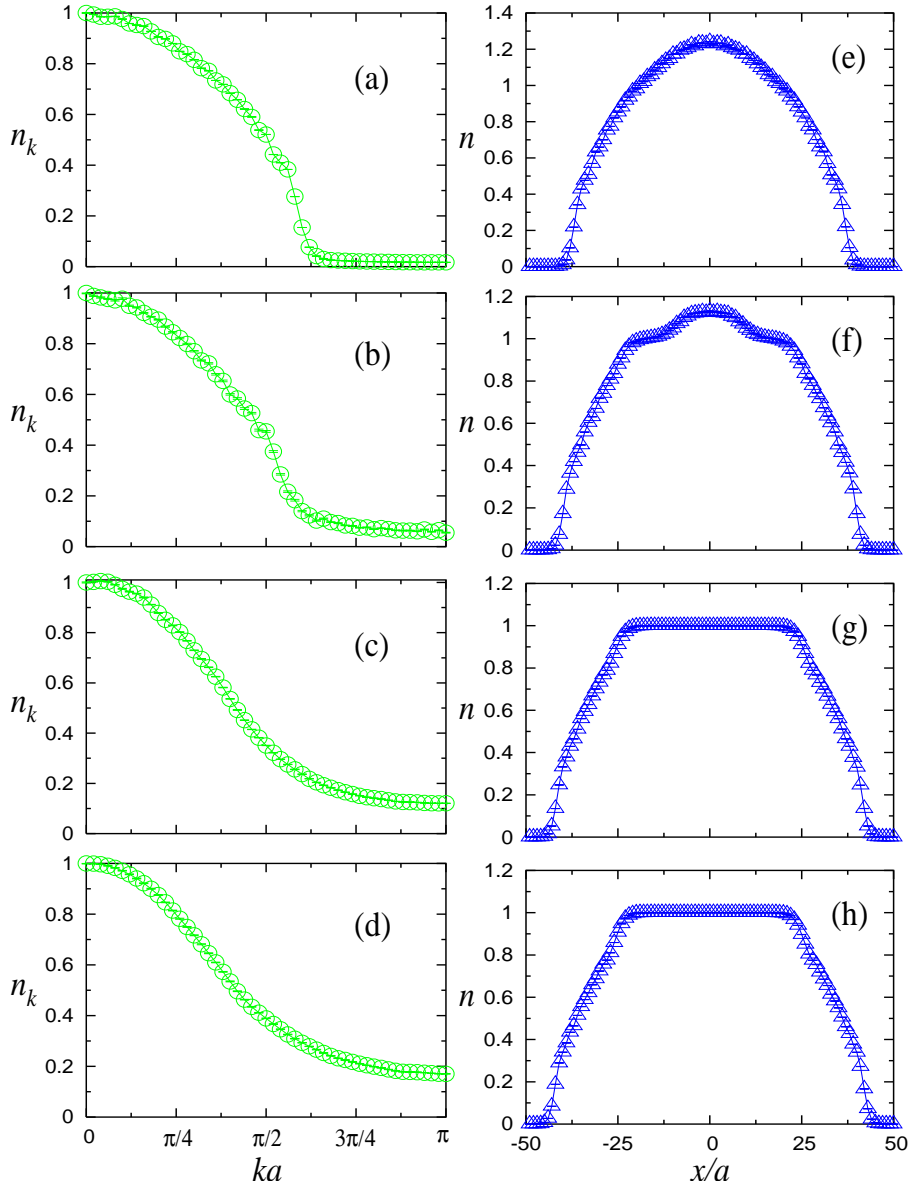


Figure 5.12: Normalized momentum distribution function (a)-(d) and their corresponding density profiles (e)-(h) for  $U/t = 2$  (a),(e), 4 (b),(f), 6 (c),(g), 8 (d),(h), and  $N = 100$ ,  $N_f = 70$ ,  $V_2a^2 = 0.0025t$ .

At this point one might think that in order to study the MMIT using the MDF, it is necessary to avoid the inhomogeneous trapping potential and use instead a kind of magnetic box with infinitely high potential on the boundaries. However, in that case one of the most important achievements of the inhomogeneous system is lost, i.e., the

possibility of creating Mott-insulating phases for a continuous range of fillings. In the perfect magnetic box, the Mott-insulating phase would only be possible at half filling, which would be extremely difficult (if possible at all) to adjust experimentally. The other possibility is to create traps which are almost homogenous in the middle and which have an appreciable trapping potential only close to the boundaries. This can be studied theoretically by considering traps with higher powers of the trapping potentials. As shown below, already non-interacting systems make clear that a sharp Fermi edge is missing in confined systems.

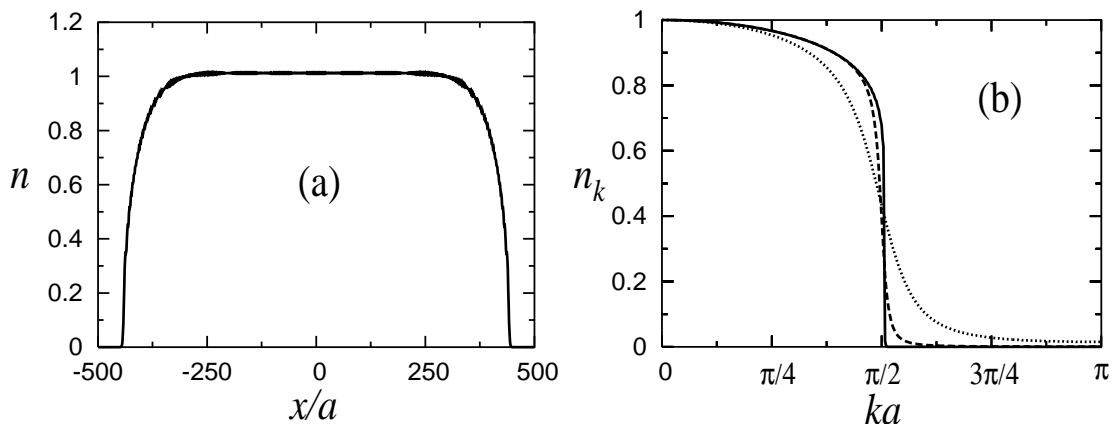


Figure 5.13: Exact results for  $N_f = 840$  noninteracting trapped fermions in a lattice with 1000 sites and a confining potential  $V_{10}a^{10} = 7 \times 10^{-27}t$ . Density profile (a) and the normalized momentum distribution function (b): the continuous line corresponds to (a), the dashed line is the result when an alternating potential  $V_a = 0.1t$  is superposed on the system, and the dotted line corresponds to  $V_a = 0.5t$ .

In Fig. 5.13(a) we show the density profile of a system with 1000 sites,  $N_f = 840$ , and a trapping potential of the form  $V_{10}x_i^{10}$  with  $V_{10}a^{10} = 7 \times 10^{-27}t$ . It can be seen that the density is almost flat all over the trap with a density of the order of one particle per site. Only a small part of the system at the borders has the variation of the density required for the particles to be trapped. In Fig. 5.13(b) (continuous line), we show the corresponding normalized momentum distribution. It can be seen that a kind of Fermi surface develops in the system but for smaller values of  $k$ ,  $n_k$  is always smooth and its value starts decreasing at  $k = 0$ . In order to see how  $n_k$  changes when an incompressible region appears in the system, we introduced an additional alternating potential (like in

Sec. 2.3), so that in this case the new Hamiltonian has the form

$$H = -t \sum_{i,\sigma} (c_{i\sigma}^\dagger c_{i+1\sigma} + \text{H.c.}) + V_{10} \sum_{i\sigma} x_i^{10} n_{i\sigma} + V_a \sum_{i\sigma} (-1)^i n_{i\sigma}, \quad (5.5)$$

where  $V_a$  is the strength of the alternating potential. For the parameters presented in Fig. 5.13(a), we obtain that a small value of  $V_a$  ( $V_a = 0.1t$ ) generates a band insulator in the trap, which extends over the region with  $n \sim 1$  (when  $V_a = 0$ ). However, the formation of this band insulator is barely reflected in  $n_k$ , as can be seen in Fig. 5.13(b) (dashed line). Only when the value of  $V_a$  is increased and the system departs from the phase transition [ $V_a = 0.5t$ , dotted line in Fig. 5.13(c)], does a quantitatively appreciable change in  $n_k$  appear.

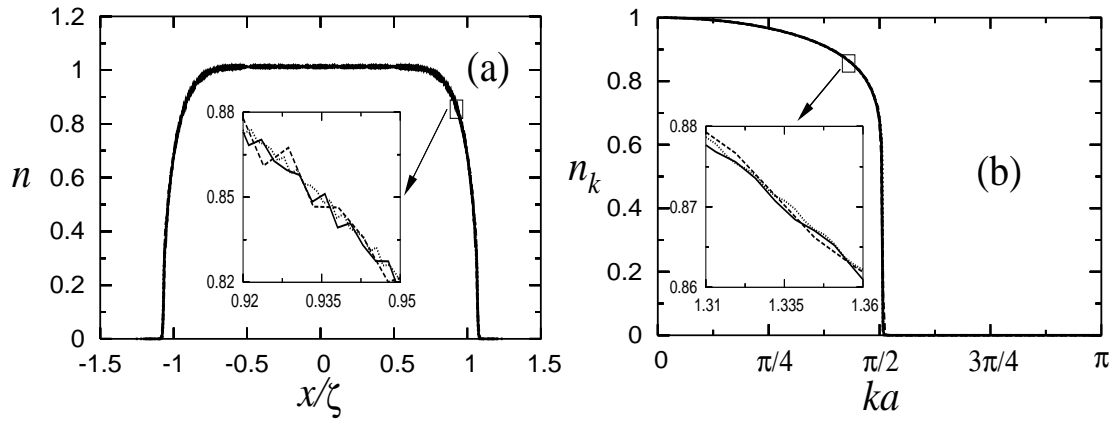


Figure 5.14: Exact results for noninteracting trapped fermions in a confining potential  $V_{10}$ . (a) Density profiles, (b) normalized momentum distribution function. Dashed line corresponds to  $V_{10}a^{10} = 6 \times 10^{-24}t$ ,  $N_f = 428$  ( $N \sim 500$ ), continuous line corresponds to  $V_{10}a^{10} = 7 \times 10^{-27}t$ ,  $N_f = 840$  ( $N \sim 1000$ ) and dotted line corresponds to  $V_{10}a^{10} = 1 \times 10^{-29}t$ ,  $N_f = 1620$  ( $N \sim 2000$ ). In the density profiles the positions are given in units of the characteristic length  $\zeta$ .

In general, it is expected that on increasing the system size, the situation in the periodic system is approached. However, in the present case it is not merely a question of boundary conditions, but the whole system is inhomogeneous. Therefore, a proper scaling has to be defined in order to relate systems of different sizes. In the case of particles trapped in optical lattices when there is a confining potential with a power  $\alpha$  and strength ( $V_\alpha$ ), a characteristic length of the system ( $\zeta$ ) is given by  $\zeta = (V_\alpha/t)^{-1/\alpha}$ , so that a characteristic density ( $\tilde{\rho}$ ) can be defined as  $\tilde{\rho} = N_f a / \zeta$ . This characteristic density

is the one meaningful in the thermodynamic limit. As shown in Chap. 2 it has always the same value when the local insulators appear in the system. In Fig. 5.14 we show three systems in which the total number of particles and the curvature of the confining potential  $V_{10}$  were changed, keeping  $\tilde{\rho}$  constant. We measured the positions in the trap in units of the characteristic length  $\zeta$ . These systems have occupied regions ( $n > 0$ ) with very different sizes, of the order of 500 lattice sites for the dashed line, of the order of 1000 sites for the continuous line, and of the order of 2000 lattice sites for the dotted line. Fig. 5.14(a) shows that the density profiles scale perfectly when the curvature of the confining potential and the number of fermions are changed in the system, so that in order to show the changes in the density profile, we introduced an inset that expands a region around a density 0.85. In the case of the momentum distribution function [Fig. 5.14(b)], it is possible to see that this quantity also scales very well so that almost no changes occur in the momentum distribution function when the occupied system size is increased, implying that in the thermodynamic limit the behavior of  $n_k$  is different from the one in the periodic system. An expanded view of the region with  $n_k$  around 0.87 is introduced to better see the magnitude of the differences in this region.

## 5.5 Mean-field approximation

The mean-field (MF) approach has been very useful in the study of dilute bosonic gases confined in harmonic potentials [1]. This theory for the order parameter associated with the condensate of weakly interacting bosons for inhomogeneous systems takes the form of the Gross-Pitaevskii theory. When the bosonic condensate is loaded in an optical lattice, it is possible to go beyond the weakly interacting regime and reach the strongly correlated limit for which a superfluid-Mott-insulator transition occurs. Also in this limit a MF study was performed [14], and the results were compared with exact diagonalization results for very small systems, reporting a qualitatively good agreement between both methods [14].

In this section, we compare a MF approximation with QMC results for a 1-D system. It will be shown that the MF approach not only violates the Mermin-Wagner theorem, as expected, leading to long-range antiferromagnetic order in one dimension, but also introduces spurious structures in the density profiles. On the other hand, the MDF

obtained within MF for inhomogeneous systems are similar to the ones obtained using QMC simulations. In order to obtain the MF Hamiltonian, we rewrite the Hubbard Hamiltonian in Eq. (5.2) in the following form (up to a constant shift in the chemical potential):

$$\begin{aligned}
H = & -t \sum_{i,\sigma} (c_{i\sigma}^\dagger c_{i+1\sigma} + \text{H.c.}) + V \sum_{i,\sigma} x_i^2 \hat{n}_{i\sigma} \\
& + \frac{(1-\Lambda)}{2} [\langle \hat{n}_i \rangle \hat{n}_i - \langle \hat{n}_i \rangle^2 + \widehat{\delta}_{n_i}^2] - \frac{\Lambda}{2} [\langle \widehat{\mu}_i \rangle \widehat{\mu}_i - \langle \widehat{\mu}_i \rangle^2 + \widehat{\delta}_{\mu_i}^2], \quad (5.6)
\end{aligned}$$

where the density and the magnetization in each site are denoted by  $\hat{n}_i = \hat{n}_{i\uparrow} + \hat{n}_{i\downarrow}$  and  $\widehat{\mu}_i = \hat{n}_{i\uparrow} - \hat{n}_{i\downarrow}$ , respectively. The fluctuations of the density and magnetization are given by  $\widehat{\delta}_{n_i} = \hat{n}_i - \langle \hat{n}_i \rangle$  and  $\widehat{\delta}_{\mu_i} = \widehat{\mu}_i - \langle \widehat{\mu}_i \rangle$ , respectively, and  $\Lambda$  is an arbitrary parameter that was introduced in order to allow for the most general variation in parameter space. The following relations for fermionic operators were used:

$$\hat{n}_{i\uparrow} \hat{n}_{i\downarrow} = \frac{1}{2} \hat{n}_i^2 - \frac{1}{2} \hat{n}_i, \quad \hat{n}_{i\uparrow} \hat{n}_{i\downarrow} = -\frac{1}{2} \widehat{\mu}_i^2 + \frac{1}{2} \hat{n}_i. \quad (5.7)$$

Neglecting the terms containing the square of the density and magnetization fluctuations in Eq. (5.6), the following MF Hamiltonian

$$\begin{aligned}
H_{MF} = & -t \sum_{i,\sigma} (c_{i\sigma}^\dagger c_{i+1\sigma} + \text{H.c.}) + V \sum_{i,\sigma} x_i^2 \hat{n}_{i\sigma} \\
& + \frac{1}{2} [(1-\Lambda) \langle \hat{n}_i \rangle - \Lambda \langle \widehat{\mu}_i \rangle] \hat{n}_{i\uparrow} + \frac{1}{2} [(1-\Lambda) \langle \hat{n}_i \rangle + \Lambda \langle \widehat{\mu}_i \rangle] \hat{n}_{i\downarrow} \\
& - \frac{(1-\Lambda)}{2} \langle \hat{n}_i \rangle^2 + \frac{\Lambda}{2} \langle \widehat{\mu}_i \rangle^2 \quad (5.8)
\end{aligned}$$

is obtained. Due to the inhomogeneity of the trapped system, an unrestricted Hartree-Fock scheme<sup>3</sup> is used to determine the local densities  $\langle \hat{n}_i \rangle$  and local magnetic moments  $\langle \widehat{\mu}_i \rangle$ . Given a MF ground state  $|\Psi_{MF}\rangle$ , the minimum energy  $E = \langle \Psi_{MF} | H | \Psi_{MF} \rangle$  (not the MF one  $E_{MF} = \langle \Psi_{MF} | H_{MF} | \Psi_{MF} \rangle$ ) is reached when  $\Lambda = 0.5$ , so that all the results that follow were obtained for this value of  $\Lambda$ .

### 5.5.1 The periodic system

We first recall some of the discrepancies between MF approximations and the known valid facts for the 1D periodic system ( $V_2 = 0$ ) as follows.

---

<sup>3</sup>Local variables are allowed to change independently.

(i) At half filling it is known that the Hubbard model exhibits a Mott-insulating phase with a charge gap while the spin sector remains gapless, so that the density-density correlations decay exponentially and the spin-spin correlations decay as a power law [125]. Within the MF approximation, there is a band insulator in the system at half filling so that both the density-density and spin-spin correlations decay exponentially. The MF value of the charge gap is an overestimation of the real one, as can be seen in Fig. 5.15 where we present the MF results for the density-density correlations as function of the distance, together with the QMC results. The slopes of the curves are proportional to the charge gap and the MF slope is approximately twice the QMC one (the results were obtained for a system with 102 sites and  $U = 6t$ ). The correlation length of  $\chi$  is the inverse of these slopes. Finally, at half filling the MF theory leads to an antiferromagnetic

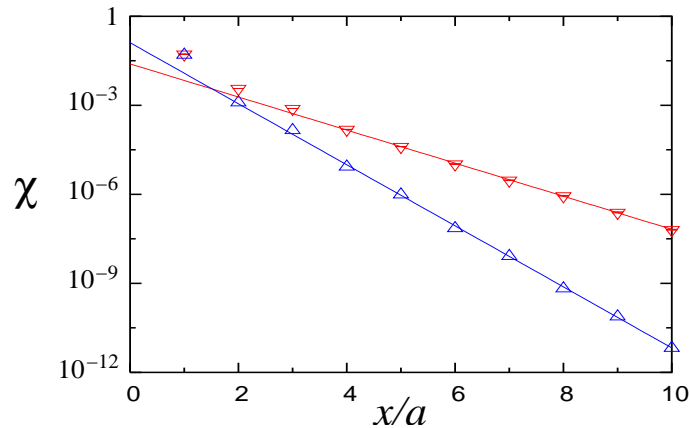


Figure 5.15: Density-density correlations for a periodic system with  $N = 102$  at half filling for  $U = 6t$ . MF ( $\Delta$ ) and QMC ( $\nabla$ ) solutions.

state, while in the Hubbard model the magnetization is always zero, although quasi-long-range antiferromagnetic correlations appear in the system. The comparison between the spin-spin correlations in both cases is shown in Fig. 5.16.

(ii) At any noncommensurate filling, the Hubbard model in 1D describes a metal (Luttinger liquid), so that no gap appears in the charge and spin excitations, and there is a  $2k_F$  modulation in the spin-spin correlation function that leads to the well-known  $2k_F$  singularity. Within the MF approximation, there is always a band insulator at any noncommensurate filling, with a gap that decreases when the system departs from half filling. The appearance of this gap for any density is due to the perfect nesting present in one dimension. The insulating nature of these solutions can be seen in the

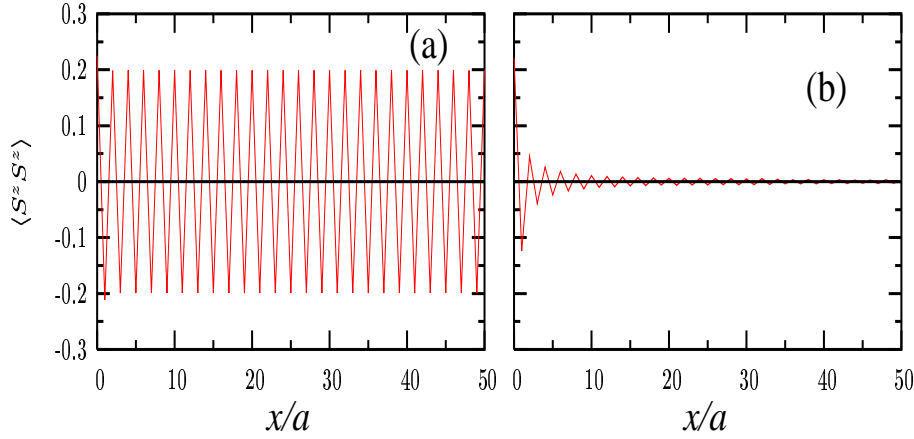


Figure 5.16: Spin-spin correlations for a periodic system with  $N = 102$  at half filling for  $U = 6t$ . MF (a) and QMC (b) solutions.

global compressibility of the system that is always zero, in the behavior of the density-density and the spin-spin correlations which decay exponentially, and in the momentum distribution function where there is no Fermi surface, as shown in Fig. 5.17 for  $N = 102$ ,  $N_f = 66$ , and  $U = 6t$ . Within this MF approach, there is a  $2k_F$  modulation of the

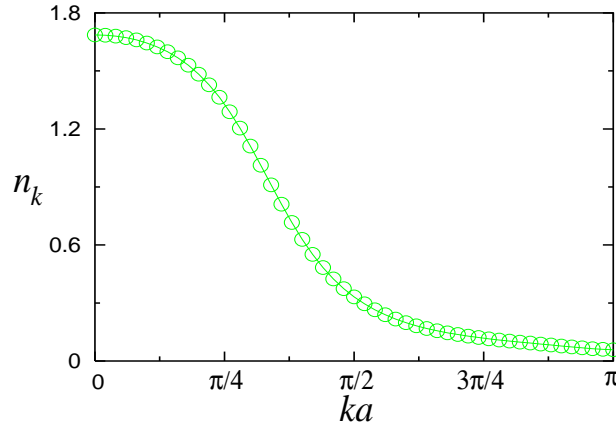


Figure 5.17: MF result for the momentum distribution function of a periodic system with  $N = 102$ ,  $N_f = 66$ , and  $U = 6t$ .

magnetization only in the  $z$  component [the  $SU(2)$  symmetry was broken], which leads to a divergence of the Fourier transform of  $\langle S^z S^z \rangle$  at  $k = 2k_F$ . In Fig. 5.18 we compare the MF result (a) for  $\langle S^z S^z \rangle_k$  with the QMC one (b), for  $N = 102$ ,  $N_f = 66$ , and  $U = 6t$ , where it can be seen that the  $2k_F$  peak is one order of magnitude bigger in the MF case compared to the QMC case. This is due to the existence of the magnetization in the MF solution (the values at the peaks will only diverge in the thermodynamic limit).



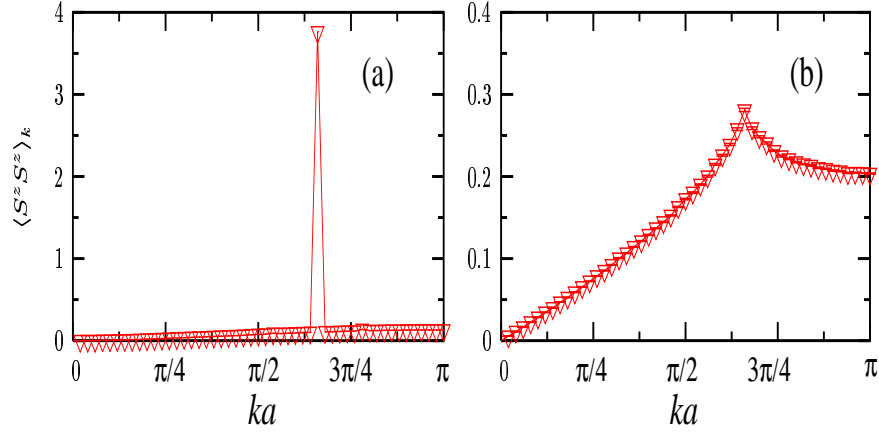


Figure 5.18: MF (a) and QMC (b) results for  $\langle S^z S^z \rangle_k$  in a periodic system with  $N = 102$ ,  $N_f = 66$ , and  $U = 6t$ .

### 5.5.2 The harmonic trap

We consider next the confined case. In Fig. 5.19(a), we show density profiles obtained for a trap with the same parameters of the one presented in Fig. 5.4, and for different values of the on-site repulsion [for more details see Figs. 5.21(e)-5.21(h)]. In the figure it can

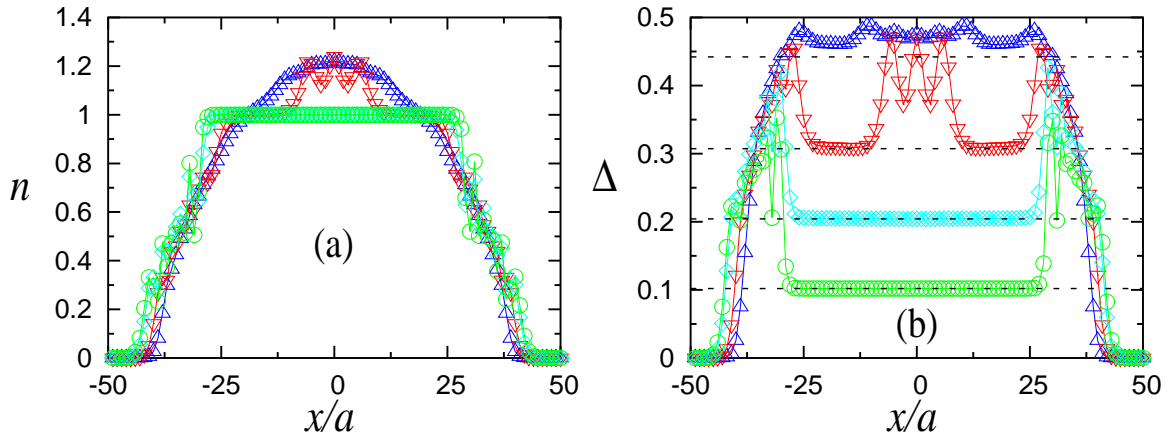


Figure 5.19: MF profiles for a trap with  $N = 100$ ,  $V_2 a^2 = 0.0025t$ , and  $N_f = 70$ , the on-site repulsions are  $U/t = 2$  ( $\triangle$ ),  $3$  ( $\nabla$ ),  $4$  ( $\diamond$ ), and  $6$  ( $\circ$ ). (a) Local density, (b) variance of the local density. The dashed lines in (b) are the MF values of the variance in the  $n = 1$  periodic system for  $U/t = 2, 3, 4, 6$  (from top to bottom).

be seen that the MF solutions also exhibit density profiles in which “metallic” ( $n \neq 1$ ) and insulating ( $n = 1$ ) phases coexist. The MF insulating plateaus with  $n = 1$  [ $U/t = 4$  in Fig. 5.19(a)] appear for smaller values of  $U$  than the ones required in the Hubbard model for the formation of the Mott-insulating plateaus [ $U/t = 6$  in Fig. 5.4(a)]. This

can be expected on the basis of the results presented for the periodic systems since MF overestimates the charge gap. We find that in the “metallic” phases density profiles show rapid spatial variations [Fig. 5.19(a)] that are not present in the QMC solutions. They are particularly large for  $n > 1$  [see  $U/t = 3$  Fig. 5.19(a), and Fig. 5.21(f)]. The variance profiles corresponding to parameters in Fig. 5.19(a), are presented in Fig. 5.19(b). They also reflect the large density variations observed in the “metallic” phases. The values of the variance on the  $n = 1$  plateaus are the same obtained in the periodic MF case for a given value of  $U$  at half filling [Fig. 5.19 (b)], like for the QMC solutions (Sec. 5.2).

Since the MF solution leads to an insulating state for incommensurate fillings in the periodic case, we analyze in the following more carefully the regions with  $n \neq 1$  in the presence of the trap. We find that the local compressibility always decays exponentially

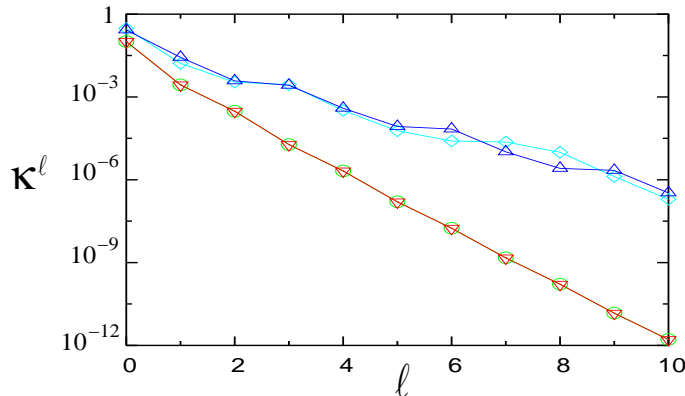


Figure 5.20: MF local compressibility as a function of  $\ell$  for the periodic and trapped ( $V_2a^2 = 0.0025t$ ,  $N_f = 70$ ) systems with  $U = 6t$ . ( $\nabla$ )  $n = 1$  periodic, ( $\circ$ )  $n_{i=0} = 1$  trapped, ( $\triangle$ )  $n \sim 0.66$  periodic, and ( $\diamond$ )  $n_{i=-30} \sim 0.66$  trapped.

as a function of  $\ell$  over the entire system, although the exponents are different depending on the density of the point analyzed. Some additional modulation appears in  $\kappa^\ell$  when  $n \neq 1$ , as shown in Fig. 5.20 where the local compressibility is displayed as a function of  $\ell$  for  $n = 1$  and  $n \sim 0.66$  in the trapped and periodic cases. Therefore, although the MF approximation leads to a density profile similar to the one obtained in QMC as long as  $n < 1$ , it gives a qualitative wrong description of the character of those regions.

The MF results for the normalized momentum distribution function are presented in Figs. 5.21(a)-5.21(d) with their corresponding density profiles [Figs. 5.21(e)-5.21(h)], for the same parameter values as in Fig. 5.19. The figure shows that normalized momentum profiles are similar to the ones obtained with QMC when the density profiles are similar,

so that the MF results are very similar to the QMC ones for this averaged quantity although the physical situation is very different. (Within MF there is always an insulator

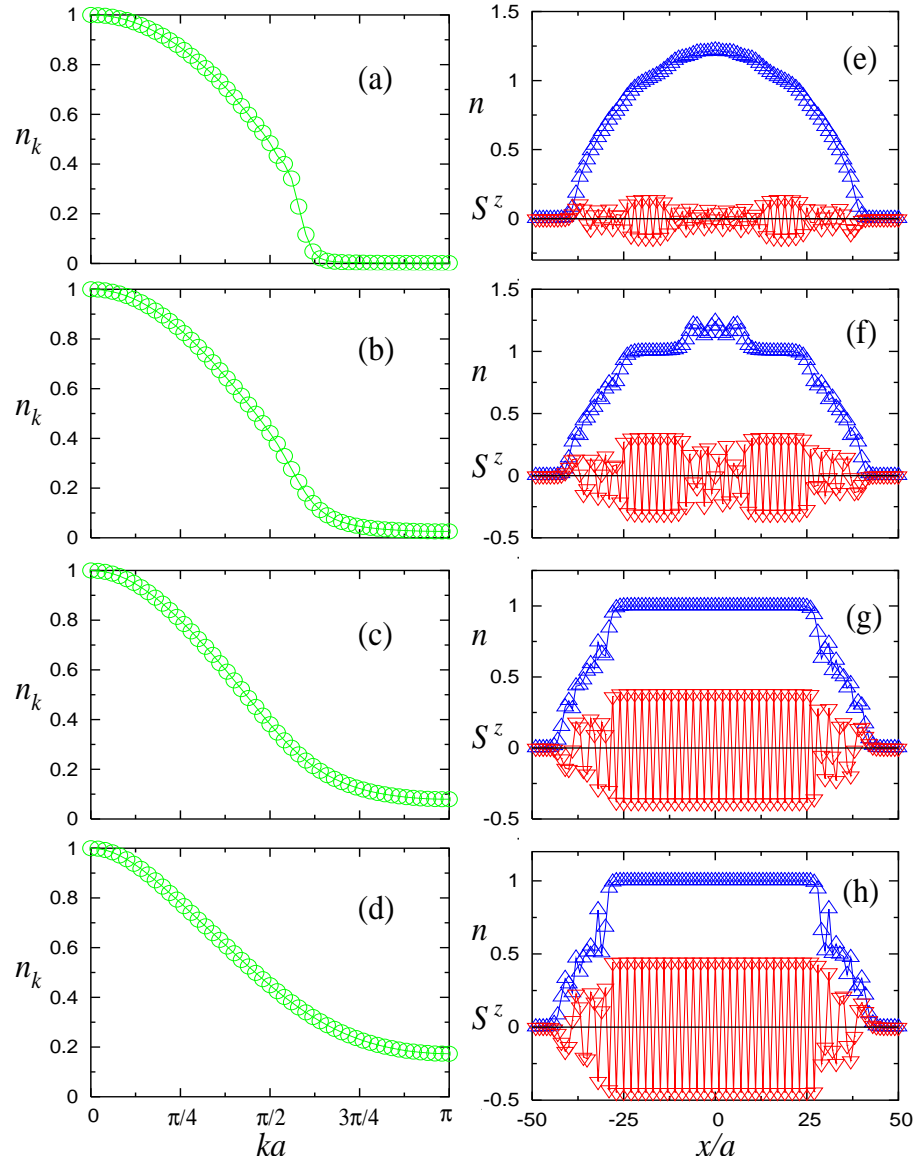


Figure 5.21: MF normalized momentum distribution function ( $\circ$ ) (a)-(d), and their corresponding density ( $\triangle$ ) and  $\langle S^z \rangle$  ( $\nabla$ ) profiles (e)-(h) for  $U/t = 2$  (a),(e), 3 (b),(f), 4 (c),(g), 6 (d),(h) and  $N = 100$ ,  $N_f = 70$ ,  $Va^2 = 0.0025t$ .

in the system and within QMC there are metallic and insulating phases coexisting.) In Figs. 5.21(e)-5.21(h), we also show the  $\langle S^z \rangle$  component of the spin on each site of the trap [ $S^z = (\hat{n}_{i\uparrow} - \hat{n}_{i\downarrow})/2$ ]. When the density is around  $n = 1$ , it can be seen that antiferromagnetic order appears, and that a different modulation exists for  $n \neq 1$ .

The presence of a finite magnetization in the MF solutions leads to long-range  $\langle S^z S^z \rangle$

order that is not present in the real solution of the Hubbard model, as it can be seen in Fig. 5.22 where we compare with the QMC results for metallic ( $n < 1$ ) [Fig. 5.22 MF (a), QMC (b)] and for insulating  $n = 1$  [Fig. 5.22 MF (c), QMC (d)] cases. As in Sec. 5.2, the spin correlations are measured with respect to the points in which it has its maximum value in the figure. In the metallic case [Fig. 5.22(a),(b)], we considered a MF and a QMC point with the same densities.

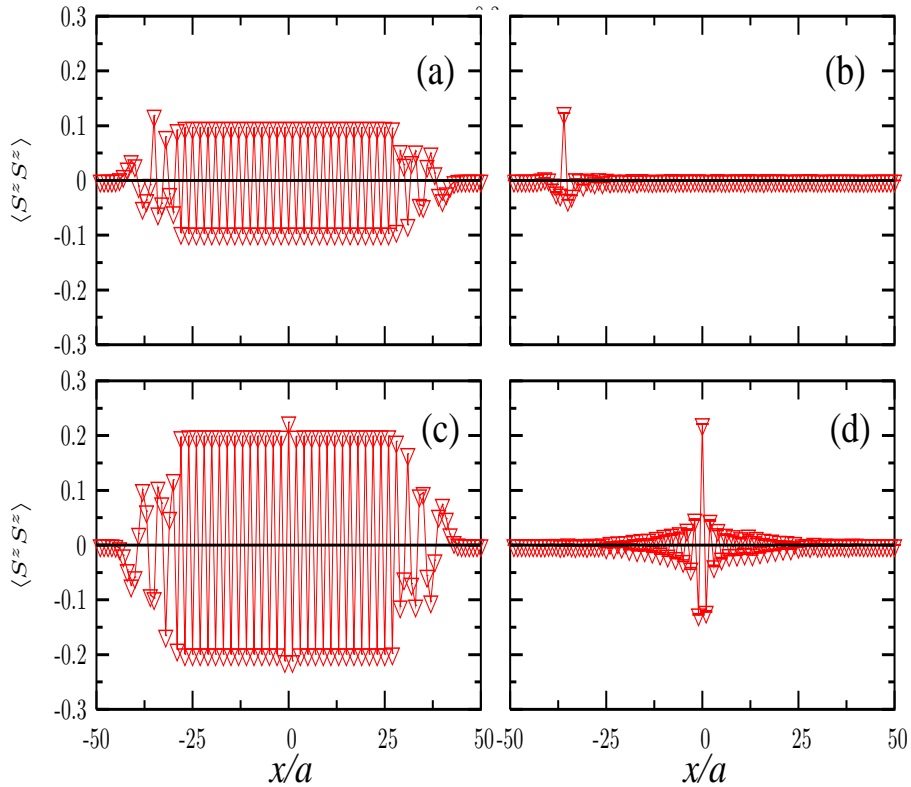


Figure 5.22: MF (a),(c) and QMC (b),(d) local spin-spin correlations in a trap. They were measured with respect to the points in which in the figure  $\langle S^z S^z \rangle$  has the maximum value. The densities at the points are  $n_{i=-35} \sim 0.51$  (a),  $n_{i=-36} \sim 0.51$  (b), and  $n_0 = 1$  (c), (d) for a trap with  $N = 100$ ,  $N_f = 70$ ,  $U = 6t$  and  $V_2 a^2 = 0.0025t$ .

Finally, we should mention that we have also found MF solutions for the trapped system where there was formation of spin domain walls in the insulating regions with  $n = 1$ , and there the variance was not constant. This case is illustrated in Fig. 5.23. Then, the formation of a plateau with  $n = 1$  does not mean that the MF solution is correct since a wrong underlying spin order could be obtained leading to wrong results for other quantities, like the variance for the case shown in Fig. 5.23.

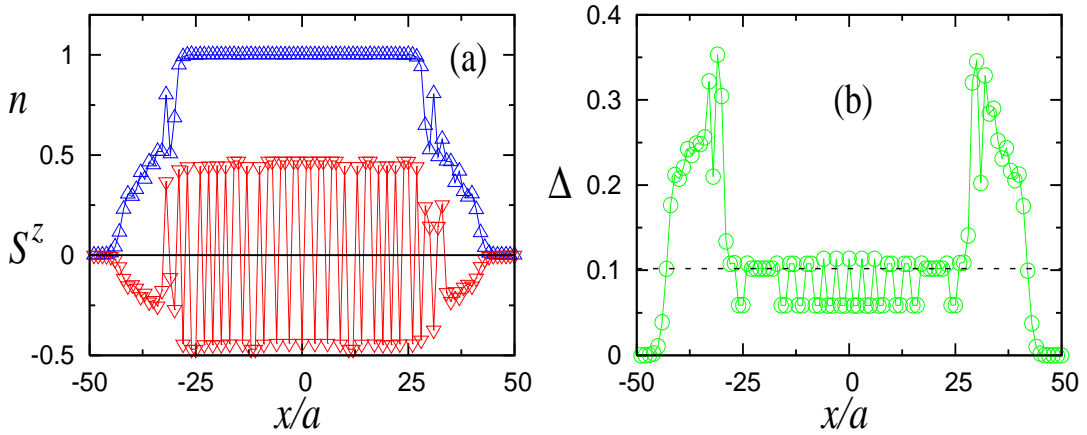


Figure 5.23: MF solution where spin domain walls were found, for a trap with  $N = 100$ ,  $V_2 a^2 = 0.0025t$ ,  $N_f = 70$ , and  $U/t = 6$ . (a) Local density ( $\triangle$ ), and  $\langle S^z \rangle$  ( $\nabla$ ) (b) Variance of the local density ( $\circ$ ). The dashed line in (b) shows the MF value of the variance in the  $n = 1$  periodic system for  $U/t = 6$ .

## 5.6 Phase Diagram

In the present section, we study using QMC simulations the phase diagram for fermions confined in harmonic traps with an underlying lattice.

As it can be inferred from Fig. 5.2, the phases present in the system are very sensitive to the values of the parameters in the model, i.e., to the curvature of the parabolic potential ( $V_2$ ), to the number of fermions present in the trap ( $N_f$ ) and to the strength of the on-site repulsion ( $U$ ). In order to be able to relate systems with different values of these parameters and different sizes, we use the characteristic density ( $\tilde{\rho}$ ) introduced in Chap. 2 for the definition of the phase diagram. This quantity was shown to be a meaningful quantity for the definition of a phase diagram for non-interacting fermions in Sec. 2.3. Furthermore, in Sec. 5.3 we have shown that density profiles (as function of  $x/\zeta$ ) and the normalized momentum distributions do not change when  $\tilde{\rho}$  is kept constant and the filling in the system (or the occupied system size) is increased. For a harmonic potential, the characteristic length is given by  $\zeta = (V_2/t)^{-1/2}$  and the characteristic density is then  $\tilde{\rho} = N_f a (V_2/t)^{1/2}$ . In Fig. 5.24 we show the phase diagrams of two systems with different strengths of the confining potential ( $V_2 a^2 = 0.006t$  and  $V_2 a^2 = 0.002t$ ) and different sizes ( $N = 100$  and  $N = 150$ , respectively). In the figure, the two phase diagrams are one on top of the other, within the errorbars, showing that the characteristic density

is the meaningful quantity in order to define a generic phase diagram. The latter allows to compare different systems, and hence to relate the results of numerical simulations with the ones of different experimental sizes.

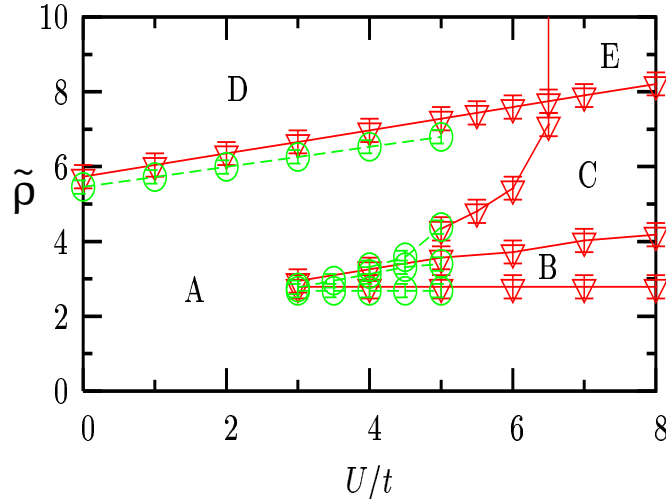


Figure 5.24: Phase diagram for systems with  $V_2a^2 = 0.006t$ ,  $N = 100$  ( $\nabla$ ) and  $V_2a^2 = 0.002t$ ,  $N = 150$  ( $\circ$ ). The different phases are explained in the text.

The phases present in the phase diagram in Fig. 5.24 can be described as follows: (A) a pure metal without insulating regions, (B) a Mott insulator in the middle of the trap always surrounded by a metal, (C) a metallic region with  $n > 1$  in the center of the Mott-insulating phase, that is surrounded by a metal with  $n < 1$ , (D) an insulator with  $n = 2$  in the middle of the trap surrounded only by a metallic phase, and finally (E) a “band insulator” in the middle of the trap surrounded by metal with  $n > 1$ , and these two phases inside a Mott insulator that as always is surrounded by a metal with  $n < 1$ .

There are some features that we find interesting in this phase diagram: (i) For all the values of  $U$  that we have simulated, we see that the lower boundary of phase B with the phase A has a constant value of the characteristic density. (ii) We have also seen that the upper boundary of phase B with phases A and C and the boundary of phases D and E with A and C, respectively, are linear within our errors. (iii) Finally, there is another characteristic of phase B, and of the metallic phase A that is below phase B, that we find intriguing and could be related to point (i). As can be seen in Fig. 5.4(a) for  $U/t = 6$  and 8, once the Mott-insulating phase is formed in the middle of the trap, a further increase of the on-site repulsion leave the density profile almost unchanged. (The two mentioned profiles are one on top of the other in that figure.) However, if we look at the variance

of these profiles it decreases with increasing  $U$ , which means that the double occupancy  $\langle n_{\uparrow}n_{\downarrow} \rangle = [\Delta - n(1 - n)]/2$  is decreasing in the system when  $U$  is increased, without a redistribution of the density. Less expected for us is that this also occurs for the metallic phase A that is below phase B. In Fig. 5.25(a) we show four density profiles and in Fig. 5.25(b) their variances, for a trap with  $V_2a^2 = 0.006t$  and  $N_f = 30$  when the on-site repulsion has values  $U/t = 2, 4, 6,$  and  $8$ . If we look at the phase diagram, the point with  $U/t = 2$  is not below phase B whereas the other three values are. In Fig. 5.25(a) we can see that as the value of  $U/t$  is increased from 2 to 4 there is a visible change in the density profile, but after a further increase the profile remains almost the same for the other values of  $U$ . The inset shows a magnification of the top of the profiles for a more detailed view. Fig. 5.25(b) shows that although the density stays almost constant for  $U/t = 4, 6,$  and  $8$ , the variance decreases. In the other phases (C, D, and E), an increase of the on-site repulsion always changes the local densities pushing particles to the edges of the trap.

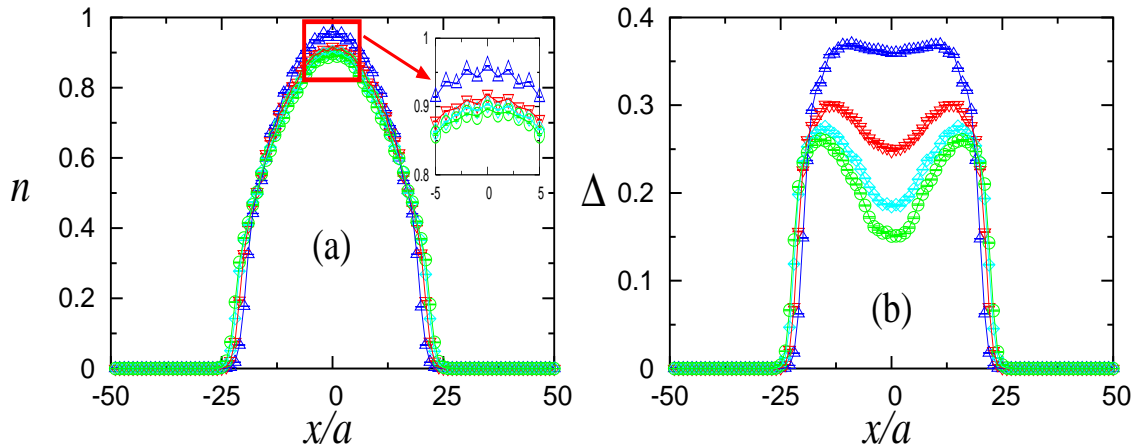


Figure 5.25: Profiles for a trap with  $V_2a^2 = 0.006t$  and  $N_f = 30$ , the on-site repulsions are  $U/t = 2$  ( $\triangle$ ),  $4$  ( $\nabla$ ),  $6$  ( $\diamond$ ), and  $8$  ( $\circ$ ). (a) Local density, (b) variance of the local density.

## 5.7 The quartic confining potential

Finally, in order to see, whether the features of the phase diagram discussed previously are particular of a harmonic confining potential, we have also performed an analogous study for a quartic confining potential. In Fig. 5.26 we show how the density profiles

evolve in a trap with a quartic confining potential ( $V_4 a^4 = 3 \times 10^{-6} t$ ) when the total filling is increased from  $N_f = 20$  to 140. It can be seen that the shape of the metallic regions is flatter than in the harmonic case. However, all the features discussed previously for the parabolic confining potential are also present in the quartic case. Local phases appear in the system, the Mott-insulating plateaus with  $n = 1$  have values of the variance equal to the ones in the periodic case for the same value of  $U$ , the local compressibility vanishes in the Mott-insulating regions and the spin and momentum distribution exhibit a behavior similar to that of the parabolic case.

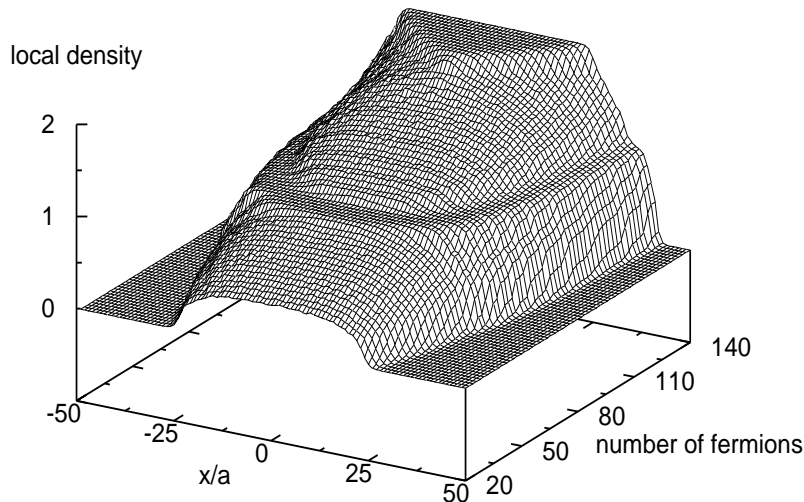


Figure 5.26: Evolution of the local density in a quartic confining potential as a function of the position in the trap and increasing total number of fermions. The parameters involved are  $N = 100$ ,  $U = 5t$ , and  $V_4 a^4 = 3 \times 10^{-6} t$ .

In addition, we also find that the form of the phase diagram for the quartic confining potential is similar to that of the harmonic trap. In Fig. 5.27 we show the phase diagram for a system with  $N = 100$  and  $V_4 a^4 = 3 \times 10^{-6} t$ , where the characteristic density is given by  $\tilde{\rho} = N_f a (V_4/t)^{1/4}$ . We have also calculated some points of the phase diagram for another system with  $V_4 a^4 = 10^{-6} t$  and  $N = 100$  in order to check that the scaling relation also works properly in this case. The phases are labeled in the same way as in Fig. 5.24, up to the largest value of  $U$  that we have studied we do not obtain the phase E which for the quartic confining case seems to be moved further towards the strong coupling regime. Hence, the form of the phase diagram in Fig. 5.24 seems to be of general applicability for any confining potential when the proper characteristic density is considered. However, we should mention that with increasing the power of the confining



potential, a decrease of the thickness of phase B is observed in the phase diagram. This means that it will be more difficult to observe it experimentally since the range of filling for which it appears reduces. In the extreme case, open boundary conditions, phase B only appears at half filling.

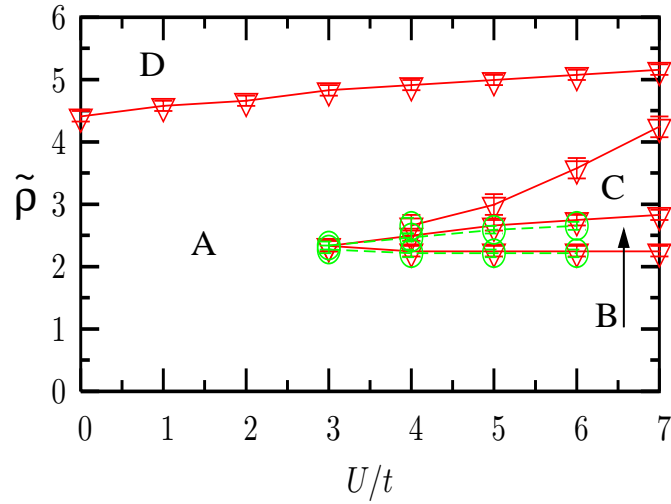


Figure 5.27: Phase diagram for systems with  $V_4 a^4 = 3 \times 10^{-6} t$ ,  $N = 100$  ( $\nabla$ ) and  $V_4 a^4 = 10^{-6} t$ ,  $N = 100$  ( $\circ$ ). The phases are labeled in the same way as in Fig. 5.24.



# Chapter 6

## Hard-core bosons on 1D lattices

We study the ground state properties of 1D trapped hard-core bosons (HCB) in the presence of a lattice. Experimentally, the introduction of an optical lattice opens new possibilities of engineering strongly interacting states [11], which otherwise are not available in dilute ultracold gases. In particular, for HCB it is possible to create pure Fock states when the occupation in some regions of the system reaches the value  $n = 1$ , such that coherence is lost there and these sites decouple from the rest of the system. The properties of continuous systems can be recovered in the low density limit in a lattice.

For the study of HCB in a 1D configuration, with an underlying lattice, we developed a new numerical approach. It is based on the Jordan-Wigner transformation, and allows the exact evaluation of physical observables and the analysis of arbitrary confining potentials [74]. The exposition is organized as follows: in Sec. 6.1, we introduce the numerical approach developed. Sec. 6.2 is devoted to the properties of HCB on periodic lattices. The harmonic confining potential is introduced in Sec. 6.3, and the results obtained are generalized for arbitrary powers of the confining potential in Sec. 6.4.

### 6.1 Exact approach to the ground state properties of hard-core bosons

In the present section we describe the exact approach we developed to study 1D HCB in the presence of a lattice. The HCB Hamiltonian can be written as

$$H = -t \sum_i \left( b_i^\dagger b_{i+1} + h.c. \right) + V_\alpha \sum_i x_i^\alpha n_i, \quad (6.1)$$

with the addition of the on-site constraints

$$b_i^{\dagger 2} = b_i^2 = 0, \quad \{b_i, b_i^\dagger\} = 1. \quad (6.2)$$

These constraints on the HCB creation ( $b_i^\dagger$ ) and annihilation ( $b_i$ ) operators avoid double occupancy. Notice that the brackets in Eq. (6.2) apply only to on-site anticommutation relation, while

$$[b_i, b_j^\dagger] = 0, \quad \text{for } i \neq j, \quad (6.3)$$

i.e. they commute on different sites. In Eq. (6.1), the hopping parameter is denoted by  $t$ , and the last term describes an arbitrary confining potential, with power  $\alpha$  and strength  $V_\alpha$ ;  $n_i = b_i^\dagger b_i$  is the particle number operator.

In order to obtain the ground state properties of HCB, we use the Jordan-Wigner transformation [130],

$$b_i^\dagger = f_i^\dagger \prod_{k=1}^{i-1} e^{-i\pi f_k^\dagger f_k}, \quad b_i = \prod_{k=1}^{i-1} e^{i\pi f_k^\dagger f_k} f_i, \quad (6.4)$$

which maps the HCB Hamiltonian into the non-interacting spinless fermion Hamiltonian

$$H = -t \sum_i \left( f_i^\dagger f_{i+1} + h.c. \right) + V_\alpha \sum_i x_i^\alpha n_i^f, \quad (6.5)$$

where  $f_i^\dagger$  and  $f_i$  are the creation and annihilation operators of spinless fermions and  $n_i^f = f_i^\dagger f_i$  is their particle number operator. This means that HCB and fermions have exactly the same spectrum. The non-trivial differences between both systems appear in the off-diagonal correlation functions as shown below.

Using the mapping above, the one-particle Green's function for the HCB can be written in the form

$$\begin{aligned} G_{ij} &= \langle \Psi_{HCB}^G | b_i b_j^\dagger | \Psi_{HCB}^G \rangle = \langle \Psi_F^G | \prod_{k=1}^{i-1} e^{i\pi f_k^\dagger f_k} f_i f_j^\dagger \prod_{l=1}^{j-1} e^{-i\pi f_l^\dagger f_l} | \Psi_F^G \rangle \\ &= \langle \Psi_F^A | \Psi_F^B \rangle, \end{aligned} \quad (6.6)$$

where  $|\Psi_{HCB}^G\rangle$  is the HCB ground state wave-function, and  $|\Psi_F^G\rangle$  is the equivalent non-interacting fermion ground state wave-function. In addition, we denote

$$\langle \Psi_F^A | = \left( f_i^\dagger \prod_{k=1}^{i-1} e^{-i\pi f_k^\dagger f_k} | \Psi_F^G \rangle \right)^\dagger, \quad | \Psi_F^B \rangle = f_j^\dagger \prod_{l=1}^{j-1} e^{-i\pi f_l^\dagger f_l} | \Psi_F^G \rangle. \quad (6.7)$$

The ground state wavefunction of the equivalent fermionic system can be obtained diagonalizing Eq. (6.5)<sup>1</sup>, and can be written in the form

$$|\Psi_F^G\rangle = \prod_{m=1}^{N_f} \sum_{n=1}^N P_{nm} f_n^\dagger |0\rangle, \quad (6.8)$$

with  $N_f$  the number of fermions ( $N_f = N_b$ ),  $N$  the number of lattice sites, and the matrix of the components  $\mathbf{P}$  is determined by the lowest  $N_f$  eigenfunctions of the Hamiltonian

$$\mathbf{P} = \begin{pmatrix} P_{11} & P_{12} & \cdot & \cdot & \cdot & P_{1N_f} \\ P_{21} & P_{22} & \cdot & \cdot & \cdot & P_{2N_f} \\ \cdot & \cdot & \cdot & \cdot & \cdot & \cdot \\ \cdot & \cdot & \cdot & \cdot & \cdot & \cdot \\ \cdot & \cdot & \cdot & \cdot & \cdot & \cdot \\ P_{N_1} & P_{N_2} & \cdot & \cdot & \cdot & P_{NN_f} \end{pmatrix} \quad (6.9)$$

In order to calculate  $|\Psi_F^A\rangle$  (and  $|\Psi_F^B\rangle$ ) we notice that

$$\prod_{k=1}^{i-1} e^{-i\pi f_k^\dagger f_k} = \prod_{k=1}^{i-1} [1 + (e^{-i\pi} - 1) f_k^\dagger f_k] = \prod_{k=1}^{i-1} [1 - 2 f_k^\dagger f_k]. \quad (6.10)$$

Then the action of  $\prod_{k=1}^{i-1} e^{-i\pi f_k^\dagger f_k}$  on the fermionic ground state [Eq. (6.8)] changes the sign of elements  $P_{nm}$  for  $n \leq i-1$ , and the further creation of a particle at site  $i$  implies the addition of one column to  $\mathbf{P}$  with the element  $P_{iN_f+1} = 1$  and all the others equal to zero (the same can be done for  $|\Psi_F^B\rangle$ ). Then  $|\Psi_F^A\rangle$  and  $|\Psi_F^B\rangle$  can be written as

$$|\Psi_F^A\rangle = \prod_{m=1}^{N_f+1} \sum_{n=1}^N P'_{nm} f_n^\dagger |0\rangle, \quad |\Psi_F^B\rangle = \prod_{m=1}^{N_f+1} \sum_{n=1}^N P'_{nm} f_n^\dagger |0\rangle, \quad (6.11)$$

where  $\mathbf{P}'^A$  and  $\mathbf{P}'^B$  are obtained from  $\mathbf{P}$  changing the required signs and adding the new column.

The Green's function  $G_{ij}$  is then calculated as

$$\begin{aligned} G_{ij} &= \langle 0 | \prod_{m=1}^{N_f+1} \sum_{n=1}^N P'_{nm} f_n \prod_{k=1}^{N_f+1} \sum_{l=1}^N P'_{lk} f_l^\dagger | 0 \rangle \\ &= \det \left[ \left( \mathbf{P}'^A \right)^\dagger \mathbf{P}'^B \right], \end{aligned} \quad (6.12)$$

where we followed the same steps of Eq. (3.28).

---

<sup>1</sup>The properties of such systems were analyzed in Chap. 2

The Green's function (6.12) is then evaluated numerically, and the one-particle density matrix is determined by the expression

$$\rho_{ij} = \langle b_i^\dagger b_j \rangle = G_{ij} + \delta_{ij} (1 - 2G_{ii}). \quad (6.13)$$

## 6.2 Hard-core bosons on periodic systems

In this section we analyze the properties of HCB in 1D periodic lattices. In this case the Hamiltonian (6.1) can be written as

$$H = -t \sum_i \left( b_i^\dagger b_{i+1} + h.c. \right). \quad (6.14)$$

This Hamiltonian, with the additional constraints (6.2), is particle-hole symmetric under the transformation  $h_i = b_i^\dagger$ ,  $h_i^\dagger = b_i$ . The operators  $h_i^\dagger$  and  $h_i$  are the creation and annihilation operator for holes, which satisfy the same commutation relations than HCB. Then HCB and holes have the same spectrum, and the number of HCB ( $N_b$ ) and holes ( $N_h$ ) satisfy the relation  $N_h = N - N_b$ . The previous symmetry has important consequences since it implies that the off-diagonal elements of the one-particle density matrix for  $N_b$  HCB [ $\rho_{ij}(N_b)$ ] and for  $N - N_b$  HCB [ $\rho_{ij}(N - N_b)$ ] are equal. Only the diagonal elements change, and they satisfy the relation  $\rho_{ii}(N_b) = 1 - \rho_{ii}(N - N_b)$ .

In the MDF ( $n_k$ ), the application of the particle-hole transformation leads to

$$\begin{aligned} n_k(N_b) &= \frac{1}{N} \sum_{ij=1}^N e^{-ik(i-j)} \langle b_i^\dagger b_j \rangle = \frac{1}{N} \sum_{ij=1}^N e^{-ik(i-j)} \left[ \langle h_j^\dagger h_i \rangle + \delta_{ij} \langle 1 - 2 h_i^\dagger h_i \rangle \right] \\ &= n_{-k}(N - N_b) + \left( 1 - \frac{N - N_b}{N/2} \right), \end{aligned} \quad (6.15)$$

so that a dependence on the density appears. This behavior is completely different to the one of non-interacting spinless fermions, where the Hamiltonian is also particle hole symmetric but under the transformation  $h'_i = (-1)^i f_i^\dagger$ ,  $h'_i = (-1)^i f_i$ . In this case the MDF for fermions [ $n_k^f(N_f)$ ] and [ $n_k^f(N - N_f)$ ] are related by the expression

$$\begin{aligned} n_k^f(N_f) &= \frac{1}{N} \sum_{ij=1}^N e^{-ik(i-j)} \langle f_i^\dagger f_j \rangle = \frac{1}{N} \sum_{ij=1}^N e^{-ik(i-j)} (-1)^{i-j} \left[ \delta_{ij} - \langle h_j^\dagger h'_i \rangle \right] \\ &= 1 - n_{-k+\pi}^f(N - N_f), \end{aligned} \quad (6.16)$$

where there is no dependence on the density.

In Fig. 6.1 we show the momentum profiles for systems with three different filling in 1000 lattice sites. Notice that we consider odd numbers of particles, which allows using periodic boundary conditions since the equivalent fermionic system has a close shell. (In the case of even number of particles antiperiodic boundary conditions are required.) The peak structure in the momentum distribution function (Fig. 6.1) reflects the bosonic nature of the particles, and is in contrast with the structure of the MDF for the equivalent non-interacting fermions shown in Chap. 2. On increasing the number of HCB two effects can be seen: (i) up to half filling the value of  $n_{k=0}$  increases, and it starts to decrease when the number of particles exceeds half filling (see also Fig. 6.3); (ii) the population of high momenta states is always increasing, showing that on increasing the density in the system HCB become more localized. The latter can be understood due to the impenetrability property of HCB and the 1D character of the system.

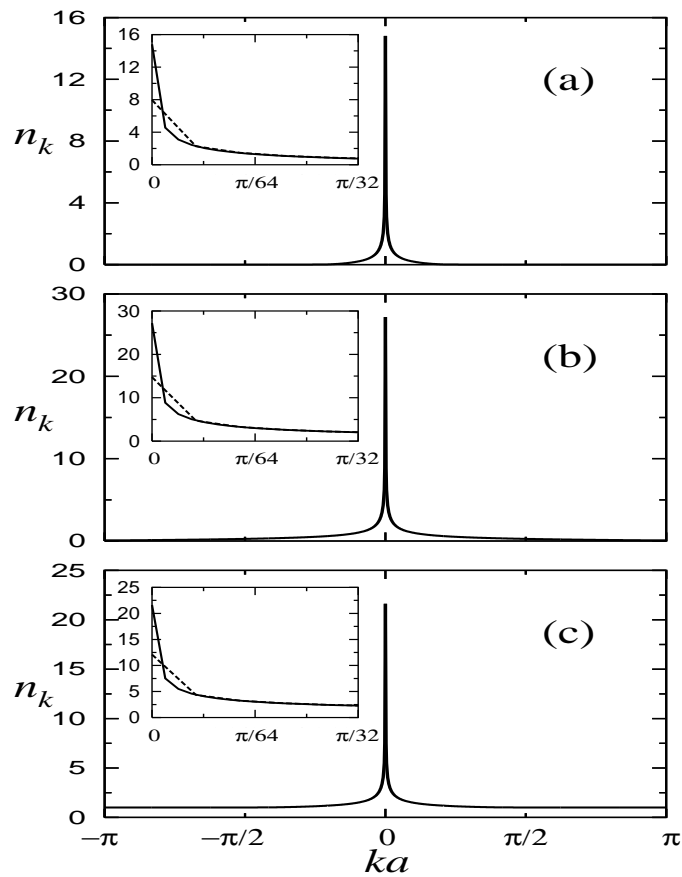


Figure 6.1: Momentum profiles for periodic systems with 1000 lattice sites and occupations of 101 (a), 501 (b) and 799 (c) HCB. The insets show the low momenta region for these systems (continuous line), and for systems with the same densities and 300 lattice sites (dashed line).

The insets in Fig. 6.1 show that an increase of the system size, keeping the density constant, modifies the very low momenta region of the MDF, as opposed to the equivalent fermionic case where the MDF remains constant when the density of the system does not change. This is due to the off-diagonal quasi-long range correlations present in the HCB one-particle density matrix. As it is shown in Fig. 6.2 they decay as  $\rho_x = A(\rho)/\sqrt{x/a}$  ( $x = |x_i - x_j|$ ).  $A(\rho)$  is a function of the density ( $\rho = N_b/N$ ) in the system. A trivial calculation shows that in the thermodynamic limit, keeping the density constant,  $n_{k=0}$  scales as

$$n_{k=0} = B(\rho)\sqrt{N_b} = C(\rho)\sqrt{N}. \quad (6.17)$$

where  $B(\rho)$  and  $C(\rho)$  are functions of the density. The previous result is valid to a good approximation for finite systems, as it can be seen in the inset in Fig. 6.2 where we plot  $n_{k=0}$  vs  $N_b$  for different systems at half filling. The straight line displays a  $\sqrt{N_b}$  behavior. The occupation of the high momenta states of the MDF is not affected by a change in the system size since short range correlations are not modified when the density is not changed (Fig. 6.2).

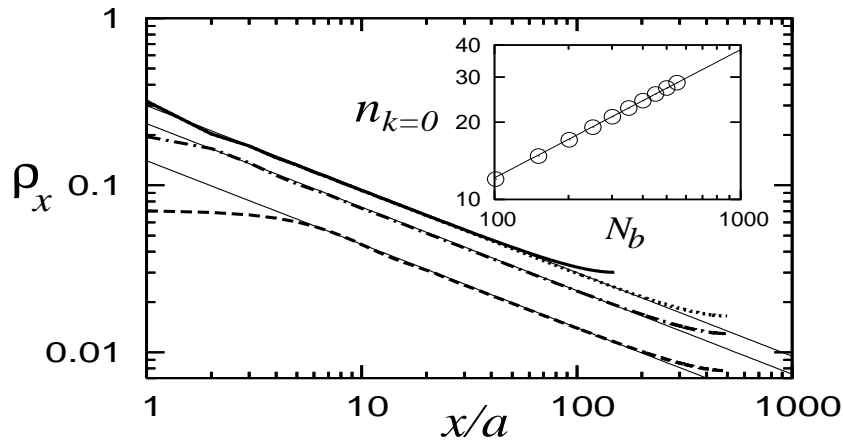


Figure 6.2: One-particle density matrix  $\rho_x$  vs  $x/a$  for periodic systems with  $N = 1000$  and:  $\rho = 0.5$  (dotted line),  $\rho = 0.211$  (dashed-dotted line),  $\rho = 0.071$  (dashed line), and for a system with  $N = 300$  and  $\rho = 0.5$  (thick continuous line). Thin continuous lines correspond to power-laws  $\sqrt{x/a}$ . The inset shows  $n_{k=0}$  vs  $N_b$  for systems at half filling ( $\circ$ ), the line exhibits  $\sqrt{N_b}$  behavior.

A global picture of the occupation of the state with zero momentum is shown in Fig. 6.3. There we plot  $n'_{k=0} = n_{k=0}/\sqrt{N}$  vs the density, and compare systems with 1000 and 300 lattice sites. The comparison shows that already for these system sizes the finite size



corrections are small. Actually, they were found to be given by

$$n_{k=0}/\sqrt{N} = C(\rho) - D(\rho)/\sqrt{N}, \quad (6.18)$$

where  $D(\rho)$  can be positive or negative depending on the density. The inset in Fig. 6.3 shows  $\delta n'_{k=0} = C(\rho) - n'_{k=0}$  vs  $N^{-1/2}$  for half filled systems. The straight line displays the result of our fit for  $C(\rho = 0.5)$  and  $D(\rho = 0.5)$ , and confirms the validity of Eq. (6.18). The same functional form of the finite size corrections was obtained for the continuous case [65], which corresponds to systems in a lattice where the average interparticle distance is much larger than the lattice constant, i.e. in the limit  $\rho = N_b/N \rightarrow 0$ .

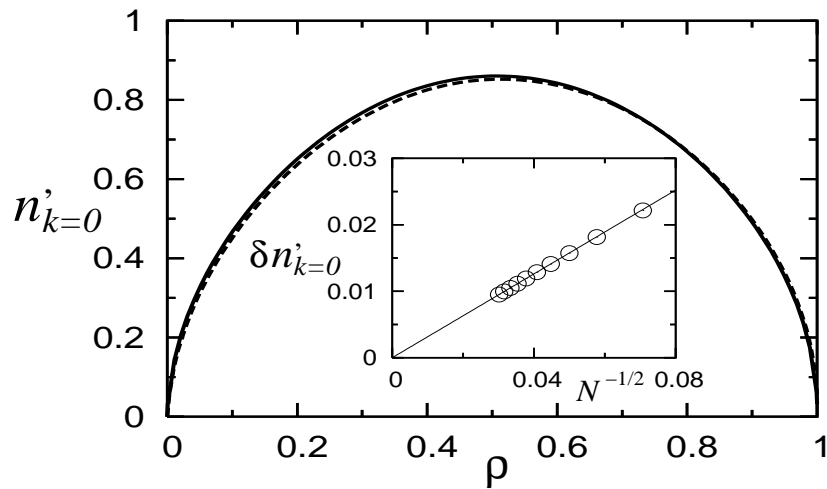


Figure 6.3: Normalized occupation of  $k = 0$  ( $n'_{k=0}$ ) as a function of the density in periodic systems with  $N = 1000$  (continuous line) and  $N = 300$  (dashed line). The inset displays  $\delta n'_{k=0}$  vs  $N^{-1/2}$  (see text) for half filled systems ( $\circ$ ), the straight line shows the result of our fit to Eq. (6.18).

In what follows we study the corrections introduced by the lattice to the occupation of the lowest momenta states in the continuous case. In a lattice at low momenta, the spectrum is quadratic in  $k$  and  $\delta k \sim 1/N$ , so that the ratio between the level spacing and the band width reduces proportionally to  $1/N^2$  when  $N$  is increased. Then we expect the low momenta occupations to approach their values in the continuous case as

$$\lambda_\eta(N_b, N) = \Lambda_\eta(N_b) - \frac{E_\eta(N_b)}{N^2}, \quad (6.19)$$

where  $\lambda_\eta(N_b, N) \equiv n_{k=2\pi\eta/N_a}(N_b)$  is the occupation of a momentum state  $\eta$  when there are  $N_b$  HCB in the system,  $\Lambda_\eta(N_b)$  is its occupation in the continuous case, and  $E_\eta(N_b)$  for a given  $\eta$  is a function of  $N_b$ .

We obtain  $\Lambda_\eta(N_b)$  and  $E_\eta(N_b)$  for the three lowest momenta states analyzing systems with fillings up to 501 particles and sizes up to 2000 lattice sites. In Fig. 6.4, we compare our results for  $\Lambda_\eta(N_b)$  with the ones in the continuous case presented in Ref. [65] [see Eqs. (56)-(58) there], the agreement is excellent. In the inset we plot  $\Delta\lambda = \Lambda_\eta(N_b) - \lambda_\eta(N_b, N)$  also for the three lowest momenta states as a function of  $1/N^2$ , the plots show that the scaling behavior proposed in Eq. (6.19) is correct.

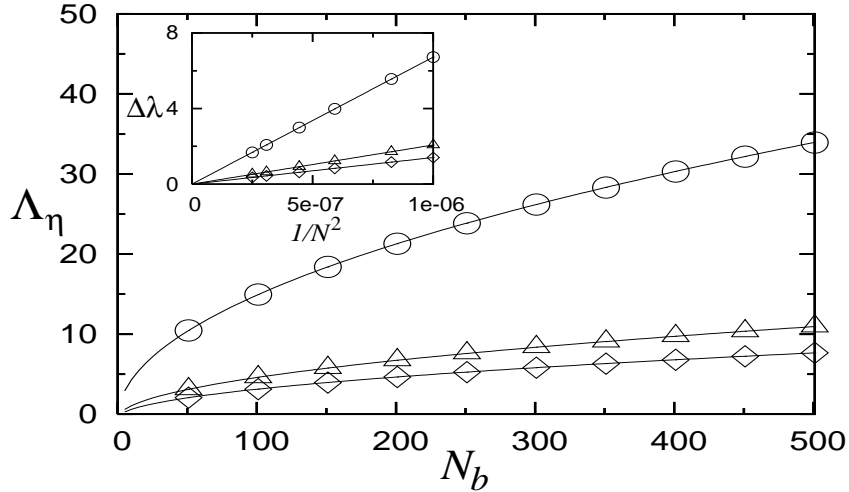


Figure 6.4: Extrapolated values of the first ( $\circ$ ), second ( $\triangle$ ), and third ( $\diamond$ ) momenta states occupations in the continuous case ( $\Lambda_\eta$ ). The lines following the data correspond to the results obtained in Ref. [65]. The inset shows  $\Delta\lambda$  (see text) vs  $1/N^2$  also for the first ( $\circ$ ), second ( $\triangle$ ), and third ( $\diamond$ ) momenta states in systems with 501 HCB and sizes between 1000 and 2000 lattice sites, the straight lines are the result of our fits.

Having shown that Eq. (6.19) is correct, the dependence of  $\Lambda_0(N_b)$  and  $E_0(N_b)$  on  $N_b$  can be determined given Eq. (6.17)

$$\Lambda_0(N_b) = b \sqrt{N_b}, \quad E_0(N_b) = c N_b^{2.5}. \quad (6.20)$$

where  $b$  and  $c$  are two constants that can be determined numerically. Both relations above were confirmed by our numerical results. Then Eq. (6.19) may be rewritten as

$$\lambda_0(N, \rho) / \sqrt{N} = \sqrt{\rho} (b - c \rho^2), \quad (6.21)$$

which allows to understand the behavior observed for  $n'_{k=0}$  vs  $\rho$  in Fig. 6.3. It is proportional to  $\sqrt{\rho}$  for low densities, and departs from this behavior (the one in the homogeneous case) as the density is increased. The latter is due to the  $(b - c \rho^2)$  factor.

## 6.3 Hard-core bosons confined in harmonic traps

We analyze in this section the case in which HCB are confined in harmonic traps. The Hamiltonian in this case is given by Eqs. (6.1) and (6.2) with  $\alpha = 2$ , and is not particle-hole symmetric like in the periodic case. In order to quantitatively characterize these systems we make use of the length scale set by the combination lattice-confining potential  $\zeta = (V_\alpha/t)^{-1/2}$ , and the associated characteristic density  $\tilde{\rho} = N_b/\zeta$ , both introduced in Chap. 2. Since the diagonal elements of the one-particle density matrix for HCB and the equivalent fermions are equal [see Eq. (6.6) for  $i = j$ ] the density properties of both systems coincide. We concentrate here in the quantities related to the off-diagonal correlations of the HCB, like the MDF and the NO.

The NO ( $\phi_i^\eta$ ) are defined as the eigenvalues of the one-particle density matrix [131],

$$\sum_{j=1}^N \rho_{ij} \phi_j^\eta = \lambda_\eta \phi_i^\eta, \quad (6.22)$$

and can be understood as being effective single particles states with occupations  $\lambda_\eta$ . The lowest NO (the highest occupied one) is considered to be the condensate. In the periodic case the NO are plane waves, so that the eigenvalues of Eq. (6.22) and the MDF coincide (the lowest NO is the state with momentum zero). In the trapped case the NO and the MDF do not coincide due to the presence of the confining potential, which breaks translational invariance.

In Fig. 6.5 we show three density profiles and their corresponding normalized MDF for traps with 1000 lattice sites. Positions are normalized by the characteristic length  $\zeta$ , and the normalized MDF is defined as  $n_k = a/\zeta \sum_{i,j=1}^N e^{-ik(i-j)} \langle b_i^\dagger b_j \rangle$ . Fig. 6.5 displays features similar to the periodic case. The normalized MDF exhibits narrow peaks at  $k = 0$  with  $n_{k=0}$  initially increasing with the number of particles, and decreasing after certain filling when more particles are added to the system. Localization effects also start to be evident at high fillings, with an increment of the population of high momenta states [Fig. 6.5(f)], and the formation of Fock states (or an insulating plateau) in the middle of the system [sites with  $n_i = 1$ , Fig. 6.5(c)]. In addition, the characteristic density plays in the trapped case a similar role to the one of the density in the periodic case. As it was shown for fermions (Chap. 5) density profiles are not modified when parameters of the system are changed keeping  $\tilde{\rho}$  constant. The insets in Fig. 6.5 show that for HCB only the

low momenta region of the normalized MDF is modified changing the trap parameters keeping  $\tilde{\rho}$  fixed.

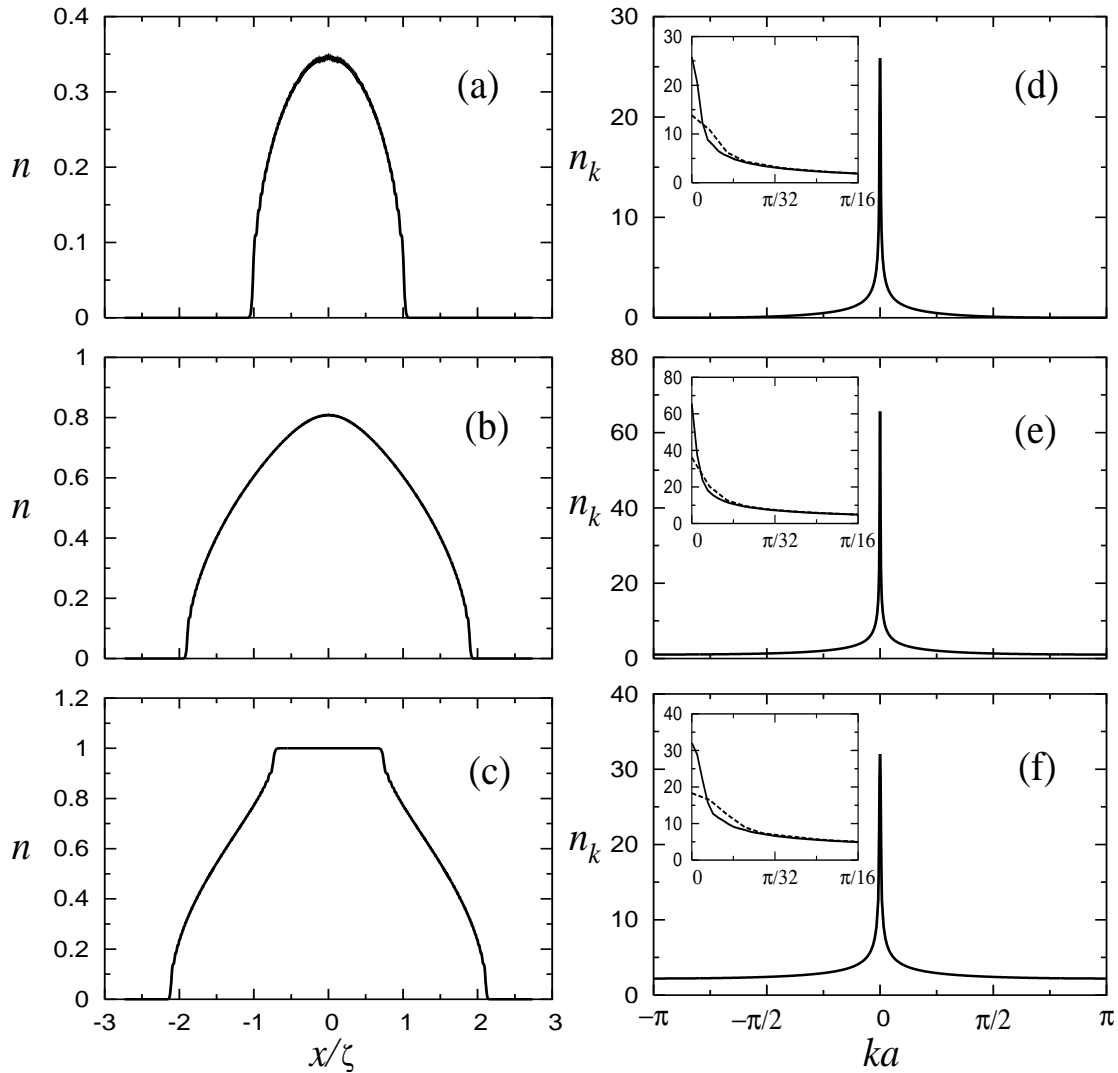


Figure 6.5: Density (a)-(c) and normalized MDF (d)-(f) for trapped systems with 1000 lattice sites,  $V_2 a^2 = 3 \times 10^{-5} t$  and occupations of 101 (a,d), 401 (b,e), and 551 (c,f) HCB. The insets in (d)-(f) show the low momenta results for the previous systems (continuous line); and for systems with 300 lattice sites,  $V_2 a^2 = 3.3 \times 10^{-4} t$  and the same characteristic densities (dashed line).

Results obtained for the occupations of the NO, in the systems of Fig. 6.5, are presented in Fig. 6.6. The occupations are plotted as a function of the orbital numbers  $\eta$ , and they were ordered starting from the highest one. The effects of increasing the filling in the system are similar to the ones observed in the MDF. The occupation of the lowest NO increases with increasing the number of particles up to certain filling where

it starts to decrease when more particles are added. In contrast to the MDF, the NO occupations exhibit clear signatures of the formation of the insulating state in the middle of the system since a plateau with  $\lambda = 1$  appears [Fig. 6.6(c)], and the NO with  $\lambda \neq 1$  become pairwise degenerated [inset in Fig. 6.6(c)]. This can be easily understood since in the region where  $n_i = 1$ , the one-particle density matrix is diagonal  $\rho_{ij} = \delta_{ij}$ , so that the one-particle density matrix can be seen as a three block diagonal matrix with the block in the middle being an identity matrix and the other two being identical. Thus, the diagonalization gives a group of eigenvalues  $\lambda_\eta = 1$  and all the other pairwise degenerate.

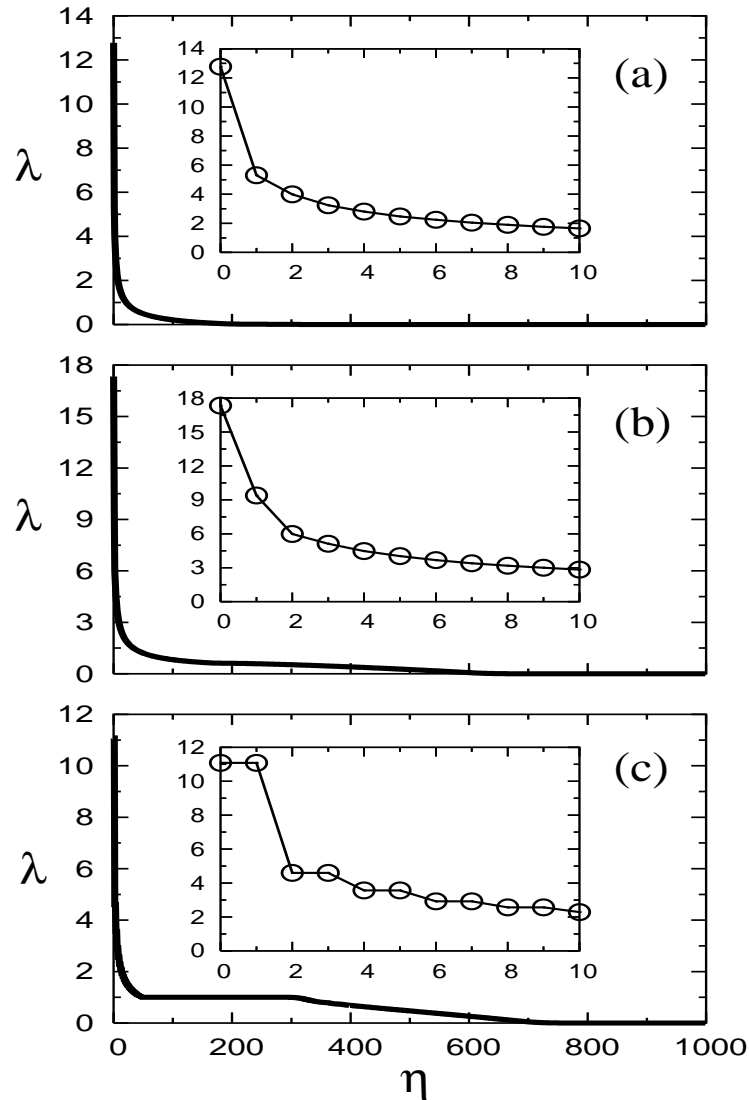


Figure 6.6: Occupation of the natural orbitals for trapped systems with 1000 lattice sites,  $V_2 a^2 = 3 \times 10^{-5} t$  and occupations of 101 (a), 401 (b) and 551 (c) HCB. The insets show the occupation of the lowest eleventh natural orbitals in each case.

Profiles of the two lowest NO, for the same parameters of Figs. 6.5 and 6.6, are presented in Fig. 6.7. The positions in the trap are also normalized by  $\zeta$  and the proper definition of the scaled NO is given by

$$\varphi^n = R^{1/2} \phi^n, \quad R = (N_b \zeta / a)^{1/2}. \quad (6.23)$$

This scaling relation is valid only for the lowest natural orbitals and is meaningful for comparing systems with the same characteristic density. Notice that for a given  $\tilde{\rho}$  the occupied system size ( $L$ ) is proportional to  $\zeta$ , i.e  $L = F(\tilde{\rho})\zeta$  with  $F(\tilde{\rho})$  depending only on the value of  $\tilde{\rho}$ . In Fig. 6.7 we have also plotted results for smaller systems (dashed line)

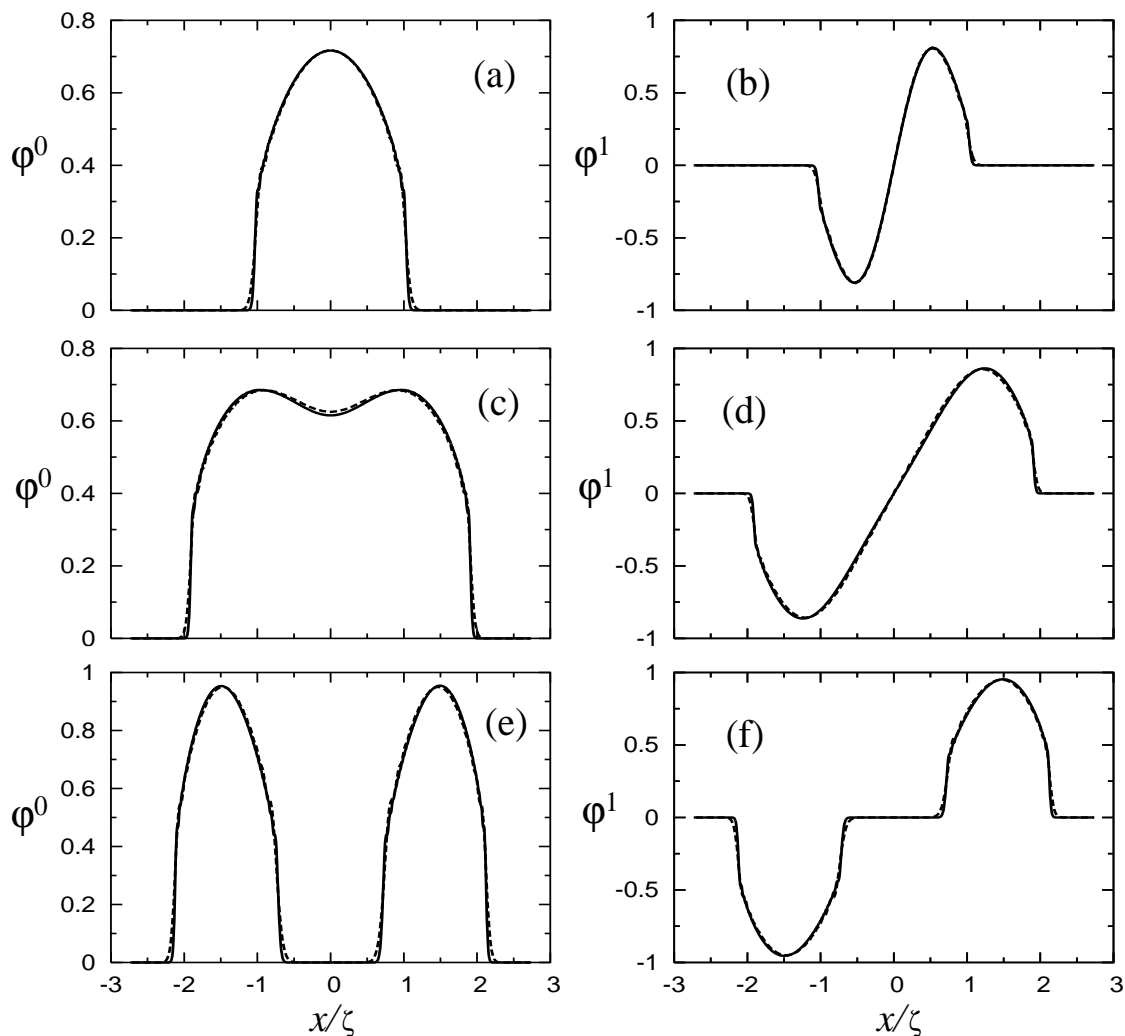


Figure 6.7: Profiles of the two lowest natural orbitals for trapped systems with: 1000 lattice sites,  $V_2 a^2 = 3 \times 10^{-5} t$  and occupations of 101 (a),(b), 401 (c),(d) and 551 (e),(f) HCB (continuous line); 300 lattice sites,  $V_2 a^2 = 3.3 \times 10^{-4} t$  and occupations of 30 (a),(b), 121 (c),(d) and 167 (e),(f) HCB (dashed line).

but fulfilling the condition of equal characteristic density. The comparison between the plots show that the scaling relation defined holds for systems larger than 100 lattice sites. In Figs. 6.7(a),(b) it can be seen that for low characteristic densities the NO are similar to the ones of systems without the optical lattice [64,65]. On increasing the characteristic density the shape of the lowest NO starts to change since its weight starts to reduce in the middle of the trap, as shown in Fig. 6.7(c). Once the insulating plateau appears in the center of the system degeneracy sets in for the lowest NO [inset in Fig. 6.6(c)], and their weight in the region with  $n = 1$  vanishes [Figs. 6.7(e),(f)].

The peaks appearing in the MDF at  $k = 0$ , and the high occupation of the lowest NO are consequences of the off-diagonal quasi-long range correlations present in the one-particle density matrix. We find that they decay as power-laws  $\rho_{ij} \sim A_2(\tilde{\rho})|x/a|^{-1/2}$  ( $x = |x_i - x_j|$ ) for large- $x$  away from  $n_i, n_j = 0, 1$ , i.e. *independently* of the local changes of the density [ $A_2(\tilde{\rho})$  depends on the characteristic density  $\tilde{\rho}$ ]. In Fig. 6.8 we show results obtained for a very dilute case, and for a system with an insulator in the middle of the trap. We plot  $\rho_{ij}$  vs  $|x_i - x_j|$  for points  $i$  with different densities to show that the local changes of the density, away from the regions with  $n_i, n_j = 0, 1$  do not change the observed power-law behavior.

Considering the previous results for the power-law decay of the one-particle density matrix and for the scaling of the lowest NO, it is possible to calculate how the lowest NO occupation will scale in the thermodynamic limit ( $\lambda_0 = \sum_{ij} \phi_i^0 \rho_{ij} \phi_j^0$ ) defined by a constant characteristic density. Replacing the sums in  $\lambda_0$  by integrals ( $L \gg a$ )

$$\begin{aligned} \lambda_0 &\sim 1/a^2 \int_{-L}^L dx \int_{-L}^L dy \frac{\phi^0(x) A_2(\tilde{\rho}) \phi^0(y)}{|(x-y)/a|^{1/2}} \\ &= (\zeta/a)^{3/2} R^{-1} \int_{-F(\tilde{\rho})}^{F(\tilde{\rho})} dX \int_{-F(\tilde{\rho})}^{F(\tilde{\rho})} dY \frac{\varphi^0(X) A_2(\tilde{\rho}) \varphi^0(Y)}{|X-Y|^{1/2}} \\ &= B_2(\tilde{\rho}) \sqrt{N_b} = C_2(\tilde{\rho}) \sqrt{\zeta/a}, \end{aligned} \quad (6.24)$$

where we did the change of variables  $x = X\zeta$ ,  $y = Y\zeta$ , and  $\phi^0 = R^{-1/2}\varphi^0$ . The integral over  $X, Y$  depends only on the characteristic density, so that  $B_2(\tilde{\rho})$  and  $C_2(\tilde{\rho})$  will also depend only on  $\tilde{\rho}$ . The previous results show that with the properly defined characteristic density, the occupation of the lowest natural orbital scales like in the homogeneous case, proportionally to  $\sqrt{N_b}$ . In addition, Eq. (6.24) is valid to a good approximation for finite systems, as it can be seen in the inset in Fig. 6.8 where we plot  $\lambda_0$  vs  $N_b$  for different

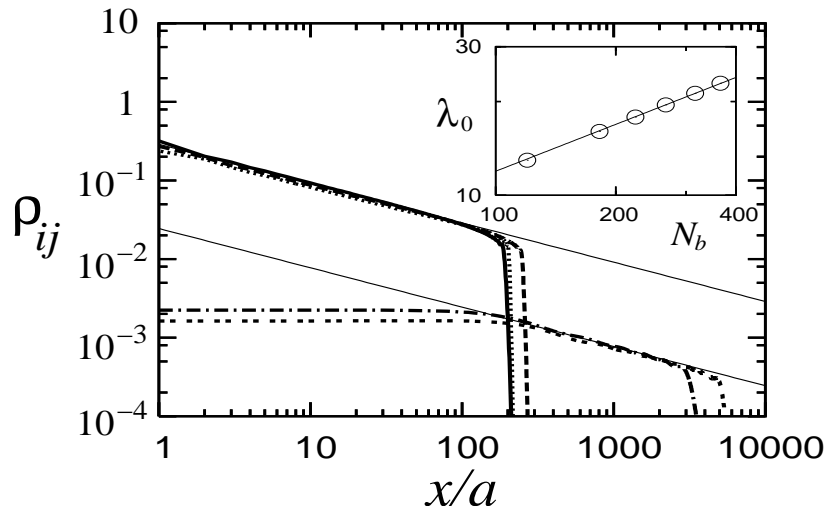


Figure 6.8: One-particle density matrix vs  $x/a$  ( $x = |x_i - x_j|$ ) for trapped HCB with:  $V_2 a^2 = 3.0 \times 10^{-5} t$ ,  $N_b = 501$  (an insulator is formed), measured from  $n_{i=171} = 0.32$  (dashed line),  $n_{i=231} = 0.5$  (thick continuous line),  $n_{i=331} = 0.73$  (dotted line); and for a very dilute system with  $V_2 a^2 = 5.0 \times 10^{-12} t$ ,  $N_b = 11$ , measured from  $n_{i=2901} = 1.6 \times 10^{-3}$  (dashed-dotted line),  $n_{i=4901} = 2.2 \times 10^{-3}$  (double-dotted line). The abrupt reduction of  $\rho_{ij}$  occurs for  $n_j \rightarrow 0, 1$ . Thin continuous lines correspond to power-laws  $\sqrt{x/a}$ . The inset shows  $\lambda_0$  vs  $N_b$  for systems with  $\tilde{\rho} = 1.0$  ( $\circ$ ), the straight line exhibits  $\sqrt{N_b}$  behavior.

systems with characteristic density  $\tilde{\rho} = 1$ , the straight line displays a  $\sqrt{N_b}$  behavior.

A global picture of the occupation of the two lowest NO is shown in Fig. 6.9. There we plot  $\lambda' = \lambda/\sqrt{\zeta/a}$  vs  $\tilde{\rho}$ , and compare systems with different curvatures of the confining potential. The insulator forms in the middle of the trap when the degeneracy appears in the NO. The comparison between the plots shows that already for these system sizes (larger than 100 lattice sites) the finite size corrections are small. They were found to be determined by the expression

$$\lambda_0/\sqrt{\zeta/a} = C_2(\tilde{\rho}) - D_2(\tilde{\rho})/\sqrt{\zeta/a}, \quad (6.25)$$

with  $D_2(\tilde{\rho})$  being a function of the characteristic density. Eq. (6.25) has the same form than Eq. (6.18), for the homogeneous case, when  $N$  is substituted by  $\zeta/a$ . In the inset in Fig. 6.3 we plot  $\delta\lambda'_0 = C_2(\tilde{\rho}) - \lambda'_0$  vs  $N^{-1/2}$  for systems with  $\tilde{\rho} = 1$ . The straight line displays the result of our fit for  $C_2(\tilde{\rho} = 1)$  and  $D_2(\tilde{\rho} = 1)$ , and confirms the validity of Eq. (6.25). In the case without the lattice [65], the same functional form was obtained for the finite size corrections in terms of the number of HCB in harmonic traps.



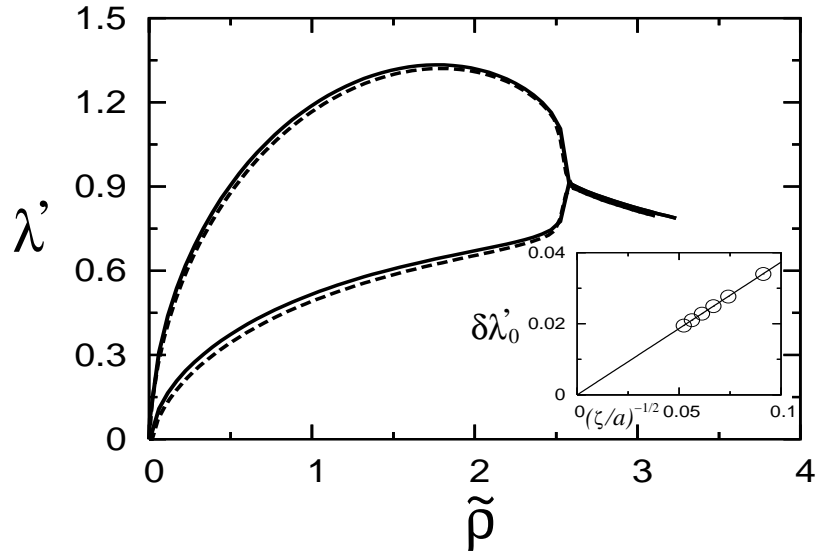


Figure 6.9: Normalized occupation of the two lowest NO (see text) vs  $\tilde{\rho}$ . The systems analyzed have  $N = 1000$ ,  $V_2 a^2 = 3 \times 10^{-5} t$  and occupations up to 600 particles (continuous line), and  $N = 300$ ,  $V_2 a^2 = 3.3 \times 10^{-4} t$  and occupations up to 270 particles (dashed line). The inset displays  $\delta\lambda'_0$  vs  $N^{-1/2}$  (see text) for traps with  $\tilde{\rho} = 1$  ( $\circ$ ), the straight line shows the result of our fit to Eq. (6.25).

Finally, we are interested in studying the corrections introduced by the lattice to the occupation of the lowest natural orbitals in the confined continuous case. Due to the combination lattice-harmonic potential the ratio between the level spacing and the band width in the low energy region is proportional to  $(\zeta/a)^{-1}$ , so that we expect the occupation of the lowest natural orbitals to approach their value in the continuous system  $\Lambda_\eta(N_b)$  as

$$\lambda_\eta(N_b, \zeta/a) = \Lambda_\eta(N_b) - \frac{E_\eta^2(N_b)}{\zeta/a}. \quad (6.26)$$

We calculate  $\Lambda_\eta(N_b)$  and  $E_\eta^2(N_b)$  for the three lowest NO analyzing systems with fillings up to 401 particles and sizes up to 2000 lattice sites. In Fig. 6.10 we compare our results for  $\Lambda_\eta(N_b)$  with the ones presented in Ref. [65] for the continuous case [see Eqs. (91)-(92) there], the agreement is excellent like in the periodic case. As an inset we plot  $\Delta\lambda = \Lambda_\eta(N_b) - \lambda_\eta(N_b, \zeta/a)$  also for the three lowest NO as a function of  $(\zeta/a)^{-1}$ . The plot shows that the scaling behavior proposed in Eq. (6.26) is correct. The results obtained for  $\Delta\lambda$  for the second and third NO are very similar, so that in the inset are one on top of the other.

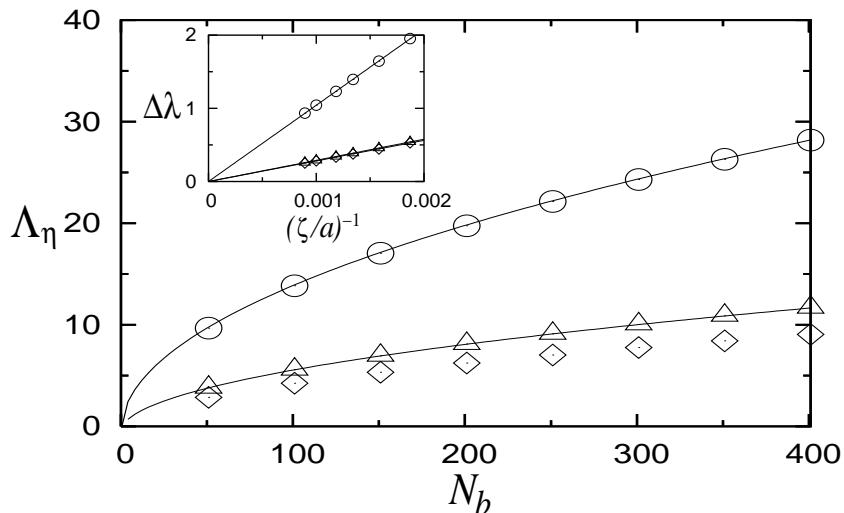


Figure 6.10: Extrapolated values of the first ( $\circ$ ), second ( $\triangle$ ), and third ( $\diamond$ ) NO occupations in the continuous system ( $\Lambda_0$ ). The lines following the data for the first two NO correspond to the results obtained in Ref. [65]. The inset shows  $\Delta\lambda$  (see text) as a function of  $(\zeta/a)^{-1}$  also for the first ( $\circ$ ), second ( $\triangle$ ), and third ( $\diamond$ ) NO in systems with 301 HCB and sizes between 1000 and 2000 lattice sites, the straight lines are the result of our fits.

Comparing Eqs. (6.26) and (6.24), it is possible to determine the dependence of  $\Lambda_0(N_b)$  [65] and  $E_0^2(N_b)$  on  $N_b$

$$\Lambda_\eta(N_b) = b_2 \sqrt{N_b}, \quad E_\eta^2(N_b) = c_2 N_b^{1.5}, \quad (6.27)$$

where  $b_2, c_2$  are parameters that can be determined numerically. Both relations above were confirmed by our numerical results. Then Eq. (6.26) may be rewritten as

$$\lambda_0(N_b, \tilde{\rho}) / \sqrt{\zeta/a} = \sqrt{\tilde{\rho}} (b_2 - c_2 \tilde{\rho}), \quad (6.28)$$

which also allows to understand the behavior observed in Fig. 6.9.

## 6.4 Hard-core bosons trapped in other confining potentials

The results obtained in the previous section for HCB confined in harmonic traps can be generalized for arbitrary powers of the confining potential when the appropriate length

scale

$$\zeta = (V_\alpha/t)^{-1/\alpha}, \quad (6.29)$$

is considered. [ $\alpha$  is the power of the confining potential in Eq. (6.1)]. In this section, we will systematically make the generalization for a power  $\alpha = 8$  of the confining potential in order to show that the statement above holds.

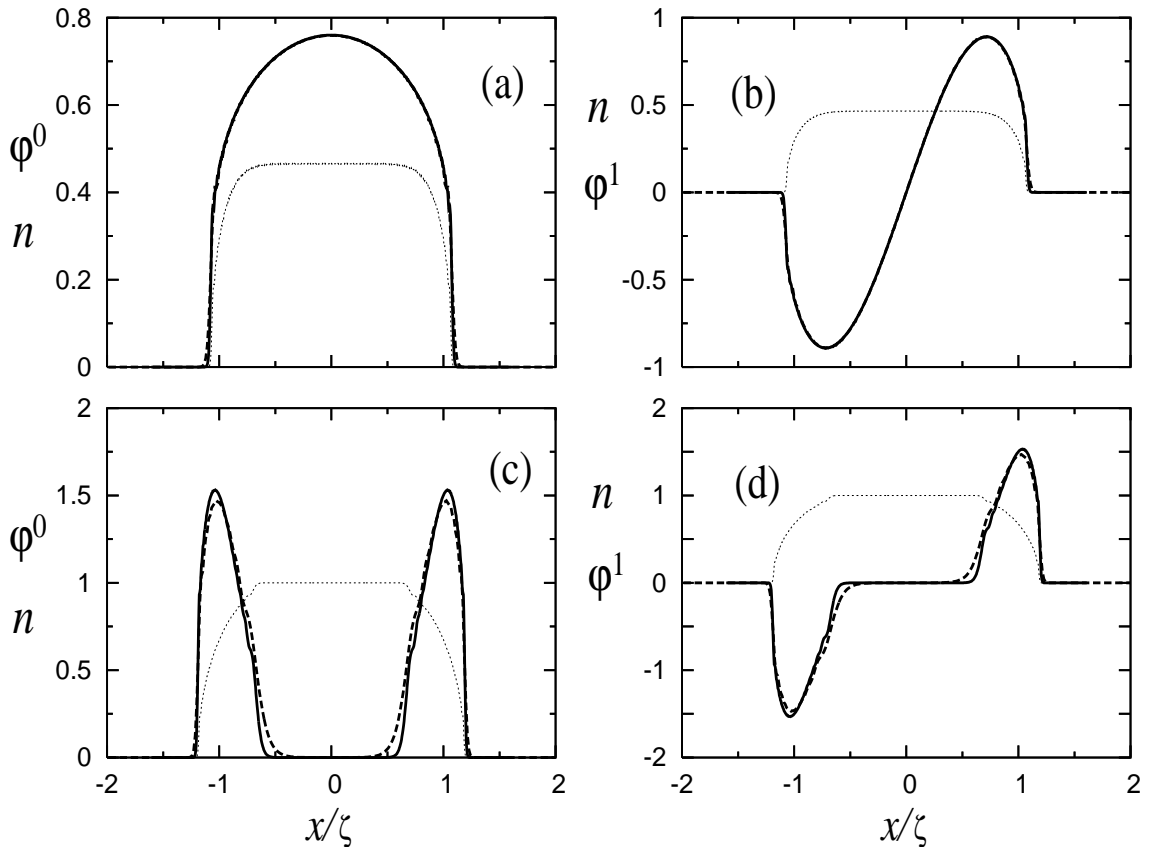


Figure 6.11: Profiles of the two lowest natural orbitals for trapped systems with: 700 lattice sites,  $V_8 a^8 = 2.0 \times 10^{-19} t$  and occupations of 201 (a),(b), and 451 (c),(d) HCB (continuous line); 300 lattice sites,  $V_8 a^8 = 1.0 \times 10^{-15} t$  and occupations of 69 (a),(b), and 155 (c),(d) HCB (dashed line). The density profiles have been included as thin dotted lines.

It has been already shown in Sec. 5.3 that density profiles as a function of the scaled positions in the trap ( $x/\zeta$ ) do not change when parameters in the system are changed keeping the characteristic density constant, this is independent of the power of the confining potential. We start this section showing that the scaling of the lowest NO, defined by [Eq. (6.23)] for the harmonic case ( $\alpha = 2$ ), also holds for  $\alpha = 8$ . In Fig. 6.11, we compare the scaled two lowest NO for systems with different filling but the same characteristic

density.  $\varphi$  was defined like in Eq. (6.23) with  $\zeta = (V_8/t)^{-1/8}$ , as corresponds to  $\alpha = 8$ . (Density profiles were included as thin dotted lines.) The plots show that indeed the scaling defined holds.

The increase of the power  $\alpha$  of the confining potential leads to the formation of more homogeneous density profiles, as shown in Fig. 6.11. The fast changes of the density are restricted to smaller regions in the borders of the system. In Fig. 6.12, it can be seen that also for these systems off-diagonal quasi-long range correlations are present in the one-particle density matrix. Like for the harmonic case, they decay as power laws  $\rho_{ij} \sim A_8(\tilde{\rho})|x/a|^{-1/2}$  for large- $x$  away from  $n_i, n_j = 0, 1$ .  $A_8(\tilde{\rho})$  depends only on the characteristic density  $\tilde{\rho}$ . In the figure, we show results for a very dilute case, and for a trap with a density  $n_i \sim 0.5$  in the middle of the system.

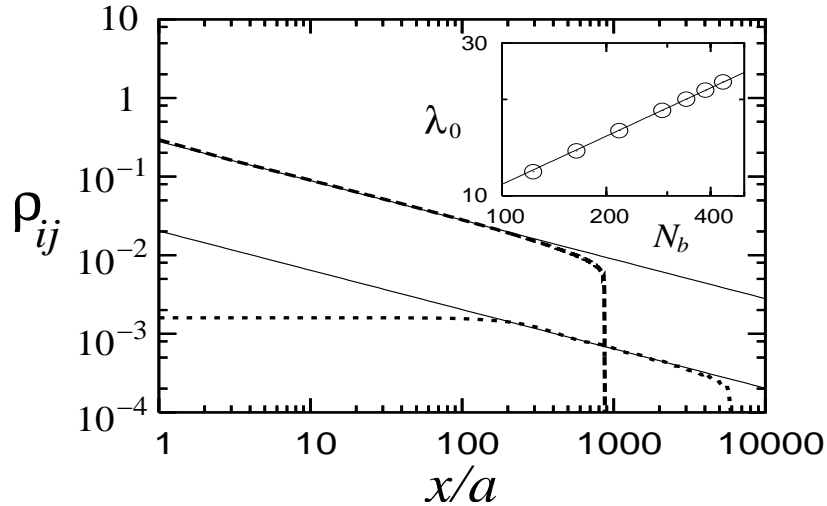


Figure 6.12: One-particle density matrix vs  $x/a$  ( $x = |x_i - x_j|$ ) for trapped HCB with:  $V_8 a^8 = 8.0 \times 10^{-22} t$ ,  $N_b = 400$  measured from  $n_{i=100} = 0.38$  (dashed line), and for a very dilute system with  $V_8 a^8 = 5.0 \times 10^{-34} t$ ,  $N_b = 11$ , measured from  $n_{i=3001} = 1.6 \times 10^{-3}$  (dotted line) The abrupt reduction of  $\rho_{ij}$  occurs for  $n_j \rightarrow 0$ . Thin continuous lines correspond to power-laws  $\sqrt{x/a}$ . The inset shows  $\lambda_0$  vs  $N_b$  for systems with  $\tilde{\rho} = 1$  ( $\circ$ ), the line exhibits  $\sqrt{N_b}$  behavior.

Considering the results above for the power-law decay of the one-particle density matrix and for the scaling of the lowest natural orbitals, it is possible to generalize for arbitrary powers of the confining potential the result obtained in the previous section for the occupation of the lowest NO in the harmonic case [Eq. (6.24)]. Then, independently of the power  $\alpha$  of the trapping potential in Eq. (6.1), the occupation of the lowest NO

will be determined in the thermodynamic limit as

$$\lambda_0^\alpha = C_\alpha(\tilde{\rho})\sqrt{N_b} = D_\alpha(\tilde{\rho})\sqrt{\zeta/a}, \quad (6.30)$$

where  $C_\alpha(\tilde{\rho})$  and  $D_\alpha(\tilde{\rho})$  are functions of  $\tilde{\rho}$  for a given power of the confining potential  $\alpha$ . The thermodynamic limit is defined keeping the characteristic density  $\tilde{\rho} = N_b/\zeta$  constant with  $\zeta$  given by Eq. (6.29). As for the periodic and harmonic cases, the scaling in the thermodynamic limit will be also valid up to a good approximation for finite size systems, as it is shown in the inset in Fig. 6.12 for  $\alpha = 8$  and  $N_b > 100$ .

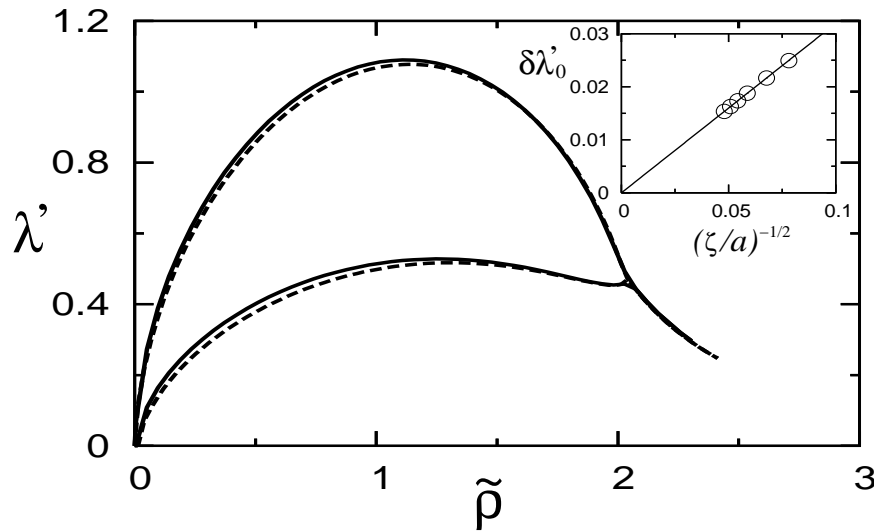


Figure 6.13: Normalized occupation of the two lowest NO (see text) vs  $\tilde{\rho}$ . The systems analyzed have  $N = 700$ ,  $V_8 a^8 = 2 \times 10^{-19} t$  and occupations up to 501 particles (continuous line), and  $N = 300$ ,  $V_8 a^8 = 1.0 \times 10^{-15} t$  and occupations up to 181 particles (dashed line). The inset displays  $\delta\lambda'_0$  vs  $(\zeta/a)^{-1/2}$  (see text) for  $\tilde{\rho} = 1.0$  ( $\circ$ ), the continuous line shows the result of our fits.

A global picture of the occupation of the two lowest NO in the case  $\alpha = 8$  is shown in Fig. 6.13(a). There we plot  $\lambda' = \lambda/\sqrt{\zeta/a}$  vs  $\tilde{\rho}$ , like in the harmonic case (Fig. 6.9), and compare systems with different curvatures of the confining potential. The insulator appears in the middle of the trap when the degeneracy sets in the NO. The comparison between the plots shows that also for  $\alpha = 8$  and the system sizes chosen, finite size corrections are small. It is still needed to check whether they will have the same functional form than for the homogeneous and harmonically trapped cases. The inset in Fig. 6.13 shows that indeed this is the case. We assume that  $\lambda_0/\sqrt{\zeta/a} = C_8(\tilde{\rho}) - D_8(\tilde{\rho})/\sqrt{\zeta/a}$ , like for the harmonic trap [Eq. (6.25)], and calculate  $C_8(\tilde{\rho})$  and  $D_8(\tilde{\rho})$ . In the inset in

Fig. 6.13, we plot  $\delta\lambda'_0 = C_8(\tilde{\rho}) - \lambda_0/\sqrt{\zeta/a}$  vs  $(\zeta/a)^{-1/2}$ , the linear behavior observed confirms our assumption.

In the following, we analyze the corrections introduced by the lattice to the occupation of the lowest natural orbitals in the confined continuous case. For a trap with power  $\alpha = 8$  of the confining potential, it can be proven numerically (Fig. 6.14) that in the low energy region the ratio between the level spacing and the band-width reduces proportionally to  $(V_8 a^8/t)^{1/5}$ , i.e. proportionally to  $(\zeta/a)^{-8/5}$ . Then the lowest NO occupations are

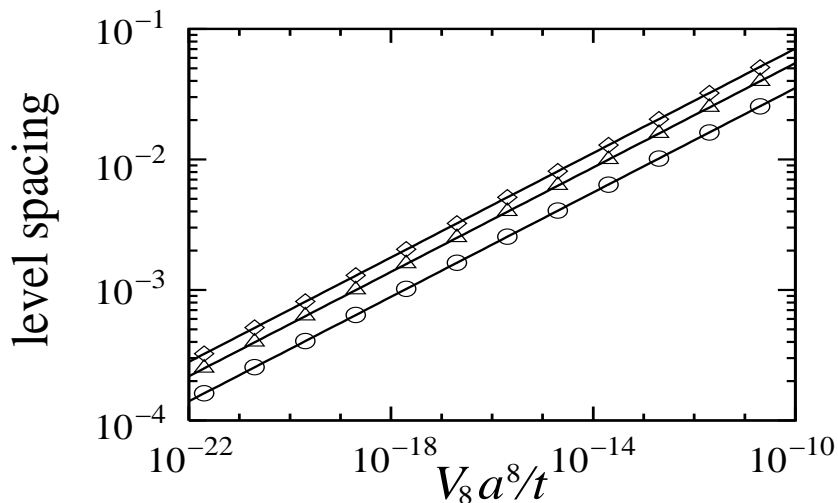


Figure 6.14: Level spacing (in units of  $t$ ) vs  $V_8 a^8/t$ . (○) between first and second level, (△) between second and third level, and (◇) between third and fourth level. The lines following the data correspond to power-laws  $(V_8 a^8/t)^{0.2}$ .

expected to approach their value in the continuous system  $\Lambda_\eta(N_b)$  as

$$\lambda_\eta(N_b, \zeta/a) = \Lambda_\eta(N_b) - E_\eta^8(N_b) (\zeta/a)^{-8/5} \quad (6.31)$$

We calculate  $\Lambda_\eta(N_b)$  and  $E_\eta^8(N_b)$  for the three lowest NO analyzing systems with fillings up to 401 particles and sizes up to 2000 lattice sites. The results obtained are shown in Figs. 6.15(a) and (b), respectively. In Fig. 6.15 we compare our results for  $\Lambda_\eta(N_b)$  and  $E_\eta^8(N_b)$  with the power-laws expected from comparing Eq. (6.31) and Eq. (6.30), i.e.  $\Lambda_\eta(N_b) = b_8 \sqrt{N_b}$  and  $E_8(N_b) = c_8 N_b^{21/10}$ . The plots show that for large occupations, basically larger than 100 HCB, the expected power-laws are observed. In addition, we plot as an inset in Fig. 6.15 (b)  $\Delta\lambda = \Lambda_\eta(N_b) - \lambda_\eta(N_b, \zeta/a)$  also for the three lowest NO as a function of  $(\zeta/a)^{-8/5}$ . These plots show that the scaling behavior proposed in Eq.

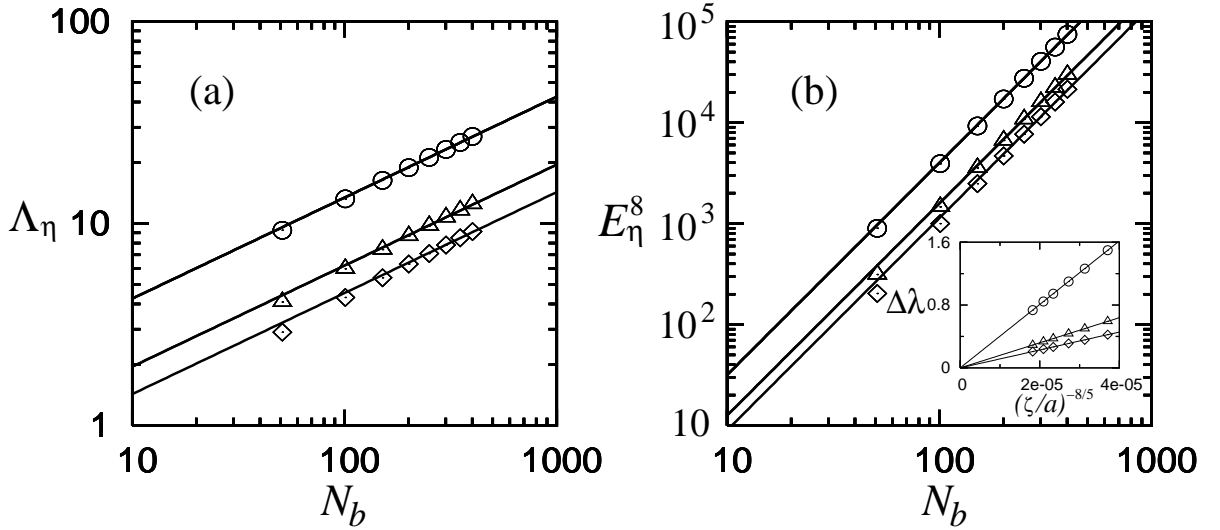


Figure 6.15: Values obtained for  $\Lambda_\eta(N_b)$  (a) and  $E_\eta^8(N_b)$  (b) vs  $N_b$ , for the first ( $\circ$ ), second ( $\triangle$ ), and third ( $\diamond$ ) NO. The lines following the data correspond to power-laws  $\sqrt{N_b}$  (a) and  $N_b^{21/10}$  (b). The inset in (b) shows  $\Delta\lambda$  (see text) as a function of  $(\zeta/a)^{-8/5}$  also for the first ( $\circ$ ), second ( $\triangle$ ), and third ( $\diamond$ ) NO in systems with 301 HCB and sizes between 1000 and 2000 lattice sites.

(6.31) is correct. Then Eq. (6.31) can be rewritten for the lowest NO as

$$\lambda_0(N_b, \zeta/a) = \sqrt{N_b} (b_8 - c_8 \tilde{\rho}^\beta) \quad (6.32)$$

with  $\beta = 8/5$ . Similar expressions can be written for the periodic (changing  $\tilde{\rho}$  by  $\rho$ ) [Eq. (6.21)] and harmonically trapped [Eq. (6.28)] systems, with  $\beta = 2$  and  $\beta = 1$ , respectively. Then, we have been able not only to obtain the scaling of the lowest natural orbitals when  $\tilde{\rho}$  (or  $\rho$  in the homogeneous case) is kept constant, but also the functional form of the proportionality constant  $C_\alpha(\tilde{\rho})$  in Eq. (6.30)

$$C_\alpha(\tilde{\rho}) = b_\alpha - c_\alpha \tilde{\rho}^\beta, \quad (6.33)$$

with  $b_\alpha$ ,  $c_\alpha$ , and  $\beta$ , being constants that depend on the power  $\alpha$  of the confining potential. In order to show the range of characteristic densities where Eq. (6.32) is a good approximation for the system sizes analyzed in Fig. 6.13, we show in Fig. 6.16 the lowest NO occupation  $\lambda_0$  vs  $\tilde{\rho}$  and compare with our fit to Eq. (6.32) with  $b_8 = 1.36$  and  $c_8 = 0.29$ . The insets show the same kind of fits for the periodic  $b = 1.51$  and  $c = 1.18$  and harmonic  $b_2 = 1.44$  and  $c_2 = 0.26$ , systems.

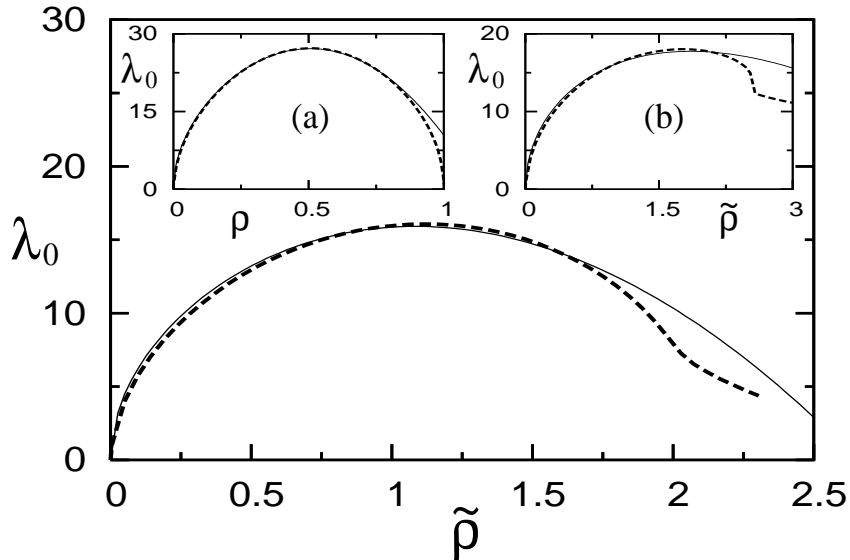


Figure 6.16: Comparison between the occupation of the lowest NO as a function of the characteristic density (dashed line), for a trap with power  $\alpha = 8$  of the confining potential, and the fit following Eq. (6.32) (thin continuous line). The insets show the same kind of fits for a periodic system (a), and a harmonic trap (b). (See text for the values of the fitted parameters in each case.)

## 6.5 Universal behavior of the natural orbital occupations

Finally, we study the large- $\eta$  behavior of the NO occupations ( $\lambda_\eta$ ). In contrast to the large- $x$  behavior of the density matrix, we do not find an universal feature in the large- $\eta$  behavior of  $\lambda_\eta$  for arbitrary values of the characteristic density  $\tilde{\rho}$ . However, for very small values of  $\tilde{\rho}$  we find that an universal power law develops in the large- $\eta$  region of  $\lambda_\eta$ , as it is shown in Fig. 6.17. The power law decay is in this case of the form  $\lambda_\eta = A_{N_b}/\eta^4$ , where  $A_{N_b}$  depends only on the number of particles in the trap independently of the confining potential, as it is shown in Fig. 6.17. Since this occurs only for very low values of  $\tilde{\rho}$  we expect this behavior to be generic for the continuous limit. In the latter limit the high momentum tail of the MDF was found to decay as  $n_k \sim |k|^{-4}$  for HCB in a harmonic trap [62], and for the Lieb-Liniger gas of free and harmonically trapped bosons for all values of the interaction strength [132]. Our results for the MDF (inset in Fig. 6.17) show that the large- $k$  behavior of  $n_k$  for low  $\tilde{\rho}$  is also universal, irrespective of the confining potential.



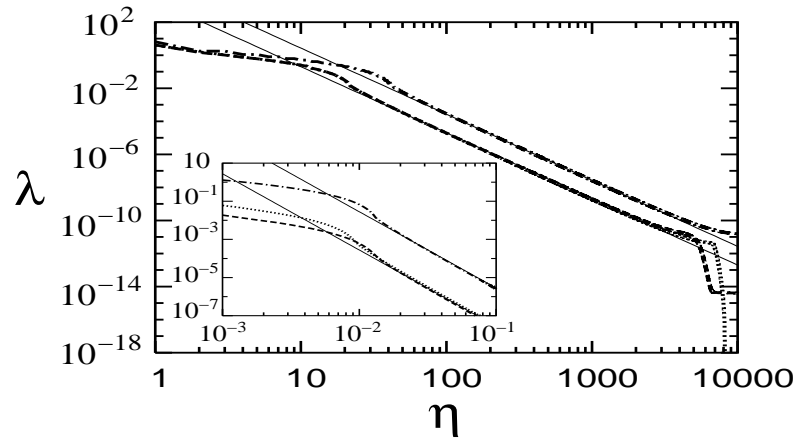


Figure 6.17: Occupation of the NO vs  $\eta$  in systems with  $N = 10000$ :  $N_b = 21$  periodic case (dashed-dotted line),  $N_b = 11$ ,  $V_2 a^2 = 5.0 \times 10^{-12} t$  (dashed line), and  $N_b = 11$ ,  $V_8 a^8 = 5.0 \times 10^{-34} t$  (dotted line). The inset shows  $n_k$  vs  $ka$  for the same parameters and the same notation. Thin continuous lines correspond to power-laws  $\eta^{-4}$ , and  $k^{-4}$  (inset).

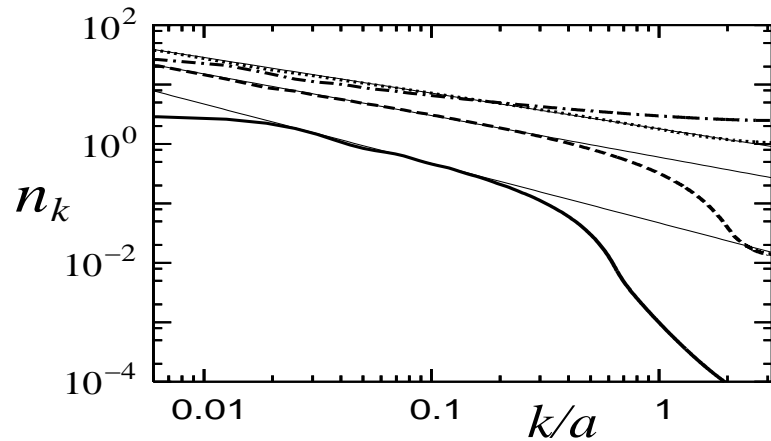


Figure 6.18: MDF for systems with  $V_2/t = 3.0 \times 10^{-5}$  and  $N_b = 11$  (continuous line),  $N_b = 101$  (dashed line), and  $N_b = 401$  (dotted line),  $N_b = 591$  (dashed-dotted line). Accompanying thin continuous lines correspond to power-laws:  $k^{-1}$  for  $N_b = 11$ ,  $k^{-0.7}$  for  $N_b = 101$ , and  $k^{-0.6}$  for  $N_b = 401$ .

At this point it is important to remark that the universal behavior and scaling relations discussed so far appear already at moderate number of particles, and hence, are relevant for experiments. However, the  $|k|^{1/2}$  singularity in  $n_k$  when  $k \rightarrow 0$  and  $N_b \rightarrow \infty$ , well known from the homogeneous system [58–60], is difficult to see explicitly in such situations, in contrast to previous claims [133]. Fitting power-laws  $n_k \sim k^{-\gamma}$  for finite

systems could lead to wrong conclusions about the large- $x$  behavior of the one-particle density matrix, as shown in Fig. 6.18. For very low fillings ( $N_b=11$ ), a “power-law” behavior with  $\gamma=1$  may be seen before the  $\gamma=4$  is established for large  $k$ . Increasing the number of particles leads to a decrease of  $\gamma$ , up to  $\gamma=0.6$  ( $N_b=401$ ). Hence, the power  $\beta$  depends strongly on the number of particles and cannot be understood as reflecting any universal property of the system. Only when reaching  $n_i = 1$  in parts of the system ( $N_b=591$  in Fig. 6.18), no power-law is observed.

## Chapter 7

# Quasi-condensation of hard-core bosons at finite momentum

The study of the non-equilibrium dynamics of quantum gases has been shown to be a very useful tool for the understanding of their properties [1]. Since the achievement of Bose-Einstein condensation (BEC) [6–8], where the anisotropic expansion of the gas revealed the importance of the inter-particle interaction, many experiments studying the dynamics of such systems have been developed. In this chapter, we study within an exact approach the non-equilibrium dynamics of hard-core bosons (HCB) on a lattice [75]. In particular, we study the time evolution of a pure Fock state of HCB. We analyze the large distance behavior of the equal-time one-particle density matrix, the momentum distribution function, and the natural orbitals (NO).

### 7.1 Exact approach to the dynamics of hard-core bosons

So far, theoretical studies of the non-equilibrium dynamics of HCB on one-dimensional systems, without a lattice, have been restricted to the analysis of density properties. As it has been shown in the previous chapter, density properties are shared by HCB and non-interacting fermions. In order to study the dynamics of HCB, the Fermi-Bose mapping [57] was generalized to the time-dependent case, where the density dynamics revealed dark soliton structures [134], breakdown of the time-dependent mean-field theory

[135–138], and interference patterns of the thermal gas on a ring [139]. In addition, the time evolution of density profiles has been studied in all the range of interactions between the weakly interacting regime and the HCB limit [140, 141] showing that in general it does not follow a self-similar solution.

In this chapter we generalize to the non-equilibrium case, the exact approach developed in the previous one for the study of HCB on a lattice in 1D. We are interested in the evaluation of the equal-time Green's function as a function of the evolution time  $\tau$

$$\begin{aligned} G_{ij}(\tau) &= \langle \Psi_{HCB}(\tau) | b_i b_j^\dagger | \Psi_{HCB}(\tau) \rangle \\ &= \langle \Psi_F(\tau) | \prod_{k=1}^{i-1} e^{i\pi f_k^\dagger f_k} f_i f_j^\dagger \prod_{l=1}^{j-1} e^{-i\pi f_l^\dagger f_l} | \Psi_F(\tau) \rangle, \end{aligned} \quad (7.1)$$

where

$$|\Psi_{HCB}(\tau)\rangle = e^{-i\tau H_{HCB}/\hbar} |\Psi_{HCB}^I\rangle \quad (7.2)$$

is the time evolution of an initial HCB wave-function  $|\Psi_{HCB}^I\rangle$  in a system with Hamiltonian  $H_{HCB}$ , and

$$|\Psi_F(\tau)\rangle = e^{-i\tau H_F/\hbar} |\Psi_F^I\rangle \quad (7.3)$$

is the corresponding time evolution for the equivalent non-interacting fermions. Since fermions are non-interacting, the time evolution of their initial wave-function

$$|\Psi_F^I\rangle = \prod_{m=1}^{N_f} \sum_{n=1}^N P_{nm}^I f_n^\dagger |0\rangle \quad (7.4)$$

can be calculated using the matrix representation introduced in Sec. 3.2, the result obtained is

$$|\Psi_F(\tau)\rangle = \prod_{m=1}^{N_f} \sum_{n=1}^N P_{nm}(\tau) f_n^\dagger |0\rangle, \quad (7.5)$$

where the matrix  $\mathbf{P}(\tau)$  can be evaluated as

$$e^{-i\tau \mathbf{H}_F/\hbar} \mathbf{P}^I = \mathbf{U} e^{-i\tau \mathbf{D}/\hbar} \mathbf{U}^\dagger \mathbf{P}^I, \quad (7.6)$$

using an unitary transformation, such that  $\mathbf{U}^\dagger \mathbf{H}_F \mathbf{U} = \mathbf{D}$ , where  $\mathbf{D}$  is diagonal. From here on the method is identical to the one followed in the previous chapter, the action of  $\prod_{l=1}^{j-1} e^{-i\pi f_l^\dagger f_l}$  on the right in Eq. (7.1) generates only a change of sign on the elements  $P_{nm}(\tau)$  for  $n \leq j-1$ , and the further creation of a particle at site  $j$  implies the addition of one column to  $\mathbf{P}(\tau)$  with the element  $P_{jN_f+1}(\tau) = 1$  and all the others equal to zero

[the same applies to the action of  $\prod_{k=1}^{i-1} e^{i\pi f_k^\dagger f_k} f_i$  on the left of Eq. (7.1)]. Then the HCB Green's function can be calculated exactly as

$$\begin{aligned} G_{ij}(\tau) &= \langle 0 | \prod_{m=1}^{N_f+1} \sum_{n=1}^N P'_{nm}{}^A(\tau) f_n \prod_{k=1}^{N_f+1} \sum_{l=1}^N P'_{lk}{}^B(\tau) f_l^\dagger | 0 \rangle \\ &= \det \left[ \left( \mathbf{P}'^A(\tau) \right)^\dagger \mathbf{P}'^B(\tau) \right], \end{aligned} \quad (7.7)$$

where  $\mathbf{P}'^A(\tau)$  and  $\mathbf{P}'^B(\tau)$  are the new matrices obtained from  $\mathbf{P}(\tau)$  when the required signs are changed and the new columns added. [The final result is obtained following the same steps of Eq. (3.28).]

The evaluation of  $G_{ij}(\tau)$  is done numerically, and the equal-time one-particle density matrix  $[\rho_{ij}(\tau)]$  is determined as

$$\rho_{ij}(\tau) = \left\langle b_i^\dagger b_j \right\rangle_\tau = G_{ji}(\tau) + \delta_{ij} (1 - 2G_{ii}(\tau)). \quad (7.8)$$

## 7.2 Momentum distribution function and the natural orbitals

In this section we apply the approach developed in previous section to the study of the non-equilibrium dynamics of a pure Fock state. Such states can be created experimentally when HCB are under the influence of a very strong confining potential, and their dynamics can be studied just switching off the trap, keeping the optical lattice on.

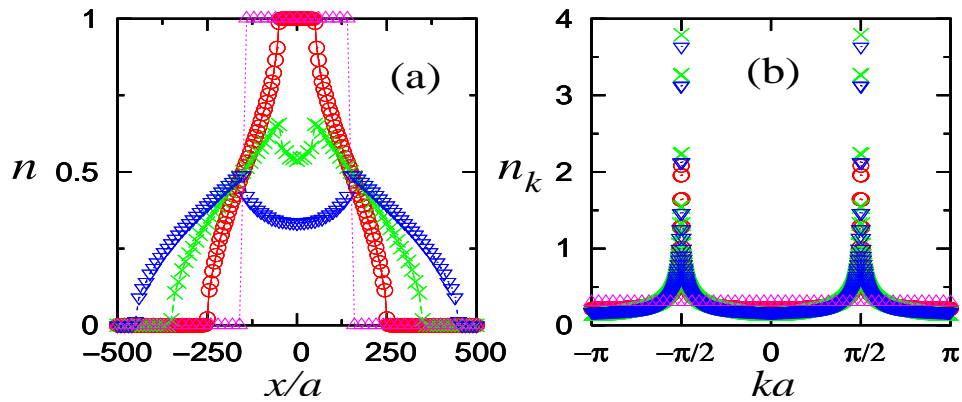


Figure 7.1: Evolution of density (a) and momentum (b) profiles of 300 HCB in 1000 lattice sites. The times are  $\tau = 0$  ( $\triangle$ ),  $50\hbar/t$  ( $\circ$ ),  $100\hbar/t$  ( $\times$ ), and  $150\hbar/t$  ( $\nabla$ ). Positions (a) and momenta (b) are normalized by the lattice constant  $a$ .

In Fig. 7.1 we show density profiles (a), and their corresponding momentum distribution functions (MDF) (b) for the time evolution a Fock state with 300 HCB. Initially, the MDF is flat as corresponds to a pure Fock state, where particles are localized in the lattice sites and hence equally distributed in momentum space. During the time evolution of the system a surprising behavior is observed in the MDF. Sharp peaks appear at  $k = \pm\pi/2a$  ( $a$  is the lattice constant). This behavior of HCB is in contrast with the one of the equivalent non-interacting fermionic system, where the density profiles are equal to the ones of the HCB, but the MDF remains flat since fermions do not interact, i.e. no momentum redistribution occurs between the particles. This result evidences the non-trivial differences in the off-diagonal correlations between both systems.

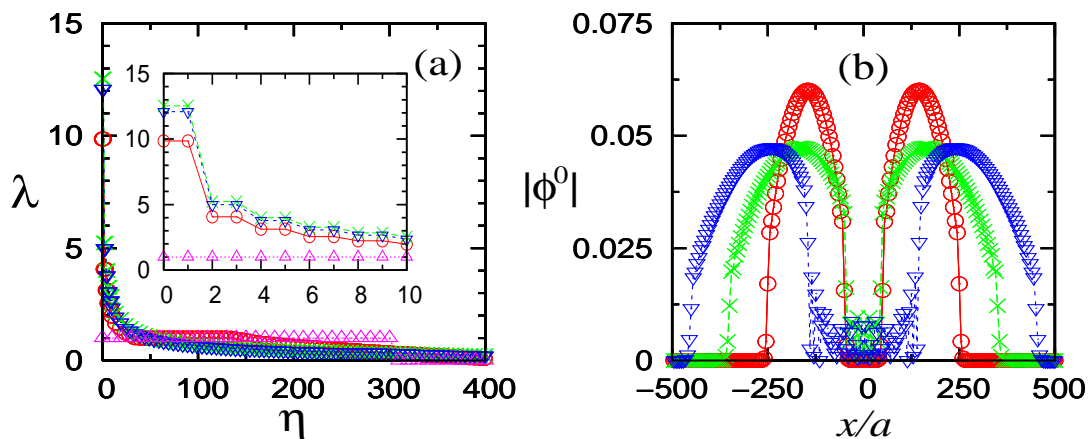


Figure 7.2: (a) Natural orbitals occupations. The inset shows in detail the occupation of the lowest eleventh NO. (b) Modulus of the lowest NO wave-function  $|\phi^0|$ . The times are  $\tau = 0$  ( $\triangle$ ),  $\tau = 50\hbar/t$  ( $\circ$ ),  $100\hbar/t$  ( $\times$ ), and  $150\hbar/t$  ( $\nabla$ ).

Since the peaks appearing in the MDF may be reflecting the formation of quasi-condensates of HCB at  $k = \pm\pi/2a$ , we diagonalize the equal-time one-particle density matrix to study the NO and their occupations. In Fig. 7.2(a) we show the NO occupations for the same times of Fig. 7.1. At  $\tau = 0$  a plateau with  $\lambda_\eta = 1$ , reflecting the Fock state, is observed. However, during the time evolution of the system some of the NO increase their occupation, and as it can be seen in the inset of Fig. 7.2(a) they are degenerated<sup>1</sup>. The modulus of the wave-function of the lowest NO is presented in Fig. 7.2(b). There we show  $|\phi^0|$  because  $\phi^0$  is complex, and only for  $\tau > 0$  since at  $\tau = 0$  the NO are just delta functions at the occupied sites. Two important observations can be obtained from

<sup>1</sup>These features are explained during the analysis of the equal-time one-particle density matrix.

Fig. 7.2(b). (i) Short time after the  $n = 1$  plateau disappears from the system, the NO lobes acquire a stable form that does not change within the same time scales in which they were formed. This is shown more clearly in Fig. 7.3(a) where the right lobe of the lowest NO is superposed at three different times without a perceptible change in its form. (ii) The velocity at which the left and right lobes move is constant and equal to  $v_{NO}^L = -2at/\hbar$  and  $v_{NO}^R = 2at/\hbar$ , respectively. This can be seen in the inset of Fig. 7.3

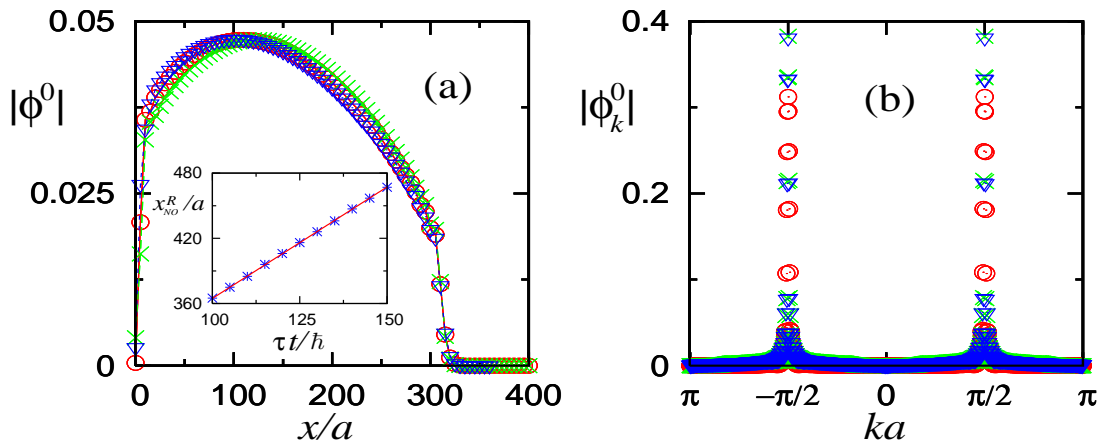


Figure 7.3: (a) Superposed right lobe of the lowest NO at times  $\tau = 100\hbar/t$  ( $\times$ ),  $125\hbar/t$  ( $\circ$ ), and  $150\hbar/t$  ( $\nabla$ ). The inset shows the evolution of the lowest NO right lobe position  $x_{NO}^R$ , the line there has a slope 2. (b) Fourier transform of the lowest NO wave-function at times  $\tau = 50\hbar/t$  ( $\circ$ ),  $100\hbar/t$  ( $\times$ ), and  $150\hbar/t$  ( $\nabla$ ).

where the position of the right lobe ( $x_{NO}^R$ ) is plotted as a function of time (the situation for the left lobe is totally symmetric to this one). The observed velocities of the left and right lobes are the group velocities  $v = 1/\hbar \partial\epsilon_k/\partial k$  for a dispersion  $\epsilon_k = -2t \cos ka$  (the one of HCB on a lattice) at  $k = \pm\pi/2a$ , establishing then a clear connection between the lowest NO and the peaks at  $k = \pm\pi/2a$  in the MDF. This is further confirmed by considering the Fourier transforms of the lowest NO [Fig. 7.3(b)], which show sharp peaks centered at quasi-momenta  $k = \pm\pi/2a$ . The peak at  $k = +\pi/2a$  appears due to the Fourier transform of the right lobe in Fig. 7.2(a) (i.e.  $\phi_i^0 \approx |\phi_i^0| e^{i\pi x_i/2a}$  for  $x_i > 0$ ), and the one at  $k = -\pi/2a$  due to the Fourier transform of the left lobe (i.e.  $\phi_i^0 \approx |\phi_i^0| e^{-i\pi x_i/2a}$  for  $x_i < 0$ ). Studying the Fourier transform of the other NO we have seen that they have very small or zero weight at  $k = \pm\pi/2a$  so that we can conclude that the peaks at  $n_{k=\pm\pi/2a}$  are indeed reflecting the large occupation of the lowest NO.

### 7.3 Equal-time one-particle density matrix and the quasi-condensates

Whether the large occupation of the lowest NO and the peaks in the MDF correspond to a quasi-condensate, can be determined studying the equal-time one-particle density matrix. Fig. 7.4(a) shows the results for  $|\rho_{ij}|$  (with  $i$  taken at the beginning of the lowest NO left lobe's and  $j > i$ ) at the same times of Figs. 7.1, 7.2 and 7.3. In the figure, it can be seen that off-diagonal quasi-long range order develops in the equal-time one-particle density matrix. It is reflected by a power-law decay of the form  $|\rho_{ij}| = 0.25 |(x_i - x_j)/a|^{-1/2}$ , that remains almost unchanged during the evolution of the system. The prefactor of the power-law (0.25) was not only found to be constant during the time evolution of the system, but also independent of the number of particles in the initial Fock state. A careful

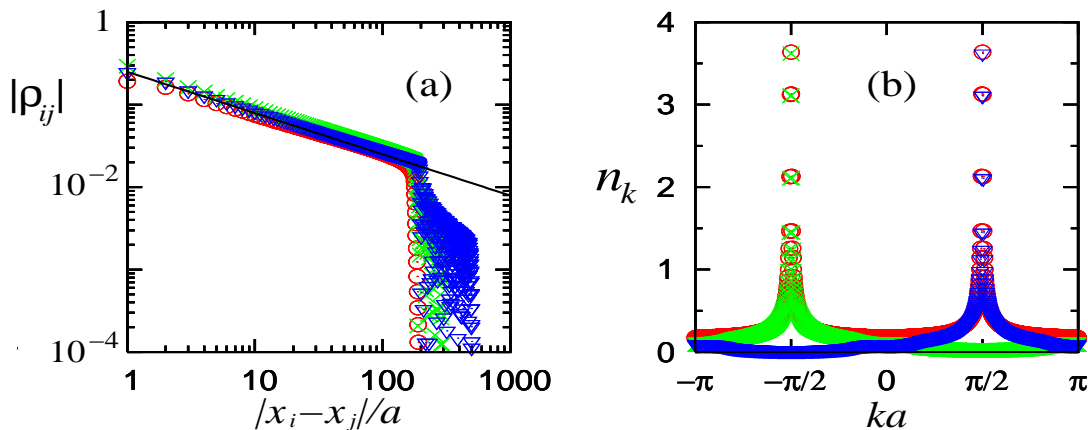


Figure 7.4: (a) Equal-time one-particle density matrix during the evolution of a Fock state with 300 HCB for:  $\tau=50\hbar/t$  ( $\circ$ ),  $100\hbar/t$  ( $\times$ ), and  $150\hbar/t$  ( $\nabla$ ), the straight line is  $0.25 |(x_i - x_j)/a|^{-1/2}$  (see text for details). (b) Comparison between the MDF ( $\circ$ ) and the Fourier transform of the equal-time one-particle density matrix for  $x_i, x_j > 0$  ( $\nabla$ ) and  $x_i, x_j < 0$  ( $\times$ ), at  $\tau = 150\hbar/t$ .

inspection shows that this power-law behavior is restricted to the regions where each lobe of the lowest NO exists, outside these regions the equal-time one-particle density matrix decays faster. This quasi-coherent behavior in two different segments of the system is the reason for the degeneracy found in the lowest NO because it means that two independent quasi-condensates appear in two different regions of the system. In addition, a detailed analysis of the equal-time one-particle density matrix Fourier's transform shows



that the peak in the MDF at  $k = +\pi/2a$  is originated by components of the equal-time one-particle density matrix with  $x_i, x_j > 0$ , and the one at  $k = -\pi/2a$  by the components with  $x_i, x_j < 0$ . This can be seen in Fig. 7.4(b), where we compare the MDF at  $\tau = 150\hbar/t$  with the Fourier transform of the equal-time one-particle density matrix for  $x_i, x_j > 0$  and  $x_i, x_j < 0$  calculated independently. Then, in the regions of the lobes one can approximate  $\rho_{ij} \approx 0.25 |(x_i - x_j)/a|^{-1/2} e^{i\pi(x_i - x_j)/2a}$  for  $x_i, x_j > 0$ , and  $\rho_{ij} \approx 0.25 |(x_i - x_j)/a|^{-1/2} e^{-i\pi(x_i - x_j)/2a}$  for  $x_i, x_j < 0$ .

After having observed off-diagonal quasi-long range correlations in the equal-time one-particle density matrix, it remains to consider how the occupation of the lowest NO behaves in the thermodynamic limit, in order to see whether it will diverge or not. The only new information we need at this point is the scaling relation (if any) of the modulus of the lowest NO with the number of particles in the initial Fock state. For this, we consider the NO at those times, where as shown in Fig. 7.3(a), they almost do not change during the evolution of the system, i.e. after the plateau with  $n = 1$  disappears. In Fig. 7.5(a)

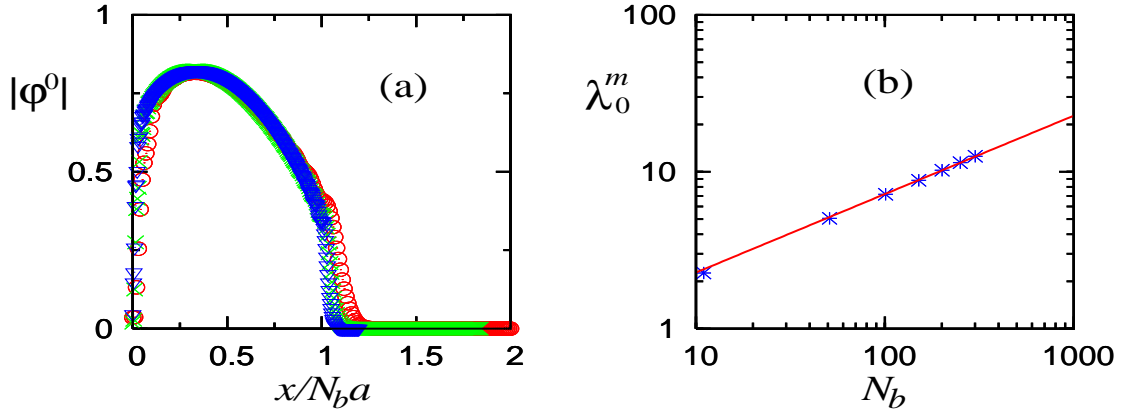


Figure 7.5: (a) Scaled lowest NO right lobe's *vs*  $x/N_b a$  for  $N_b = 101$  ( $\circ$ ),  $201$  ( $\times$ ), and  $301$  ( $\nabla$ ). (b) Maximum occupation of the lowest NO *vs*  $N_b$  of the initial Fock state, the straight line is  $0.72 N_b^{1/2}$ .

we show that a scaled NO ( $|\varphi_0| = N_b^{1/2} |\phi^0|$ ) exists when its size is normalized by  $N_b a$ . (The results for the left lobe are identical due to inversion symmetry.) Figure 7.5(a) also shows that the lobe size  $L$  is approximately  $N_b a$ . Then evaluating  $\lambda_0 = \sum_{ij} \phi_i^{*0} \rho_{ij} \phi_j^0$  as twice the integral over a single lobe ( $L \gg a$ ) one obtains

$$\begin{aligned} \lambda_0 &\sim 2/a^2 \int_0^L dx \int_0^L dy \phi^{*0}(x) \rho(x, y) \phi^0(y) \\ &= N_b^{1/2} \int_0^1 dX \int_0^1 dY \frac{|\varphi^0(X)| 0.25 |\varphi^0(Y)|}{|X - Y|^{-1/2}} = A \sqrt{N_b}, \end{aligned} \quad (7.9)$$

where we did the change of variables  $x = XN_b a$ ,  $y = YN_b a$ ,  $\phi^0 = N_b^{-1/2} \varphi^0$ , and we notice that the phase factors between the NO and the equal-time one-particle density matrix cancel out. The integral over  $X, Y$  is a constant that we call  $A$ . A confirmation of the validity of the previous calculation is shown in Fig. 7.5(b). There we plot the maximum occupation of the lowest NO (reached when the lobes of the NO have a stable form), as a function of the number of particles in the initial Fock state. The  $\sqrt{N_b}$  power law behavior is evident and a fit allowed to obtain the constant  $A = 0.72$ . Hence, this and the previous results demonstrate that the peaks of the MDF in Fig. 7.1(b) correspond to the formation of two independent quasi-condensates with momenta  $k = \pm\pi/2a$ .

The appearance of such quasi-condensates at  $k = \pm\pi/2a$  can be understood on the basis of total energy conservation. Given the dispersion relation of HCB on a lattice, since the initial Fock state has a flat MDF, its total energy is  $E_T = 0$ . Would all the particles condensate into one state, it would be to the one with an energy corresponding to  $\bar{\epsilon}_k = E_T/N$ . Taking into account the dispersion relation for HCB on a lattice ( $\epsilon_k = -2t \cos ka$ ),  $\bar{\epsilon}_k = 0$  corresponds to  $k = \pm\pi/2a$ . Actually, in the 1-D case there is only quasi-condensation, so that the argument above applies only to maximize the occupation of a given state. In addition, the minimum in the density of states at these quasi-momenta reinforces quasi-condensation into a single momentum state, as shown in Figs. 7.1(b) and 7.3(b).

The process of formation of the quasi-condensate is also characterized by a power-law. In Fig. 7.6(a) we plot the occupation of the lowest NO as a function of the evolution time. The *log-log* scale shows that the occupation of the quasi-condensate increases quickly and decays slowly. A more detailed examination shows that the population of the quasi-condensate increases in an universal way [ $1.38\sqrt{\tau t/\hbar}$ , continuous line in Fig. 7.6(a)] independently of the initial number of particles in the Fock state. The power-law is determined by the universal behavior of the off-diagonal part of the equal-time one-particle density matrix shown before, and the fact that during the formation of the quasi-condensate, the NO increases its size linearly with time at a rate given by  $|v_{NO}| = 2at/\hbar$ . Such a power-law is followed almost up to the point where the maximal occupation is reached. The time at which it is reached depends linearly on the number of particles of the initial Fock state ( $\tau_m = 0.32N_b\hbar/t$ ) as shown in the inset of Fig. 7.6(b).

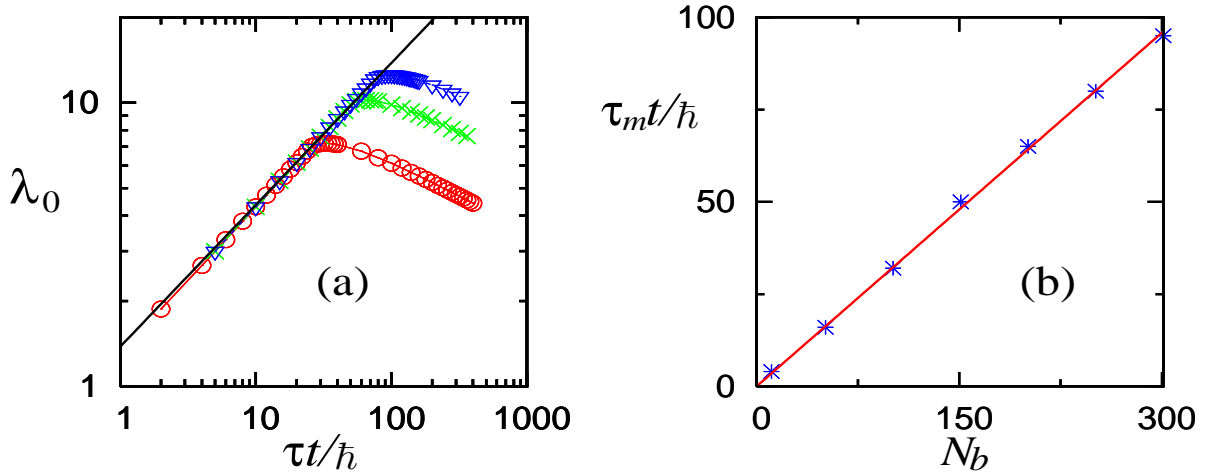


Figure 7.6: (a) Time evolution of the lowest NO occupation for  $N_b = 101$  ( $\circ$ ),  $201$  ( $\times$ ), and  $301$  ( $\nabla$ ), the straight line is  $1.38\sqrt{\tau t/\hbar}$ . (b) Time at which the maximum occupation of the NO is reached ( $\tau_m t/\hbar$ ) vs  $N_b$ , the line is  $0.32N_b$ .

## 7.4 An atom laser

The results above showing that a quasi-coherent matter front forms spontaneously from Fock states of HCB, suggest that such an arrangement could be used to create atom lasers with a wave-length that can be fully controlled given the lattice parameter  $a$ . No additional effort is needed to separate the quasi-coherent part from the rest since the quasi-condensate is traveling at the maximum possible velocity on the lattice so that the front part of the expanding cloud is the quasi-coherent part. The actual realization would imply to restrict the evolution of the initial Fock state to one direction, as shown in Fig. 7.7(a) and (b). There we display the density profiles and the MDF, respectively, of 150 HCB restricted to evolve to the right in 1000 lattice sites, and at the same evolution times of Fig. 7.1. It can be seen that the values of  $n_{k=\pi/2}(\tau)$  are almost the same in both situations, although in Fig. 7.7(a) the initial Fock state has almost half of the particles. The same occurs to the occupation of the lowest NO that in the latter case is not degenerated anymore.

The previous results suggest how to proceed in order to obtain lasers in higher dimensional systems where real condensation can occur [142]. One can employ Mott insulator states with one particle per lattice site created by a very strong on-site repulsive potential  $U$ . The latter is required in order to obtain a close realization of a pure Fock state, since quantum fluctuations of the particle number present in a Mott insulator for any finite

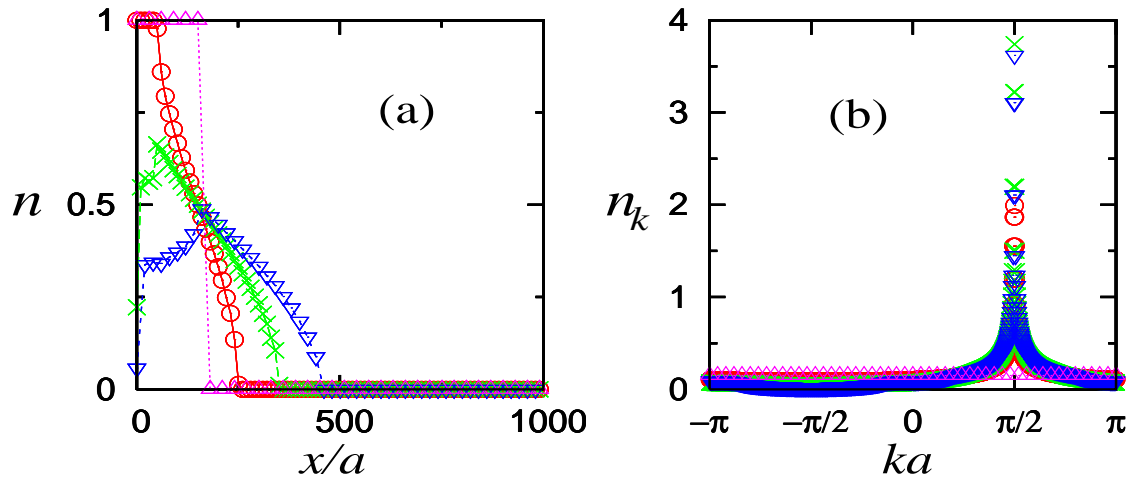


Figure 7.7: Density profiles (a) and MDF (b) of 150 HCB restricted to evolve only to the right in 1000 lattice sites, for  $\tau = 0$  ( $\triangle$ ),  $50\hbar/t$  ( $\circ$ ),  $100\hbar/t$  ( $\times$ ), and  $150\hbar/t$  ( $\nabla$ ).

$U$  [23, 72, 73] will be strongly suppressed. Then the geometry of the lattice should be designed in order to restrict the evolution of the Mott insulator to one direction only, and to have a low density of states around the mean value of energy per particle in the initial state. With these conditions the sharp features obtained for the quasi-condensate in 1-D should be reproduced by a condensate in higher dimensions.

## Chapter 8

# Summary and Conclusions

In this thesis, we have studied properties of ultracold quantum gases confined on optical lattices. Depending on the nature of the gas different established numerical techniques were used, like the world-line quantum Monte Carlo for soft-core bosons, and the zero temperature projector quantum Monte Carlo for two-component fermions. In the hard-core boson case, we have developed a new approach, which is not only exact but also allows to study the non-equilibrium dynamic of those strongly correlated particles.

In Chap. 1, we motivated our study on the framework of the most recent experimental developments on the field of ultracold quantum gases, and their loading on optical lattices. We showed there how the introduction of an optical lattice enables the almost ideal realization of a system described by the bosonic Hubbard Hamiltonian [17] for an ultracold gas of bosons, and by the fermionic Hubbard Hamiltonian [123, 124] for an ultracold gas of fermions.

In Chap. 2, we studied properties of single species fermions confined on 1D lattices [46]. These systems are of interest since their recent experimental realization [42–45, 48]. Due to the very low temperatures achieved in the experiments, fermions can be considered as non-interacting particles. This is so because at very low temperatures only *s*-wave scattering is possible, but due to the Pauli principle it is forbidden for identical fermions. Hence, the Hamiltonian can be diagonalized numerically for very large systems. We showed that the combination lattice-confining potential leads to confinement of particles in a fraction of the available system size. This confinement was found to be directly related to the formation of insulating regions in fermionic systems. However, since the results obtained correspond to non-interacting particles they can be also explained in

a single particle picture due to the realization of Bragg conditions, and are also valid for bosons. We also studied the consequences of the above mentioned confinement in the non-equilibrium dynamics of trapped particles in 1-D when the center of the trap is suddenly displaced, and confirmed the evolution of the center of mass observed in recent experiments [42, 43, 48].

The region over which particles are confined in the trap can be controlled in various ways. The most obvious one is by changing the strength of the confining potential, where the extension of such regions can be regulated. Another way is changing the periodicity of the lattice, which leads to a different ‘slicing’ of the system. We have studied the latter case. We have shown that although insulating phases appear, the gaps that are locally opened are not seen in the single particle spectrum. In order to observe them it is necessary to study the local density of states. A scalable phase diagram for these systems was also presented.

In Chap. 3, we shortly introduced the basis of the classical Monte Carlo method. Then, we reviewed in more detail the two quantum Monte Carlo techniques that were used in the study of correlated quantum gases on optical lattices, i.e. the worldline quantum Monte Carlo and the zero temperature projector quantum Monte Carlo.

Chap. 4 was devoted to the analysis of the ground state properties of soft-core bosons on 1D lattices [23]. We discussed there the nature of locally incompressible Mott-insulating phases in a confining potential at  $T = 0$ . We found that because of the destruction of translation invariance due to the presence of the space varying trapping potential, local Mott insulating phases appear at incommensurate fillings and always co-exist with compressible phases. The latter feature was reflected by the behavior of the global compressibility, which never vanished. The variance of the local density was used in order to characterize the local Mott-insulating phases since this quantity was found to exhibit a local minimum in such phases. A sketch of a phase diagram was also analyzed.

Ground state properties of two-species fermions confined on 1D optical lattices were studied in Chap. 5 [72, 73]. There, we have defined a local-order parameter, that we called local compressibility, which characterizes the local insulating regions in an unambiguous way. It vanishes in the insulating phases and is finite in the metallic ones. This local compressibility gives a measure of the local change in density due to a constant shift of the potential over finite distances larger than the correlation length of the density-density

correlation function for the Mott-insulating phase in the unconfined system. We found that the local compressibility exhibits critical behavior (a power-law decay  $\kappa^l \sim |1 - n|^\varpi$ ) on entering the Mott-insulating regions. Due to the microscopic nature of the phases, spatial correlations appear not to contribute to the critical behavior discussed there. This is a new form of metal-Mott-insulator transition not observed so far in simple periodic systems, and that might be realized in fermionic gases trapped on optical lattices. The exponent of the power-law ( $\varpi$ ) was obtained to be independent of the confining potential and/or strength of the interaction, excluding, however, the unconfined case. Universal behavior was also observed for the variance  $\Delta \sim |1 - n|$  when  $n \rightarrow 1$ . In this case, the observed behavior is shared by the unconfined model.

As opposed to periodic systems, where the appearance of the gap in the insulating phase can be seen by the disappearance of the Fermi surface in the momentum distribution function, we found that due to the presence of a harmonic confining potential such a feature is much less evident. In a non-interacting case, we have shown that although increasing the power of the confining potential sharpens the features connected with the Fermi edge, it remains qualitatively different from the homogeneous case. Increasing the system size with a proper definition of the thermodynamic limit, does not change the behavior of the density and momentum distribution functions in the trapped case, such that, in fermionic systems the momentum distribution function does not seem to be the appropriate quantity to detect experimentally the formation of Mott-insulating domains.

Our mean field study in 1D showed that within this approach the trapped system is an insulator for all the densities in the trap, a qualitatively wrong picture in contradiction with the quantum Monte Carlo results. In addition, the metallic regions showed large oscillations in the density that are not present in the real solutions. However, it was possible to obtain some qualitative information from mean field, such as the coexistence of  $n \neq 1$  regions with  $n = 1$  plateaus, the shape of the momentum distribution function, and the existence of antiferromagnetic correlations in the insulating regions with  $n = 1$ .

Finally, we determined a generic form for the phase diagram that allows to compare systems with different values of all the parameters involved in the model. It can be used to predict the phases that will be present in future experimental results. The phase diagram also reveals interesting features such as reentrant behavior in some phases when parameters are changed, and phase boundaries with linear forms. A similar form of the

phase diagram was found for a quartic confining potential, such that the results obtained can be generally applied to cases beyond a perfect harmonic potential.

In Chap. 6, we described a recently developed exact numerical approach [74] that allows to study ground state properties of hard-core bosons confined on 1D lattices. Results obtained for the off-diagonal behavior of the one-particle density matrix showed that it decays with the same power-law known from periodic systems [68], independently of the power of the confining potential. These results are equally valid for the 1D  $XY$  model with a space-varying transverse field. Furthermore, we have shown how the occupation of the lowest natural orbital is determined by the large distance behavior of the one particle density matrix. Even in the cases where a region with  $n_i=1$  builds up in the middle of the system we find that both quantities scale proportionally to the square root of the number of particles (at constant characteristic density). The functional form of the constant of proportionality, as a function of the characteristic density, was also determined in the cases where the  $n_i = 1$  region is not present in the density profiles. Finite size corrections to the square root behavior of the lowest natural orbital occupation were also studied. Finally, a further universal power-law decay was found for the eigenvalues of the one-particle density matrix ( $\lambda_\eta$ ) for large values of  $\eta$  at low densities ( $\lambda_\eta \sim \eta^{-4}$ ). This behavior translates into a corresponding power-law decay of the momentum distribution function ( $n_k \sim |k|^{-4}$ ) at large momenta also independently of the power of the confining potential, pointing to scale invariance also in the ultraviolet limit of the continuous case.

The approach followed in Chap. 6 was generalized to study the non-equilibrium dynamics of hard-core bosons on a lattice in Chap. 7. In particular, we have studied the non-equilibrium dynamics of a Fock states of hard-core bosons when they are allowed to evolve freely. We have shown that quasi-long range correlations develop dynamically in these systems and that they lead to the formation of quasi-condensates of hard-core bosons at quasi-momenta  $k \pm \pi/2a$ . We have studied the dynamics of the formation of these quasi-condensates, and their maximal occupations were found to scale proportionally to the square root of the number of particles in the initial Fock state. These systems can be used to create atom lasers since the quasi-condensate develops quickly and decays slowly. The wave-length of such lasers is simply determined by the lattice parameter. Finally, we have discussed the possibility of creating atom lasers in higher dimensional systems where true condensation can occur.



# Appendix A

## Single species fermions confined on 2D optical lattices

We analyze in this appendix non-interacting fermions confined in 2D optical lattices. In this way, we extend the results obtained in Chapter 2 to the 2D case. The Hamiltonian in this case can be written as

$$H = -t \sum_{\langle i,j \rangle} (c_i^\dagger c_j + \text{H.c.}) + \sum_i (V_{\alpha_x, x} x_i^{\alpha_x} + V_{\alpha_y, y} y_i^{\alpha_y}) n_i, \quad (\text{A.1})$$

where the hopping of the particles is restricted to the nearest neighbors ( $\langle i, j \rangle$ ), and its parameter is denoted by  $t$ . The coordinates of a site  $i$  are given by  $(x_i, y_i)$ . The last term in Eq. (A.1) represents the confining potential, and it is written in a general form that allows considering different strengths  $V_{\alpha_x, x}$ ,  $V_{\alpha_y, y}$  and powers  $\alpha_x$ ,  $\alpha_y$  in the  $x$ ,  $y$  directions. We will denote in what follows  $N_x$  and  $N_y$  the number of lattice sites in the  $x$ - and  $y$ -directions respectively.

In Fig. A.1 we show the single particle spectrum and its corresponding level spacing for a system with  $N_x = N_y = 100$  lattice sites confined by a harmonic potential with  $V_{2,x} a^2 = V_{2,y} a^2 = 5 \times 10^{-3} t$ . Fig. A.1(b) shows that degeneracy sets in at the very beginning of the spectrum. This degeneracy results from the symmetries of the combination lattice-confining potential. In 2D the formation of the insulator in the middle of the trap does not generate additional degeneracies in the system since it does not split the trap in independent identical parts. Then in contrast to the 1D case no information of its formation can be obtained from the level spacing.

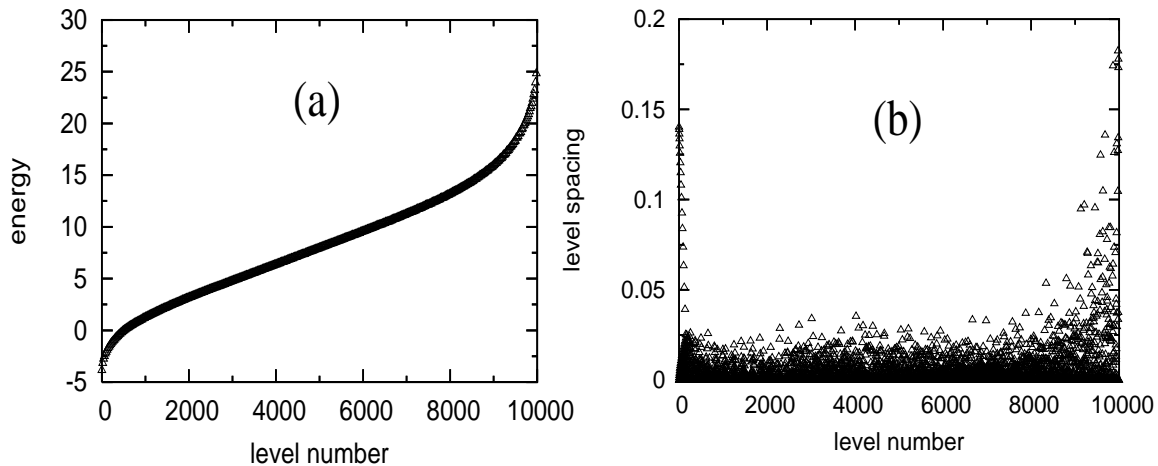


Figure A.1: Single particle spectrum (a) and level spacing (b) for a system with  $N_x = N_y = 100$ , and  $V_{2,x}a^2 = V_{2,y}a^2 = 5 \times 10^{-3}t$ .

Two density profiles and their corresponding normalized MDF for  $N_f = 1000$  and  $N_f = 4000$ , and the same trap parameters of Fig. A.1, are presented in Fig. A.2. The  $x$  and  $y$  coordinates in the trap are normalized by the characteristic lengths  $\zeta_x = (V_{2,x}/t)^{-1/2}$  and  $\zeta_y = (V_{2,y}/t)^{-1/2}$  respectively. The density profile in Fig. A.2(a) corresponds to a pure metallic phase in the 2D trap, the corresponding MDF [Fig. A.2(b)] is smooth and for some momenta it is possible to see that  $n_k = 0$  like in the 1D case. When the filling of the system is increased, the insulator appears in the middle of the trap [Fig. A.2(d)] and all the regions with  $n_k = 0$ , present in the pure metallic phase, disappear from the MDF [Fig. A.2(e)]. Figs. A.2(c),(f) show as intensity plots the normalized MDF of Figs. A.2(b),(e).

In 2D it is possible to define a characteristic density as  $\tilde{\rho} = N_f a^2 / \zeta_x \zeta_y$ . Also in this case it has always the same value when the insulator appears in the middle of the system, independently of the values and relations between  $V_{2x}$  and  $V_{2y}$ . The density profiles as function of the normalized coordinates and the MDF remain unchanged when the characteristic density is kept constant and the values and relations between  $V_{2x}$  and  $V_{2y}$  are changed (in the thermodynamic limit they will have the same form shown in Fig. A.2). This implies that the results shown in Fig. A.2 for a symmetric trap will not change for an asymmetric trap with the same characteristic density. The value of the characteristic density for the formation of the insulator in a harmonic 2D trap is  $\tilde{\rho}_C \sim 13.5$ .

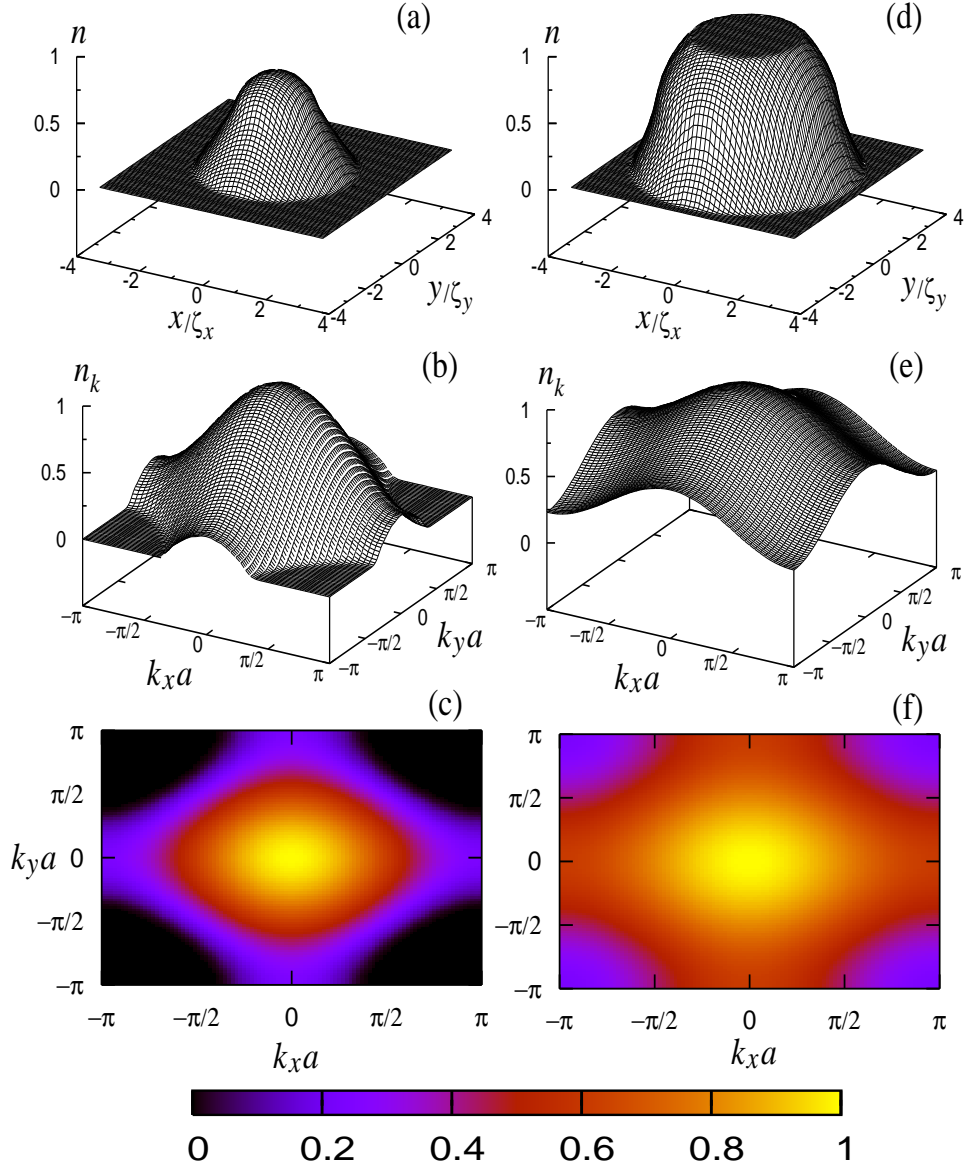


Figure A.2: 2D density profiles (a),(d), 2D normalized MDF (b),(e), and intensity plots of the 2D normalized MDF (c),(f), for  $N_f = 1000$  (a)-(c) and  $N_f = 4000$  (d)-(f) fermions in a system with  $N_x = N_y = 100$  and  $V_{2,x}a^2 = V_{2,y}a^2 = 5 \times 10^{-3}t$ .

The addition of the alternating potential leads to results similar to those presented for the 1D case (Chapter 2). Four density profiles showing the possible local phases in the 2D trap, and intensity plots of their corresponding MDF are shown in Fig. A.3. In the pure metallic case [Figs. A.3(a),(d)] the additional structure in the MDF, due to the increase of the periodicity, is present for  $k_x, k_y > \pi/2a$ . This structure also disappears when the insulator appears in the middle of the system [Figs. A.3(b),(f)], reflecting the fact that the Bragg conditions introduced by the doubling of the periodicity are fulfilled. Increasing the filling a new metallic phase appears in the center of the trap [Figs. A.3(c),(g)].

For the highest filling the insulator with  $n = 1$  develops in the middle of the trap and the MDF becomes flatter with  $n_k \neq 0$  everywhere. In a way similar to the 1D case there are confined states in the radial direction, i.e. particles are confined in rings around the center of the trap, and they can be all explained in terms of Bragg conditions. The phase diagram of the 2D case is also similar to the one in the 1D case and it is not discussed here.

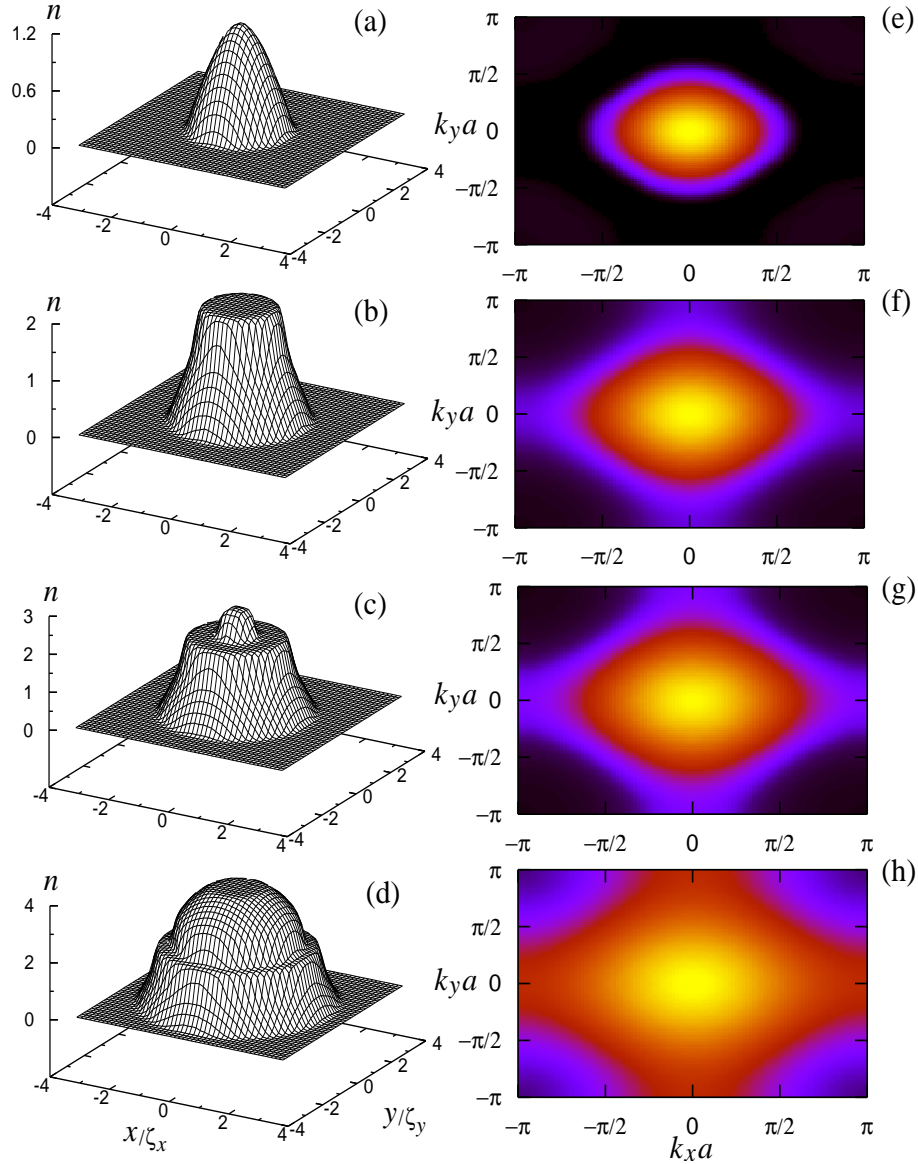


Figure A.3: Density per unit cell (a)-(d) and intensity plots of the normalized MDF (e)-(h) profiles for  $N_f = 200$  (a),(e), 800 (b),(f), 1100 (c),(g), and 3000 (d),(h) in a system with  $N_x=N_y=100$ ,  $V_{2,x}a^2=V_{2,y}a^2=5 \times 10^{-3}t$  and  $V_a=t$ . The color scale in the intensity plots of the normalized MDF is the same than in Fig. A.2.

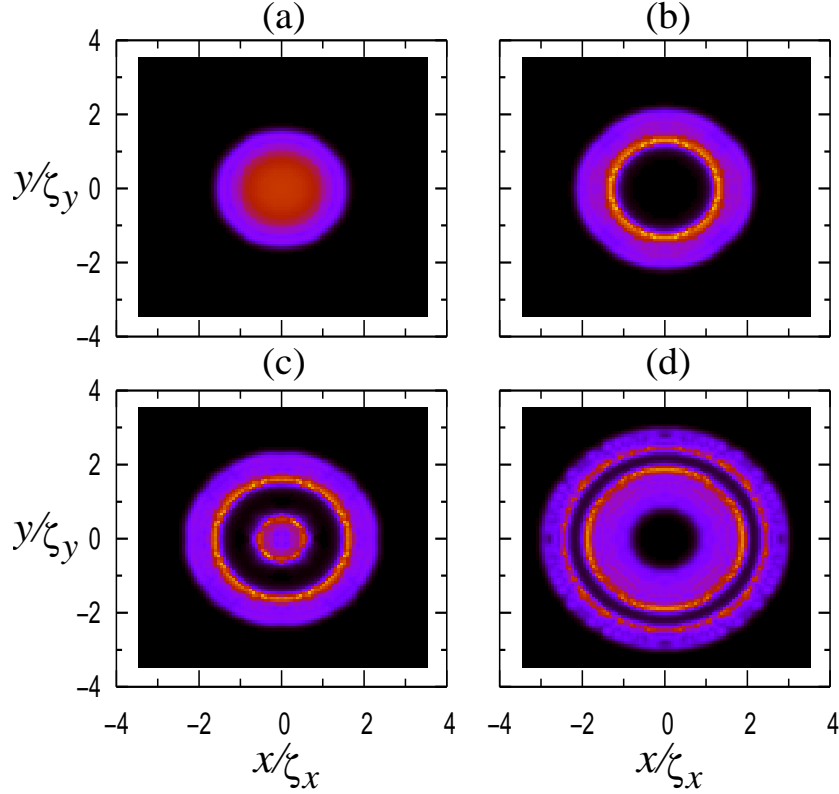


Figure A.4: Intensity plots of the local compressibility as a function of the normalized coordinates for systems with  $N_x = N_y = 100$ ,  $V_{2,x}a^2 = V_{2,y}a^2 = 5 \times 10^{-3}t$  and  $V_a = t$ . The fillings are the same that in Fig. A.3 (a)  $N_f = 200$ , (b)  $N_f = 800$ , (c)  $N_f = 800$  and (d)  $N_f = 1100$ . Black color means zero compressibility.

We close the discussion of the 2D case analyzing the local compressibility as defined in Eq. (5.3). This quantity was introduced in Chapter 5 as the local order parameter devised to characterize the local Mott insulating states in 1D. We generalize the definition to analyze the local insulating phases obtained by the combination lattice-confining potential in 2D. In this case, the extension of Eq. (5.3) is given by

$$\kappa_{i_x i_y}^\ell = \sum_{|j_x, j_y| \leq \ell(V_a)} \chi_{i_x i_y, i_x + j_x i_y + j_y}, \quad (\text{A.2})$$

where

$$\chi_{i_x i_y, j_x j_y} = \langle n_{i_x i_y} n_{j_x j_y} \rangle - \langle n_{i_x i_y} \rangle \langle n_{j_x j_y} \rangle, \quad (\text{A.3})$$

is the density-density correlation function in 2D, and  $\ell(V_a) \simeq b \xi(V_a)$ .  $\xi(V_a)$  is the correlation length of  $\chi_{i,j}$  in the homogeneous system at half-filling for a given value of  $V_a$ . Since there is a band gap in the latter case  $\chi_{i,j}$  decays exponentially, and  $\xi(V_a)$  can be determined. The parameter  $b$  is considered  $\sim 10$  as discussed in Chapter 5). The results

obtained for the local compressibility, for the same parameters of Fig. A.3, are presented in Fig. A.4. There it can be seen that the rings of local insulators of Fig. A.3 are represented in Fig. A.4 by rings of incompressible regions (black rings) so that this definition works also perfectly in the 2D case. Then we expect that the local compressibility should be a relevant quantity to characterize the local Mott insulating phases also in the trapped 2D Hubbard model.

## Appendix B

### The central limit theorem

The Monte Carlo method for evaluating integrals is based on the central limit theorem. Suppose that we have a  $d$ -dimensional integral with the following general form

$$\langle f \rangle_P = \int d^d x f(\vec{x}) P(\vec{x}), \quad (\text{B.1})$$

with  $\vec{x}$  a vector in  $d$ -dimensions and  $P(\vec{x})$  a probability distribution satisfying the conditions

$$\int d^d x P(\vec{x}) = 1, \quad P(\vec{x}) \geq 0 \quad (\text{B.2})$$

We try to approximate  $\langle f \rangle_P$  by forming the average of  $M$  independent samples of the probability distribution  $P(\vec{x})$

$$X = \frac{1}{M} \sum_{\substack{i=1 \\ \vec{x}_i \in P(\vec{x})}}^M f(\vec{x}_i), \quad (\text{B.3})$$

where  $\vec{x}_i \in P(\vec{x})$  means that the variable  $\vec{x}$  is sampled according to  $P(\vec{x})$ .

The central limit tell us that for large  $M$  the average in Eq. (B.3) becomes normally distributed about  $\langle f \rangle_P$

$$\mathcal{P}(X) \xrightarrow{M \rightarrow \infty} \frac{1}{\sqrt{2\pi}\sigma} e^{-\frac{(X - \langle f \rangle_P)^2}{2\sigma^2}}, \quad (\text{B.4})$$

with standard deviation

$$\sigma = \sqrt{\frac{1}{M} (\langle f^2 \rangle_P - \langle f \rangle_P^2)}, \quad (\text{B.5})$$

where  $\mathcal{P}(X)$  is the probability of obtaining a particular value of  $X$  when all its  $\vec{x}_i$  [Eq. (B.3)] are distributed according to  $P(\vec{x})$ . The result above is totally independent of the distribution  $P(\vec{x})$ , the function  $f(\vec{x})$ , and the dimension  $d$  of the integral. Then, a general

integral may be approximated by

$$\int d^d x f(\vec{x}) P(\vec{x}) = \frac{1}{M} \sum_{\substack{i=1 \\ \vec{x}_i \in P(\vec{x})}}^M f(\vec{x}_i) \pm \frac{1}{\sqrt{M}} (\langle f^2 \rangle_P - \langle f \rangle_P^2)^{1/2}, \quad (\text{B.6})$$

and the variance may be evaluated as

$$\langle f^2 \rangle_P - \langle f \rangle_P^2 \approx \frac{M}{M-1} \left[ \frac{1}{M} \sum_{\substack{i=1 \\ \vec{x}_i \in P(\vec{x})}}^M f(\vec{x}_i)^2 - \left( \frac{1}{M} \sum_{\substack{i=1 \\ \vec{x}_i \in P(\vec{x})}}^M f(\vec{x}_i) \right)^2 \right], \quad (\text{B.7})$$

where we note that for large  $M$  the prefactor  $\frac{M}{M-1}$  is irrelevant.

In what follows we prove that Eqs. (B.4) and (B.5) hold<sup>1</sup>.

The probability of obtaining a particular value of  $X$  when each  $\vec{x}$  is distributed according to  $P(\vec{x})$  can be calculated as

$$\mathcal{P}(X) = \int \prod_{i=1}^M d^d x_i P(\vec{x}) \delta \left[ \frac{1}{M} \sum_{j=1}^M f(\vec{x}_j) - X \right], \quad (\text{B.8})$$

which using the integral representation of the  $\delta$ -function may be written as

$$\begin{aligned} \mathcal{P}(X) &= \int \prod_{i=1}^M d^d x_i P(\vec{x}) \int \frac{M d\lambda}{2\pi} e^{i\lambda [MX - \sum_{j=1}^M f(\vec{x}_j)]} \\ &= \frac{M}{2\pi} \int d\lambda e^{i\lambda MX + M \ln \left[ \int d^d y e^{-i\lambda f(\vec{y})} P(\vec{y}) \right]} \\ &\equiv \frac{M}{2\pi} \int d\lambda e^{MF(\lambda, X)}, \end{aligned} \quad (\text{B.9})$$

where

$$F(\lambda, X) \equiv i\lambda X + g(\lambda), \quad g(\lambda) \equiv \ln \left[ \int d^d y e^{-i\lambda f(\vec{y})} P(\vec{y}) \right]. \quad (\text{B.10})$$

The integral over  $\lambda$  in Eq. (B.9) is performed, for a given  $X$ , using the stationary phase approximation<sup>2</sup>, the stationary value of  $\lambda$  is denoted as  $\tilde{\lambda}(X)$ . The stationary condition  $\frac{\partial F(\lambda, M)}{\partial \lambda} \Big|_{\tilde{\lambda}(X)} = 0$  leads to

$$X = ig' \left[ \tilde{\lambda}(X) \right] = \frac{\int d^d y f(\vec{y}) e^{-i\tilde{\lambda}(X)f(\vec{y})} P(\vec{y})}{\int d^d y e^{-i\tilde{\lambda}(X)f(\vec{y})} P(\vec{y})}, \quad (\text{B.11})$$

<sup>1</sup>We follow the proof given in Ref. [79]

<sup>2</sup>The stationary phase approximation is also known as the saddle point approximation. It is explained in what follows.

Suppose we have an integral

$$I = \lim_{M \rightarrow \infty} \int_{-\infty}^{\infty} d\lambda e^{Mf(\lambda)}.$$

Assuming that  $f(\lambda)$  has a global maximum at  $\lambda = \lambda_0$  (i.e.  $f'(\lambda_0) = 0$ ), which is significantly higher than the other maxima, the dominant contributions to the integral  $I$  when  $M \rightarrow \infty$  will come from the



which implicitly defines  $\tilde{\lambda}(X)$ . Then the probability distribution [Eq. (B.9)] can be written as

$$\mathcal{P}(X) = \left[ \frac{-M}{2\pi g''[\tilde{\lambda}(X)]} \right]^{\frac{1}{2}} e^{MF[\tilde{\lambda}(X), X]} \left[ 1 + O\left(\frac{1}{M}\right) \right]. \quad (\text{B.12})$$

However, the previous expression does not show explicitly the  $X$ -dependence of the exponent. In order to obtain it, we find its extrema

$$\frac{dF[\tilde{\lambda}(X), X]}{dX} = \frac{\partial F[\tilde{\lambda}(X), X]}{\partial X} + \frac{\partial F[\tilde{\lambda}(X), X]}{\partial \tilde{\lambda}(X)} \frac{\partial \tilde{\lambda}(X)}{\partial X} = i\tilde{\lambda}(X) = 0, \quad (\text{B.13})$$

where the stationary condition,  $\frac{\partial F[\tilde{\lambda}(X), M]}{\partial \tilde{\lambda}(X)} = 0$ , was used. We note that the extrema of  $F[\tilde{\lambda}(X), M]$  corresponds to the only solution  $[\tilde{\lambda}(X) = 0]$  for which by Eq. (B.11)  $X = \langle f \rangle_P$ . To expand up to second order around this point we calculate

$$\left. \frac{d^2 F[\tilde{\lambda}(X), X]}{dX^2} \right|_{\tilde{\lambda}(X)=0} = i \left. \frac{d\tilde{\lambda}(X)}{dX} \right|_{\tilde{\lambda}(X)=0} = \frac{1}{g''[\tilde{\lambda}(X)=0]} = \frac{-1}{\langle f^2 \rangle_P - \langle f \rangle_P^2}, \quad (\text{B.14})$$

where to obtain  $\frac{d\tilde{\lambda}(X)}{dX}$  we have differentiated Eq. (B.11) with respect to  $X$ . Eq. (B.14) shows that the extrema of  $F[\tilde{\lambda}(X), M]$  corresponds to a maximum<sup>3</sup>. In the limit  $M \rightarrow \infty$  higher terms in the expansion of the exponent almost do not contribute to the distribution. Then in the sense of distributions,  $\mathcal{P}(X)$  approaches to a normal distribution

$$\mathcal{P}(X) \xrightarrow{M \rightarrow \infty} \sqrt{\frac{M}{2\pi (\langle f^2 \rangle_P - \langle f \rangle_P^2)}} e^{-\frac{(X - \langle f \rangle_P)^2}{\frac{2}{M} (\langle f^2 \rangle_P - \langle f \rangle_P^2)}}, \quad (\text{B.15})$$

which is the results we wanted to proof [Eqs. (B.4) and (B.5)].

---

integration region around  $\lambda_0$ . In this case one may expand  $f(\lambda)$  about this point

$$f(\lambda) = f(\lambda_0) + \frac{1}{2} f''(\lambda_0) (\lambda - \lambda_0)^2.$$

The substitution of this expansion in  $I$  leads to the following result

$$\begin{aligned} I &= \lim_{M \rightarrow \infty} e^{Mf(\lambda_0)} \int_{-\infty}^{\infty} d\lambda e^{\frac{1}{2} M f''(\lambda_0) (\lambda - \lambda_0)^2} \\ &= \lim_{M \rightarrow \infty} \left[ \frac{-2\pi}{M f''(\lambda_0)} \right]^{\frac{1}{2}} e^{Mf(\lambda_0)}. \end{aligned}$$

<sup>3</sup>The second derivative  $\left. \frac{d^2 F[\tilde{\lambda}(X), X]}{dX^2} \right|_{\tilde{\lambda}(X)=0}$  is negative since the variance  $(\langle f^2 \rangle_P - \langle f \rangle_P^2)$  is positive definite.



## Appendix C

# The Hubbard-Stratonovich transformation

The Hubbard-Stratonovich transformation [143] is used to map an interacting fermion problem to a system of non-interacting fermions coupled to an auxiliary field  $s$ . It is based on the identity

$$e^{\frac{1}{2}\hat{A}^2} = \frac{1}{\sqrt{2\pi}} \int_{-\infty}^{\infty} ds e^{-\frac{1}{2}s^2 - s\hat{A}}, \quad (\text{C.1})$$

in which the right hand side is a Gaussian integral, and  $\hat{A}$  is an arbitrary operator. In the case of the Hubbard model (Eq. (3.12)) we are interested in decoupling a two body interacting term of the form

$$e^{-\Delta\tau H_U} = e^{-\Delta\tau U n_{\uparrow} n_{\downarrow}}, \quad (\text{C.2})$$

where  $n_{\sigma}$  is the site occupation for a given spin  $\sigma$ <sup>1</sup>. In order to obtain a square of an operator within Eq. (C.2), to be able to apply Eq. (C.1), we use the following identities for fermionic operators

$$\begin{aligned} n_{\uparrow} n_{\downarrow} &= -\frac{1}{2} (n_{\uparrow} - n_{\downarrow})^2 + \frac{1}{2} (n_{\uparrow} + n_{\downarrow}), \\ n_{\uparrow} n_{\downarrow} &= \frac{1}{2} (n_{\uparrow} + n_{\downarrow} - 1)^2 + \frac{1}{2} (n_{\uparrow} + n_{\downarrow} - 1), \end{aligned} \quad (\text{C.3})$$

which allow to decouple the interacting term only using real quantities for positive and negative values of  $U$ . Eq. (C.2) then can be written as

$$e^{-\Delta\tau U n_{\uparrow} n_{\downarrow}} = \frac{1}{\sqrt{2\pi}} \begin{cases} e^{-\frac{1}{2}\Delta\tau U (n_{\uparrow} + n_{\downarrow})} \int ds e^{-\frac{1}{2}s^2 + \sqrt{\Delta\tau U} s (n_{\uparrow} - n_{\downarrow})} & \text{for } U > 0 \\ e^{-\frac{1}{2}\Delta\tau U (n_{\uparrow} + n_{\downarrow} - 1)} \int ds e^{-\frac{1}{2}s^2 + \sqrt{\Delta\tau |U|} s (n_{\uparrow} + n_{\downarrow} - 1)} & \text{for } U < 0 \end{cases} \quad (\text{C.4})$$

---

<sup>1</sup>Note that we have dropped the site index  $i$  (Eq. (3.12)) to simplify the expressions.

It was later noticed by Hirsch [112], that since the fermion occupation  $n_\sigma$  is discrete and can only take values 0 and 1, in order to eliminate the fermionic interaction is enough to consider an auxiliary field with two discrete values  $s = +1$  and  $-1$ . In this case the Hubbard-Stratonovich takes the form

$$e^{-\Delta\tau U n_\uparrow n_\downarrow} = \frac{1}{2} \begin{cases} e^{-\frac{1}{2}\Delta\tau U (n_\uparrow + n_\downarrow)} \sum_s e^{\alpha s (n_\uparrow - n_\downarrow)} & \text{for } U > 0 \\ e^{-\frac{1}{2}\Delta\tau U (n_\uparrow + n_\downarrow - 1)} \sum_s e^{\alpha s (n_\uparrow + n_\downarrow - 1)} & \text{for } U < 0 \end{cases} \quad (\text{C.5})$$

with  $\cosh \alpha = e^{\frac{1}{2}\Delta\tau |U|}$ . It is interesting to note that in Eqs. (C.4) and (C.5) the auxiliary field couples to the spin degree of freedom for the repulsive case ( $U > 0$ ) and to the charge degree of freedom for the attractive case ( $U < 0$ ). Finally, it was found by Hirsch [112] that the use of the discrete transformation reduces the statistical errors produced during the quantum Monte Carlo simulations. This is the reason for which we use the discrete Hubbard-Stratonovich transformation to obtain the results shown in Chap. 5.

## Appendix D

# Determinants of different-sized matrices

To prove the identity

$$\det(\mathbf{1}_N + \mathbf{A}\mathbf{B}) = \det(\mathbf{1}_M + \mathbf{B}\mathbf{A}), \quad (\text{D.1})$$

where  $\mathbf{1}_N$  is an  $N \times N$  unit matrix,  $\mathbf{A}$  is an  $N \times M$  rectangular matrix,  $\mathbf{1}_M$  is an  $M \times M$  unit matrix, and  $\mathbf{B}$  is an  $M \times N$  rectangular matrix, we prove that in general  $f_N(\lambda) = f_M(\lambda)$  [89], where

$$f_N(\lambda) = \det(\mathbf{1}_N + \lambda\mathbf{A}\mathbf{B}), \quad f_M(\lambda) = \det(\mathbf{1}_M + \lambda\mathbf{B}\mathbf{A}). \quad (\text{D.2})$$

The functions  $f_N(\lambda)$  and  $f_M(\lambda)$  are polynomials in  $\lambda$  of order at most  $N$  and  $M$ , respectively. In addition, for  $\lambda = 0$ ,  $f_N(0) = f_M(0) = 1$ . Then, expanding  $\ln[f_N(\lambda)]$  as power series about  $\lambda = 0$  and using the relation  $\det(\mathbf{M}) = e^{\text{Tr} \ln \mathbf{M}}$ , one obtains

$$\begin{aligned} \ln[f_N(\lambda)] &= \text{Tr} \ln(\mathbf{1}_N + \lambda\mathbf{A}\mathbf{B}) = \text{Tr} \sum_{n=1}^{\infty} \frac{(\lambda\mathbf{A}\mathbf{B})^n}{n} \\ &= \text{Tr} \sum_{n=1}^{\infty} \frac{(\lambda\mathbf{B}\mathbf{A})^n}{n} = \text{Tr} \ln(\mathbf{1}_M + \lambda\mathbf{B}\mathbf{A}) = \ln[f_M(\lambda)], \end{aligned} \quad (\text{D.3})$$

where the cyclic property of the trace was used to reverse the order between  $\mathbf{A}$  and  $\mathbf{B}$  in an intermediate step.



# Bibliography

- [1] F. Dalfovo, S. Giorgini, L. P. Pitaevskii, and S. Stringari, *Rev. Mod. Phys.* **71**, 463 (1999).
- [2] Review articles, in *Proceedings of the International School of Physics “Enrico Fermi”*, edited by M. Inguscio, S. Stringari, and C. E. Wieman (IOS Press, Amsterdam, 1999).
- [3] A. J. Leggett, *Rev. Mod. Phys.* **73**, 307 (2001).
- [4] C. J. Pethick and H. Smith, *Bose-Einstein Condensation in Dilute Gases* (Cambridge University Press, Cambridge, 2002).
- [5] L. P. Pitaevskii and S. Stringari, *Bose-Einstein Condensation* (Oxford University Press, Oxford, 2003).
- [6] M. H. Anderson, J. R. Ensher, M. R. Matthews, C. E. Wieman, and E. A. Cornell, *Science* **269**, 198 (1995).
- [7] C. C. Bradley, C. A. Sackett, J. J. Tollett, and R. G. Hulet, *Phys. Rev. Lett.* **75**, 1687 (1995).
- [8] K. B. Davis, M.-O. Mewes, M. R. Andrews, N. J. van Druten, D. S. Durfee, D. M. Kurn, and W. Ketterle, *Phys. Rev. Lett.* **75**, 3969 (1995).
- [9] E. A. Cornell and C. E. Wieman, *Rev. Mod. Phys.* **74**, 875 (2002).
- [10] W. Ketterle, *Rev. Mod. Phys.* **74**, 1131 (2002).
- [11] M. Greiner, O. Mandel, T. Esslinger, T. W. Hänsch, and I. Bloch, *Nature* **415**, 39 (2002).

- [12] R. Grimm and Y. B. Ovchinnikov M. Weidemüller, *Adv. At. Mol. Opt. Phys.* **42**, 95 (2000).
- [13] P. Meystre and M. Sargent III, *Elements of Quantum Optics* (Springer-Verlag, Berlin, Heidelberg and New York, 1999).
- [14] D. Jaksch, C. Bruder, J. I. Cirac, C. W. Gardiner, and P. Zoller, *Phys. Rev. Lett.* **81**, 3108 (1998).
- [15] Mathieu's Equation, in *Handbook of Mathematical Functions*, edited by M. Abramowitz and I. A. Stegun (Dover Publications, New York, 1970).
- [16] W. Zwerger, *J. Opt. B.* **5**, S9 (2003).
- [17] M. P. A. Fisher, P. B. Weichman, G. Grinstein, and D. S. Fisher, *Phys. Rev. B* **40**, 546 (1989).
- [18] G. G. Batrouni, R. T. Scalettar, and G. T. Zimanyi, *Phys. Rev. Lett.* **65**, 1765 (1990).
- [19] W. Krauth and N. Trivedi, *Europhys. Lett.* **14**, 627 (1991).
- [20] M. Cha, M. P. A. Fisher, S. M. Girvin, M. Wallin, and A. P. Young, *Phys. Rev. B* **44**, 6883 (1991).
- [21] J. K. Freericks and H. Monien, *Phys. Rev. B* **53**, 2691 (1996).
- [22] T. Stöferle, H. Moritz, C. Schori, M. Köhl, and T. Esslinger, *Phys. Rev. Lett.* **92**, 130403 (2004).
- [23] G. G. Batrouni, V. Rousseau, R. T. Scalettar, M. Rigol, A. Muramatsu, P. J. H. Denteneer, and M. Troyer, *Phys. Rev. Lett.* **89**, 117203 (2002).
- [24] V. A. Kashurnikov, N. V. Prokof'ev, and B. V. Svistunov, *Phys. Rev. A* **66**, 031601(R) (2002).
- [25] C. Kollath, U. Schollwöck, J. von Delft, and W. Zwerger, *Phys. Rev. A* **69**, 031601(R) (2004).
- [26] S. Bergkvist, P. Henelius, and A. Rosengren, *cond-mat/0404395*.



- [27] S. Wessel, F. Alet, M. Troyer, and G. G. Batrouni, cond-mat/0404552.
- [28] B. DeMarco and D. S. Jin, *Science* **285**, 1703 (1999).
- [29] S. R. Granade, M. Gehm, K. M. O'Hara, and J. E. Thomas, *Phys. Rev. Lett.* **88**, 120405 (2002).
- [30] A. G. Truscott, K. E. Strecker, W. I. McAlexander, G. B. Partridge, and R. G. Hulet, *Science* **291**, 2570 (2001).
- [31] F. Schreck, L. Khaykovich, K. L. Corwin, G. Ferrari, T. Bourdel, J. Cubizolles, and C. Salomon, *Phys. Rev. Lett.* **87**, 080403 (2001).
- [32] Z. Hadzibabic, C. A. Stan, K. Dieckmann, S. Gupta, M. W. Zwierlein, A. Görlitz, and W. Ketterle, *Phys. Rev. Lett.* **88**, 160401 (2002).
- [33] G. Roati, F. Riboli, G. Modugno, and M. Inguscio, *Phys. Rev. Lett.* **89**, 150403 (2002).
- [34] K. M. O'Hara, S. L. Hemmer, M. E. Gehm, S. R. Granade, and J. E. Thomas, *Science* **298**, 2179 (2002).
- [35] F. Gleisberg, W. Wonneberger, U. Schlöder, and C. Zimmermann, *Phys. Rev. A* **62**, 063602 (2000).
- [36] P. Vignolo, A. Minguzzi, and M. P. Tosi, *Phys. Rev. Lett.* **85**, 2850 (2000).
- [37] A. Minguzzi, P. Vignolo, and M. P. Tosi, *Phys. Rev. A* **63**, 063604 (2001).
- [38] P. Vignolo, A. Minguzzi, and M. P. Tosi, *Phys. Rev. A* **64**, 023421 (2001).
- [39] J. Schneider and H. Wallis, *Phys. Rev. A* **57**, 1253 (1998).
- [40] M. Brack and B. P. van Zyl, *Phys. Rev. Lett.* **86**, 1574 (2001).
- [41] P. Vignolo and A. Minguzzi, *Phys. Rev. A* **67**, 053601 (2003).
- [42] G. Modugno, F. Ferlaino, R. Heidemann, G. Roati, and M. Inguscio, *Phys. Rev. A* **68**, 011601(R) (2003).

- [43] H. Ott, E. de Mirandes, F. Ferlaino, G. Roati, G. Modugno, and M. Inguscio, *Phys. Rev. Lett.* **92**, 160601 (2004).
- [44] G. Roati, E. de Mirandes, F. Ferlaino, H. Ott, G. Modugno, and M. Inguscio, *cond-mat/0402328*.
- [45] H. Ott, E. de Mirandes, F. Ferlaino, G. Roati, V. Türck, G. Modugno, and M. Inguscio, *cond-mat/0404201*.
- [46] M. Rigol and A. Muramatsu, *cond-mat/0311444*, to appear in *Phys. Rev. A*.
- [47] C. Hooley and J. Quintanilla, *Phys. Rev. Lett.* **93**, 080404 (2004).
- [48] L. Pezze', L. Pitaevskii, A. Smerzi, S. Stringari, G. Modugno, E. de Mirandes, F. Ferlaino, H. Ott, G. Roati, and M. Inguscio, *cond-mat/0401643*.
- [49] T. A. B. Kennedy, *cond-mat/0402166*.
- [50] V. Ruuska and P. Törmä, *cond-mat/0403429*.
- [51] A. Görlitz, J. M. Vogels, A. E. Leanhardt, C. Raman, T. L. Gustavson, J. R. Abo-Shaer, A. P. Chikkatur, S. Gupta, S. Inouye, T. Rosenband, and W. Ketterle, *Phys. Rev. Lett.* **87**, 130402 (2001).
- [52] M. Greiner, I. Bloch, O. Mandel, T.W. Hänsch, and T. Esslinger, *Phys. Rev. Lett.* **87**, 160405 (2001).
- [53] H. Moritz, T. Stöferle, M. Köhl, and T. Esslinger, *Phys. Rev. Lett.* **91**, 250402 (2003).
- [54] M. Olshanii, *Phys. Rev. Lett.* **81**, 938 (1998).
- [55] D. S. Petrov, G. V. Shlyapnikov, and J. T. M. Walraven, *Phys. Rev. Lett.* **85**, 3745 (2000).
- [56] V. Dunjko, V. Lorent, and M. Olshanii, *Phys. Rev. Lett.* **86**, 5413 (2001).
- [57] M. Girardeau, *J. Math. Phys.* **1**, 516 (1960).
- [58] A. Lenard, *J. Math. Phys.* **5**, 930 (1964).

- [59] A. Lenard, *J. Math. Phys.* **7**, 1268 (1966).
- [60] H. G. Vaidya and C. A. Tracy, *Phys. Rev. Lett.* **42**, 3 (1979).
- [61] M. D. Girardeau, E. M. Wright, and J. M. Triscari, *Phys. Rev. A* **63**, 033601 (2001).
- [62] A. Minguzzi, P. Vignolo, and M. P. Tosi, *Phys. Lett. A* **294**, 222 (2002).
- [63] G. J. Lapeyre, M. D. Girardeau, and E. M. Wright, *Phys. Rev. A* **66**, 023606 (2001).
- [64] T. Papenbrock, *Phys. Rev. A* **67**, 041601(R) (2003).
- [65] P. J. Forrester, N. E. Frankel, T. M. Garoni, and N. S. Witte, *Phys. Rev. A* **67**, 043607 (2003).
- [66] B. Paredes, A. Widera, V. Murg, O. Mandel, S. Fölling, I. Cirac, G. V. Shlyapnikov, T. W. Hänsch, and I. Bloch, *Nature* **429**, 277 (2004).
- [67] E. Lieb, T. Shultz, and D. Mattis, *Ann. Phys. (NY)* **16**, 406 (1961).
- [68] B. M. McCoy, *Phys. Rev.* **173**, 531 (1968).
- [69] H. G. Vaidya and C. A. Tracy, *Phys. Lett. A* **68**, 378 (1978).
- [70] B. M. McCoy, J. H. Perk, and R. E. Schrock, *Nucl. Phys. B* **220**, 35 (1983).
- [71] B. M. McCoy, J. H. Perk, and R. E. Schrock, *Nucl. Phys. B* **220**, 269 (1983).
- [72] M. Rigol, A. Muramatsu, G. G. Batrouni, and R. T. Scalettar, *Phys. Rev. Lett.* **91**, 130403 (2003).
- [73] M. Rigol and A. Muramatsu, *Phys. Rev. A* **69**, 053612 (2004).
- [74] M. Rigol and A. Muramatsu, cond-mat/0403078, to appear in *Phys. Rev. A* (R).
- [75] M. Rigol and A. Muramatsu, cond-mat/0403387.
- [76] C. Zener, *Proc. R. Soc. Lond. A* **145**, 523 (1934).
- [77] G. D. Mahan, *Many-Particle Physics* (Plenum Press, New York and London, 1986).
- [78] R. P. Feynman and A. R. Hibbs, *Quantum Mechanics and Path integrals* (McGraw-Hill, New York, 1965).

- [79] J. W. Negele and H. Orland, *Quantum many-particle systems* (Addison-Wesley, Redwood City, 1988).
- [80] L. Fosdick, *Methods Comp. Phys.* **1**, 245 (1963).
- [81] K. Binder, *Advan. Phys.* **23**, 917 (1974).
- [82] N. Metropolis, A. W. Rosenbluth, M. N. Rosenbluth, A. H. Teller, and E. Teller, *J. Chem. Phys.* **21**, 1087 (1953).
- [83] D. J. Scalapino and R. L. Sugar, *Phys. Rev. Lett.* **46**, 519 (1981).
- [84] R. Blankenbecler, D. J. Scalapino, and R. L. Sugar, *Phys. Rev. D* **24**, 2278 (1981).
- [85] D. J. Scalapino and R. L. Sugar, *Phys. Rev. B* **24**, 4295 (1981).
- [86] G. Sugiyama and S. Koonin, *Ann. Phys. (NY)* **168**, 1 (1986).
- [87] S. Sorella, E. Tosatti, S. Baroni, R. Car, and M. Parrinello, *Int. Jour. Mod. Phys. B* **1**, 993 (1988).
- [88] S. Sorella, S. Baroni, R. Car, and M. Parrinello, *Europhys. Lett* **8**, 663 (1989).
- [89] E. Y. Loh and J. E. Gubernatis, in *Modern Problems in Condensed Matter Sciences*, edited by W. Hanke and Y. V. Kopayev (North-Holland, Amsterdam, 1992), Vol. 32, pp. 177–235.
- [90] A. Muramatsu, in *Quantum Monte Carlo Methods in Physics and Chemistry*, edited by M. P. Nightingale and C. J. Umrigar (NATO Science Series, Kluwer Academic Press, Dordrecht, 1999), pp. 343–373.
- [91] F. F. Assaad, in *Quantum Simulations of Complex Many-Body Systems: From Theory to Algorithms*, edited by J. Grotendorst, D. Marx, and A. Muramatsu (John von Neumann Institute for Computing (NIC) Series, Vol. 10, FZ-Jülich, 2002), pp. 99–155.
- [92] J. E. Hirsch, R. L. Sugar, D. J. Scalapino, and R. Blankenbecler, *Phys. Rev. B* **26**, 5033 (1982).
- [93] R. H. Swendsen and J.-S. Wang, *Phys. Rev. Lett.* **58**, 86 (1987).

- [94] H. G. Evertz, G. Lana, and M. Marcu, *Phys. Rev. Lett.* **70**, 875 (1993).
- [95] N. Kawashima, J. E. Gubernatis, and H. G. Evertz, *Phys. Rev. B* **50**, 136 (1994).
- [96] H. G. Evertz, *Adv. Phys.* **52**, 1 (2003).
- [97] N. Trivedi and D. M. Ceperley, *Phys. Rev. B* **41**, 4552 (1990).
- [98] K. J. Runge, *Phys. Rev. B* **45**, 7229 (1992).
- [99] S. Sorella, *Phys. Rev. Lett.* **80**, 4558 (1998).
- [100] H. J. M. van Bemmelen, D. F. B. ten Haaf, W. van Saarloos, J. M. J. van Leeuwen, and G. An, *Phys. Rev. Lett.* **72**, 2442 (1994).
- [101] D. F. B. ten Haaf, H. J. M. van Bemmelen, J. M. J. van Leeuwen, and W. van Saarloos, *Phys. Rev. B* **51**, 13039 (1995).
- [102] S. Zhang, J. Carlson, and J. E. Gubernatis, *Phys. Rev. B* **55**, 7464 (1997).
- [103] S. Sorella and L. Capriotti, *Phys. Rev. B* **61**, 2599 (2000).
- [104] E. Y. Loh, J. E. Gubernatis, R. T. Scalettar, S. R. White, D. J. Scalapino, and R. L. Sugar, *Phys. Rev. B* **41**, 9301 (1990).
- [105] M. Brunner, F. F. Assaad, and A. Muramatsu, *Eur. Phys. J. B* **16**, 209 (2000).
- [106] M. Brunner, F. F. Assaad, and A. Muramatsu, *Phys. Rev. B* **62**, 15480 (2000).
- [107] M. Brunner, F. F. Assaad, and A. Muramatsu, *Phys. Rev. B* **63**, 180511 (R) (2001).
- [108] M. Brunner, C. Lavalley, F. F. Assaad, and A. Muramatsu, *Comp. Phys. Comm.* **147**, 690 (2002).
- [109] C. Lavalley, M. Arikawa, S. Capponi, F. F. Assaad, and M. Muramatsu, *Phys. Rev. Lett* **90**, 216401 (2003).
- [110] H. F. Trotter, *Proc. Am. Math. Soc.* **10**, 545 (1959).
- [111] M. Suzuki, *Commun. Math. Phys.* **51**, 183 (1976).
- [112] J. E. Hirsch, *Phys. Rev. B* **28**, 4059 (1983).

- [113] A. L. Fetter and J. D. Walecka, *Quantum Theory of Many-Particle Systems* (McGraw-Hill, New York, 1971).
- [114] J. R. Rice, *Numerical Methods, Software and analysis* (McGraw-Hill, New York, 1983).
- [115] W. H. Press, B. P. Flannery, S. A. Teukolski, and W. T. Vetterling, *Numerical Recipes: The Art of Scientific Computing* (Cambridge University Press, Cambridge, 1988).
- [116] R. T. Scalettar, in *Quantum Monte Carlo Methods in Physics and Chemistry*, edited by M. P. Nightingale and C. J. Umrigar (NATO Science Series, Kluwer Academic Press, Dordrecht, 1999), pp. 65–100.
- [117] R. M. Fye, Phys. Rev. B **33**, 6271 (1986).
- [118] G. G. Batrouni and R. T. Scalettar, Phys. Rev. B **46**, 9051 (1992).
- [119] N. Hatano, J. Phys. Soc. of Japan **64**, 1529 (1995).
- [120] G. G. Batrouni and R. T. Scalettar, Phys. Rev. Lett. **84**, 1599 (2000).
- [121] A. van Otterlo and K.-H. Wagenblast, Phys. Rev. Lett. **72**, 3598 (1994).
- [122] R. T. Scalettar, G. G. Batrouni, and G. T. Zimanyi, Phys. Rev. Lett. **66**, 3144 (1991).
- [123] P. W. Anderson, Phys. Rev. **115**, 2 (1959).
- [124] J. Hubbard, Proc. R. Soc. London A **276**, 238 (1963).
- [125] M. Imada, A. Fujimori, and Y. Tokura, Rev. Mod. Phys. **70**, 1039 (1998).
- [126] D. A. Butts and D. S. Rokhsar, Phys. Rev. A **55**, 4346 (1997).
- [127] G. Yuval and P. Anderson, Phys. Rev. B **1**, 1522 (1970).
- [128] E. H. Lieb and F. Y. Wu, Phys. Rev. Lett. **20**, 1445 (1968).
- [129] A. Schadschneider and J. Zittartz, Z. Phys. B **82**, 387 (1991).
- [130] P. Jordan and E. Wigner, Z. Phys. **47**, 631 (1928).

- [131] O. Penrose and L. Onsager, Phys. Rev. **104**, 576 (1956).
- [132] M. Olshanii and V. Dunjko, Phys. Rev. Lett. **91**, 090401 (2003).
- [133] G. E. Astrakharchik and S. Giorgini, Phys. Rev. A **68**, 031602(R) (2003).
- [134] M. D. Girardeau and E. M. Wright, Phys. Rev. Lett. **84**, 5691 (2000).
- [135] M. D. Girardeau and E. M. Wright, Phys. Rev. Lett. **84**, 5239 (2000).
- [136] E. B. Kolomeisky, T. J. Newman, J. P. Straley, and X. Qi, Phys. Rev. Lett. **85**, 1146 (2000).
- [137] R. K. Bhaduri and D. Sen, Phys. Rev. Lett. **86**, 4708 (2001).
- [138] E. B. Kolomeisky, T. J. Newman, J. P. Straley, and X. Qi, Phys. Rev. Lett. **86**, 4709 (2001).
- [139] K. K. Das, M. D. Girardeau, and E. M. Wright, Phys. Rev. Lett. **89**, 170404 (2002).
- [140] P. Öhberg and L. Santos, Phys. Rev. Lett. **89**, 240402 (2002).
- [141] P. Pedri, L. Santos, P. Öhberg, and S. Stringari, Phys. Rev. A **68**, 043601 (2003).
- [142] E. H. Lieb and R. Seiringer, Phys. Rev. Lett. **88**, 170409 (2002).
- [143] J. Hubbard, Phys. Rev. Lett. **3**, 77 (1959).





# Publications

Parts of the work presented in this thesis have been published in the following articles:

1. **G. G. Batrouni, V. Rousseau, R. T. Scalettar, M. Rigol, A. Muramatsu, P. J. H. Denteneer, and M. Troyer**  
*Mott Domains of Bosons Confined on Optical Lattices*  
Phys. Rev. Lett. **89**, 117203 (2002).
2. **M. Rigol, A. Muramatsu, G. G. Batrouni, V. Rousseau, R. T. Scalettar, P. J. H. Denteneer, and M. Troyer**  
*Mott domains of bosons and fermions confined in optical lattices*  
AIP Conf. Proc. **678**, 283-292 (2003).  
Lectures on the Physics of Highly Correlated Electron Systems VII: Seventh Training Course in the Physics of Correlated Electron Systems and High-Tc Superconductors, Salerno, Italy, October 14-25, 2002. Edited by A. Avella and F. Mancini, American Institute of Physics, Melville, New York, 2003.
3. **M. Rigol, A. Muramatsu, G. G. Batrouni, and R. T. Scalettar**  
*Local quantum criticality in confined fermions on optical lattices*  
Phys. Rev. Lett. **91**, 130403 (2003).
4. **C. Lavallo, M. Rigol, M. Feldbacher, M. Arikawa, F. F. Assaad, and A. Muramatsu**  
*Quantum Monte-Carlo simulations of correlated bosonic and fermionic systems*  
High Performance Computing in Science and Engineering 2003, Edited by E. Krause, W. Jäger and M. Resch, Springer-Verlag, Berlin, Heidelberg, New York, 2003.
5. **C. Lavallo, M. Rigol, and A. Muramatsu**  
*Starken Korrelationen auf der Spur (On the track of strong correlations)*  
Physik Journal **5**, 57 (2004).  
Invited paper to a special issue on Computational Physics (in German).
6. **M. Rigol and A. Muramatsu**  
*Quantum Monte Carlo study of confined fermions in one-dimensional optical lattices*  
Phys. Rev. A **69**, 053612 (2004).

7. **M. Rigol, A. Muramatsu, G. G. Batrouni, and R. T. Scalettar**

*Local Mott metal-insulator transition in confined fermions on optical lattices*

AIP Conf. Proc. **715**, 225-234 (2004).

Lectures on the Physics of Highly Correlated Electron Systems VIII: Eighth Training Course in the Physics of Correlated Electron Systems and High-Tc Superconductors, Salerno, Italy, October 6-17, 2003. Edited by A. Avella and F. Mancini, American Institute of Physics, Melville, New York, 2004.

8. **M. Rigol and A. Muramatsu**

*Confinement control by optical lattices*

To appear in Phys. Rev. A., cond-mat/0311444.

9. **M. Rigol and A. Muramatsu**

*Universal properties of hard-core bosons confined on one-dimensional lattices*

To appear in Phys. Rev. A (R), cond-mat/0403078.

10. **M. Rigol and A. Muramatsu**

*Emergence of quasi-condensates of hard-core bosons at finite momentum*

Submitted to Phys. Rev. Lett., cond-mat/0403387.

11. **C. Lavallo, M. Rigol, J. Hub, and A. Muramatsu**

*Dynamics and criticality of correlated electrons and quantum gases*

To appear in High Performance Computing in Science and Engineering 2004.

12. **M. Rigol and A. Muramatsu**

*Numerical simulations of strongly correlated fermions confined in 1D optical lattices*

To appear in Opt. Commun.

13. **M. Rigol and A. Muramatsu**

*Hard-core Bosons and Spinless Fermions Trapped on 1D Lattices*

To appear in J. Low Temp. Phys.

Proceedings of the International Symposium on Quantum Fluids and Solids, Trento, Italy, July 5-9, 2004.

14. **M. Rigol and A. Muramatsu**

*Exact numerical approach to hard-core bosons on one-dimensional lattices*

Submitted to the Proceedings of the Conference on Computational Physics 2004, Genoa, Italy, September 1-4, 2004.

15. **M. Rigol and A. Muramatsu**

*Ground state properties of hard-core bosons confined on 1D optical lattices*

Submitted to Phys. Rev. A, cond-mat/0409132.



# Curriculum Vitae

Surname: Rigol Madrazo  
First name: Marcos  
Nationality: Cuban  
Date of birth: November 21<sup>st</sup>, 1976  
Place of birth: Holguín, Cuba  
Marital status: single

- 1982-1986: Primary school: *Escuela Primaria "Rafael Freyre"*, Holguín, Cuba
- 1986-1988: Primary school: *Ateneo Deportivo "Fernando de Dios"*, Holguín, Cuba
- 1988-1991: Secondary school: *Escuela Secundaria Básica "José Antonio Echeverría "*,  
Holguín, Cuba
- 1991-1994: High school: *Instituto Preuniversitario Vocacional de Ciencias Exactas (IPVCE) "José Martí"*, Holguín, Cuba
- 1994-1999: Bachelor of Science in Nuclear Physics (Summa Cum Laude):  
*Instituto Superior de Ciencias y Tecnología Nucleares*, Habana, Cuba  
Thesis: *About an Alternative Vacuum State for Perturbative QCD*  
Supervisor: Dr. Alejandro Cabo Montes de Oca
- 1999-2000: Master of Science in Nuclear Physics:  
*Instituto Superior de Ciencias y Tecnología Nucleares*, Habana, Cuba  
Thesis: *Gluon, Quark and Hadron Masses from a Modified Perturbative QCD*  
Supervisor: Dr. Alejandro Cabo Montes de Oca
- 2001-2004 PhD in Physics (Summa Cum Laude): *Universität Stuttgart*, Germany  
Thesis: *Numerically exact studies of ultracold atoms on optical lattices*  
Supervisor: Prof. Dr. Alejandro Muramatsu



# Acknowledgments

After almost three years in Stuttgart, and with my thesis finished, I would like to thank all the people that directly or indirectly have contributed to my work and life here.

First of all I would like to thank Prof. Alejandro Muramatsu for inviting me to carry out this project, for innumerable stimulating discussions, for the support, and for the nice atmosphere that has surrounded my work here. I also thank Prof. Alejandro Muramatsu for many important (and not always work related) advises and conversations, and for all the help I have received from him during these years.

I would like to thank Prof. George G. Batrouni and Prof. Richard T. Scalettar for their fruitful collaboration, which generated one chapter (Chap. 4) and contributed to part of another one (Chap. 5) of this thesis. I also thank Prof. George G. Batrouni for his kindness and hospitality during my visit to the INLN in Nice.

I thank Prof. U. Weiß for being referee (*Mitberichter*) of this thesis and examiner in my Ph.D. examination.

I thank Prof. T. Pfau for insightful discussions on some of the subjects of this work, and for being the other examiner (*Vorsitzender*) in the exam.

During the first years of my Ph.D. work, when using QMC to study two component fermions, I received a lot of help and advise from Prof. Fakhre F. Assaad. Many thanks go to him. I also appreciate useful conversations we had at that time and the mean-field code he provided me, which was the starting point for the mean-field calculations presented in Sec. 5.5.

I would like to thank Prof. Reinhard Noack for the big help with computers during his stay in our institute. When everything crashed, which happened more than once, he was there (no matter the time) to help building everything again.

I am in debt with Fr. Ildiko Poljak for her help with all kind of problems or difficult situations that I have had here in Germany. Her kindness and nice smile were always the beginning and the end of the solution.

Many thanks go to everybody in our institute. To Fernando de León Perez for his careful reading of the manuscript. Many initial missprints were corrected thanks to him (any remaining one is all of my responsibility). To Catia Lavallo for her partnership as system manager of our computer system. We have had a lot of fun together (Right Catia?). To Martin Feldbacher for pleasant conversations (not always about physics!!) and for his help with QMC. To Mitsuhiro Arikawa for his knowledge of the one-dimensional world and for several useful references. To Heiko Gimperlein for translating the *Zusammenfassung* of this thesis and to Stefan Harrer for his careful correction of it. To Salvatore Rosario Manmana for many nice conversations.

Although geographically far from here, I would like to thank my parents, sister and grandmother Aida for their infinite love and support. Talking to them was not only a pleasure but also a big stimulus to continue. I thank also the rest of my family for their constant support, and to Jorge Rigol for useful comments on the manuscript.

A BIG thank to Raul Cruz Hidalgo. I thank him for all his help when I was coming to Stuttgart, and since then for his continuous help and advice, not to talk about the Cuban meals which, in company of Carmen Aimara and Carmen Rosa, I enjoyed infinitely.

I would like to thank Prof. Sergio Duarte and Alejandro J. Dimarco for their hospitality and invaluable help during my visit to the Brazilian Center of Research Physics (CBPF) in Rio de Janeiro (Brasil).

Here in Stuttgart, I give special thanks to Kalinca Vicente for her love and support (patience included) during the realization of this work.

Thanks go also also to all my friends here, to: Esther Barrena, Vladimir Damljanovic, Christopher Fiegel, Frank Lechermann, Magalí Lingenfelder, Ana Madrazo, Carlos Manzano, Alicia Maroto, María José Mula Portales, Alicia Nieto, Dimas Oteyza, David Quirion, Julius Reiss, Diego Repetto, Gaspar Saez (el Gaspi), Jorge Serrano, and Ana María Yelmo García, all of them have contributed to make enjoyable my stay in Stuttgart.

Finally, I gratefully acknowledge financial support from LFSP Nanomaterialien during my first two years of work and from SFB 382 during the last year. I am also grateful to a Franco-German cooperative grant (PROCOPE) for the support during my stay in Nice. Most of the calculations in this thesis were carried out on the HITACHI SR8000 of the HLR-Stuttgart (Project DynMet).





